Design, synthesis and characterisation of advanced switchable functional materials

Knichal, Jane

Award date:
2017

Awarding institution:
University of Bath

Design, Synthesis and Characterisation of Advanced Switchable Functional Materials

Jane Veronique Knichal

A thesis submitted for the degree of Doctor of Philosophy

University of Bath
Department of Chemistry

June 2017

Contents

Declaration of work done in conjunction with others

I declare that the refinement in Chapter 4 for compound **23** was completed with assistance from Dr. Chris Cameron, who is also associated with performing the SQUEEZE calculations on **21**. Computational modelling of the colour change of compounds **22** to **23** was carried out by Dr. Jonathan Skelton.

Deuterated DMF ^{1}H-NMR analysis in Chapter 5 of **27** and **28** and the associated glovebox work was carried out by Dr. Will Gee. The crystallographic modelling of the ipp guest within **28** was performed by Dr. Helena Shepherd.

Abstract

This thesis is part of an EPSRC-supported Metastable Materials project which focuses on designing new classes of solid-state advanced switchable materials. This thesis represents an important addition to exploring structure-property relations in the design, characterisation and analysis of switchable functional materials within the extent of coordination polymers (CPs).

The properties, synthesis and design of CPs are introduced in Chapter 1. Recently published developments and applications for switchable CPs are also introduced. The aims and objectives of this thesis are included.

The effects of reaction conditions and components upon lead-based CP architecture is studied in Chapter 2. 5-Ethynyl- and 5-allenyl- functionalised 1,3-benzenedicarboxylate linkers (ebdc and abdc) are reacted with $Pb(OAc)\cdot 3H_2O$, and the effect of weak intermolecular interactions on CP packing and behaviour is discussed. Two single-crystal to single-crystal (SCSC) transitions and one metallogel are observed and characterised.

Within Chapter 3, linkers ebdc and abdc were reacted with a series of first-row transition metal salts under varying conditions from which six structures in total were obtained and characterised. The extent of the effects of intermolecular interactions on resulting CP architecture is discussed, drawing on comparisons between the allenyl abdc and ethynyl ebdc functional groups.

In Chapter 4 the synthesis and characterisation of ten new frameworks comprising 4-(phenylethynyl)pyridine and a range of silver(I) salts are compared. The effects of intermolecular interactions on the resulting structures are discussed. Two structures were found to exhibit SCSC transitions on desolvation and heating, and the latter transition has been explored through DFT.

Chapter 5 details two cascade gas-induced reactions of a 1,8-bis(phenylethynyl)naphthalene guest loaded crystalline molecular flask $[(ZnI_2)_3(tpt)_2]$ (tpt = 2,4,6-tris(4-pyridyl)-1,3,5-triazine). A combination of crystallographic, gravimetric and spectroscopic techniques confirm the products and yields of both reactions.

Acknowledgements

First, I would like to thank my three supervisors Prof. Chick Wilson, Prof. Andy Burrows and Prof. Paul Raithby for their constant support over the course of my postgraduate degree. Their successful efforts in securing much needed further funding for me has been greatly appreciated. I would also like to thank both the EPSRC and the Metastable Materials groups for financial support, making the research carried out in this thesis possible.

I would like to address my thanks to my colleagues who have worked with me and alongside me; Laura Cadman, Harina Amer Hamzah, Dr. Rob Dawson, Dan Rixson and Dr. Sebastien Rochat for our frequent and often enlightening chats over tea in the office. Most importantly, I want to thank my former colleague Dr. Will Gee for his motivation, advice and support over the years, for supplying inspiration and always a thoughtful answer to my every question. Also for reading and correcting a lot of what I produced, thanks a lot, Will.

I would not have gotten far in my research without the patience and guidance of Dr. Lauren Hatcher and Dr. Helena Shepherd, who sat with and taught me structure refinement even through the small hours of the long shifts at the ALS. Their efforts added a great deal of the knowledge I needed for the completion of this thesis. I would also like to extend my sincere gratitude to Ilia A. Guzei from the University of Wisconsin-Madison for publishing and maintaining the invaluable 'Notes on Olex^2' that has been my guide through structure refinement.

A thank you also to colleagues outside of the Burrows group; Dr. Karen Ross, Dr. Fabienne Pradaux-Caggiano, Dr. Rémi Castaing, Dr. Lawrence Kershaw Cook, Pierre-Baptiste Flandrin, Dr. Dyanne Cruickshank, Dr. Anneke Klapwick and Dr. Kate Wittering for their valued direction and invaluable expertise.

Finally, I would like to direct loving thanks to my partner, friends, family and Tiger for their unwavering emotional support and encouragement, all with whom these past few years have been so enjoyable.

Dissemination

Publications

J. V. Knichal, W. J. Gee, A. D. Burrows, P. R. Raithby, S. J. Teat and C. C. Wilson, "A facile single crystal to single crystal transition with significant structural contraction on desolvation" *Chem. Comm.*, **2014**, 50, 14436-14439.

J. V. Knichal, W. J. Gee, A. D. Burrows, P. R. Raithby and C. C. Wilson, "Role of ethynyl-derived weak hydrogen-bond interactions in the supramolecular structures of 1D, 2D, and 3D coordination polymers containing 5-ethynyl-1,3-benzenedicarboxylate" *Cryst. Growth & Des.*, **2015**, 15, 465-474.

J. V. Knichal, W. J. Gee, A. D. Burrows, P. R. Raithby and C. C. Wilson, "A new small molecule gelator and 3D framework ligator of lead(II)" *CrystEngComm*, **2015**, 17, 8139-8145.

J. V. Knichal, H. J. Shepherd, C. C. Wilson, P. R. Raithby, W. J. Gee and A. D. Burrows, "An iodine-vapor-induced cyclization in a crystalline molecular flask" *Angew. Chem. Int. Ed.*, **2016**, 55, 5943-5946.

H. J. Shepherd, G. Tonge, L. Hatcher, M. Bryant, J. V. Knichal, P. R. Raithby, M. Halcrow, R. Kulmaczewski, K. J. Gagnon, S Teat, "a high pressure investigation of the order-disorder phase transition and accompanying spin crossover in $[FeL1_2](ClO_4)_2$ (L1 = 2,6-bis{3-methylpyrazol-1-yl}-pyrazine)" *Magnetochemistry*, **2016,** 2(1), 9.

J. V. Knichal, W. J. Gee, C. A. Cameron, J. M. Skelton, K. J. Gagnon, A. D. Burrows, P. R. Raithby, and C. C. Wilson, "Exploring structure-property relationships of silver 4-(phenylethynyl)pyridine complexes" *Eur. J. Inorg. Chem.*, **2017**, 2017(13), 1855-1867.

Chapter 2 "Tuning the properties of metal-organic frameworks by post-synthetic modification" by A. D. Burrows, L. K. Cadman, W. J. Gee, H. Amer-Hamzah, J. V. Knichal and S. Rochat in the upcoming Wiley book entitled *Metal Organic Frameworks: Applications in Separations and Catalysis* that will be published in late 2017.

Posters and Presentations

J. Knichal, W. Gee, A. Burrows, P. Raithby and C. Wilson, "Novel coordination polymers containing alkyne ligands exhibiting solvent-induced single-crystal-to-single-crystal transitions" [poster] *Inorganic Chemistry Joint Interest Group Meeting*, Warwick, UK, April 2014.

J. Knichal, W. Gee, A. Burrows, P. Raithby and C. Wilson, "Incorporating cycloaddition reactions into metal-organic frameworks" [poster] *Department of Chemistry Metastable Meeting*, Bath, UK, May 2014.

J. Knichal, A. Burrows, P. Raithby and C. Wilson, "Incorporating [2+2] cycloaddition reactions into coordination networks" [presentation] *Department of Chemistry Metastable Meeting*, Bath, UK, July 2014.

J. Knichal, A. Burrows, P. Raithby and C. Wilson, "Coordination networks containing carboxylate ligands" [presentation] *Department of Chemistry 2nd year PhD talks*, Bath, UK, February 2015.

J. Knichal, W. Gee, A. Burrows, P. Raithby and C. Wilson, "A new small molecule gelator and 3D framework ligator of lead(II)" [poster] *RSC CODG Meeting*, Oxford, UK, September 2015.

J. Knichal, A. Burrows, P. Raithby and C. Wilson, "Silver(I) 4-(phenylethynyl)pyridine coordination polymer morphologies" [poster] *39th BZA Annual Meeting*, Bath, UK, March 2016.

J. Knichal, A. Burrows, P. Raithby and C. Wilson, "Observing single-crystal to single-crystal transitions in coordination polymers" [presentation] *Department of Chemistry Postgraduate Symposium*, Bath, UK, May 2016.

J. Knichal, H. Shepherd, C. Wilson, P. Raithby, W. Gee, A. Burrows, "Gas-induced cascade reactions in a crystalline molecular sponge" [poster] *Faculty of Science Postgraduate School Research Afternoon*, Bath, UK, June 2017.

List of units and abbreviations

1D	One dimensional
2D	Two dimensional
3D	Three dimensional
abdc	5-Allenyl-1,3-benzenedicarboxylate
ALS	Advanced Light Source
bpen	1,8-Bis(phenylethynyl)naphthalene
CCDC	Cambridge crystallographic data centre
CN	Coordination number
CMF	Crystalline molecular flask
CP	Coordination polymer
CTC	Crystal-to-crystal
D	X···A hydrogen bond distance
d	Doublet
d	H···A hydrogen bond distance
dd	Doublet of doublets
δ	NMR Chemical shift scale
DCM	Dichloromethane
DEA	Diethyl formamide
DFT	Density functional theory
DMA	Dimethyl acetamide
DMF	Dimethyl formamide
DSC	Differential scanning calorimetry
ebdc	5-Ethynyl-1,3-benzenedicarboxylate
ESI	Electrospray ionisation
FTIR	Fourier transform infrared spectroscopy
g	Gram
h	Hour
hipp	12-Hydroxy-7-iodo-2-phenylindeno[2,1-α]phenalen-1(12 *H*)-one
ipp	7-Iodo-12-phenylindeno[2,1-α]phenalene
K	Kelvin
M	Molar
m	Multiplet
mg	Milligram
MHz	Megahertz
mL	Millilitre
mmol	Millimole
MOF	Metal-organic framework
mp	Melting point
m/z	Mass-to-charge ratio

NMP	*N*-Methyl-2-pyrrolidone
NMR	Nuclear magnetic resonance
PCP	Porous coordination polymer
pep	4-(Phenylethynyl)pyridine
PFA	Paraformaldehyde
PSM	Post-synthetic modification
PXRD	Powder X-ray diffraction
RT	Room temperature
s	Singlet
SBU	Secondary building unit
SCSC	Single-crystal to single-crystal
SEM	Scanning electron microscope
t	Triplet
TFH	Tetrahydrofuran
TGA	Thermogravimetric analysis
θ	X–H···A approach angle
TM	Transition metal
Tos	p-Toluene sulphonate
tpt	2,4,6-Tris(4-pyridyl)-1,3,5-triazine
UV	Ultraviolet
VSEPR	Valence shell electron-pair repulsion
% w/v	Weight to volume percentage

Chapter 1

Introduction

1.1. Coordination polymers

Metal organic coordination polymers (CPs) are materials consisting of repeating units of metal centres bridged by organic linkers *via* coordination bonds which self-assemble to create a crystalline motif.[1] In order for a compound to be classified as a CP, the bridging organic linker must contain at least one carbon atom sandwiched between two donor atoms which act as the coordination site to the metal.[2] Over the past 20 years, CPs have received increasing attention as a potential platform in applications such as gas sorption and separation,[3,4] catalysis,[5,6,7] sensing,[8,9,10] porous conductive materials,[11] and as templates and precursors for nanoscale molecular assembly.[12] Coordination polymers can adopt various dimensionalities which can determine their properties, forming 1D chains, 2D sheets and 3D frameworks, as illustrated in Figure 1 below. Although 0D coordination complexes are not classed as coordination polymers, they nonetheless can serve as important instances of molecular crystal engineering, offering interesting structural counterpoints to the 1D, 2D and 3D CPs.

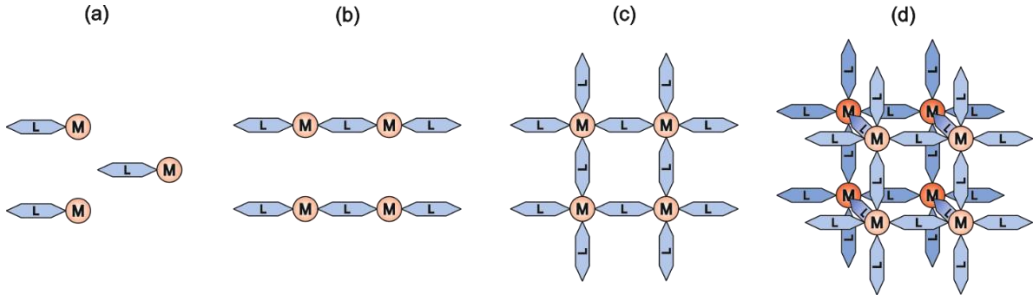

Figure 1: *Metal nodes (M) and organic linkers (L) in (a) a 0D coordination compound and (b) 1D, (c) 2D and (d) 3D dimensionalities of coordination polymers.*

Metal-Organic Frameworks (MOFs) are a class of coordination polymer. There has been some debate about what terminology should be used on what compounds. The choice of MOF or CP tends to arise from different groups having different preconceptions of chemical bonding; specifically scientists with a solid-state background versus chemists predominantly practicing coordination chemistry.[13] A

consensus of an IUPAC expert group assembled in 2009 was given in the 2013 IUPAC recommendations on definitions of metal-organic frameworks and coordination polymers.[14] The proposal defined a coordination polymer as "A coordination compound with repeating coordination entities extending in 1, 2 or 3 dimensions" and a metal-organic framework was defined as "A Metal-Organic Framework, abbreviated to MOF, is a Coordination Network with organic ligands containing potential voids". For the purposes of this thesis, the term coordination polymer (CP) will be used throughout.

From the stoichiometric combination of a metal ion and an organic linker, a limitless possibility of both structurally and functionally interesting structures can be obtained. Unlike covalent bond-derived organic polymers, the labile coordination bonds of CPs allow a crystallographically ordered periodic 3D structure to be achieved. This ordering of the CP lattice allows detailed structural determination through X-ray crystallography, and consequently detailed structure-property correlations.

1.1.1. Connector and linker components

Coordination polymers contain two central components; metal units and organic linkers. These components are defined as starting reagents with which the principal framework, and potentially secondary building units (SBUs) (section 1.1.3.), of the CP are constructed. Auxiliary components such as solvents, counterions and guest molecules which may interact with or direct the self-assembly process of the CP will be introduced later.

An important characteristic of both connector and linker components is the number and orientation of their binding sites (coordination numbers and coordination geometries) which govern their nodal connectivity and ultimately the architecture of the resulting framework. Due to their predictable yet versatile coordination geometries, transition metal (TM) ions are often utilised in the construction of CPs.[15] Depending on the metal and its oxidation state, coordination numbers usually range from 2 to 7, giving rise to various geometries which can be linear, T- or Y-shaped, tetrahedral, square-planar, square-pyramidal, trigonal-bipyramidal, octahedral, trigonal-prismatic, pentagonal-bipyramidal, as well as their corresponding distorted forms (Figure 2).

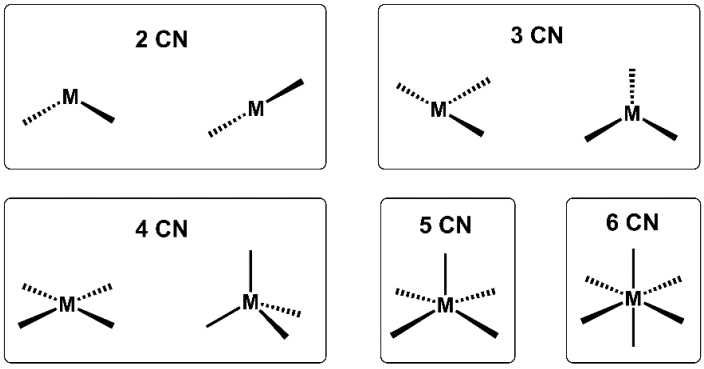

Figure 2: *A range of possible transition metal coordination numbers (CN).*

Although using transition metals has the advantage of allowing the prediction of which structures may be formed, whether the connector is a single metal centre or within an SBU, it is less common to exceed a coordination number of six within the TM series. For this reason lanthanide and heavier main group metals are often used in synthesis as they have been shown to have coordination numbers up to 12.[16] These often labile coordination environments are, however, much more flexible, and so the architectures of the resulting networks are harder to predict.

Although the nature of the metal salt chosen is important, the diversity in coordination polymers comes largely through the wide variability and creativity of ligand design. Nonetheless, there are a number of features common to most ligands used. Typically, a ligand might have two or more divergent coordination sites and these are usually pyridyl, nitrile or carboxylate functional groups. By varying the aliphaticity of the bridging linker, these ligands can range from very rigid to completely flexible. Examples of commonly used neutral and anionic CP linkers are illustrated in Figure 3.

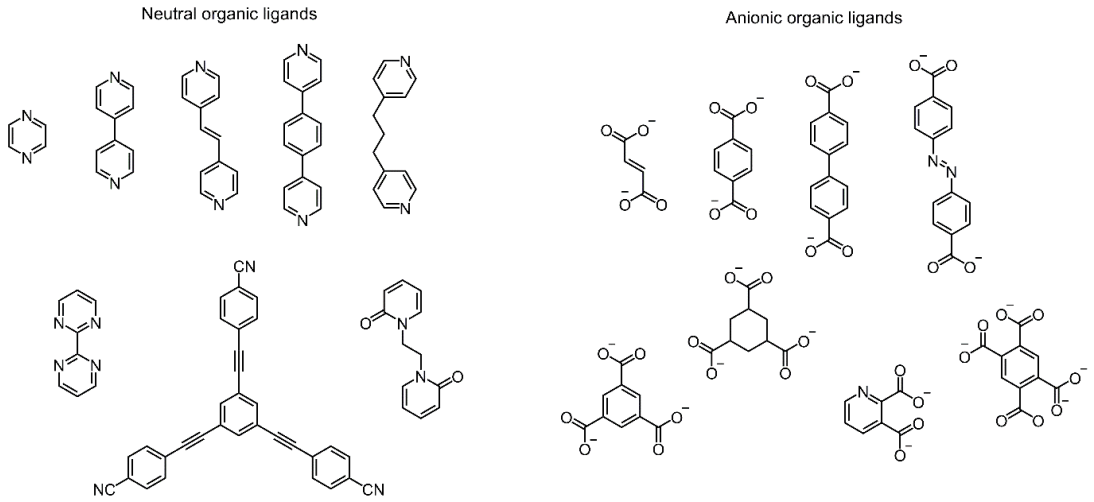

Figure 3: *Examples of linkers used in coordination polymers.*

The inclusion of an organic linker with variable binding sites or a co-ligand increases the potential self-assembly routes between the components and the outcome becomes harder to predict.

1.1.2. Classifications

When the metals and linkers are simplified down to geometrically connecting nodes and linear linkers, most coordination polymers can be reduced into repeating motifs ranging in periodicity. Categorising CPs is an important step in the characterisation and analysis of these materials. Schläfli, point and vertex symbols mathematically surmise the sequences of vertices making up a framework, taking into account the number and size of ring motifs emanating from each vertex in the structure.[13,17] For nets of higher coordination and complexity, however, such symbols can get cumbersome. A reticular-based system, the RCSR (Reticular Chemistry Structure Resource), lists all the most common topologies of frameworks and polyhedra by a three letter code according to their symmetry and connectivity.[18] When used appropriately, these descriptors can be powerful techniques in defining CPs, and can aid the description of complicated structures.

Perhaps the most basic characterisation of CPs is by periodicity. Discrete complexes can be described as zero-dimensional coordination compounds, and although not linked through coordination bonds, these complexes pack together into crystalline lattices by intermolecular bonds and can have important properties, for example in use as drug delivery systems due to their high solubility.[19] Coordination compounds can form extended structures through hydrogen bonds or π···π interactions. The same principles for the synthesis of these materials are used as those for generating their polymer counterparts described below.

1D systems represent the simplest of the crystalline motifs for CPs. These can assemble into a variety of single periodicity motifs, including ribbons, ladders, zig-zag patterns and the less common helical and rotaxane polymers (Figure 4). The helix motif remains quite rare in the context of coordination polymers, but there is added interest because it is inherently chiral regardless of what its components might be, with the chirality originating from the spatial disposition of the assembled components rather than the presence of chiral atoms.[20,21]

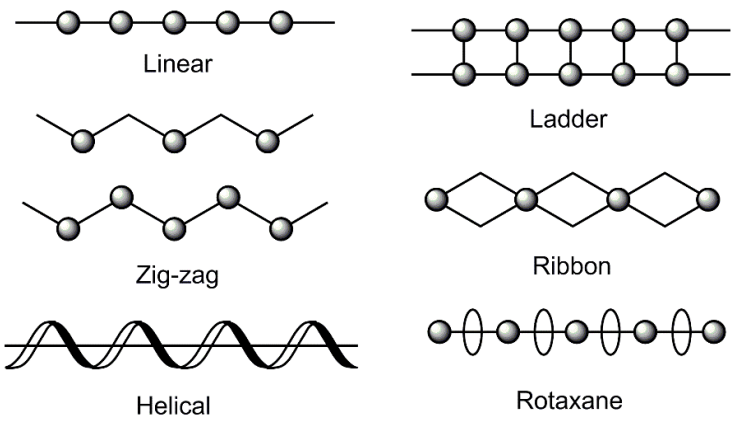

Figure 4: *Schematic representations of common 1D CP motifs.*

One-dimensional CPs can contain higher dimensional aspects, such as the 2D node components within ladder motifs as shown in the illustration above. The structure of a 1D tube-like polymer formed by Ag(I) and 1,3,5-triaminocyclohexane was constructed by Cronin et al.[22] (Figure 5), in which both the metal and ligand components act as 3-connecting nodes. Although the polymer has a definitive tubular geometry, a side-on perspective of the architecture is reminiscent of a ladder formation.

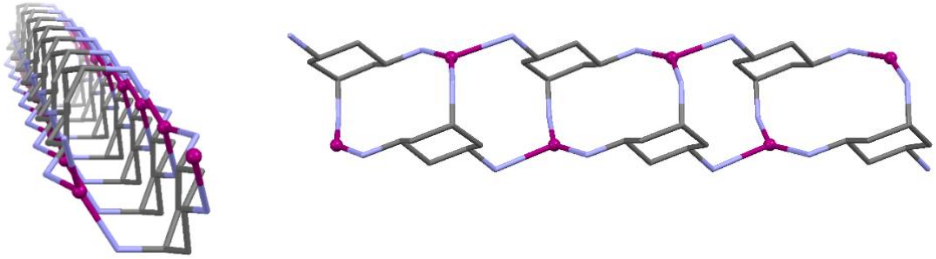

Figure 5: *A 1D tube network constructed from Ag(I) and 1,3,5-triaminocyclohexane, viewed (left) end-on and (right) side-on.*

The strategy of utilising known coordination geometries of metals to propagate 2D structures *via* coordination with linear bridging spacer ligands has yielded many examples of coordination polymers with various architectures. Figure 6 illustrates some of the 2D nets that have thus far been observed in CPs, including nets which exhibit mixed connectivities as well as pore types.

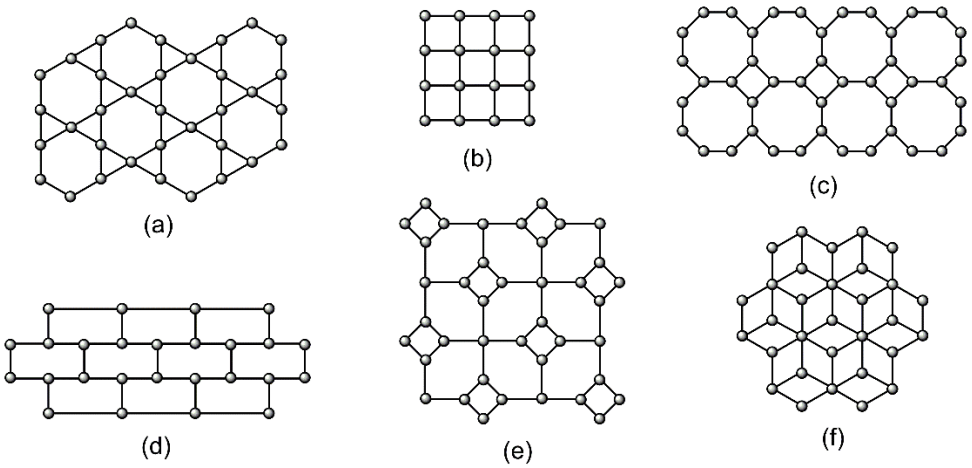

Figure 6: *Schematic representations of 2D CP motifs (a) 4-connected Kagomé net (b) 4-connected square-based net (c) 3-connected net (d) 3- brick wall net (e) 3- and 4- connected net (f) 3- and 6-connected net.*

Similar to 1D coordination polymers, 2D nets can also exhibit higher dimensionality aspects. A common example are 2D bilayer assemblies. The 2D CP $\{[Yb(L)_3](CF_3SO_3)_3\}_\infty$ (L = 4,4'-bipyridine-N,N'-dioxide) was obtained by Schröder et al. through direct synthesis of $Yb(CF_3SO_3)_3$ and L in MeOH and $CHCl_3$, the resulting structure within which excess ligands bridge pairs of 2D nets (Figure 7).[23]

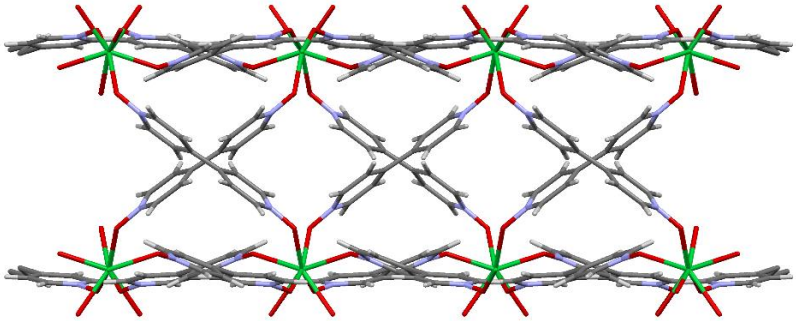

Figure 7: *A 2D bilayer formed from a pair of 2D nets and bridging 4,4'-bipyridine-N,N'-dioxide ligands.*

The 'node' and 'linker' strategy can also be applied to the classification of three-dimensional CPs. There are a large number of possible 3D nets, yet through computational methods, a significant proportion of them can be categorised into a relatively small number of basic nets, according to a study by Yaghi and O'Keeffe et al. in 2004.[24] The study analysed all reported 3D CPs available at the time and found that most fit into five basic nets, each distinguished by the geometry of its building block. The study found that tetrahedral nodes are predisposed to generate 4-connected 'diamondoid' architectures, whereas octahedral nodes are expected to afford 6-

connected cubic networks (Figure 8). Thus, node connectivity is a useful method to categorise these frameworks. The most common framework connectivities are 3, 4 and 6, with 5- connected or higher connectivity frameworks being less common.

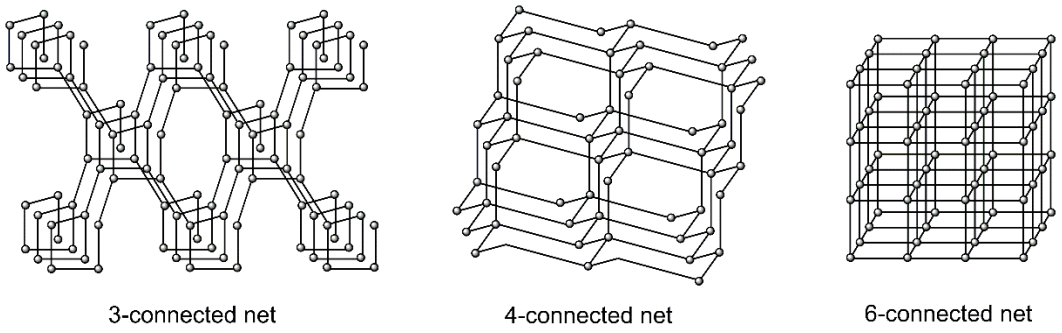

Figure 8: *Examples of 3-, 4-connected 'diamondoid' and 6- connected 3D nets.*

Three-dimensional CPs are most disposed to display porosity, and would therefore be termed porous coordination polymers, PCPs. Not all 3D frameworks constitute the conventional 'linker' and 'node' architecture, for example when characterising infinite fused inorganic backbones that propagate through the structure. Bu et al. and Wang et al. individually synthesised a 3D rigid coordination polymer $[M_2(btr)_2]\cdot 2NO_3\cdot x$ (btr = 4,4′-bis(1,2,4-triazole), x = lattice solvents), from Cu and Ag salts respectively, consisting of intersecting helical rod building units (Figure 9), each comprising one M centre connected by two N atoms.[25,26] The 'nodes' within the structure are essentially fused into continuous helical motifs running throughout the structure, and thus could be categorised as having infinite connectivities.

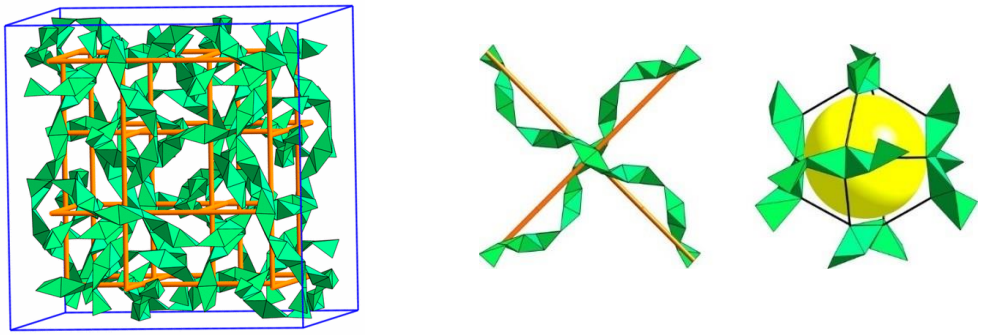

Figure 9: *Computational models of helical motif of $[M_2(btr)_2]\cdot 2NO_3\cdot x$ of the (left) unit cell and (right) two intersecting fragments by bridging linkers illustrated as heavy lines.*[27]

These two groups characterised their structures very differently and both believed their structures to be unique; Gao et al. described the framework as nested 'cores' within larger 'shell' polyhedra, while Wang et al. described the structure as a series of

fused cages. Through computational modelling of both structures by Proserpio et al., a common helical motif was found.[27] This presents the potential subjectivity of node and linker determination when characterising a complex framework.

1.1.3. Secondary building units and isoreticular series

The idea of determining the topology of the CP by counting each metal atom as a node breaks down with the introduction of the formation of secondary building units (SBUs) within the framework. These are structural entities representing the inorganic clusters or coordination spheres that may act as nodes within the framework. Examples of some SBUs that are commonly encountered in metal carboxylate CPs are illustrated in Figure 10. The coordination geometry of each individual metal atom environment does not necessarily correspond with the overall connector geometry of the SBU.

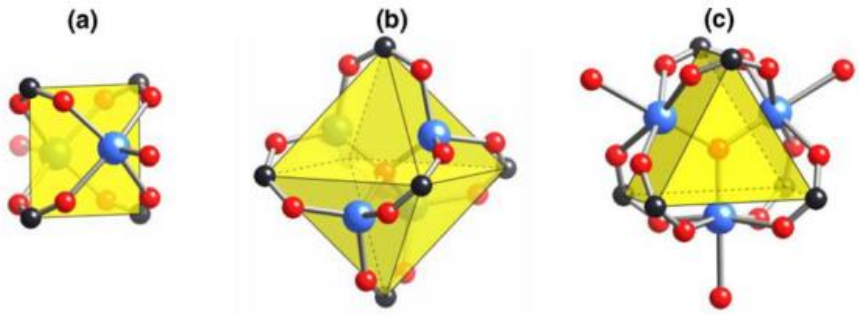

Figure 10: *Inorganic SBUs that commonly occur in metal carboxylates include (a) the square "paddlewheel", (b) the octahedral "basic zinc acetate" cluster, and (c) the trigonal prismatic oxo-centered trimer.*[1]

Although many of these units have been observed in coordination polymers,[28,29] they are generally not introduced directly, but are formed as a result of specific conditions within CP self-assembly. Kaskel et al. tuned the flexibility of a porous CP $[Zn_3(bpydc)_2(HCOO)_2]$ (bpydc = 2,2'-bipyridyl-5,5'-dicarboxylate) by functionalising the SBU with monocarboxylic acids of varying backbone length.[30] Functionalisation with small carboxylic acids resulted in complete closing of the framework pores after solvent removal whereas bulkier carboxylates lead to incomplete closing of the framework pores after desolvation.

This systematic functionalisation of a model framework can result in the synthesis of an isoreticular series, in which the modified CPs consist of the same structural skeleton but exhibit different functionalities and dimensions. Perhaps the most well-known reticular series is of functionalised MOF-5 synthesised by Yaghi et al., demonstrating the potential for functionalisation and expansion of porous three-dimensional frameworks (Figure 11).[31]

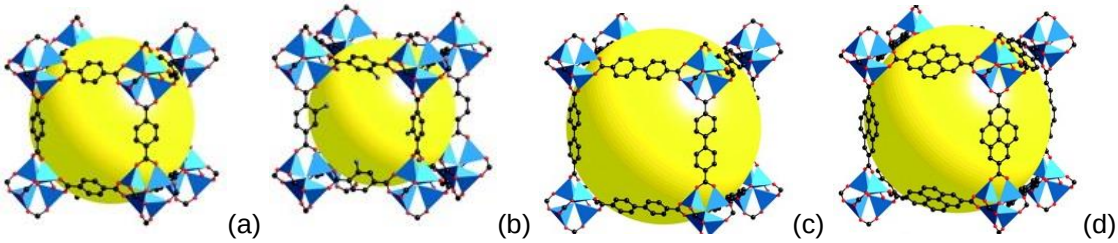

Figure 11: *Four examples from Yaghi's isoreticular series including the linkers (a) benzenedicarboxylate, (b) 3-bromobenzenedicarboxylate (c) 4,4'-biphenyldicarboxylate (d) 2,7-pyrenedicarboxylate. The yellow spheres represent the largest van der Waals spheres that would fit in the cavities without touching the frameworks.*[31]

1.1.4. Interpenetration and interdigitation

One of the consequences of energy minimisation during the self-assembly process of a CP is the diminishing of void space within the framework. Structures alleviate the formation of these voids by three common ways: intercalation, interdigitation, or interpenetration.[32] Intercalation is the inclusion of void filling guest molecules, usually solvent, counterion or uncoordinated ligand (Figure 12a). Interdigitation is when ligands or groups from one polymer project into the other adjacent polymer (Figure 12b). Interpenetration is the complete interweaving of two or more polymers, such that they cannot be separated topologically without the breaking of bonds (Figure 12c).

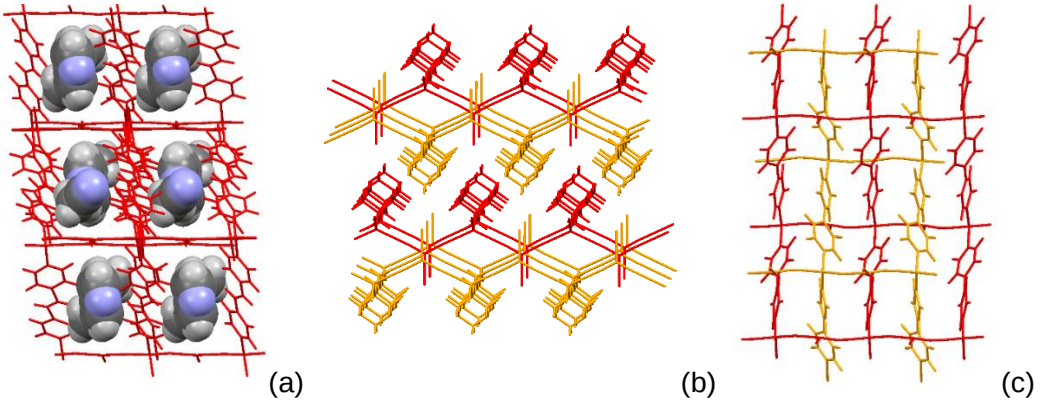

Figure 12: *Examples of void-filling within frameworks; (a) intercalation of ligands and solvent molecules within the framework void spaces, (b) interdigitation of 2D nets via C≡N groups and (c) interpenetration of two identical 2D nets.*

Often structures artificially increase in dimensionality through interpenetration, as illustrated for 1D → 2D and 2D → 3D in Figures 13a and 13b. Sometimes a net of a different architecture can be interpenetrated into another, although this is less commonly observed (Figure 13c).

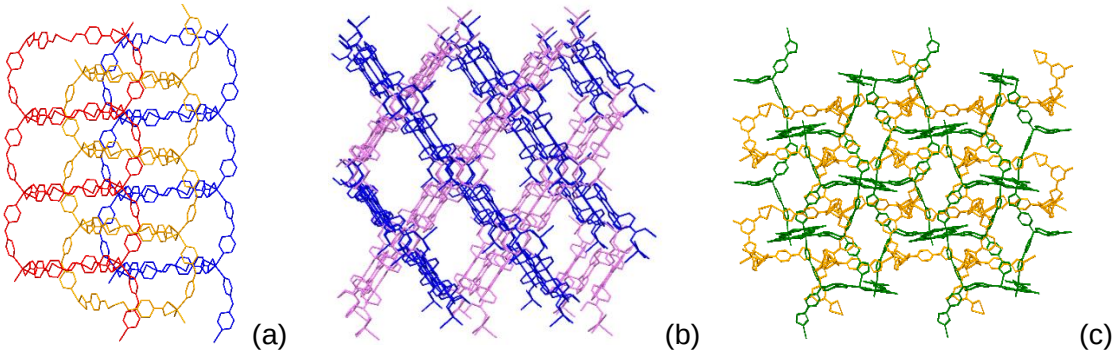

Figure 13: *Examples of interpenetration within CPs. (a) 1D → 2D three-fold interpenetration,*[33] *(b) 2D → 3D sheet interpenetration,*[34] *and (c) heterogeneous interpenetration of two 3D frameworks.*[35]

1.2. Coordination polymer synthesis

It is well known that the resultant structures and properties of CPs do not depend solely on the components, they are also based on many synthetic conditions such as temperature,[36,37] molar ratio of starting materials,[38] concentration,[39] solvent type,[40,41] time,[42] and presence of counterions.[43] Synthetic conditions applied when preparing a coordination polymer can have a strong impact on the nature of the product. Properties such as yield, reaction time, crystal size, topology and morphology can be affected.[44-49]

1.2.1. Influence of metal and linker components

The linker and node design approach often assumes the geometries and connectivities of the ligand and metal are fixed, however, metals often have variable geometries and ligands can bind differently to expectation. As mentioned in Section 1.1.1., flexible ligands can be unpredictable, and even rigid linkers can exhibit multiple binding modes. Changing the component ratio[50] or functional group on the ligand[51,52] can have dramatic changes on the resulting architecture and properties of a coordination polymer. Itoh et al. obtained one capsule 0D compound and one zig-zag 1D CP from the reaction of square-planar Pd(II) and Cu(II) with 1,3,5-triethylbenzene, despite the coordination geometry of the metal centres of both complexes being the same.[53]

Chen et al. showed that the structural variations of a CP can be entirely dependent upon the coordination properties of an anionic co-ligand.[54] The group reported the assembly of the Ag(hmt) (hmt = hexamethylenetetramine) polymer to change in architecture and dimensionality in a series of mixed ligand CPs depending on the nature of the co-ligand. Scheme 1 displays the schematic diagram of observed CP structures generated by reacting Ag_2O and hmt with various co-ligands including 4-hydroxybenzoic acid, 4-aminobenzoic acid, 4,4'-biphenyldicarboxylic acid, 4-pyridinecarboxylic acid, benzenesulfinic acid, and 1,4-butanedioic acid.

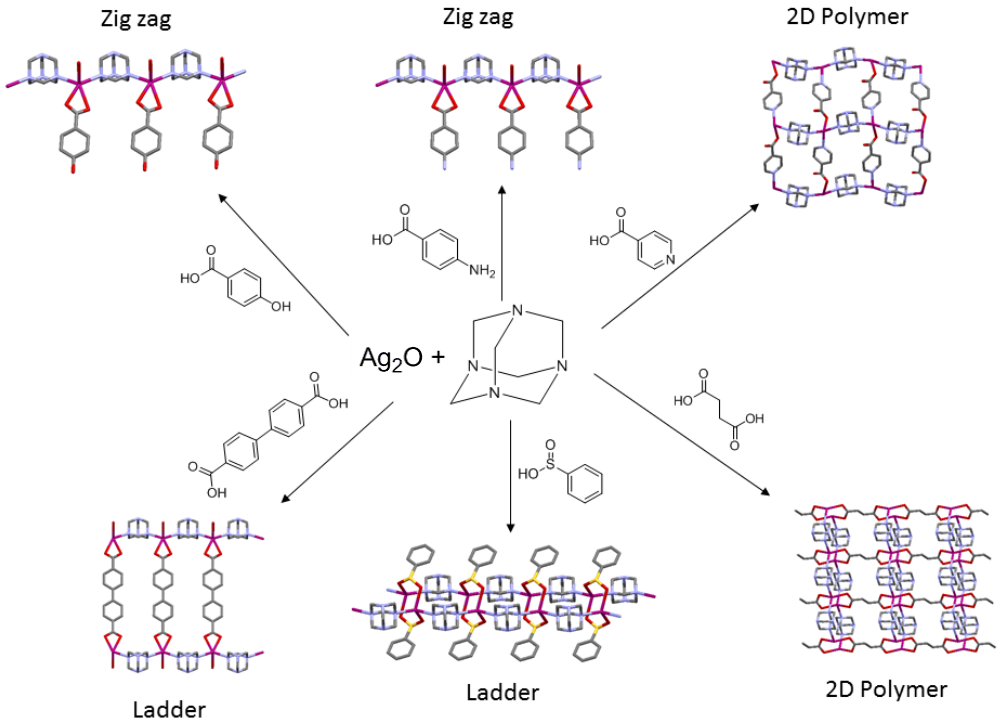

Scheme 1: *Various CP structures generated by linking [Ag(hmt)] chains with different co-ligands.*

The authors found that both monocarboxylate co-ligands generated 1D zig-zag CPs while dicarboxylate ligands linked the zig-zag chains into ladder-like structures. The 4-pyridinecarboxylic acid co-ligand with two binding sites coordinated to the Ag(I) ions to build a 2D grid network. Benzenesulfinate and 1,4-butanedioate ligands formed bilayer 2D net structures.

1.2.2. Influence of solvent and temperature

The modulation of size and morphology of the CP crystals by controlling the solvent composition has been widely applied, for example in cases of incorporating environmentally benign solvents such as water into CP synthesis,[55] or for tuning crystal sizes for the purpose of drug delivery or biomedical imaging.[56] Factors such as solvent and temperature can also have profound effects on the architectural outcome of the target CP. Banerjee et al. investigated the degree of interdigitation in 2D structures depending on the solvent used.[57] Two isomeric fluorinated frameworks $[Cu_2(hfbba)_2(3\text{-mepy})_2]$ hfbba = 4,4'-(hexafluoroisopropylidene)bisbenzoate, mepy = 3-methyl pyridine) were synthesised in the presence of N,N'-diethyl formamide (DEF) or N,N'-dimethyl formamide (DMF) from which the former solvent gave a two-fold interpenetrated 2D net, and the latter a non-interpenetrated net with excess DMF and uncoordinated 3-mepy occupying the lattice voids.

Three 1D, 2D, and 3D CPs comprising Mg(II) and 4,5-imidazoledicarboxylate (idc) were synthesised by Maji et al. *via* a hydrothermal technique through careful control of the temperature and pH.[58] Reacting a 1:1 ratio of metal to linker at 150 °C afforded a 1D porous network, increasing the temperature to 180 °C afforded a 2D net, and a 3D framework was obtained as a result of further increasing the temperature to 200 °C coupled with an increase in the reaction pH (Scheme 2).

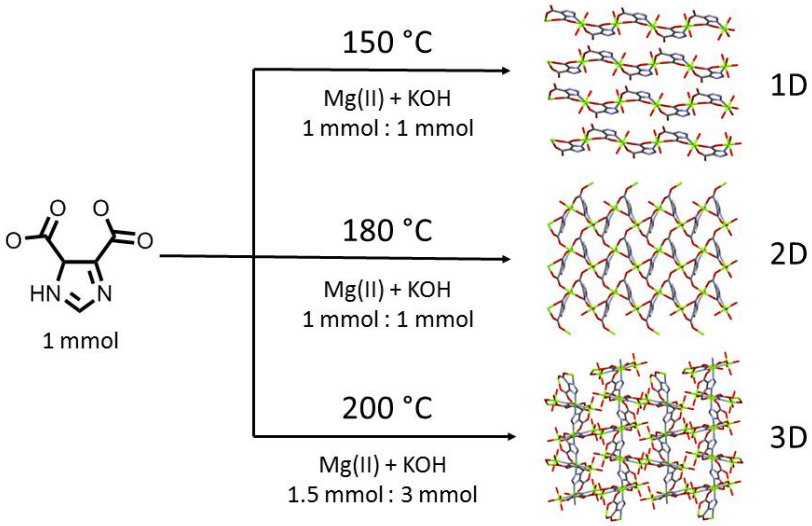

Scheme 2: *Overview of the synthetic conditions and CP products of reacting Mg(II), KOH and idc.*

1.2.3. Influence of counterions

Besides metal and ligand interactions, counterions also have an important role in the assembly of coordination polymers. This is especially apparent if working with neutral ligands which cannot charge balance the metal centres, such as N- donor ligands. Changing anions of metal salts coupled with neutral ligands often alters the structural topologies, sometimes even the overall physical properties of polymeric complexes.[59]

It is often observed that the size, coordination ability and weak supramolecular interactions of these anions exert complicated influences on the self-assembly of CPs. Highly coordinating anions for example can increase the dimensionality of polymeric structures by bridging metal centres, while others may act as templating molecules for the cavities and channels of the framework.[60]

1.2.4. Influence of weak intermolecular interactions

The interplay between weak intermolecular interactions such as hydrogen bonds, π···π stacking, van der Waals forces, and metal-metal interactions can contribute to the stability of, and possibly ultimately determine the topology of, a coordination polymer. The ability to predict the dominant interaction within the self-assembly process is a vital tool in supramolecular chemistry, crystal engineering and CP design.

Hydrogen bonding interactions, including conventional N/O–H···X (X = N, O, F) hydrogen bonds and non-classical weak C–H···X (X = O, N, π, etc.) hydrogen bonds, are potentially the most important of the intermolecular interactions in the field of CPs and in many cases direct the overall framework packing. Hydrogen bonds lie on a spectrum ranging from strong to weak according to their strength and character, as illustrated by Desiraju (Figure 14). Jeffrey defines a hydrogen bond as an electrostatic interaction formed by a hydrogen atom between two structural moieties. Strong hydrogen bonds consist of donor and acceptor atoms of moderate to high electronegativity and can include X–H···O (X = O/N) interactions and are able to control supramolecular packing.[61] A weak hydrogen bond occurs between moieties of moderate to low electronegativity, of which C–H···X (X = O/π) interactions are a key example; their influence on CP structure and packing is variable. Different terminologies of what constitute ‘strong’ and ‘weak’ hydrogen bonds have been proposed by other authors;[62] these categorisations serve as a broad definition.

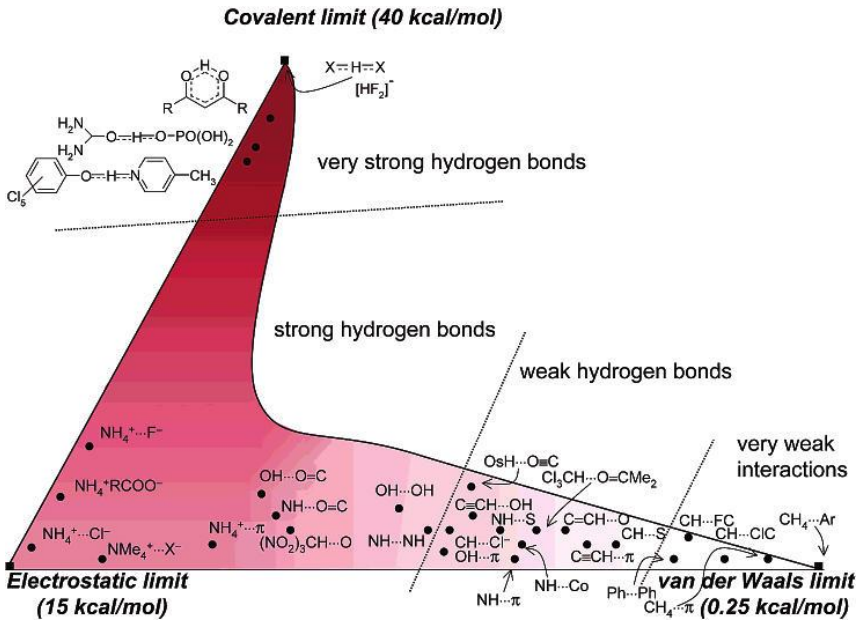

Figure 14: *Desiraju's illustration of 'the hydrogen bridge', which serves as a rough guide to the electrostatic, van der Waals, and covalency balance of each X–H···A interaction, with positions of select hydrogen interactions shown. The bridge transitions from 'very strong' hydrogen bonds (red) to 'very weak' interactions (white).*[63]

There are known instances wherein weak hydrogen bonds are formed preferentially over interactions involving available strong donors or acceptors.[64,65] This preference for weak hydrogen bonds ensures that structural predetermination will fail if predictive methods rely solely on the traditional hierarchy of bonding strengths. Thus, the crystal engineer must view the sum of all interactions, both weak and strong, in order to predict the intermolecular architecture and crystal packing of a material, as opposed to focusing only on the strongest few interactions.

A majority of functional CPs are synthesised using aromatic linkers, due to their rigid properties. Through the inclusion of aromatic linkers, there is potential for π- oriented interactions. This tends to increase the stability of the overall framework.[66] Generally there exist three stacking configurations for π···π interactions: face-to-face (sandwich) stacking, edge-to-face (T-shaped) interactions, and offset face-to-face (parallel-displaced) stacking.[67] The interaction types are illustrated in Figure 15.

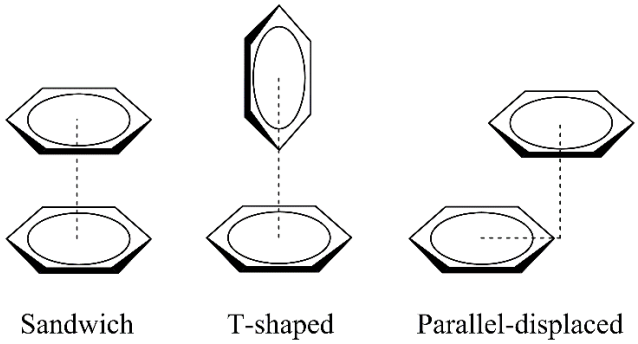

Figure 15: *The three main configurations of phenyl···phenyl interactions.*

The latter two (T-shaped and parallel-displaced) are stable in energy, while face-to-face stacking is rarely observed because of the higher interaction energy between the stacked phenyl rings. Formally, the T-shaped interaction should be classed as a weak C–H···π bond, as the interaction passes through an H atom. Perpendicular or parallel-displaced configurations are often seen in the crystal structures of small aromatic compounds[68] or in pairs of interacting aromatic side chains in proteins.[69]

Metal-metal interactions are attractive interactions between closed d-shell ions such as Ag(I) and Cu(I). Although much rarer in the field of CPs, these interaction strengths can at times rival hydrogen bonds.[70,71]

1.2.5. Supramolecular Isomerism

Supramolecular isomerism is the existence of more than one type of network superstructure for the same molecular building blocks. Even when the local coordination geometries of the metals and ligands are identical, very different networks can be produced when reacted under different conditions. The structures of CPs containing flexible bidentate ligands are less predictable due to the possible occurrence of supramolecular isomerism.[72] For example, Bai et al. reported the construction of three isomeric coordination polymers of the overall formula $[Zn_2(ebtc)(H_2O)_2]$ (ebtc = 1,1'-ethynebenzene-3,3',5,5'-tetracarboxylate) exhibiting different frameworks by manipulating solvent and additive conditions of each, presenting an interesting example of additive- induced isomerism (Figure 16).[73]

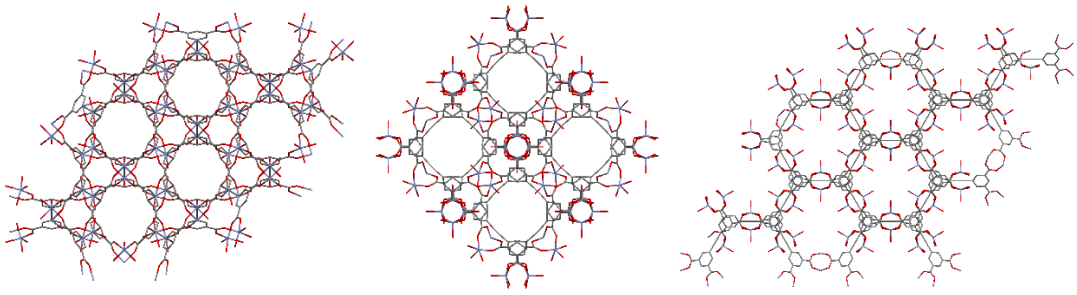

Figure 16: *Three resulting coordination isomeric assemblies comprising Zn and ebtc, viewed from the crystallographic* c *axis, synthesised from different mixtures of solvents and additives. (AIP = 5-aminoisophthalic acid, BPP = 1,3-bi-4-pyridylpropane.)*

1.2.6. Synthetic and crystallisation techniques

Once synthesised, the principal method to unambiguously determine the structure of a CP is single-crystal X-ray diffraction.[74] One of the challenges of CP synthesis is therefore to obtain single crystals suitable for detailed crystallographic analysis. A common CP synthesis technique is a solvothermal or hydrothermal synthesis; directly evolved from the production of zeolites.[75] In a typical thermal synthesis a metal salt and linker precursor are dissolved together, sealed and placed in an oven until crystals are obtained. These syntheses usually take place over several days and often depend on vessel walls for nucleation, and prolonged reaction times can lead to crystal degradation.[76] Although some CPs crystallise well from directly mixed solutions, other systems benefit from slowing down the combination of the CP components. This is usually done by allowing two separate solutions of metal ions and ligands to diffuse into each other, often through a buffer layer consisting of pure solvent. Variations of this technique include the use of H-tubes or U-tubes to limit the contact area between interacting solutions, or the use of a gelling agent such as Agar[77-79] or sodium metasilicate[80] to reduce the speed of diffusion, and provide a support platform for emerging crystals (Figure 17).

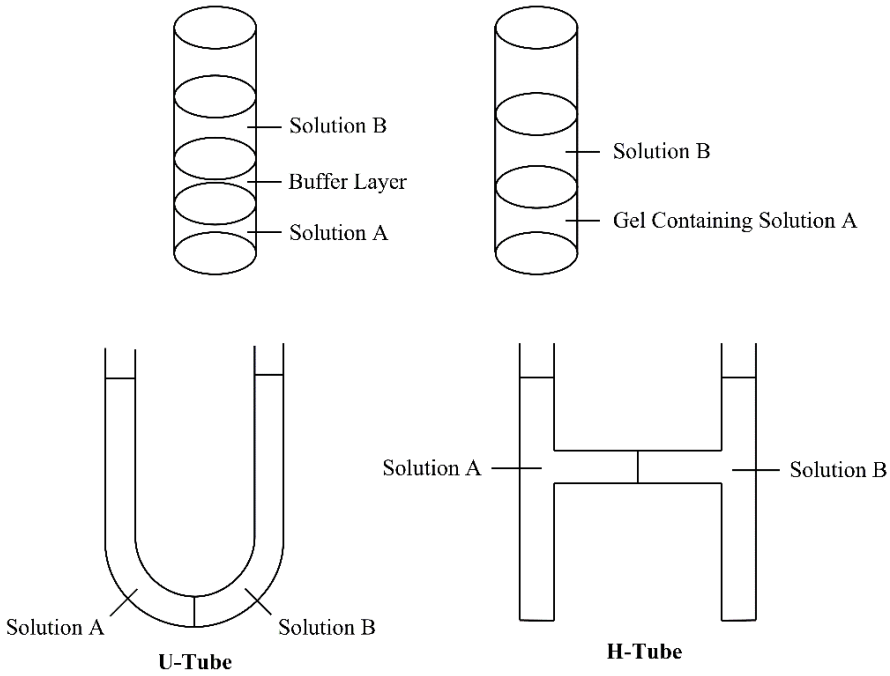

Figure 17: *Various methods for the slow diffusion of separate solutions to produce coordination polymer crystals.*[81]

Other important synthetic routes include microwave-assisted reactions[82] as well as mechanochemical[83] and sonochemical[84] syntheses. Although these are high efficiency methods for the production of CPs, they tend to produce nanoscale crystals unsuitable for single-crystal XRD analysis. Seeding a synthesis with the sought after product may improve the yield of particularly difficult reactions, for example to resolve competing crystallisations, where a mixture of two or more products are formed.

Since CP synthesis is often a one-pot process, it is critical that the bulk sample be pure and of a single phase, as determined by powder diffraction (PXRD) analysis. The newly synthesised CP is likely to contain excess unreacted components or unwanted solvents trapped within the framework, which can usually be removed by solvent exchange or air drying. For PCPs, exchange and removal of solvent molecules is an important step in framework activation for gas adsorption or guest inclusion experiments,[85] although in less robust PCPs these often harsh processes can cause significant changes in the morphology of the crystal or even a complete collapse of the framework.[86,87] Softer activation techniques, for example using $scCO_2$ and freeze-drying,[88] are efficient methods to promote the internal surface areas of PCPs. Hupp et al. found that several zinc PCPs activated by $scCO_2$ showed significantly higher internal surface areas than those of the PCPs activated by other conventional activation processes, such as thermal evacuation and solvent exchange.[89]

1.3. Coordination polymer design

The challenge of designing a CP has been present since the first coordination polymer was synthesised, and over the years multiple approaches to this problem have been developed. When the linker and metal have predictable geometries and behaviours, the coordination chemistry tends to be directional, allowing design to be attempted *via* a 'node' and 'linker' approach. Snurr et al. devised a computational method based on the use of modular building blocks that self-assemble into crystal structures to predict and screen the topologies and properties of CP structures.[90] From a library of 102 metal and ligand building blocks the group generated 137,953 hypothetical CPs, and found that atom positions matched very closely in the experimental and generated structures, with atom positions typically varying by an average of less than ~0.1 Å. This modular approach has also been demonstrated experimentally by Yaghi et al., based on the cubic structure of MOF-5, $Zn_4O(bdc)_3$ (bdc = 1,4-benzenedicarboxylate), in which the framework was systematically functionalised, resulting in an isoreticular series[31] which has led to the design of highly porous coordination polymers.[91,92]

Other methods of framework design include in-situ templating of CPs. Templating molecules intercalate into the assembling CP, thus preventing interpenetration or interdigitation.[93] With appropriate molecular templates, frameworks of different-sized pores can be obtained.[94] Using framework templates in the field of post-synthetic modification (PSM) for the design of CPs is a rapidly expanding field.[95,96] (More information on PSM in Section 1.4.3.) Li et al. demonstrated how ordered vacancies in a CP framework can be produced and subsequently exploited to obtain a new framework.[97] Ordered metal vacancies were created in a CP based on Zn(II) and pyrazolecarboxylic acid, and subsequently filled with new metals and linkers, synthesising multiple ordered multicomponent CPs, which could not have been made directly.

The direct synthesis and design of CPs is still an uncertain process due to the complex interplay of interactions and functional groups during the self-assembly process. The analysis of such interactions has been greatly facilitated by ongoing improvements in the theory and practise of X-ray crystallography, allowing the determination of crystal structures rapidly and in great detail, or from small crystals using high intensity instruments, while also frequently allowing the detection of disorder and solvent structure.

1.4. Structural dynamism in coordination polymers

The work in this thesis is part of a larger EPSRC funded research directive called the Metastable Materials project. The focus of the Metastable Materials project is the discovery and development of new classes of solid-state switchable materials through dynamic approaches based on synthesis, assembly, characterisation and modelling techniques. The approach used in this thesis towards the creation of switchable materials relies on dynamic coordination polymers.

Occasionally molecular rearrangements within a crystalline framework of a CP occur as a response to a variety of external chemical or physical factors. Transformations in CPs can either occur *via* a single-crystal to single-crystal (SCSC) transformation where the crystalline order of a solid is maintained through a transformation, or *via* a crystal-to-crystal (CTC) transformation, in which the single-crystalline state of the initial CP is lost. Occasionally the crystallinity can be lost completely as a result of the transformation. The preservation of the single-crystal state is important for allowing direct visualisation of the transformation *via* X-ray crystallography. Characterisation of the molecular structure before and after transformation is important for rationalising how and why such structural modifications take place. Crystal transformation triggers include exposure to temperature, solvent, gas, mechanical force, light, and pressure.[98-103]

Three categories of CP SCSC transformations are introduced in this section. These transformations include the liberation or exchange of guest molecules within the networks,[104,105] structural transformations[101] and alterations of the metal clusters or organic linkers through post-synthetic modification (PSM).[106,107] Compounds that transform in the SCSC manner, particularly ones that transform reversibly, are important for the development of new and technologically useful devices including actuators and sensors.

1.4.1. Lattice guest molecule induced dynamism

CPs can undergo SCSC transitions on removal, introduction or exchange of guest molecules.[108] These guests tend to be solvent molecules, but small guest molecule reactants can be included also. Some transformations occur without a change of the overall framework structure, but others do change through a significant

rearrangement of the CP components leading to unit cell changes as well as pore swelling/shrinkage.

Kitagawa's group outlined some of the fundamental mechanisms that two-dimensional frameworks undergo when incorporating guest molecules, without dramatic differences to the gross structure (Figure 18).[109] They identified several characteristics with regard to dynamic guest-responsive phenomena, including interlayer separations, framework flexibility in terms of sliding of the 2D layers or opening/closing of available pores and framework rearrangement by cleavage and formation of coordination bonds between the layers, leading to expansion/shrinkage of the 2D layered structures by the guest molecules. These characteristics can lead to mutual sliding of layers,[110,111] gate closing/opening mechanisms,[112,113] contracting or expanding of porous channels[114] and the cleavage or formation of bonds.[115] Usually guest-induced transition mechanisms include a combination of two or more of these pathways.

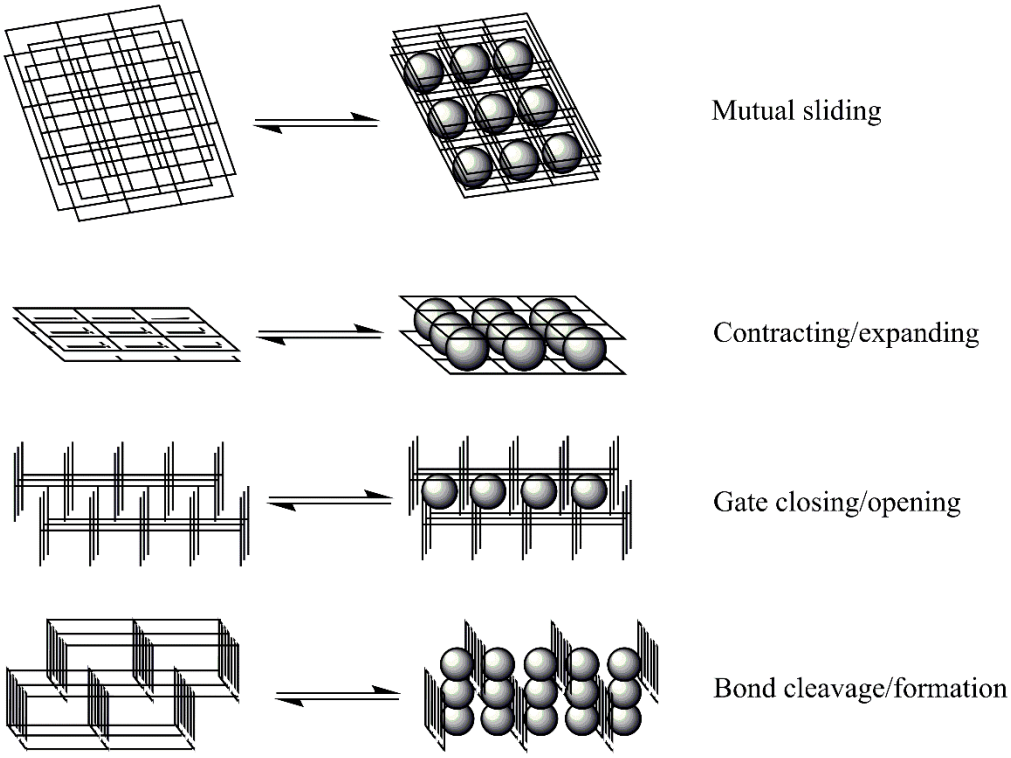

Figure 18: *A schematic representation of fundamental motifs observed for dynamic guest sorption/desorption involving 2D coordination frameworks.*

Perhaps the simplest example of a SCSC transition is the exchange or loss of interstitial solvent molecules from a permanently porous framework. Ma et al.[116] reported that the porous CP $[Cu_3(tp)_4(N_3)_2(DMF)_2]\cdot 2H_2O\cdot 2DMF$ (tp = 4-tetrazole

pyridine) could undergo reversible solvent exchange with a variety of solvents including cyclohexane, cyclopentane and 1,4-dioxane in a SCSC manner, while managing to retain the gross structure of the CP framework. The cyclohexane infused framework could further be completely converted by heating into a solvent-free analogue. This principle can also be applied to gas adsorption, in which a PCP can selectively and reversibly uptake gases such as C_2H_4 and CO_2 without framework degradation.[117]

The gross structure of the coordination framework is not always retained during guest gain or removal. Examples of extensive and perhaps counterintuitive cooperation between the components that constitute the framework have been also been found. A three dimensional framework that shows shrinkage of pores upon guest inclusion and pore expansion on guest release was reported by Dybtsev et al.[118] The framework comprises Zn, 1,4-benzenedicarboxylate (1,4-bdc) and 1,4-diazabicyclo[2.2.2]octane (dabco) which pack in a cubic lattice, and exhibits a significant bend in the 1,4-bdc linker. This bending results in the severe twisting of the metal nodes of the framework in the presence of guest molecules. Upon removal of these molecules, the 1,4-bdc linkers straighten, consequently increasing the volume of the crystal structure (Figure 19).

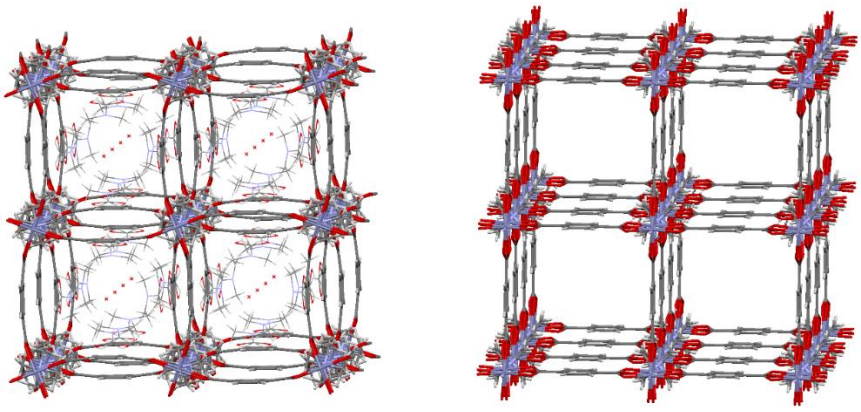

Figure 19: *Left: Guest filled framework, displaying bent 1,4-bdc linkers, disordered guest molecules are displayed within the cubic channels. Right: The evacuated framework, in which the 1,4-bdc linkers are linear.*

In the synthesis of charged frameworks in which a counterion is important, the templating effect a counterion can have on the framework can be exploited to trigger switchability within the structure. This can be done by an exchange of the counterion with another.[119] Anantharaman et al.[120] reported the reversible exchange of PF_6^- with

NO_3^- anions within a Cd and 2,6-bis(imidazol-1-yl)pyridine (pyim) based framework, inducing a structural variation from a 1D to a 2D framework. The transformation was achieved by immersing the respective single crystals in solutions containing either KPF_6 or NH_4NO_3 for up to two weeks, and were monitored by powder X-ray diffraction (PXRD) and single crystal X-ray analysis. Similarly, another anion induced CP transformation was reported by Chao et al.[121] in which Ag and di(3-pyridylmethyl)amine (dpma) based 1D interpenetrated helical spirals decreased in dimensionality to 0D hoops upon the anion exchange of NO_3^- to NO_2^-.

1.4.2. Dynamic frameworks

Structural transformation is a modification in the architecture of a CP induced through external factors such as a change in temperature, pressure, mechanical trigger or solvent. The crystal structure rearrangement observed in this class of transformation can be substantial, such as pore distortions, slippage, shrinking or swelling, bending or rotational motion. In these cases, considerable changes in the framework structures, due to extensive movements of the molecular components, are expected because of extensive cooperation among the components that constitute the framework.

Wang et al. synthesised an entangled 3D CP showing colour-changing behaviour associated with solid-state structural transformation during a reversible thermally induced rehydration/dehydration process.[122] Reacting Cu(II), 1,2-bis(4-pyridyl)ethane (dpe) and benzenetricarboxylate (btc) resulted in four crystallographically independent polymeric structures, two 1D polymeric chains and two interdigitated 2D double-layers, tightly interpenetrated together in a unique 3D array. Controlled heating of the crystalline sample to ~140 °C caused a desolvation and accompanying colour change from pink to deep-blue, after which the pink colour was regenerated by cooling and exposure to water vapour (Figure 20).

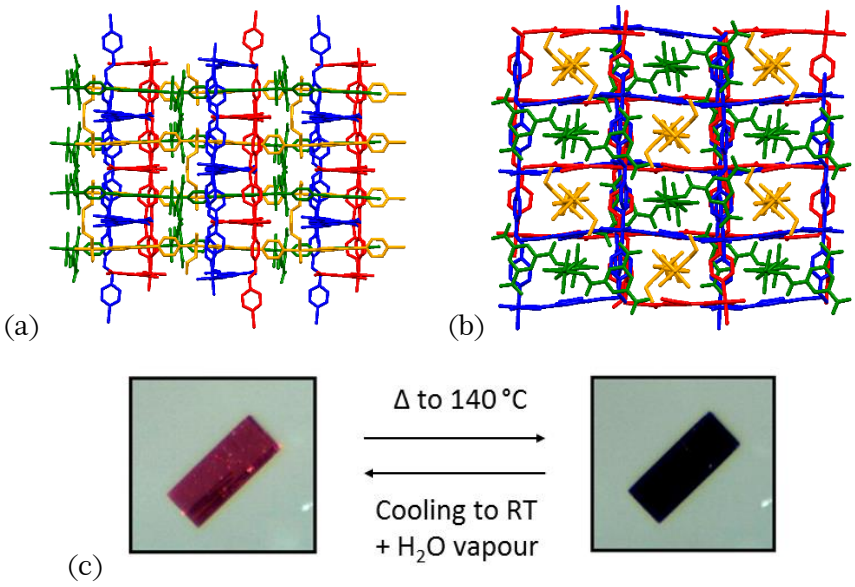

Figure 20: *(a) Two interdigitated 2D nets (red and blue) interpenetrated by two 1D chains (green and yellow) shown along the crystallographic* a *axis; (b) the alternating pattern of the interpenetrating 1D chains as viewed down the crystallographic* c *axis; (c) a schematic including photographs of the reversible thermal-induced colour change.*[122]

Although an X-ray structure of the desolvated form could not be obtained, it was surmised that the colour change was the result of the leaving coordinated solvent molecules creating open sites on the metal centres for the approach of neighbouring uncoordinated oxygen atoms of dpe and btc ligands. A subsequent rehydration would cleave these coordination bonds and reform the original architecture.

Bond cleavage/formation within the coordination framework has a large potential to change the dimensionality of the polymer.[123] Sheu et al. developed a series of 1D double zig-zag frameworks $\{[Zn(papo)_2(H_2O)_2](ClO_4)_2\}_n$ and 2D polyrotaxane frameworks $[Zn(papo)_2(ClO_4)_2]_n$ (papo = *N*,*N*′-bis(pyridylcarbonyl)-4,4′-diaminodiphenyl ether) based on similar ligand analogues, and found that these frameworks could be reversibly interconverted by heating and grinding in the presence of moisture (Figure 21).[124] During the transformation, the octahedral Zn centre undergoes a ligand exchange at the axial positions of water with ClO_4^- thus switching from an ordered octahedral geometry to a disordered environment. The structural transformation could also be proven experimentally by powder and single-crystal X-ray diffraction studies.

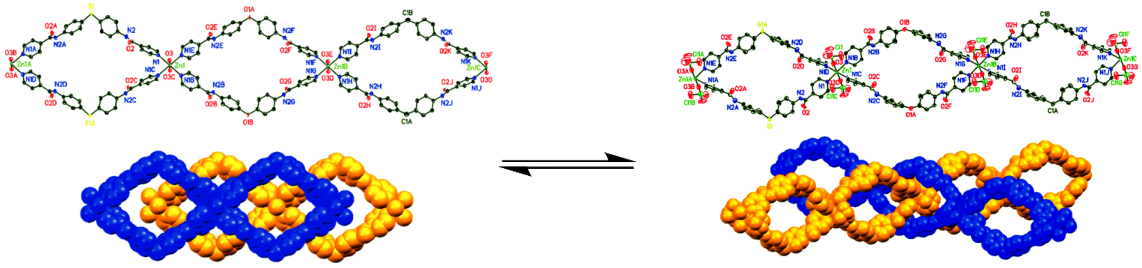

Figure 21: *Left: The 1D double-zigzag component framework of* $\{[Zn(papo)_2(H_2O)_2](ClO_4)_2\}_n$ *with a space filling model below. Right: The 1D double-zigzag component framework of* $[Zn(papo)_2(ClO_4)_2]_n$ *with a space filling model below showing the interlocking of two polymeric chains.*[124]

1.4.3. Post-synthetic modification

Post-synthetic modification (PSM) in PCPs can be defined as a chemical modification of the solid-state framework.[125,126] A key to accessing advanced PCP materials suitable for more specialised and sophisticated applications is to integrate functionalities of greater complexity into these materials. Although highly desirable, incorporating complex functionalities into the self-assembly process of a PCP can be challenging, either through incompatibility with the synthetic conditions used (insolubility, chemical or thermal instability) or because of undesirable interference with the formation of the desired framework. PSM enables a wide variety of chemical reactions for the modification of PCPs,[95] assuming the framework is sufficiently robust and porous to allow late-stage transformations without compromising the single crystallinity of the desired product.

Cohen et al. carried out a clean and efficient PSM method for the cyanation of the Zr^{4+} based UiO-66-Br with CuCN *via* microwave irradiation to produce UiO-66-CN.[127] The PSM pathway reduced the potential synthesis of the UiO-66-CN from ~91 hours and a 31% yield by conventional ligand synthesis followed by direct self-assembly, to two steps in ~24 hours and in 90% yield (Scheme 3).

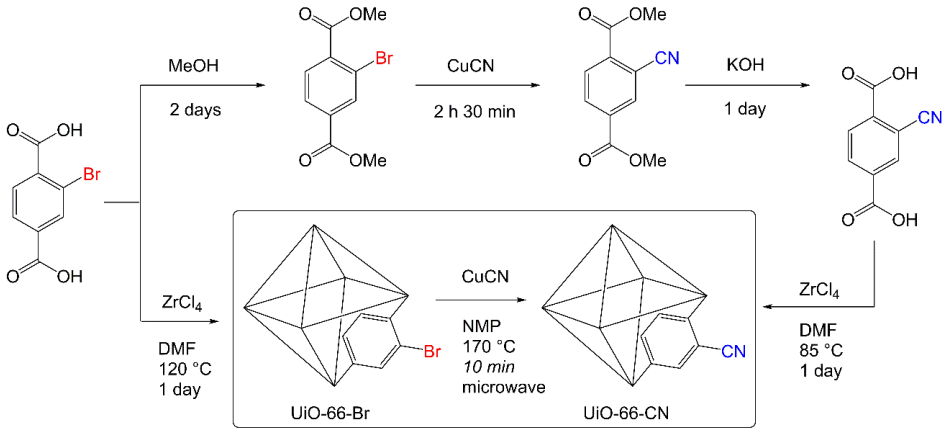

Scheme 3: *Reaction schematic comparing number of steps and reaction times of conventional synthesis to PSM synthesis of UiO-66-CN.*

Alternative methods to the covalent PSM reaction on a functional group are the exchange or insertion of structure-building organic linkers. Zhou et al. first successfully demonstrated organic linker replacement reactions using metal-organic polyhedra, forming an isoreticular series with various pore sizes, shapes, and functionalities.[128] This method was swiftly adopted into multidimensional coordination polymers; Burnett et al.[129] reported two cases of post-synthetic exchange reactions of structure-building linkers in 2D and 3D CP systems that resulted in SCSC transformations, as well as a 2D to 3D transformation that occurred *via* a linker-insertion mechanism upon the introduction of excess linkers.

Transformations where two linkers close to each other undergo photochemical condensation reactions to form a four-membered cyclic product is another type of post-synthetic modification of CPs. Park et al.[130] utilised the well-known [2+2] cycloaddition reaction in a SCSC polymerisation in which alternate 1,4-bis[2-(4-pyridyl)ethenyl]benzene (bpeb) ligands in the polyrotaxane 2D coordination polymer [Cd(bpeb)(sdb)]·DMA (sdb = 4,4'-sulfonyldibenzoate) selectively undergo polymerization to form a polyrotaxane based 3D structure (Figure 22).

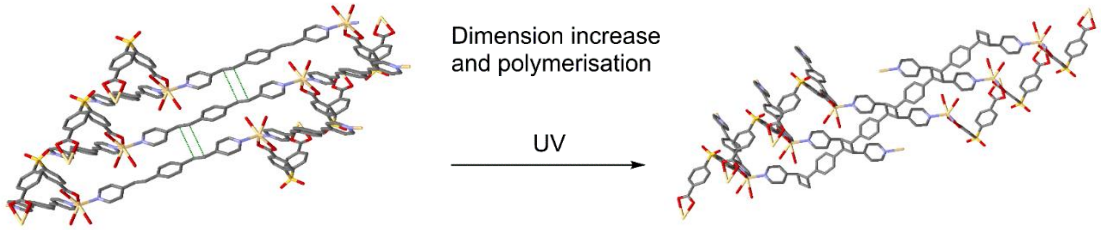

Figure 22: *A perspective view of the formation of a 3D polyrotaxane CP by the polymerisation of aligned bpeb ligands via a [2+2] photo-cycloaddition reaction.*

1.5. Crystalline molecular flasks

Porous coordination polymers (PCPs) can act as crystalline molecular flasks (CMFs),[131] also known as molecular sponges, in which guest molecules can either be clathrates within pores or incorporated into the open channels of the framework. The framework of a PCP thus can act as a matrix for isolating and ordering the structures of these moieties. This concept has had broad scope for development as an analytical tool in the crystallographic visualisation of chemical processes where obtaining single crystal data of a target molecule presents a significant challenge.[132,133] It additionally offers potential for obtaining insights into chemically reactive species that can be stabilised within the pore network.[134] CMFs have also been developed into nano-vessels for carrying out small-scale reactions, as the limited sterics inside the molecular cage can induce unexpected reaction profiles and stereoisomer products.[135,136]

Fujita et al. have delivered a number of studies of the characterisation of compounds within molecular sponges, namely with the PCP $[(ZnI_2)_3(tpt)_2 \cdot x(\text{solvent})]_n$ (tpt = tri(4-pyridyl)-1,3,5-triazine) which expands upon guest inclusion and shrinks on guest removal without loss in crystallinity.[137] One recent study utilised this molecular sponge for the X-ray structure analysis of highly explosive ozonide compounds.[138] Small molecule ozonides were synthesised and subsequently infused into and characterised within single crystal samples of the PCP (Figure 23), requiring only microgram quantities of the compound and eliminating all risk of explosion.

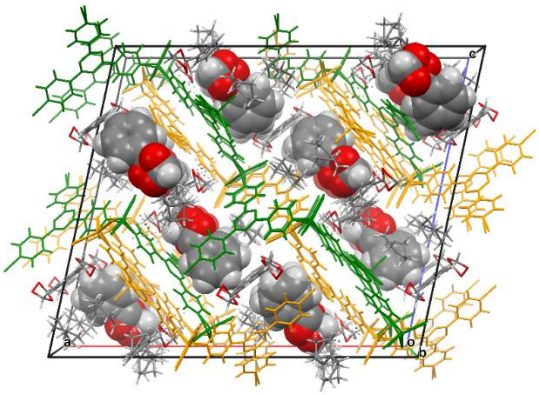

Figure 23: *A styrene ozonide moiety embedded in the* $[(ZnI_2)_3(tpt)_2 \cdot x(hexane)]_n$ *host framework.*

Another interesting outcome of the ability to easily observe compounds in these crystalline sponges *via* X-ray crystallography is monitoring the outcome of close-

proximity, microscale reactions. Fujita and co-workers reported the direct observation of a reversible Michael addition reaction within the pores of $[(ZnI_2)_3(tpt)_2 \cdot x(solvent)]_n$.[139] Importantly, they were able to determine the structure of the temporary reaction intermediate *via in situ* crystallographic analysis, leading to strong support for a previously postulated, yet quite unusual, mechanism.

CMFs are unique from most CPs in that the network has the ability to expand upon guest molecule absorption and contract upon guest loss meanwhile retaining their framework integrity and crystalline nature. More information on CMFs can be found in Chapter 5.

1.6. Applications of switchable coordination polymers

Many potential applications that involve solid-state dynamics do not require retention of crystallinity. However, the phenomenon of SCSC transformations is important for when a crystal is incorporated into a device such as a substrate-triggered sensor or actuator, mono-crystallinity would be essential for repeated operation. Over the last decade the applications for these materials have come into fruition as the field has advanced, and in some areas the properties of PCPs have reached and even surpassed traditional procedures, particularly in molecular sieving and separation.[140]

The storage and stabilisation of guest molecules within crystalline CP lattices is a rapidly developing field, namely with the use of the CMF method as utilised by Fujita's group, mentioned in Section 1.5. The incorporation of guest molecules into frameworks through SCSC transitions includes the stabilisation of bio-sensitive[141,142] or volatile[143] molecules and reaction intermediates.[144] The capture, storage and release of guest molecules *via* SCSC transformation has the advantage of recoverability and recyclability of the framework.[145]

Separations constitute an important component in many industrial processes. Recently there has been a rising demand for separation of low concentration impurities with the increasing awareness of environmental sustainability.[146] Switchable PCPs fulfil that role due to their high selectivity and efficiency. Abrahams et al. investigated the porous CP $[Ni_2(\mu_2\text{-}OH_2)(1,3\text{-bdc})_2(tpcb)]_n$ (1,3-bdc = 1,3-benzenedicarboxylate, tpcb = tetrakis(4-pyridyl)cyclobutane) for the separation of a solid mixture of naphthalene and anthracene at room temperature, involving a SCSC transition.[147] The group found that naphthalene was favourably absorbed into the CP over anthracene, resulting in 99.5% purity in the framework. The host framework could be regenerated by exchange with, and subsequent removal of, ethanol. Continuous regeneration of the host did not result in loss of crystallinity or significant reduction of adsorption capacity.

Another potential application of SCSC transitions within CPs is the removal of contaminants such as toxic metal ions. Thallapally et al. found that a series of flexible anionic CPs, containing divalent Co, Mn, Cd and tetrakis[4-(carboxyphenyl)oxamethyl]methane, transformed *via* SCSC transition into neutral hetero-bimetallic systems invoked by metal cation insertion.[148] These transformations

were directed by cooperative bond breakage and formation of metal-carboxylate coordination bonds, resulting in expansion or contraction of the 3D framework by up to 33% due to the flexible nature of the organic linker. These CPs display highly selective uptake of divalent transition-metal cations (e.g. Co^{2+} and Ni^{2+}) over alkali-metal cations (Li^{+} and Na^{+}).

PCPs have also been investigated as chemical sensors capable of utilising a range of host– guest interactions, primarily towards small organic molecules.[149] Zhang's group in 2014 reported the first sensor based on a CP with multi-responsive optical sensing properties.[150] The CP $[Eu_3(bpydb)_3(HCOO)(\mu^3\text{-}OH)_2(DMF)]\cdot(DMF)_3(H_2O)_2$ (pbydb = 4,4′-(4,4′-bipyridine-2,6-diyl)dibenzoate) is capable of sensing and distinguishing a variety of small organic molecules and inorganic ions, based on the luminescent intensity of the sample. Additionally, it can discriminate among homologs and isomers of aliphatic alcohols as well as detect highly explosive 2,4,6-trinitrophenol (TNP) in water or in the vapour phase.

1.7. Aims of this thesis

This work is part of the EPSRC-supported Metastable Materials project looking at the design and synthesis of classes of new solid-state materials that exhibit different functions and properties when in non-equilibrium states compared to those displayed when the materials are in their ground states.

This thesis pursues solid-state single-crystal to single-crystal (SCSC) transitions within coordination compounds and coordination polymers (CPs), through the lens of structure-property determination, from which postulates can be suggested toward the rational design of switchable CPs. This will include looking at how weak interactions influence the self-assembly process and consequently the resulting architecture of CPs, in the presence of varying synthetic conditions.

Methods of influencing the resulting CP architectures will be explored through systematic studies utilising two linkers, 5-ethynyl and 5-allenyl functionalised 1,3-benzenedicarboxylate ligands, as well as through variation of synthesis techniques within labile systems. Controlled variation of reaction conditions will aim to reveal the influence of weak intramolecular interactions within the self-assembly process of CPs and CP switchability thereafter.

Crystalline molecular flasks (CMFs) present an alternative to switchable CP design by acting as flexible hosts into which switchable molecules can directly be inserted. The aim therefore for the use of CMFs is to input and observe a switchable moiety within the framework pores.

Characterisation by single crystal X-ray diffraction will be the main analytical technique supplemented by powder X-ray diffraction to yield structural information of the synthesised compounds and to collect detailed information on any observed SCSC transitions.

1.8. References

[1] Rowsell, J. L. C.; Yaghi, O. M., *Micropor. Mesopor. Mat.,* **2004**, *73*, 3-14.

[2] Janiak, C., *Dalton Trans.,* **2003**, 2781-2804.

[3] Wen, H. M.; Wang, H.; Li, B.; Cui, Y.; Wang, H.; Qian, G.; Chen, B., *Inorg. Chem.,* **2016**, *55*, 7214-7218.

[4] Huang, Y.-L.; Jiang, L.; Lu, T., *ChemPlusChem,* **2016**, *81*, 780-785.

[5] Katz, M. J.; Mondloch, J. E.; Totten, R. K.; Park, J. K.; Nguyen, S. T.; Farha, O. K.; Hupp, J. T., *Angew. Chem. Int. Ed.,* **2014**, *53*, 497-501.

[6] Li, B.; Belmabkhout, Y.; Zhang, Y.; Bhatt, P.; He, H.; Zhang, D.; Han, Y.; Eddaoudi, M.; Perman, J. A.; Ma, S., *Chem. Commun.,* **2016**, *52*, 13897-13900.

[7] Wan, Y.; Chen, C.; Xiao, W.; Jian, L.; Zhang, N., *Micropor. and Mesopor. Mat.,* **2013**, *171*, 9-13.

[8] Yang, W.; Chang, G.; Wang, H.; Hu, T.-L.; Yao, Z.; Alfooty, K.; Xiang, S.; Chen, B., *Eur. J. Inorg. Chem.,* **2016**, 4470-4475.

[9] Jackson, S. L.; Rananaware, A.; Rix, C.; Bhosale, S. V.; Latham, K., *Cryst. Growth & Des.,* **2016**, *16*, 3067-3071.

[10] Roushani, M.; Valipour, A.; Saedi, Z., *Sensor. Actuat. B-Chem.,* **2016**, *233*, 419-425.

[11] Pili, S.; Argent, S. P.; Morris, C. G.; Rought, P.; Garcia-Sakai, V.; Silverwood, I. P.; Easun, T. L.; Li, M.; Warren, M. R.; Murray, C. A.; Tang, C. C.; Yang, S.; Schroder, M., *J. Am. Chem. Soc.,* **2016**, *138*, 6352-6355.

[12] Tanaka, D.; Kitagawa, S., *Chem. Mater.,* **2008**, *20*, 922-931.

[13] Öhrström, L., *Crystals,* **2015**, *5*, 154-162.

[14] Batten, S. R.; Champness, N. R.; Chen, X.-M.; Garcia-Martinez, J.; Kitagawa, S.; Öhrström, L.; O'Keeffe, M.; Paik Suh, M.; Reedijk, J., *Pure Appl. Chem.,* **2013**, *85*, 1715-1724.

[15] Kitagawa, S.; Kitaura, R.; Noro, S., *Angew. Chem. Int. Ed.,* **2004**, *43*, 2334-2375.

[16] Cotton, S. A.; Harrowfield, J. M., *Lanthanides: Coordination Chemistry*. John Wiley & Sons Ltd.: **2012**.

[17] Blatov, V. A.; O'Keeffe, M.; Proserpio, D. M., *CrystEngComm,* **2010**, *12*, 44-48.

[18] O'Keeffe, M.; Peskov, M. A.; Ramsden, S. J.; Yaghi, O. M., *Acc. Chem. Res.,* **2008**, *41*, 1782-1789.

[19] Ma, Z.; Moulton, B., *Coordin. Chem. Rev.,* **2011**, *255*, 1623-1641.

[20] Shao, Y.; Li, C. X.; Chen, Y. G.; Zhu, D. S.; Liu, Q., *Synth. React. Inorg. M.,* **2005**, *35*, 571-574.

[21] Yang, Q.; Chen, Z.; Hu, J.; Hao, Y.; Li, Y.; Lu, Q.; Zheng, H., *Chem. Commun.,* **2013**, *49*, 3585-3587.

[22] Pickering, A. L.; Seeber, G.; Long, D. L.; Cronin, L., *Chem. Commun.,* **2004**, 136-137.

[23] Hill, R. J.; Long, D. L.; Turvey, M. S.; Blake, A. J.; Champness, N. R.; Hubberstey, P.; Wilson, C.; Schroder, M., *Chem. Commun.,* **2004**, 1792-1793.

[24] Ockwig, N. W.; Delgado-Friedrichs, O.; O'Keeffe, M.; Yaghi, O. M., *Acc. Chem. Res.,* **2005**, *38*, 176-182.

[25] Gao, Q.; Xu, J.; Cao, D.; Chang, Z.; Bu, X. H., *Angew. Chem. Int. Ed.,* **2016**, *55*, 15027-15030.

[26] Li, X.; Xu, H.; Kong, F.; Wang, R., *Angew. Chem. Int. Ed.,* **2013**, *52*, 13769-13773.

[27] Alexandrov, E. V.; Goltsev, A. V.; O'Keeffe, M.; Proserpio, D. M., *Cryst. Growth & Des.,* **2017**, *17*, 2941-2944.

[28] Sun, D.; Ke, Y.; Collins, D. J.; Lorigan, G. A.; Zhou, H. C., *Inorg. Chem.,* **2007**, *46*, 2725-2734.

[29] Brozek, C. K.; Dinca, M., *Chem. Soc. Rev.,* **2014**, *43*, 5456-5467.

[30] Bon, V.; Kavoosi, N.; Senkovska, I.; Muller, P.; Schaber, J.; Wallacher, D.; Tobbens, D. M.; Mueller, U.; Kaskel, S., *Dalton Trans.,* **2016**, *45*, 4407-4415.

[31] Eddaoudi, M.; Kim, J.; Rosi, N.; Vodak, D.; Wachter, J.; O'Keeffe, M.; Yaghi, O. M., *Science,* **2002**, *295*, 469-472.

[32] Batten, S. R.; Hoskins, B. F.; Robson, R., *Chem.-Eur. J.,* **2000**, *6*, 156-161.

[33] Du, J.; Zou, G.; Guo, F., Z. *Anorg. Allg. Chem.,* **2016**, *642*, 704-708.

[34] Ma, S.; Sun, D.; Forster, P. M.; Yuan, D.; Zhuang, W.; Chen, Y. S.; Parise, J. B.; Zhou, H. C., *Inorg. Chem.,* **2009**, *48*, 4616-4618.

[35] Yao, X.-Q.; Cao, D.-P.; Hu, J.-S.; Li, Y.-Z.; Guo, Z.-J.; Zheng, H.-G., *Cryst. Growth & Des.,* **2011**, *11*, 231-239.

[36] Forster, P. M.; Burbank, A. R.; Livage, C.; Ferey, G.; Cheetham, A. K., *Chem. Commun.,* **2004**, 368-369.

[37] Calderone, P. J.; Banerjee, D.; Plonka, A. M.; Kim, S. J.; Parise, J. B., *Inorg. Chim. Acta,* **2013**, *394*, 452-458.

[38] Cadman, L. K.; Bristow, J. K.; Stubbs, N. E.; Tiana, D.; Mahon, M. F.; Walsh, A.; Burrows, A. D., *Dalton Trans.,* **2016**, *45*, 4316-4326.

[39] Kim, D.; Song, X.; Yoon, J. H.; Lah, M. S., *Cryst. Growth & Des.,* **2012**, *12*, 4186-4193.

[40] Sun, F.; Zhu, G., *Inorg. Chem. Commun.,* **2013**, *38*, 115-118.

[41] Liu, T.; Luo, D.; Xu, D.; Zeng, H.; Lin, Z., *Inorg. Chem. Commun.,* **2013**, *29*, 110-113.

[42] Burrows, A. D.; Frost, C. G.; Mahon, M. F.; Winsper, M.; Richardson, C.; Attfield, J. P.; Rodgers, J. A., *Dalton Trans.,* **2008**, 6788-6795.

[43] Awaleh, M. O.; Badia, A.; Brisse, F., *Cryst. Growth & Des.,* **2006**, *6*, 2674-2685.

[44] Hu, Y. X.; Ma, H. B.; Zheng, B.; Zhang, W. W.; Xiang, S.; Zhai, L.; Wang, L. F.; Chen, B.; Ren, X. M.; Bai, J., *Inorg. Chem.,* **2012**, *51*, 7066-7074.

[45] Bunzen, H.; Grzywa, M.; Hambach, M.; Spirkl, S.; Volkmer, D., *Cryst. Growth & Des.,* **2016**, *16*, 3190-3197.

[46] Bustamante, E. L.; Fernandez, J. L.; Zamaro, J. M., *J. Colloid Interf. Sci.,* **2014**, *424*, 37-43.

[47] Son, W. J.; Kim, J.; Kim, J.; Ahn, W. S., *Chem. Commun.,* **2008**, 6336-6338.

[48] Lee, Y.-R.; Jang, M.-S.; Cho, H.-Y.; Kwon, H.-J.; Kim, S.; Ahn, W.-S., *Chemical Eng. J.,* **2015**, *271*, 276-280.

[49] Seetharaj, R.; Vandana, P. V.; Arya, P.; Mathew, S., *Arab. J. Chem.,* **2016**, ahead of print.

[50] Bosch, E.; Barnes, C. L., *Inorg. Chem.,* **2002**, *41*, 2543-2547.

[51] Wen, H. M.; Wang, H.; Li, B.; Cui, Y.; Wang, H.; Qian, G.; Chen, B., *Inorg. Chem.,* **2016**, *55*, 7214-7218.

[52] Ma, L.-F.; Wang, L.-Y.; Hu, J.-L.; Wang, Y.-Y.; Yang, G.-P., *Cryst. Growth & Des.,* **2009**, *9*, 5334-5342.

[53] Ohi, H.; Tachi, Y.; Itoh, S., *Inorg. Chem.,* **2004**, *43*, 4561-4563.

[54] Zheng, S.-L.; Tong, M.-L.; Yu, X.-L.; Chen, X.-M., *J. Chem. Soc. Dalton,* **2001**, 586-592.

[55] Zhang, B.; Zhang, J.; Liu, C.; Sang, X.; Peng, L.; Ma, X.; Wu, T.; Han, B.; Yang, G., *RSC Adv.,* **2015**, *5*, 37691-37696.

[56] Cheng, X.; Zhang, A.; Hou, K.; Liu, M.; Wang, Y.; Song, C.; Zhang, G.; Guo, X., *Dalton Trans.,* **2013**, *42*, 13698-13705.

[57] Pachfule, P.; Das, R.; Poddar, P.; Banerjee, R., *Cryst. Growth & Des.,* **2011**, *11*, 1215-1222.

[58] Gurunatha, K. L.; Uemura, K.; Maji, T. K., *Inorg. Chem.,* **2008**, *47*, 6578-6580.

[59] Thapa, K. B.; Chen, J.-D., *CrystEngComm,* **2015**, *17*, 4611-4626.

[60] Halper, S. R.; Do, L.; Stork, J. R.; Cohen, S. M., *J. Am. Chem. Soc.,* **2006**, *128*, 15255-15268.

[61] Jeffrey, G. A., *An Introduction To Hydrogen Bonding*. Oxford University Press: New York, **1997**.

[62] Desiraju, G. R.; Steiner, T., *The Weak Hydrogen Bond in Structural Chemistry and Biology*. Oxford University Press: Oxford, **1999**.

[63] Desiraju, G. R., *Accounts Chem. Res.,* **2002**, *35*, 565-573.

[64] Desiraju, G. R.; Sharma, C. V. K. M., *J. Chem. Soc. Chem. Commun.,* **1991**, 1239-1241.

[65] Scheiner, S., *Phys. Chem. Chem. Phys.,* **2011**, *13*, 13860-13872.

[66] Blake, A. J.; Champness, N. R.; Khlobystov, A. N.; Lemenovskii, D. A.; Li, W.-S.; Schröder, M., *Chem. Commun.,* **1997**, 1339-1340.

[67] Sinnokrot, M. O.; Sherrill, C. D., *J. Phys. Chem. A.,* **2006**, *110*, 10656-10668.

[68] Burley, S.; Petsko, G., *Science,* **1985**, *229*, 23-28.

[69] Hunter, C. A.; Singh, J.; Thornton, J. M., *J. Mol. Biol.,* **1991**, *218*, 837-846.

[70] Pyykkö, P., *Chem. Rev.,* **1997**, *97*, 597-636.

[71] Senchyk, G. A.; Bukhan'ko, V. O.; Lysenko, A. B.; Krautscheid, H.; Rusanov, E. B.; Chernega, A. N.; Karbowiak, M.; Domasevitch, K. V., *Inorg. Chem.,* **2012**, *51*, 8025-8033.

[72] Zhang, J. P.; Huang, X. C.; Chen, X. M., *Chem. Soc. Rev.,* **2009**, *38*, 2385-2396.

[73] Hu, Y. X.; Ma, H. B.; Zheng, B.; Zhang, W. W.; Xiang, S.; Zhai, L.; Wang, L. F.; Chen, B.; Ren, X. M.; Bai, J., *Inorg. Chem.,* **2012**, *51*, 7066-7074.

[74] Zhang, J. P.; Liao, P. Q.; Zhou, H. L.; Lin, R. B.; Chen, X. M., *Chem. Soc. Rev.,* **2014**, *43*, 5789-5814.

[75] Stock, N.; Biswas, S., *Chem. Rev.,* **2012**, *112*, 933-969.

[76] Millange, F.; El Osta, R.; Medina, M. E.; Walton, R. I., *CrystEngComm,* **2011**, *13*, 103-108.

[77] Want, B., *J. Cryst. Growth,* **2011**, *335*, 90-93.

[78] Want, B.; Dar, F., *JCPT,* **2012**, *2*, 137-141.

[79] Want, B.; Samad, R., *J. Mater. Sci.,* **2014**, *49*, 4891-4898.

[80] Raj, A. M. E.; Jayanthi, D. D.; Jothy, V. B.; Jayachandran, M.; Sanjeeviraja, C., *Cryst. Res. Technol.,* **2008**, *43*, 1307-1313.

[81] Batten, S. R.; Neville, S. M.; Turner, D. R., *Coordination Polymers: Design, Analysis and Application*. The Royal Society of Chemistry: Cambridge, **2009**.

[82] Ni, Z.; Masel, R. I., *J. Am. Chem. Soc.,* **2006**, *128*, 12394-12395.

[83] Pilloni, M.; Padella, F.; Ennas, G.; Lai, S.; Bellusci, M.; Rombi, E.; Sini, F.; Pentimalli, M.; Delitala, C.; Scano, A.; Cabras, V.; Ferino, I., *Micropor. and Mesopor. Mat.,* **2015**, *213*, 14-21.

[84] Bigdeli, M.; Morsali, A., *Ultrason. Sonochem.,* **2015**, *27*, 416-422.

[85] Mondloch, J. E.; Karagiaridi, O.; Farha, O. K.; Hupp, J. T., *CrystEngComm,* **2013**, *15*, 9258-9264.

[86] Nagarathinam, M.; Vittal, J. J., *Angew. Chem. Int. Ed.,* **2006**, *45*, 4337-4341.

[87] Bloch, W. M.; Sumby, C. J., *Chem. Commun.,* **2012**, *48*, 2534-2536.

[88] He, Y. P.; Tan, Y. X.; Zhang, J., *Inorg. Chem.,* **2012**, *51*, 11232-11234.

[89] Nelson, A. P.; Farha, O. K.; Mulfort, K. L.; Hupp, J. T., *J. Am. Chem. Soc.,* **2009**, *131*, 458-460.

[90] Wilmer, C. E.; Leaf, M.; Lee, C. Y.; Farha, O. K.; Hauser, B. G.; Hupp, J. T.; Snurr, R. Q., *Nat. Chem.,* **2011**, *4*, 83-89.

[91] Chae, H. K.; Siberio-Perez, D. Y.; Kim, J.; Go, Y.; Eddaoudi, M.; Matzger, A. J.; O'Keeffe, M.; Yaghi, O. M., *Nature,* **2004**, *427*, 523-527.

[92] Zhang, K.; Qiao, Z.; Jiang, J., *Cryst. Growth & Des.,* **2016**, *17*, 543-549.

[93] Tanaka, D.; Kitagawa, S., *Chem. Mater.,* **2008**, *20*, 922-931.

[94] Campos-Fernandez, C. S.; Schottel, B. L.; Chifotides, H. T.; Bera, J. K.; Bacsa, J.; Koomen, J. M.; Russell, D. H.; Dunbar, K. R., *J. Am. Chem. Soc.,* **2005**, *127*, 12909-12923.

[95] Cohen, S. M., *J. Am. Chem. Soc.,* **2017**, *139*, 2855-2863.

[96] Burnett, B. J.; Barron, P. M.; Hu, C.; Choe, W., *J. Am. Chem. Soc.,* **2011**, *133*, 9984-9987.

[97] Tu, B.; Pang, Q.; Wu, D.; Song, Y.; Weng, L.; Li, Q., *J. Am. Chem. Soc.,* **2014**, *136*, 14465-14471.

[98] Bernini, M. C.; Gandara, F.; Iglesias, M.; Snejko, N.; Gutierrez-Puebla, E.; Brusau, E. V.; Narda, G. E.; Monge, M. A., *Chemistry,* **2009**, *15*, 4896-4905.

[99] Ma, J.-P.; Liu, S.-C.; Zhao, C.-W.; Zhang, X.-M.; Sun, C.-Z.; Dong, Y.-B., *CrystEngComm,* **2014**, *16*, 304-307.

[100] Ke, S.-Y.; Wang, C.-C., *CrystEngComm,* **2015**, *17*, 8776-8785.

[101] Ito, H.; Muromoto, M.; Kurenuma, S.; Ishizaka, S.; Kitamura, N.; Sato, H.; Seki, T., *Nat. Commun.,* **2013**, *4*, 2009-2012.

[102] Shepherd, H.; Tonge, G.; Hatcher, L.; Bryant, M.; Knichal, J.; Raithby, P.; Halcrow, M.; Kulmaczewski, R.; Gagnon, K.; Teat, S., *Magnetochemistry,* **2016**, *2*, 1-9.

[103] Andrzejewski, M.; Katrusiak, A., *J. Phys. Chem. Lett.,* **2017**, *8*, 929-935.

[104] Wen, L.; Cheng, P.; Lin, W., *Chem. Commun.,* **2012**, *48*, 2846-2848.

[105] Murase, T.; Horiuchi, S.; Fujita, M., *J. Am. Chem. Soc.,* **2010**, *132*, 2866-2867.

[106] Yao, Q.; Sun, J.; Li, K.; Su, J.; Peskov, M. V.; Zou, X., *Dalton Trans.,* **2012**, *41*, 3953-3955.

[107] Wang, Z.; Cohen, S. M., *Chem. Soc. Rev.,* **2009**, *38*, 1315-1329.

[108] Wu, C. D.; Lin, W., *Angew. Chem. Int. Ed.,* **2005**, *44*, 1958-1961.

[109] Ghosh, S. K.; Kaneko, W.; Kiriya, D.; Ohba, M.; Kitagawa, S., *Angew. Chem. Int. Ed.,* **2008**, *47*, 8843-8847.

[110] Seo, J.; Matsuda, R.; Sakamoto, H.; Bonneau, C.; Kitagawa, S., *J. Am. Chem. Soc.,* **2009**, *131*, 12792-12800.

[111] Biradha, K.; Hongo, Y.; Fujita, M., *Angew. Chem. Int. Ed.,* **2002**, *41*, 3395-3398.

[112] Sugiyama, H.; Watanabe, S.; Tanaka, H.; Miyahara, M. T., *Langmuir,* **2012**, *28*, 5093-5100.

[113] Wang, C.; Li, L.; Bell, J. G.; Lv, X.; Tang, S.; Zhao, X.; Thomas, K. M., *Chem. Mater.,* **2015**, *27*, 1502-1516.

[114] Kondo, A.; Noguchi, H.; Ohnishi, S.; Kajiro, H.; Tohdoh, A.; Hattori, Y.; Xu, W. C.; Tanaka, H.; Kanoh, H.; Kaneko, K., *Nano. Lett.,* **2006**, *6*, 2581-2584.

[115] Maji, T. K.; Mostafa, G.; Matsuda, R.; Kitagawa, S., *J. Am. Chem. Soc.,* **2005**, *127*, 17152-17153.

[116] He, Y. C.; Yang, J.; Liu, Y. Y.; Ma, J. F., *Inorg. Chem.,* **2014**, *53*, 7527-7533.

[117] Wang, F.; Kusaka, S.; Hijikata, Y.; Hosono, N.; Kitagawa, S., *ACS Appl. Mater. Interfaces,* **2017**, ahead of print.

[118] Dybtsev, D. N.; Chun, H.; Kim, K., *Angew. Chem. Int. Ed.,* **2004**, *43*, 5033-5036.

[119] Noro, S.-i.; Kitaura, R.; Kondo, M.; Kitagawa, S.; Ishii, T.; Matsuzaka, H.; Yamashita, M., *J. Am. Chem. Soc.,* **2002**, *124*, 2568-2583.

[120] Tripathi, S.; Srirambalaji, R.; Patra, S.; Anantharaman, G., *CrystEngComm,* **2015**, *17*, 8876-8887.

[121] Wu, J. Y.; Liu, Y. C.; Chao, T. C., *Inorg. Chem.,* **2014**, *53*, 5581-5588.

[122] Ke, S.-Y.; Chang, Y.-F.; Wang, H.-Y.; Yang, C.-C.; Ni, C.-W.; Lin, G.-Y.; Chen, T.-T.; Ho, M.-L.; Lee, G.-H.; Chuang, Y.-C.; Wang, C.-C., *Cryst. Growth & Des.,* **2014**, *14*, 4011-4018.

[123] Kole, G. K.; Peedikakkal, A. M.; Toh, B. M.; Vittal, J. J., *Chemistry,* **2013**, *19*, 3962-3968.

[124] Tzeng, B.-C.; Chang, T.-Y.; Tsai, M.-H.; Lin, Y.-T.; Lee, S.-F.; Sheu, H.-S., *ChemPlusChem,* **2015**, *80*, 878-885.

[125] Wang, Z.; Cohen, S. M., *Chem. Soc. Rev.,* **2009**, *38*, 1315-1329.

[126] Pirzada, T. J.; MacGregor, S. A.; Ahmed, S.; Edler, K. J.; Hamzah, H. A.; Jiang, D.; Burrows, A. D.; Mitchels, J. M.; Hassan, I. A.; Halls, J. E.; Marken, F., *Chem. Commun.,* **2013**, *49*, 10593-10595.

[127] Kim, M.; Garibay, S. J.; Cohen, S. M., *Inorg. Chem.,* **2011**, *50*, 729-731.

[128] Li, J. R.; Zhou, H. C., *Nat. Chem.,* **2010**, *2*, 893-898.

[129] Burnett, B. J.; Barron, P. M.; Hu, C.; Choe, W., *J. Am. Chem. Soc.,* **2011**, *133*, 9984-9987.

[130] Park, I. H.; Medishetty, R.; Lee, S. S.; Vittal, J. J., *Chem. Commun.,* **2014**, *50*, 6585-6588.

[131] Inokuma, Y.; Kawano, M.; Fujita, M., *Nat. Chem.,* **2011**, *3*, 349-358.

[132] Inokuma, Y.; Yoshioka, S.; Ariyoshi, J.; Arai, T.; Hitora, Y.; Takada, K.; Matsunaga, S.; Rissanen, K.; Fujita, M., *Nature,* **2013**, *495*, 461-466.

[133] Bloch, W. M.; Champness, N. R.; Doonan, C. J., *Angew. Chem. Int. Ed.,* **2015**, *54*, 12860-12867.

[134] Ohtsu, H.; Choi, W.; Islam, N.; Matsushita, Y.; Kawano, M., *J. Am. Chem. Soc.,* **2013**, *135*, 11449-11452.

[135] Koblenz, T. S.; Wassenaar, J.; Reek, J. N., *Chem. Soc. Rev.,* **2008**, *37*, 247-262.

[136] Ohara, K.; Kawano, M.; Inokuma, Y.; Fujita, M., *J. Am. Chem. Soc.*, **2010**, *132*, 30-31.

[137] Biradha, K.; Fujita, M., *Angew. Chem. Int. Ed.,* **2002**, *41*, 3392-3395.

[138] Yoshioka, S.; Inokuma, Y.; Duplan, V.; Dubey, R.; Fujita, M., *J. Am. Chem. Soc.,* **2016**, *138*, 10140-10142.

[139] Duplan, V.; Hoshino, M.; Li, W.; Honda, T.; Fujita, M., *Angew. Chem. Int. Ed.,* **2016**, *55*, 4919-4923.

[140] Gu, Z. Y.; Yang, C. X.; Chang, N.; Yan, X. P., *Acc. Chem. Res.*, **2012**, *45*, 734-745.

[141] Wang, X.; Makal, T. A.; Zhou, H.-C., *Aust. J. Chem.,* **2014**, *67*, 1629.

[142] Anstoetz, M.; Rose, T. J.; Clark, M. W.; Yee, L. H.; Raymond, C. A.; Vancov, T., *PLoS One,* **2015**, *10*, e0144169.

[143] Riddell, I. A.; Smulders, M. M.; Clegg, J. K.; Nitschke, J. R., *Chem. Commun.,* **2011**, *47*, 457-459.

[144] Kawamichi, T.; Haneda, T.; Kawano, M.; Fujita, M., *Nature,* **2009**, *461*, 633-635.

[145] Gong, L. L.; Feng, X. F.; Luo, F.; Yi, X. F.; Zheng, A. M., *Green Chem.,* **2016**, *18*, 2047-2055.

[146] Belmabkhout, Y.; Guillerm, V.; Eddaoudi, M., *Chem. Eng. J.,* **2016**, *296*, 386-397.

[147] Liu, D.; Lang, J. P.; Abrahams, B. F., *J. Am. Chem. Soc.,* **2011**, *133*, 11042-11045.

[148] Tian, J.; Saraf, L. V.; Schwenzer, B.; Taylor, S. M.; Brechin, E. K.; Liu, J.; Dalgarno, S. J.; Thallapally, P. K., *J. Am. Chem. Soc.,* **2012**, *134*, 9581-9584.

[149] Khatua, S.; Goswami, S.; Biswas, S.; Tomar, K.; Jena, H. S.; Konar, S., *Chem. Mater.,* **2015**, *27*, 5349-5360.

[150] Song, X.-Z.; Song, S.-Y.; Zhao, S.-N.; Hao, Z.-M.; Zhu, M.; Meng, X.; Wu, L.-L.; Zhang, H.-J., *Adv. Funct. Mater.,* **2014**, *24*, 4034-4041.

Chapter 2

Ethynyl and allenyl functionalised 1,3-benzenedicarboxylate as linkers in a series of lead coordination polymers and a metallogel

2.1. Introduction

There has recently been a resurgence of interest in the coordination chemistry of divalent lead,[1] motivated by the damaging toxicity of lead in aqueous habitats and the need for its safe removal from the environment.[2] A knowledge of the coordination properties leading to preferential binding of lead to a target ligand is crucial for understanding its toxicological properties, the design of selective chelation-therapy agents,[3] and the development of efficient ligation agents for the treatment of polluted wastewater.[4]

This chapter focuses on a series of Pb(II) based coordination polymers (CPs) synthesised under varying conditions. Lead(II) centres can adopt a wide range of coordination modes with coordination numbers ranging from 2 – 10,[5] and due to a lack of crystal field splitting, can provide flexible coordination environments that are not restricted to the ideal geometries of the valence shell electron-pair repulsion model. Recent publications have indicated that lead(II) is a suitable candidate for the investigation of single-crystal to single-crystal (SCSC) transformations.[6-9]

The $5d^{10}6s^2$ electronic configuration of divalent lead involves a $6s^2$ pair of electrons, and depending on the stereoactivity of this lone pair, the lead(II) coordination environment can be classified into one of two structural categories; holodirected and hemidirected. Bock et al.[10] defined the two coordination sphere configurations as *"holodirected, in which the bonds to ligand atoms are directed throughout the surface of an encompassing*

globe" and *"hemidirected, in which the bond to ligand atoms are directed throughout only part of the globe, that is, there is an identifiable void (or gap) in the distribution of bonds to the ligands"*. The authors observed that for coordination numbers from 2 to 5, all Pb(II) coordination geometries were hemidirected, while for coordination numbers 9 and 10, all Pb(II) compounds exhibited holodirected geometry. For intermediate coordination numbers (6 - 8) both holodirected and hemidirected environments were observed to be possible. These results suggest that as coordination number increases, ligands experience greater 'crowding' around the metal centre and thus the stereoactivity of the lone pair diminishes (Figure 24).

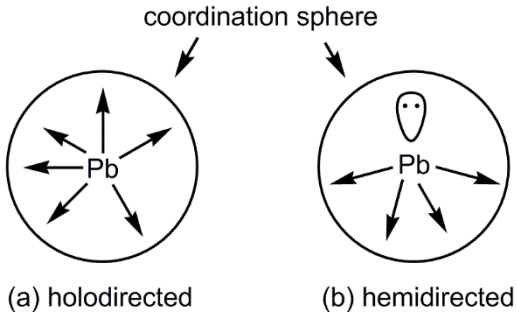

Figure 24: *Lead coordination sphere environments: (a) Holodirected and (b) Hemidirected supporting a stereoactive lone pair.*

Coordination bonds to lead(II) can also be described in terms of inner and outer coordination sphere bonding, depending on the lengths of the interactions. By the addition of outer coordination bonds to Pb(II) centres, complexes can convert from a hemidirected to a holodirected geometry.[11,12] The inherent flexibility of the lead coordination sphere opens up the possibility of flexibility within Pb(II) based coordination polymers. By first investigating and eventually manipulating which interactions dominate the self-assembly of the crystal structure through the interplay of steric and electrostatic factors, a higher energy and thus metastable topology may be obtained.

To determine the correct topology of the material in question, a definition of the length of the Pb–O bond is important. According to Bondi et al.,[13] the sum of the van der Waals radii of Pb and O is equal to 3.54 Å. In a review by Davidovich,[14] the limiting value for a Pb–O bond is considered as 3.30 Å. The review also takes into account the length of the primary coordination sphere: < 2.70 Å. For the purposes of this thesis, Pb–O bond lengths will be categorised as up to 2.70 Å for inner coordination interactions and 2.70 – 3.30 Å for outer coordination interactions, as defined by the above authors.

Moving beyond the coordination sphere, weak hydrogen bonding can constitute a major role in the packing and stabilisation of one and two dimensional CPs. The length of a hydrogen bond must be defined in order to identify these interactions in the solid state. Strong hydrogen bonding such as O–H···O is very distinct, displaying a narrow range around values of less than the sum of van der Waals radii for the interacting atoms. For example, typical O···O distances are within 2.6 Å and 2.8 Å. For weaker C–H···O/N hydrogen bonding however the situation is far less clear cut.[15] These interactions can be easily affected by solid-state forces, thus cannot be defined using van der Waals ranges. The main differential between van der Waals interactions and weak hydrogen bonds is bond directionality. A typical ethynyl-derived weak hydrogen bond to carboxylate approach angle is 152°, which is that of conventional hydrogen bonds such as those formed by hydroxy groups.[16] This angle becomes less directional the less acidic the donor carbon becomes, until the distance and approach angle become fundamentally incompatible, in which circumstance the contact can only be classed as a van der Waals interaction. For these weaker interactions distances of $3.0 < D < 4.0$ Å and $2.0 < d < 3.0$ Å are usual, whereas the approach angle can have a wide range of $180 < \theta < 100°$. In this case D is the heavy atom donor-acceptor distance, d is the hydrogen-acceptor distance and θ is the approach angle.

The conditions of CP synthesis can greatly affect the morphology of how competing interactions steer the self-assembly of the resulting lead(II) based materials, taking into account the solvent, temperature and the ligand present.[17] In this chapter the ligand is a meta- substituted 1,3-benzenedicarboxylic acid, where the substituent is either an ethynyl or allenyl group.

Due to the multi-carboxylate nature of the ligand and flexible coordination environment of the lead(II) centres, the gross structure of the resultant coordination polymer is difficult to predict. A systematic synthesis of a series of CP structures can give an insight into the hierarchy of the aforementioned competing interactions during the self-assembly process of the two substituents. Crystallographic data for all crystalline samples are given in Appendix II.

2.2. Results

A series of coordination polymers were synthesised from the two components $Pb(OAc)_2 \cdot 3H_2O$ and 5-ethynyl-1,3-benzenedicarboxylic acid (H_2ebdc) under various conditions. In total six crystal structures were obtained, two of which are derived from a SCSC transition.

2.2.1. 5-ethynyl-1,3-benzenedicarboxylic acid

Benzenedicarboxylic acid (H_2bdc) derived CPs are well-studied, and usually assemble into porous structures[18] as well as well-known functional materials such as UiO-66 (Zr-bdc MOF).[19] Functionalising the bdc linker with an ethynyl group adds potential weak hydrogen bonding and steric limitations that would influence the final structure of the resulting CP. The H_2ebdc ligand possesses two carboxylic acid functional groups to allow coordination of metal nodes upon deprotonation and an ethynyl group to promote weak hydrogen-bonding interactions. Interactions that are allowed by this ligand include weak C–H···X hydrogen bonding from the ethynyl functional group, π···π stacking derived from the central aromatic ring as well as strong hydrogen bonding to the carboxylate functionality. The previously synthesised H_2ebdc ligand was prepared by a three-step reaction from the commercially available dimethyl 5-hydroxyisophthalate. A substitution of the hydroxyl group for a triflate was followed by a Sonogashira coupling to give dimethyl-5-(trimethylsilylethynyl) benzene-1,3-dicarboxylate. A subsequent one-step ester and trimethylsilyl deprotection resulted in H_2ebdc (Scheme 4).

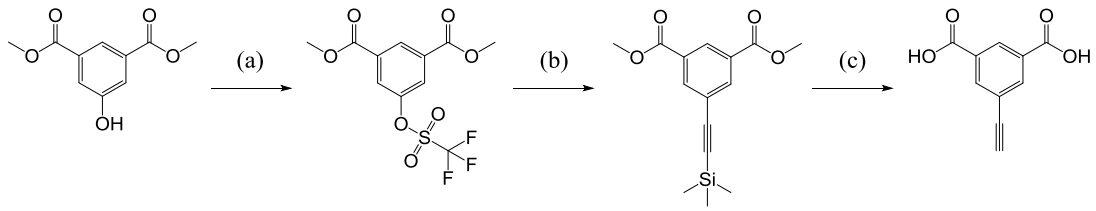

Scheme 4: *Three step synthesis of H_2ebdc. a) $(CF_3SO_2)_2O$ in pyridine, CH_2Cl_2 at 0 °C; b) $(CH_3)_3SiC{\equiv}CH$, $Pd(PPh_3)_2Cl_2$, CuI in THF, NEt_3 at RT; c) NaOH, THF at RT.*

The overall yield for this synthesis was 90%, and the product matched previously reported ^{1}H-NMR and FTIR data.[40,41]

H_2ebdc has not been previously crystallographically analysed. Crystals of H_2ebdc·H_2O were obtained through slow layer diffusion of H_2ebdc in methanol and water. The

asymmetric unit consists of one H_2ebdc molecule and a single corresponding water molecule. The structure crystallises in a triclinic $P\,\bar{1}$ space group and propagates in layered 2D sheets assembled together by hydrogen bonding. A repeating hydrogen bonding motif is observed around the central water molecules and surrounding carboxylic acid groups as shown in Figure 25.

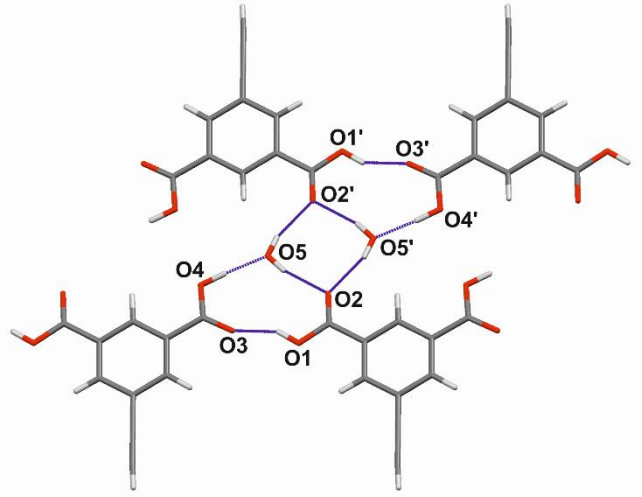

Figure 25: *Part of a single layer of H_2ebdc·H_2O showing the hydrogen bonding motif between the carboxylic acid groups and water. Hydrogen bonds are coloured blue.*

The hydrogen bond pattern can be described using the Etter and Bernstein[20] graph set notation; the two outer rings as $R_3^3(10)$, and the inner ring as $R_4^2(8)$. Hydrogen bond distances *D* from 2.5889(2) to 2.8372(3) Å were observed. Furthermore, significant π···π interactions are observed between the hydrogen bonded layers from the aromatic group to the adjacent group parallel, adding to the integrity of the overall structure. The π···π interplanar separation between parallel molecules is 3.3726(3) Å, with a phenyl to phenyl lateral shift of 1.4158(5) Å (Figure 26). The calculated centroid to centroid distance was determined to be 3.6577(13) Å which is within the range (3.316 – 4.197 Å), albeit below the average of 3.755 Å, found for meta- substituted benzenedicarboxylic acid derivatives from the CCDC database.[21] The shorter than average interaction implies that the ethynyl group increases the strength of interactions between stacked phenyl groups.

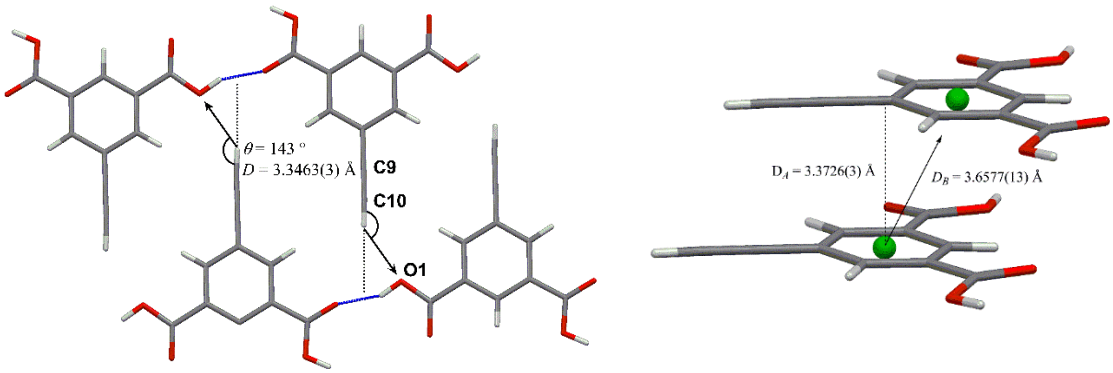

Figure 26: *Crystalline packing of the H_2ebdc groups showing (left) the nearest contact between the ethynyl group and O1 (right) phenyl – phenyl interactions between adjacent H_2ebdc groups.*

Hydrogen bonding is an important factor when it comes to the ethynyl functional group. As shown in Figure 26, the C10 terminal ethynyl atom acts as a potential hydrogen bond donor to the O1 oxygen of the symmetry generated H_2ebdc molecule $(2 - x, -y, 1 - z)$. However, based on the combined observed distance D of 3.3463(3) Å and wide approach angle θ of 143 ° any hydrogen bonding is likely to be extremely weak. The positions of ethynyl groups are therefore most likely influenced by the much stronger hydrogen bond interactions of the carboxylic acid groups with water. The IR vibration frequency of this loosely interacting ethynyl C–H stretching band is assigned at 3301 cm^{-1}, which is the most convincing evidence for this to be a non-interacting C–H, as IR analysis is arguably the best method for monitoring the ethynyl hydrogen bond in the solid state.[23] This 'non-interaction' can consequently provide a useful reference point for any bathochromic shifts that might occur with hydrogen bond formation in the coordination polymers of this ligand described below. Along with the ability to coordinate to lead(II) through four coordination sites, its potential for solid state π···π stacking and ethynyl C-H···π interactions, gives this ligand potential to direct CP self-assembly in a diverse manner.

2.2.2. 1D CP chains

Two one-dimensional CPs were obtained from the reaction of lead(II) acetate trihydrate and H_2ebdc in either DMSO or DMF under the same heating conditions. Both CPs are structured around ligated inorganic Pb–O backbones which are self-assembled by terminal ethynyl C–H···O interactions.

Prismatic crystals of $[Pb(ebdc)(DMSO)_2]$ (**1**) were obtained by a reaction of H_2ebdc and $Pb(OAc)_2{\cdot}3H_2O$ in DMSO at 100 °C for four days. The asymmetric unit consists of one

Pb(II) centre coordinated to an ebdc ligand and two DMSO molecules, one of which is disordered over two positions. The network propagates through fused pairs of repeating lead(II) and ebdc linker ribbons (Figure 27) forming linear 1D interdigitated bilayer chains which pack through $P2_1/n$ symmetry (Figure 28).

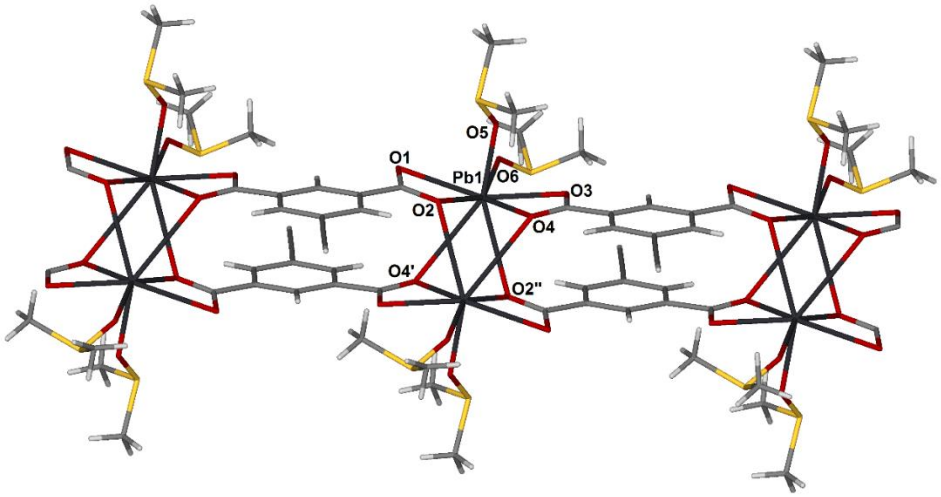

Figure 27: *Structure of the 1D chain of* ***1****. Only one position of the disordered DMSO has been shown for clarity.*

The crosslinked nature of the fused ribbons results in the lead(II) centre supporting a hemidirected eight-coordinate geometry, supporting five inner sphere coordination bonds ranging from 2.355(6) to 2.611(6) Å and three outer sphere coordination bonds ranging from 2.753(7) to 3.248(7) Å. Each ebdc ligand bridges four metal centres through six coordination bonds *via* a $\mu_4(\mu_2+\mu_2)$ fashion to the 3-connected Pb nodes.

Interactions between the 1D ribbons of **1** consist of bifurcated C–H···O hydrogen bonding derived from the C9 atom of the ethynyl group bonding to O2' and O4' of symmetry generated carboxylate groups (Figure 28). Distances for C9···O2' of 3.279(12) Å and C9···O4' of 3.210(11) Å were observed, with hydrogen bond lengths *d* and approach angles in Table 1 below. The approach angle of the ethynyl group is 170° relative to the plane of the carboxylate oxygen atoms which favours the observed hydrogen-bonding interactions.

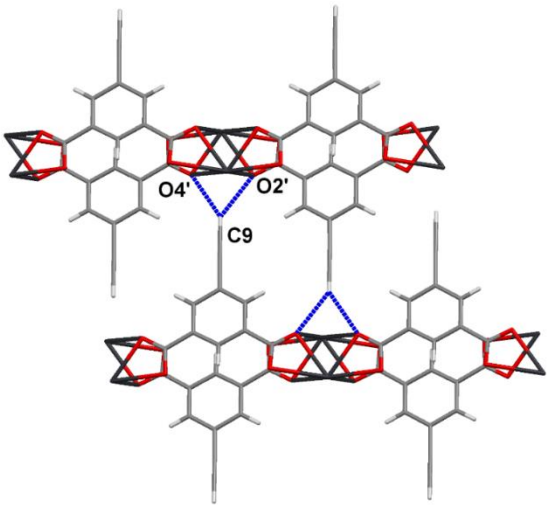

Figure 28: *Hydrogen bonding in* ***1*** *between the ebdc ethynyl groups and adjacent carboxylate moieties. Hydrogen bonds are shown in blue. Symmetry operators: O4' = (1 – x, – y, 3 – z), O2' = (2 – x, – y, 3 – z).*

Interaction	*D* (Å)	*d* (Å)	*θ* (°)
C9–H9···O2'	3.279(12)	2.47	142.3(8)
C9–H9···O4'	3.210(11)	2.39	143.8(7)

Table 1: *Hydrogen bond interactions between 1D ribbons of* ***1****.*

The product was also analysed using IR spectroscopy, in which expected bands corresponding to the alkyne and DMSO moieties were observed. Bands at 3001 cm^{-1}, 2913 cm^{-1} and 1356 cm^{-1} correspond to the CH_3 groups in DMSO whereas the alkyne C≡C–H stretch was observed at 3221 cm^{-1}. A comparison to the non-interacting ethynyl C–H band position in H_2ebdc·H_2O crystals shows a significant bathochromic shift of 80 cm^{-1}, and along with the favourable ethynyl to carboxylate approach angle, lead to the hydrogen bond interactions collectively yielding a 2D hydrogen-bonded network between solid-state one-dimensional chains that pack in a herringbone arrangement (Figure 29).

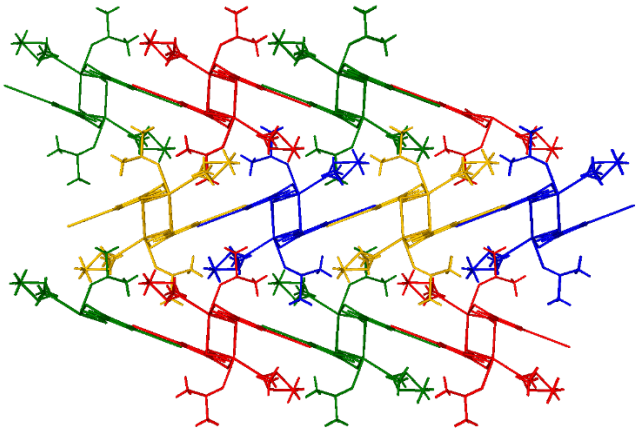

Figure 29: *A cross section of* ***1****, showing the packing of the Pb–O chains in a herringbone motif down the crystallographic* a *axis. Each symmetry generated 1D chain is differentiated by a colour.*

The reaction between $Pb(OAc)_2{\cdot}3H_2O$ and H_2ebdc was also carried out in DMF at 100 °C, with this reaction affording yellow cubic crystals with the molecular formula $[Pb_3(ebdc)_3(DMF)_3]{\cdot}0.5H_2O$ (**2**). The asymmetric unit contains three unique lead(II) centres that are ligated by three ebdc ligands and three coordinated molecules of DMF, two of which are disordered over two positions. The lead centres and ligands propagate by symmetry to give a backbone that resembles repeating bridged hexagonal rings. This bonding arrangement results in one nine-coordinate holodirected lead centre (Pb1), and two hemidirected lead centres; one of which is seven coordinate (Pb2) and the other eight coordinate (Pb3). All Pb1, Pb2 and Pb3 metal centres support five inner coordination bonds each ranging from 2.411(9) to 2.695(8) Å, and respectively support four, two and three additional outer coordination sphere bonds of the range 2.753(8) to 3.134(8) Å. Pb–O bond lengths for each metal centre can be found in Table 29 in Appendix II. The 1D tape motif of **2** is shown in Figure 30.

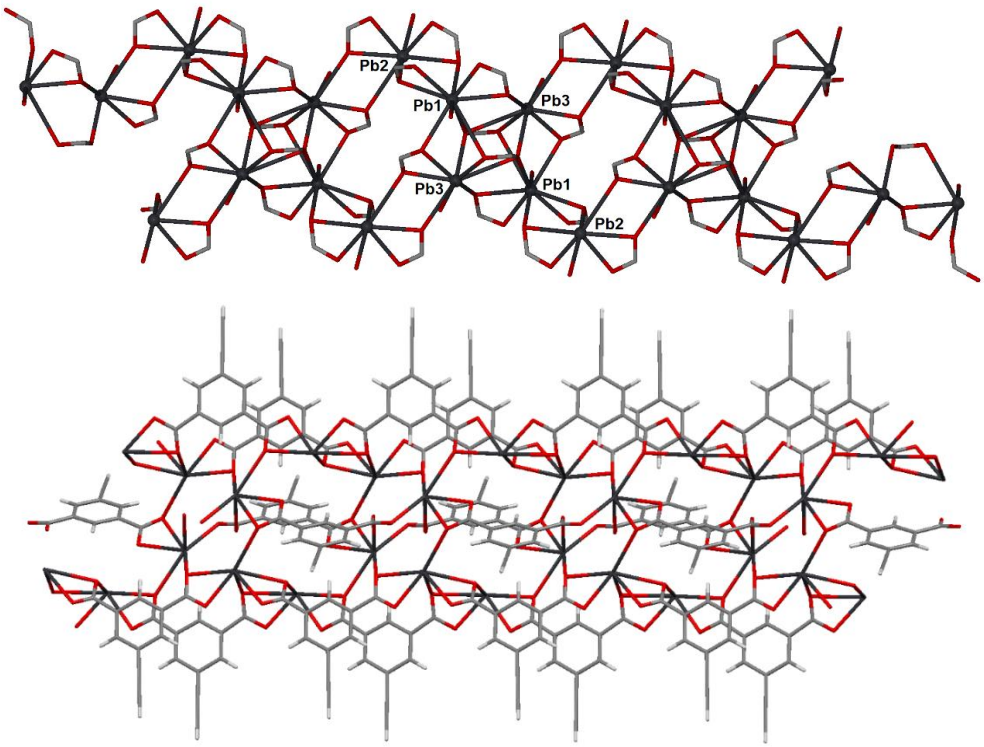

Figure 30: *Top: The linked chain Pb–O backbone of* **2** *showing coordination environments of Pb1, Pb2 and Pb3. Bottom: Orientation of the ebdc ligands in the 1D tapes of* **2**. *Coordinated DMF molecules have been removed for clarity.*

A seen from Figure 30 (bottom), pairs of ligands direct ethynyl groups to the top and bottom of the chains, and a single ligand extrudes from the orthogonal faces, ensuring that the all edges of the 1D chains are connected to neighbouring chains by hydrogen bonding. This hydrogen bonding mostly consists of bifurcated ethynyl C–H···O interactions from the terminal ethynyl carbon to carboxylate oxygens, analogous to those observed in **1**. Two parallel ethynyl groups form this interaction (Figure 31); where the terminal carbon atoms are C10 and C20 whereas the lone orthogonal ethynyl group forms a single hydrogen bond C39···O5''' of which the donor-acceptor distance is 3.560(2) Å. Heavy atom distances, bond lengths and approach angles for these are displayed in Table 2. No other significant interactions form between the 1D chains, suggesting that weak hydrogen-bonding interactions are solely responsible for the crystal packing in **2**.

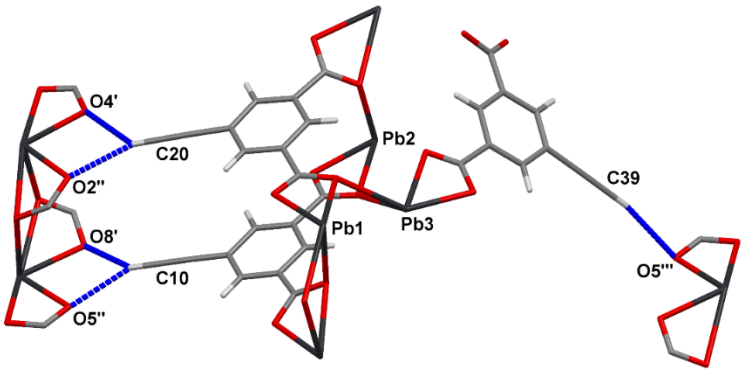

Figure 31: *The three unique ethynyl groups hydrogen bonding to adjacent carboxylate units in* **2**. *Symmetry operators: (') = (– x, 1 – y, 1 – z), ('') = (1 – x, 1 – y, 1 – z), (''') = (1 + x, y, – 1 + z).*

Interaction	*D* (Å)	*d* (Å)	*θ* (°)
C10–H10···O5''	3.277(16)	2.48	140.7(8)
C10–H10···O8'	3.307(16)	2.49	143.4(8)
C20–H20···O2''	3.281(16)	2.45	145.1(8)
C20–H20···O4'	3.196(15)	2.42	138.0(8)
C39–H39···O5'''	3.560(2)	2.61	170.0(12)

Table 2: *Hydrogen bond interactions between 1D tapes of* **2**.

The ethynyl groups interdigitate in such a way as to create a distinct 'zipper' motif within the crystal structure, held together by the afore-mentioned ethynyl hydrogen bonding as well as π···π interactions between pairs of phenyl groups. Sandwiched between each lead-ligand layer are interdigitating DMF groups filling in any potential void spaces within the crystal structure (Figure 32).

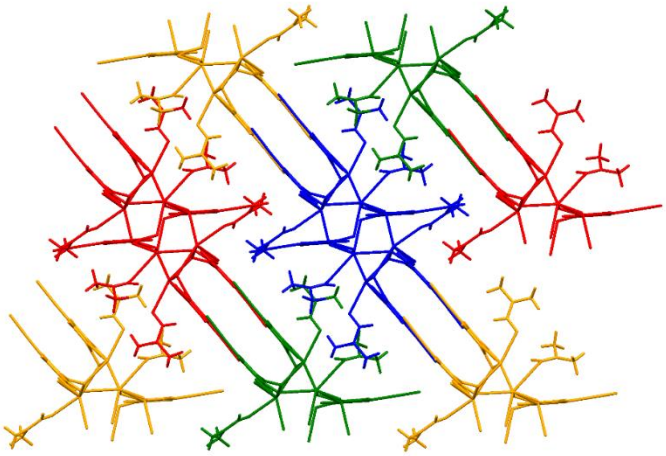

Figure 32: *A cross section of* **2**, *showing the packing of the Pb–O chains and ethynyl 'zipper' motif. Each symmetry generated 1D chain is differentiated by a colour.*

Despite the presence of three crystallographically unique ethynyl groups within the asymmetric unit of **2**, only a single C≡C–H band at 3247 cm^{-1} with a prominent shoulder directed toward lower wavenumbers was observed in the FTIR spectrum. The dominant vibrational band exhibited a bathochromic shift of 56 cm^{-1} relative to the band relating to the non-interacting ethynyl group in H_2ebdc·H_2O, and has been assigned to the bifurcated pair of terminal alkynes labelled C10 and C20 in Figure 31. The shoulder part of the peak exhibits greater red-shifting, which has been observed for directly aligned, as opposed to bifurcated, C–H···O interactions and thus has been assigned to the single alkyne labelled C39 in Figure 31. Infrared analysis also shows strong bands at 1642 cm^{-1} and 1102 cm^{-1} corresponding to the C=O and N–C bonds in DMF respectively.

2.2.3. 2D CP nets

Increasing the reaction temperature for the preparation of **2** from 100 °C to 140 °C yielded a higher dimensional structure. Yellow crystals obtained from a reaction of $Pb(OAc)_2·3H_2O$ and H_2ebdc at 140 °C have the overall formula $[Pb_4(ebdc)_4(DMF)_8]·H_2O$ (**3**). The asymmetric unit contains a single lead(II) centre coordinated to one ebdc group and two DMF molecules, one of which is disordered over two positions, and a single quarter-occupancy water molecule. The central Pb(II) metal supports a holodirected eight-coordinate geometry, supporting four inner sphere coordination interactions with Pb–O distances in the range 2.372(4) - 2.514(5) Å, and four outer coordination sphere interactions: Pb1–O4', 2.910(6) Å, Pb1–O4'', 2.786(4) Å, Pb1–O6, 2.905(3) Å and Pb1–O4''': 3.021(5) Å. The lead(II) centres aggregate to form 4-connected Pb_4O_4 cubane SBUs (secondary building units) as shown in Figure 33, left. These are positioned at the nodes of a 2D net, in which each node is linked to four others by pairs of bridging ebdc linkers (Figure 33, right). The layers are interdigitated by DMF and ethynyl groups and stack in an alternating (ABA) fashion, where the SBU of each consecutive layer sits atop the voids of the neighbouring layer.

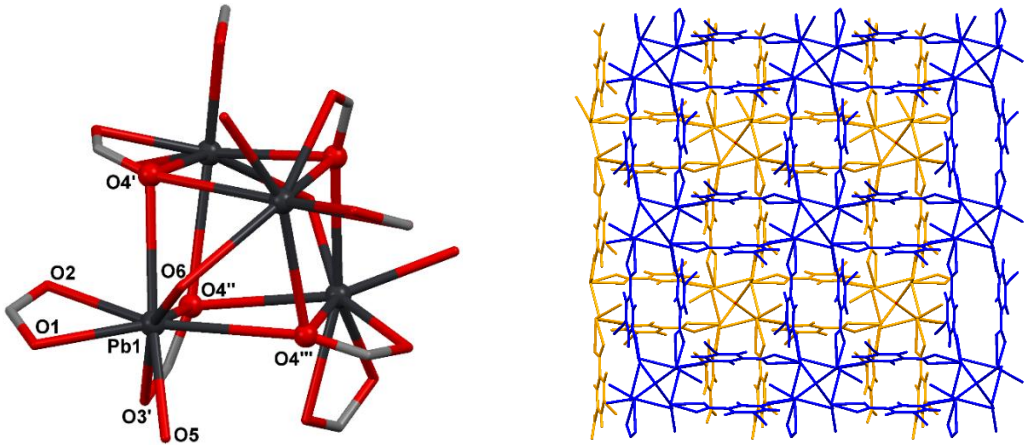

Figure 33: *Left: Pb_4O_4 cubane motif that acts as a secondary building unit in* **3**. *Only the carboxylate groups of ebdc and the oxygen atoms of coordinated DMF molecules have been shown for clarity. Right: Two layers of* **3** *showing the alternate (ABA) stacking of the 2D nets, coloured in blue and yellow, viewed down the crystallographic* c *axis. Coordinated DMF molecules and interstitial waters have been omitted for clarity.*

Ethynyl-derived weak hydrogen bonds constitute the only intermolecular interactions linking the 2D sheets, with the ethynyl groups interacting with carboxylate groups located above or below the net (Figure 34). The C10···O1' ethynyl hydrogen bond to the carboxylate group of a symmetry generated SBU ($^3/_2 - x$, $-^1/_2 + y$, $^3/_2 - z$) has a heavy atom distance D of 3.152(6) Å and a hydrogen bond length d of 2.209(5) Å with a favourable angle for bonding of 171°.

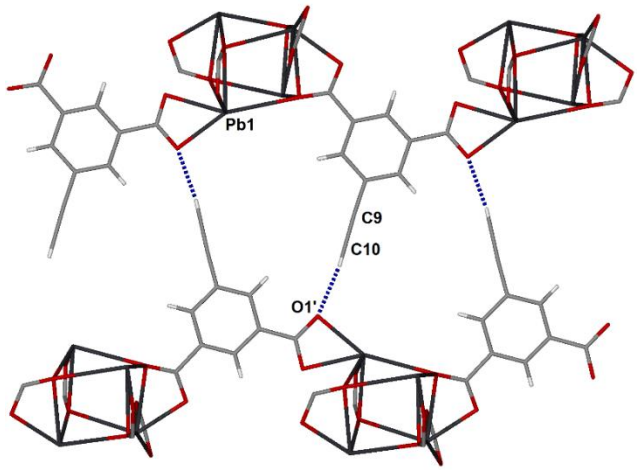

Figure 34: *Weak hydrogen-bonding interactions between C10 and O1' link 2D sheets of* **3** *in the solid state.*

Compound **3** exhibits the largest bathochromic shift of the structures discussed so far, wherein the terminal C−H stretch shifts 89 cm^{-1} from the non-bonding reference

3301 cm^{-1} to 3212 cm^{-1} in **3**. This observation can be explained by the alkyne group aligning to a single oxygen site O1', unlike in cases **1** and **2**, where the interaction is spread over two oxygen receptors, weakening the strength of the hydrogen bond interaction.

A different synthesis methodology was implemented for the next series of structures; the high affinity for carboxylate groups to lead(II) centres suggested that high temperatures were not necessary. Slow contact of the two components ensured that single crystals suitable for single crystal diffraction were obtained. A methanol and water layered diffusion method under ambient conditions was employed, to ensure sufficiently slow mixing.

Colourless needle crystals of [Pb(ebdc)(MeOH)]·0.5H_2O (**4**) were obtained by layered diffusion at room temperature using $Pb(OAc)_2·3H_2O$ and H_2ebdc. The resulting material crystallises in the monoclinic space group *C*2/*c*. The asymmetric unit of compound **4** contains a single divalent lead centre coordinated to one ebdc ligand and a methanol molecule. A half occupancy interstitial water molecule is also present. The coordination environment of the lead(II) centre Pb1 is formed of four oxygen atoms from ebdc ligands O1, O2, O3' and O4 and one oxygen from a methanol group O5, of which the bond lengths range from 2.440(5) to 2.531(6) Å for the carboxylates and 2.646(7) Å for the methanol. The coordination sphere is completed by two outer sphere coordination bonds, Pb–O3 and Pb–O4' for which the bond lengths are 2.876(6) and 2.837(5) Å respectively. The overall coordination sphere results in a seven coordination bond hemidirected environment around the central lead(II) atom. The gross structure as well as the lead(II) centre coordination environment is displayed in Figure 35 below.

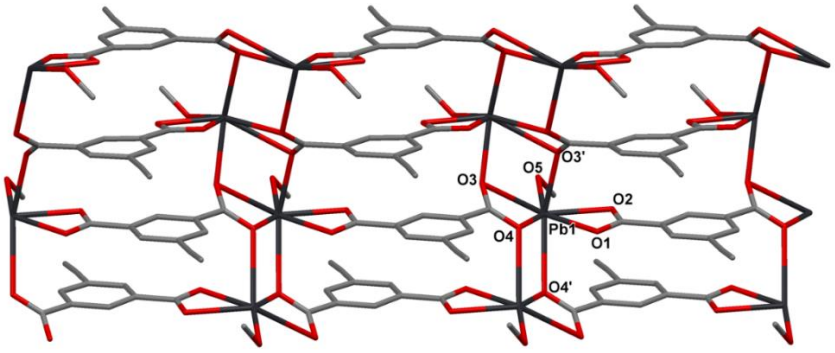

Figure 35: *2D net showing the coordination environment of the central Pb(II) atom in* **4**. *Water molecules and hydrogens have been omitted for clarity. Symmetry operators: O3' = (1 – x, y, ³/₂ – z), O4' = (½ – x, ½ – y, 1 – z).*

In **4**, each ebdc ligand bridges four Pb centres, in a $\mu_4(\mu_1+\mu_3)$ manner, as can be seen in Figure 35. This alternating ligand and lead(II) environment propagates *via* a 2D net along the crystallographic *c* axis, interdigitated by hydrogen bonded ebdc and methanol groups (Figure 36).

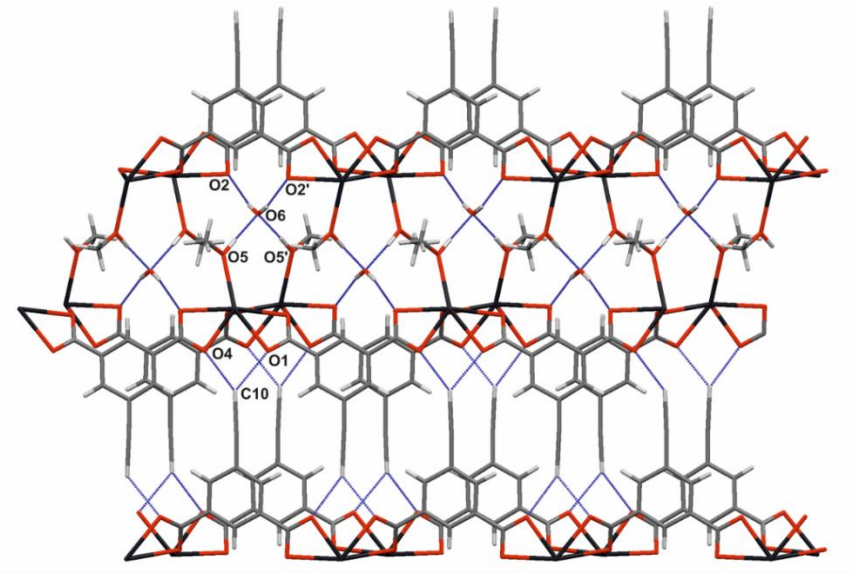

Figure 36: *4 viewed down the crystallographic* a *axis, showing the hydrogen bonding (blue) and the 'zipper' like interdigitation of the ebdc groups. Symmetry operators: (') = (1 – x, y, $^3/_2$ – z).*

Between the adjacent 2D layers of network **4**, water molecules act as hydrogen bond acceptors and donors, linking the layers together in the solid state. The water oxygen O6 acts as a hydrogen bond acceptor to methanol oxygens O5 and O5' and also acts as a hydrogen bond donor, interacting with O2 and O2' carboxylate oxygen atoms on an adjacent layer. In the non-polar regions of the network, interdigitated terminal alkynes tightly interdigitate to form a 'zipper' type motif, analogous to that in structure **2** (Figure 32). This motif is formed by bifurcated hydrogen bonding from the terminal carbon of the ebdc linker ethynyl group C10 to two carboxylate oxygens O1 and O4. The heavy atom distances, hydrogen bond lengths and approach angles are in Table 3.

Interaction	*D* (Å)	*d* (Å)	*θ* (°)
O5,O5'–H5···O6	2.726(9)	1.90(4)	161(10)
O6–H6···O2,O2'	2.746(9)	1.96	152.4(5)
C10–H10···O4	3.237(12)	2.46	138.6(6)
C10–H10···O1	3.246(12)	2.43	143.5(6)

Table 3: *Hydrogen bond interactions between layers of* ***4****. Symmetry operators: (') = (1 – x, y, $^3/_2$ – z).*

Within the 'zipper' conformation, π···π stacking of the ebdc ligands is observed, where the interplanar distance between a pair of interacting ebdc phenyl groups is 3.257(9) Å, centroid to centroid distance is 3.7578(7) Å, and the offset approach angle is 36.0°. These terminal hydrogen bonding and π···π interactions promote the closure of the distinct 'zipper' motifs propagating through the structure.

Spectroscopic data supports the evidence for hydrogen bonding between the ethynyl and carboxylate groups. A bathochromic shift of 52 cm^{-1} from 3301 cm^{-1} to 3249 cm^{-1} of the C≡C–H ethynyl bond was observed. Due to the bifurcated nature of the hydrogen interactions of the alkyne group, this fairly subtle shift is to be expected. Significant bands corresponding to the interstitial waters are present at 3338 cm^{-1} and a strong C-O methanol stretching band was observed at 1013 cm^{-1}.

When removed from the mother liquor and left under ambient conditions for one hour, network **4** was found to undergo a single-crystal to single-crystal (SCSC) transition. Initially, any of the resulting desolvated crystals were too small to collect single crystal data when network **4** was left to air-dry, however sufficiently large crystals of the product for single crystal analysis were eventually obtained by placing crystals of **4** in a controlled environment with limited air diffusion for several days. The resulting structure is a fully desolvated network [Pb(ebdc)] (**5**).

The colourless crystals of **5** consist of layered 2D nets of alternating Pb(II) metal centres and ebdc ligands similar to network **4**. The asymmetric unit packs in the triclinic $P\bar{1}$ space group and contains two crystallographically distinct ebdc ligands and two crystallographically unique lead(II) centres. Each ebdc ligand bridges four lead(II) centres in a bridging $\mu_4(\mu_2+\mu_2)$ manner (Figure 37).

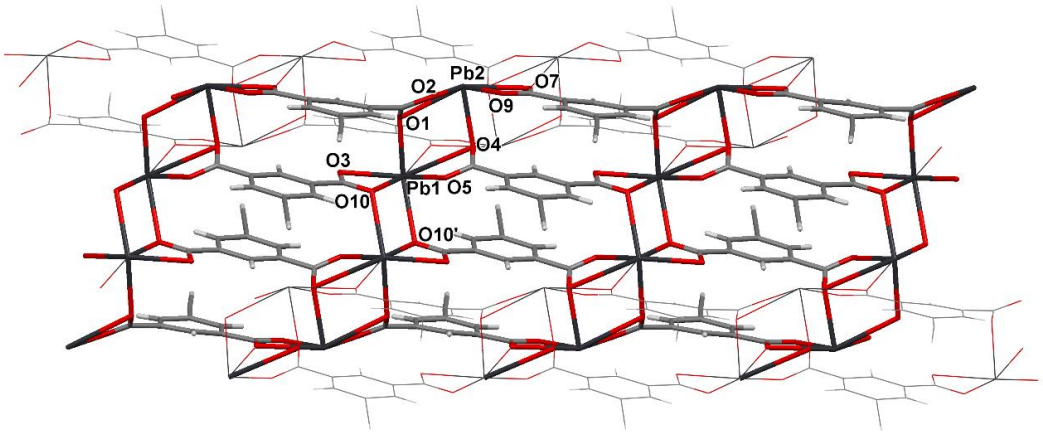

Figure 37: *2D net of* **5** *showing the coordination environment of the Pb(II) metal centres. The furthermost and foremost metal-ligand motifs are depicted in a 'wireframe' style for clarity. O10' has a symmetry operator of* $(2 - x, 1 - y, 2 - z)$.

The Pb1 lead centre displayed in Figure 38 supports seven Pb–O coordination bonds: five inner coordination bonds with lengths ranging from 2.414(9) to 2.506(7) Å, and two outer coordination sphere bonds, Pb1–O4 and Pb1–O7, of which the bond lengths are 2.989(7) and 2.817(8) Å respectively. The carboxylate O7 resides in the symmetry generated $(1 - x, 1 - y, 2 - z)$ group. The Pb2 lead centre supports six coordination bonds of lengths 2.330(8) to 2.771(7) Å; the Pb2–O1 bond length is 2.771(7) Å, which places this bond just beyond the inner coordination sphere radius. Both lead(II) centres exhibit identifiable voids in the distribution of coordination bonds in the coordination sphere and thus can be classed as hemidirected.

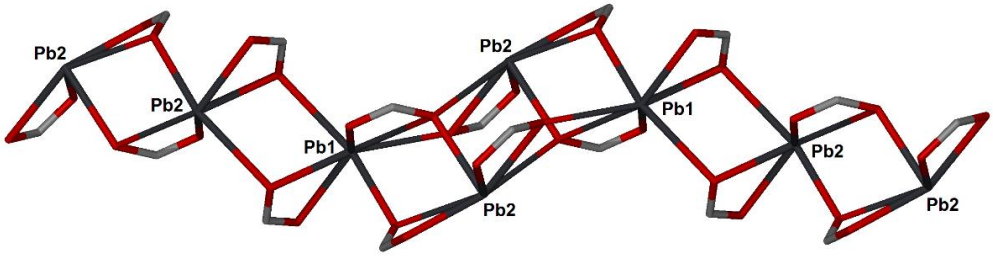

Figure 38: *Inorganic Pb–O motif showing coordination environments of Pb1 and Pb2 lead(II) atoms in* **5**.

Similarly to **4**, structure **5** exhibits bifurcated hydrogen bonding from the terminal ethynyl hydrogen in a 'zipper' type motif, acting as a donor to two carboxylate oxygen acceptors. Figure 39 shows two crystallographically distinct intermolecular bifurcated hydrogen bonds, where C9 interacts with carboxylate oxygen atoms O9 and O2, and

where C19 interacts with O10 and O5 of the adjacent 2D net. The heavy atom distances, hydrogen bond lengths and approach angles of these interactions are in Table 4.

Interaction	*D* (Å)	*d* (Å)	*θ* (°)
C9–H9···O9	3.285(6)	2.47	142.6(7)
C9–H9···O2	3.182(7)	2.39	139.8(7)
C19–H19···O10	3.237(8)	2.55	129.3(7)
C19–H19···O5	3.206(7)	2.31	155.1(7)

Table 4: *Hydrogen bond interactions of* **5**, *showing bond lengths and approach angles.*

These hydrogen bonds, as with compound **4**, enable close interdigitation of the terminal ethynyl groups thus adding stability to the overall structure. The π···π stacking remains similar in **5** as in structure **4**, with a phenyl interplanar distance of 3.309(11) Å and with a phenyl centroid to centroid distance of 3.797(6) Å within the 'zipper' channel.

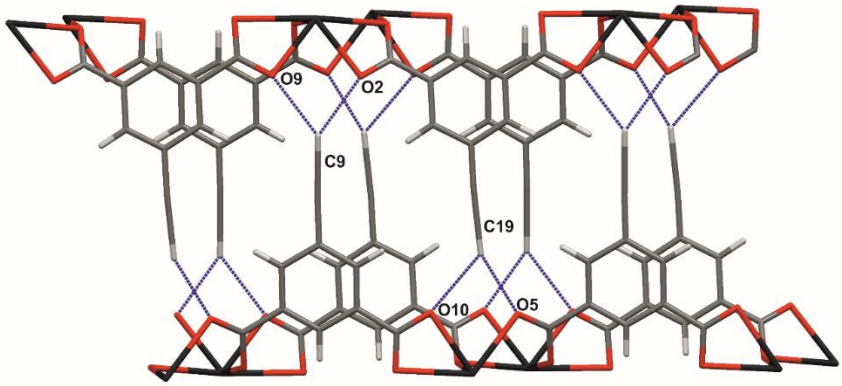

Figure 39: *Hydrogen bond interactions between 2D layers of* **5**, *showing hydrogen bonding in blue.*

By comparing structures **4** and **5**, a mechanism for the SCSC transformation can be suggested. The largest transformation happens along the *b* axis, where the lead(II) centres of the individual polymer nets approach closest to each other facilitated by the desolvation of the hydrogen-bonded methanol molecules. This enables new outer sphere Pb-O coordination bonds to form, namely Pb1–O7, 2.817(7) Å, and Pb2–O4, 2.989(7) Å. The distance between adjacent Pb(II) centres shows the contraction of this axis; from 17.7 Å in network **4** to 14.1 Å in network **5**. This shrinkage totals more than 20% of the asymmetric unit along the *b* axis. The interdigitated zipper motifs above and below therefore shift from alternating to askew (Figure 40), and contract toward each other slightly from 15.2 Å in **4** to 13.7 Å in **5**. This enables the formation of a new outer sphere coordination interaction Pb1–O7, of 2.817(8) Å, in place of the methanol and water

groups, and the contraction of the outer sphere Pb1–O4, 2.837(5) Å, interaction to Pb1-O10', 2.719(8) Å. Such a significant shift in the crystalline molecular structure renders this transformation irreversible. This was confirmed experimentally by PXRD, showing no change after crystals of **5** were suspended in a 1:1 methanol/water solution for two weeks.

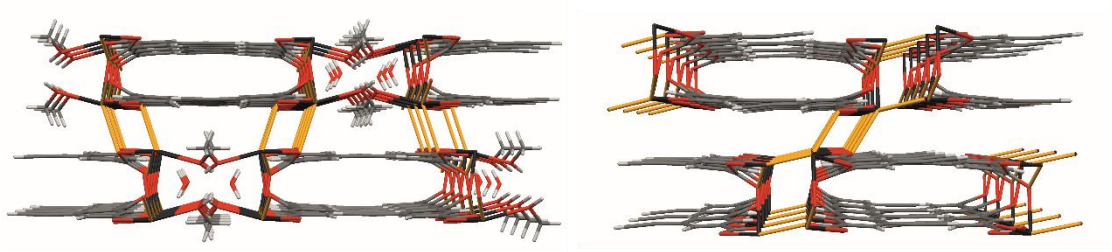

4 **5**

Figure 40: *Expanded cross-sections of networks* **4** *viewed down the crystallographic* c *axis and* **5** *viewed down the b axis. The outer coordination bonds are highlighted in gold.*

The transformation of **4** into **5** could also be monitored by infrared spectroscopy. Strong O–H (3297 cm^{-1}) and C–OH (1016 cm^{-1}) stretches were observed in **4**, corresponding to the water and methanol molecules. A peak at 1362 cm^{-1} can be assigned to the symmetric stretching of coordinated carboxylate groups. After full transformation into network **5**, the methanol and water peaks completely disappeared, and a bathochromic shift of the carboxylate stretching band was observed, which is consistent with the formation of the new outer sphere Pb–O coordination bonds. Peaks corresponding to the terminal alkyne C≡C–H stretch at 3240 cm^{-1} and C≡C stretch at 2100 cm^{-1} remain unchanged.

When placed under an optical microscope, single crystals of **4** were observed to fracture at approximately 63 °C and continue fracturing into microcrystals with heating. This is close to the boiling point of methanol (64 °C) suggesting a rapid solvent loss of the methanol. Figure 41 shows that the crystalline sample of **4** continues decomposing beyond 63 °C up to 106 °C, providing evidence for a subsequent loss of the interstitial water molecules.

Figure 41: *Rapid heating of a single crystal sample of* **4** *yielded microcrystalline particles. Rate of heating: 10 °C per minute.*

The crystalline sample required 50 minutes to convert completely to the desolvated form at room temperature as gauged by FTIR by the complete loss of the water and methanol OH and C-OH bands, and the structural transformation resulting from that which was confirmed by X-ray powder diffraction measurements in Figure 42 by the loss of peaks at 15.6 and 16.5° 2Θ in **4** and the gain of peaks at 11.3 and 14.9° 2Θ in **5**.

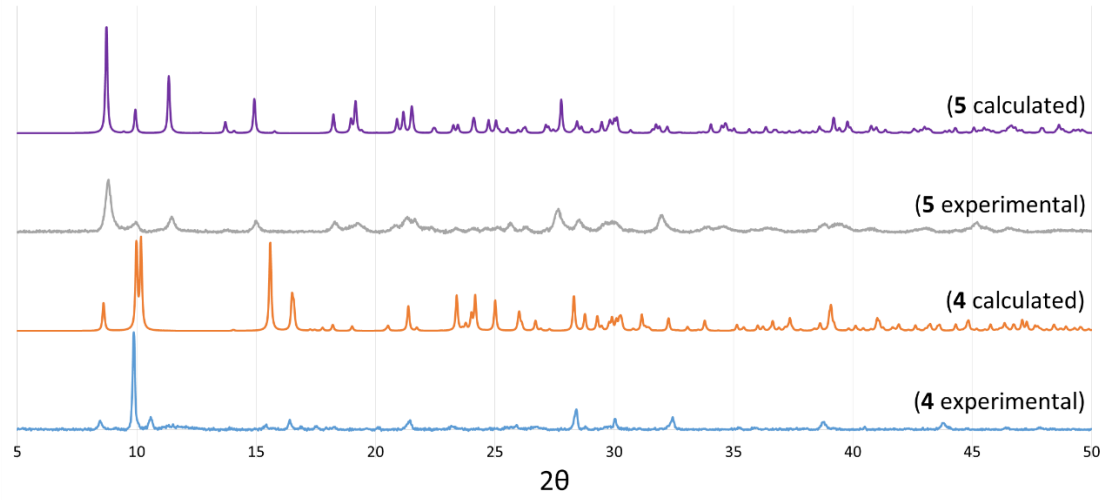

Figure 42: *Powder patterns highlighting the structural differences between* **4** *and* **5**, *where the bottom two patterns are experimentally and theoretically derived powder patterns of* **4** *and the top two patterns are experimentally and theoretically derived powder patterns of* **5**.

Thermogravimetric analysis was used to understand better the desolvation behaviour of **4**. A fresh, methanol moistened sample was placed on the balance at room temperature under a constant stream of nitrogen and the loss of weight monitored. After approximately 34 minutes 90% of the solvent mass had been lost, and 99% solvent loss was observed after 48 minutes. Monitoring was continued for 14 hours to allow the sample weight to equilibrate completely. After this time the converted sample of **5** was heated slowly to 600 °C, whereupon the sample degraded to lead(II) oxide in a two-step process beginning at 200 °C and reaching completion at 480 °C (observed mass loss: 45%, predicted mass loss: 44%) (Figure 43).

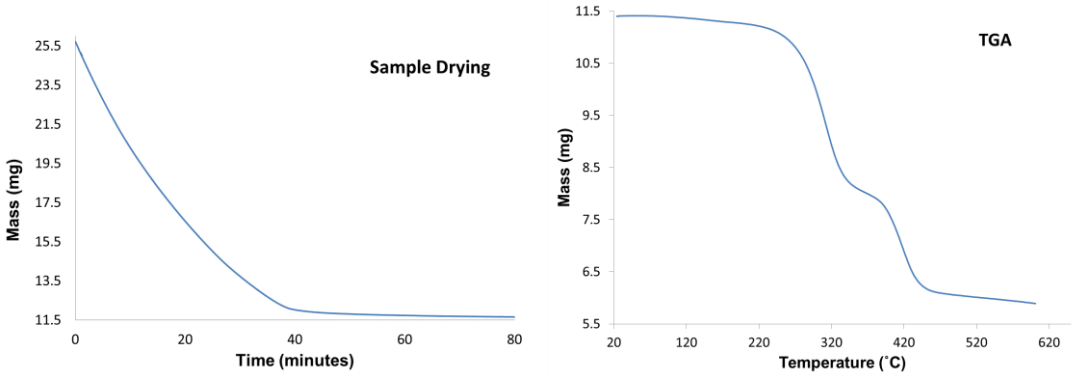

Figure 43: *Left: Pre-drying of a solvated sample of* **4** *freshly removed from mother-liquor on the TGA balance under a stream of nitrogen at ambient temperature. Right: TGA analysis of* **4** *once a steady weight was attained post-drying.*

Further investigation into the structure of network **4** suggested that the wide accessible channels could be prone to solvent exchange as well as direct loss. Single crystals of [Pb(ebdc)(MeOH)]·0.5H_2O were suspended in the solvents H_2O, ethanol and diethyl ether for one week. A change in crystallographic unit cell dimensions and space group from *C*2/*c* to *I*2 (crystallographic Tables 23 and 24 in Appendix II) was observed in the sample suspended in ethanol, of which the resulting crystal structure was confirmed by full single crystal data collection as [Pb_2(ebdc)$_2$(EtOH)]·0.5H_2O (**6**). Compound **6** has the same gross structure as **4**, but the two coordinated methanol groups in **4** have been replaced with one coordinated ethanol group and the total number of included water molecules is reduced by 50%.

Compound **6** contains interdigitated 2D CP nets with alternating lead(II) centres and ebdc ligands (Figure 44). The asymmetric unit of **6** contains two crystallographically distinct lead(II) centres, ligated by two distinct ebdc groups. One ethanol molecule coordinates to the lead centre Pb1, and a water molecule of half occupancy resides in an interstitial position completing the asymmetric unit. The hemidirected metal centre Pb1 supports seven coordination bonds and is similar to Pb1 in network **4**, exhibiting five inner sphere coordination interactions with bond lengths ranging from 2.414(10) to 2.640(14) Å and two outer sphere coordination bonds, Pb1–O3'(1 – x, y, 1 – z) and Pb1–O5, where the bond lengths are 2.885(9) and 2.861(9) Å respectively. The Pb2 atom supports six coordination bonds, of which one (Pb2–O6'(– 1 + x, y, z)) is in the outer coordination sphere at 2.879(10) Å. A hemidirected coordination sphere configuration is observed for both Pb1 and Pb2 atoms.

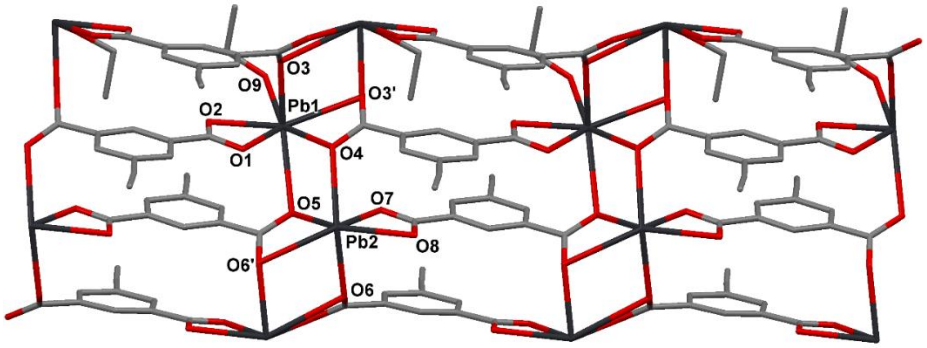

Figure 44: *Cross-section of network* **6** *showing the coordination environment of central Pb1 and Pb2 atoms. Symmetry operators: O3' = (1 – x, y, 1 – z), O6' = (– 1 + x, y, z).*

Analogous to networks **4** and **5**, this coordination polymer also exhibits hydrogen bonding originating from the interstitial water, coordinated solvent and ligand ethynyl groups, adding to the structural stability of the extended network. As can be seen from Figure 45, the interstitial water molecule acts as a hydrogen bond donor to two adjacent carboxylate nodes (O8 and O8') and also acts as a hydrogen bond acceptor from two coordinated ethanol oxygens O9 and O9'. Hydrogen bonding also originates from two crystallographically distinct carbon atoms on the ethynyl groups, acting as bifurcated hydrogen donors to the carboxylate segments adjacent, involving C19–H19 interacting with O4 and O1 atoms, and C9–H9 interacting with O5 and O7 carboxylate atoms. All heavy atom distances (D), hydrogen bond lengths (d) and approach angles (θ) of these interactions are in Table 5. π···π stacking occurs within the closed 'zipper' motif as it does in networks **4** and **5**, with a vertical phenyl-phenyl interplanar distance of 3.294(15) Å, and where the phenyl centroid to centroid distance is 3.794(13) Å.

Interaction	D (Å)	d (Å)	θ (°)
O10–H10···O8,O8'	2.756(11)	1.90	167.6(6)
O9,O9'–H9···O10	2.732(10)	1.82	159.0(9)
C19–H19···O4	3.222(8)	2.53	140.6(10)
C19–H19···O1	3.317(7)	2.45	139.4(10)
C9–H9···O5	3.204(9)	2.48	133.3(10)
C9–H9···O7	3.170(10)	2.31	151.8(10)

Table 5: *Hydrogen bond interactions of* **6**, *showing bond lengths and approach angles. Symmetry operators: O8' = (3/2 – x, – ½ + y, 3/2 – z), O9' = (2 – x, y, 1 – z).*

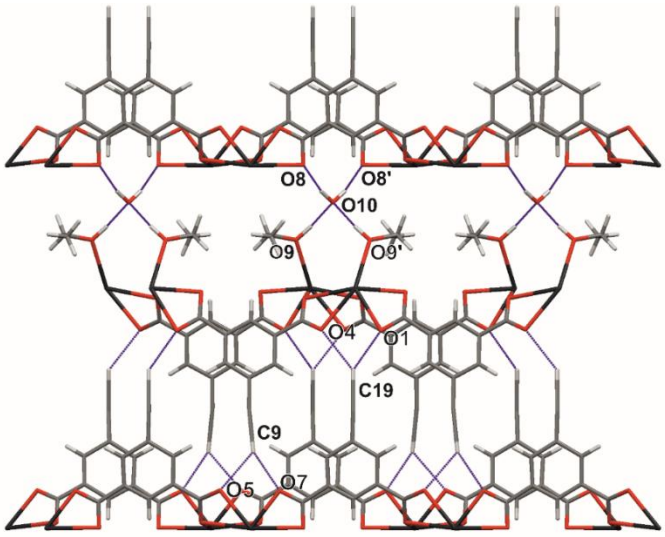

Figure 45: *The view down crystallographic axis* c *in* **6**, *showing the hydrogen bonds in blue dashed lines and the interdigitation of ebdc groups.*

The structure of **6** differs to that of **4** in the degree of solvation within the hydrophilic channels and the conversion of an outer to an inner coordination sphere bond (Figure 47). By replacing the two methanol ligands in **4** with one ethanol in **6**, the ethyl chains limit the number of hydrogen bonding sites within the channel, reducing the number of included water molecules per unit cell and thus yield a system with only half the hydrogen bonding interactions found in **4**. As anticipated, there is no significant change in the PXRD patterns of **4** and **6** (Figure 46) due to the gross structure remaining largely unchanged.

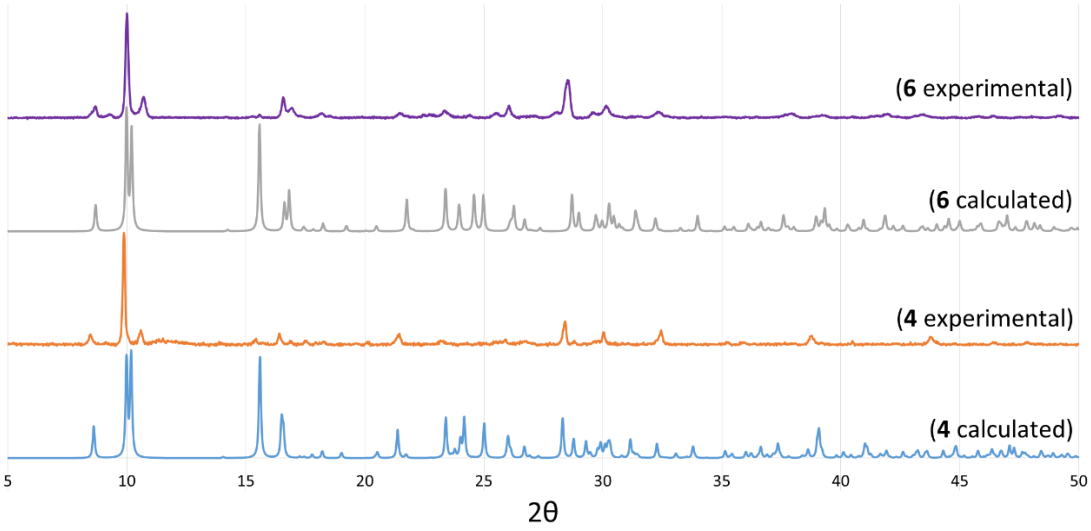

Figure 46: *Similar X-ray powder patterns of networks* **4** *and* **6**, *in which the gross structures exhibit little change.*

A shortening of the outer coordination sphere bond Pb1–O4 from 2.837(5) Å in **4** to 2.622(14) Å in **6** and a decrease in distance between repeating 'zipper' motifs along the vertical orientation from 15.2 Å along the [101] plane in **4** to 12.5 Å along the [100] plane in **6** is consistent with the reduction in cell volume from 2238.1(4) $Å^3$ in **4** to 2197.1(8) $Å^3$ in **6** due to the overall reduced number of solvent moieties in the channels. The distance between repeating 'zipper' motifs along the lateral orientation (corresponding to the [011] plane in **4** and the [110] plane in **6**) remains the same at 17.7 Å. The retention of the 'zipper' motif of the interdigitated ethynyl groups suggests that along with π···π interactions between the stacked ligands and hydrogen bond interactions between the ethynyl and carboxylate groups, these 'zipper' motifs are strongly held segments of the structure. Interestingly, the vertical distance between equivalent 'zipper' motifs of the desolvated form **5** is 13.7 Å which is greater than those in the solvated structures **4** and **6**, each having equivalent lateral 'zipper' to 'zipper' distances of 12.6 Å and 12.4 Å. This could be attributed to repulsion forces between the closely stacked π- orbital rich ligand phenyl groups that make up the motifs.

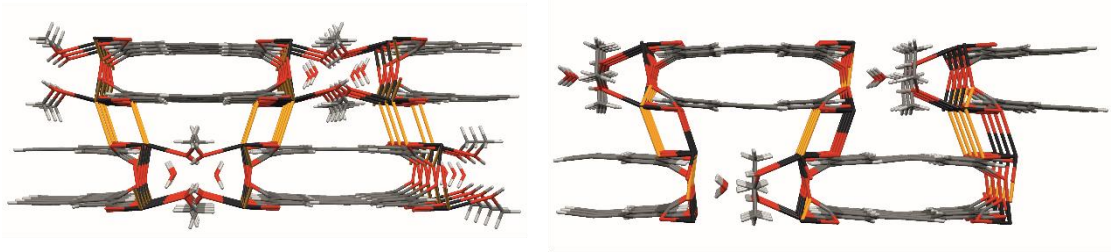

4 **6**

Figure 47: *Expanded cross-sections of networks* ***4*** *viewed down the crystallographic* b *axis and* ***6*** *viewed down the* a *axis. The outer coordination bonds are highlighted in gold.*

The solvent exchange from **4** to **6** was monitored spectroscopically. The most prominent change in the IR spectra is a weakening of the O–H stretch at 3338 cm^{-1} due to a reduction in the number of alcohol and water molecules, from two methanol groups and one H_2O per formula unit in **4** to one ethanol molecule and 0.5 H_2O per formula unit in **6**. A band at 1013 cm^{-1} can be assigned to the C–OH stretch of the methanol group in **4**, which appears at 1040 cm^{-1} with the transition to ethanol. The alkyne stretching C≡C–H band in **6** remains at 3238 cm^{-1}, similar to structures **4** and **5**.

The solid-state transformation between networks **4** and **6** is not reversible. After suspending crystals of **6** in a 1:1 methanol/water solution for two weeks, no change in

the PXRD pattern was observed. Furthermore the desolvation of **6** into **5** was significantly slower at room temperature than the desolvation of **4** into **5**. A reason for this may be the lower volatility of ethanol compared to that of methanol coupled with a lower polarity, which grants a higher affinity for the molecule to reside in the apolar ethynyl bordered channels. Heating a sample of **6** at 100 °C for one hour gave an amorphous powder which was confirmed by FTIR analysis to be devoid of both ethanol and water. A crystalline sample of the desolvated structure **5** was eventually obtained after one month of air drying a crystalline sample of network **6**.

2.2.4. 5-allenyl-1,3-benzenedicarboxylic acid

The meta- substituted functionality of H_2ebdc was modified from alkyne to allene resulting in 5-allenyl-1,3-benzenedicarboxylic acid to explore the self-assembly of coordination polymers under the effect of a larger, non-symmetrical functional group that does not display linear hydrogen bonding behaviour.

Dimethyl-5-(trimethylsilylethynyl) isophthalate (prepared in reaction b from Scheme 1) was converted to the allene species by a deprotection of the TMS group and subsequent addition of *p*-formaldehyde mediated by copper(I) iodide to form the allenyl species (Me_2abdc), followed by the deprotection of the esters to the diacid form (H_2abdc) with sodium hydroxide and an acidic workup (Scheme 2). The overall yield for this three-step process was 45%.

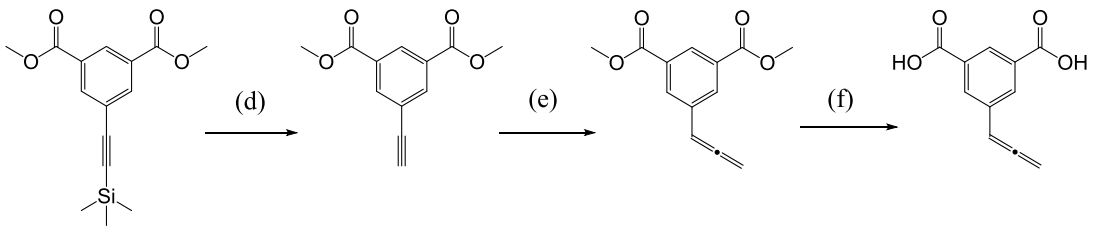

Scheme 5: *Three step synthesis of H_2abdc. d) K_2CO_3 in MeOH at RT; e) Diisopropylamine, PFA, CuI, dioxane, reflux; f) NaOH, THF at RT.*

Similar to H_2ebdc, the H_2abdc ligand possesses two carboxylic acid functional groups to allow coordination of metal nodes upon deprotonation and an allenyl group to promote weak hydrogen-bonding interactions. Interactions that are allowed by this ligand include weak C–H···X hydrogen bond interactions from the allenyl functional group, π···π

stacking derived from the central aromatic ring as well as strong hydrogen bonding from the carboxylate oxygen atoms.

The ^{1}H-NMR spectrum (DMSO-d_6) of H_2ebdc contains a singlet at δ 4.43 ppm corresponding to the ethynyl group. The remaining aryl resonances were observed at δ 8.15 and 8.44 ppm. The allenyl functionalised ligand H_2abdc showed a similar pattern of resonances albeit with shifts mediated by solvent effects and the replacement of the ethynyl singlet with a characteristic doublet and triplet at δ 5.41 ppm (J = 6.78 Hz) and 6.58 ppm (J = 6.78 Hz) that are assigned to the allene group. In both the ethynyl and allenyl forms, the carboxylic acid functionality was observed using IR spectroscopy at 1708 cm^{-1} and 1685 cm^{-1}. The change of functional group effected a loss of the prominent C≡C–H ethynyl band at 3301 cm^{-1} and an emergence of a band at 1936 cm^{-1} corresponding to the allenyl group.

Single crystals of this ligand could not be obtained, but slow evaporative techniques did yield microcrystals from which a PXRD pattern was collected (Figure 48).

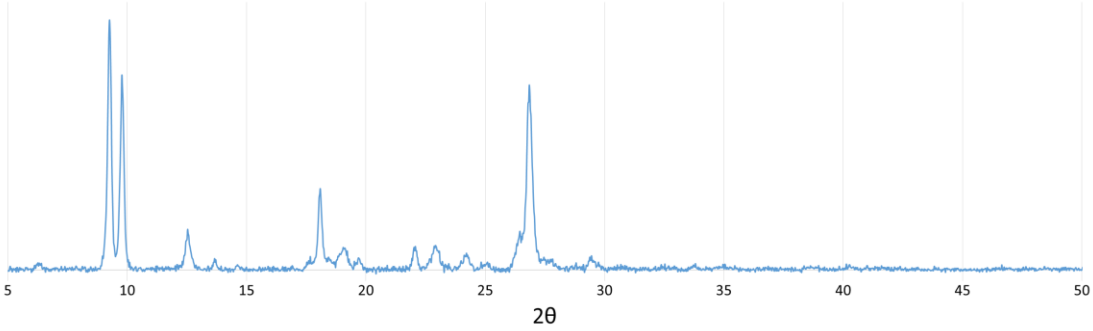

Figure 48: *The PXRD pattern of a microcrystalline sample of H_2abdc.*

2.2.5. CP metallogel

A lead(II) metallogel was obtained from the reaction of lead(II) acetate trihydrate with H_2abdc at 100 °C for 72 hours in DMF. Analysis of the air-dried product yielded an elemental composition consistent with an empirical formula [Pb(abdc)(H_2O)] (**7**), supported by further analyses including FTIR and ^{1}H-NMR spectroscopy, and scanning electron microscopy (SEM).

Further investigation into the conditions leading to gel formation yielded 100 °C as the most favourable temperature for gelation, and the critical gelation concentration of H_2abdc and lead(II) acetate to be 1% w/v. This gel forming concentration compares favourably to those of low-molecular weight organogelators which are known to form gels at very low concentrations (<2% w/v).[22] Metallogel samples of **7** at and above the 1% w/v concentration all passed the tube inversion test (Figure 49). The metallogel, once formed, was fully resistant to short bursts of sonication and remained gel-like indefinitely (> 1 year). Upon shaking, however, the metallogel became a slow flowing liquid in which the gel structure was fragmented. Such behaviour is indicative of the initial gel possessing a rigid internal structure.[24] Heating of this material did not reform the rigid gel, as gauged by the tube inversion test.

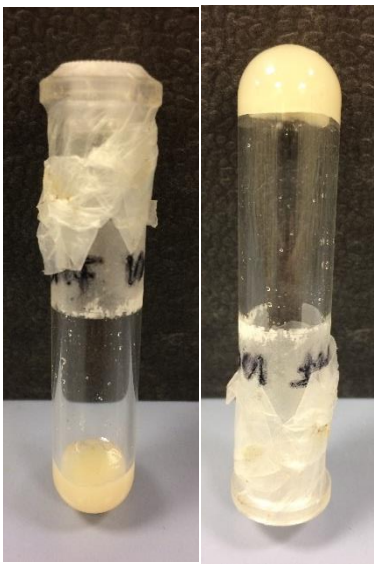

Figure 49: *Metallogel* **7** *undergoing a tube inversion test.*

The nanoscale morphology of a freeze-dried sample of **7** was visualised using SEM, which revealed an extended network of fibrous structures that aggregate into large entangled worm-like morphologies (Figure 50). Well-defined fibres were observed at the periphery of the image, and are analogous to fibrils present in similar gel materials.[25] The average diameter of these fibres was found to be 40 nm, while the densely entangled worm-like structures were found to be larger in size, varying in diameter from 40 to 160 nm. Only limited structural information could be gauged from the gel sample as powder diffraction (PXRD) analysis found that a dried sample of **7** contained only amorphous character and analysis by small-angle X-ray scattering (SAXS) was not possible due to the large size of the nanofibers.

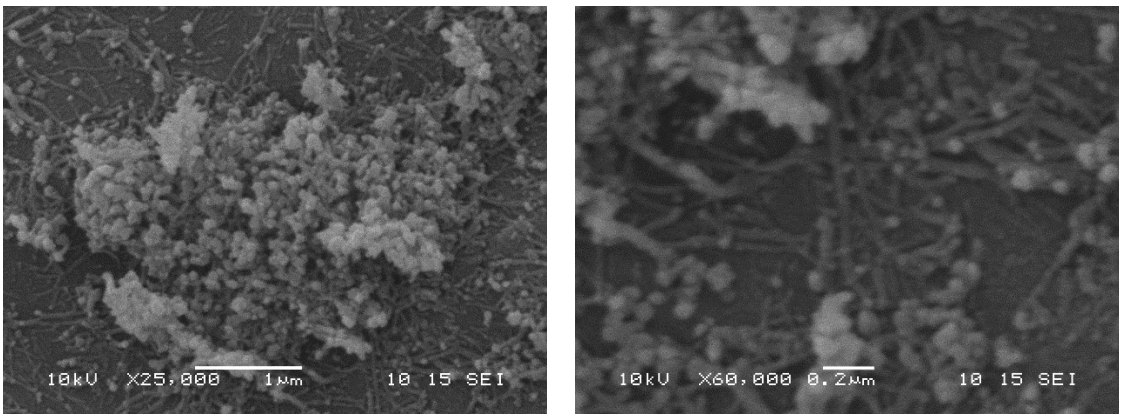

Figure 50: *SEM image of* **7** *showing the two most prominent morphological features. (Left)* ×*25,000 magnification: rod-like fibres are present at the periphery around a large agglomeration of worm-like morphologies in the centre; (right)* ×*60,000 magnification: a more detailed view of the fibres.*

Metallogelators self-assemble into complex 3D networks through metal–ligand coordination bonds, which serve as cross-linkers to bring individual ligands together to form stable metallogels. The gelation process also includes interactions such as hydrogen bonding, π···π stacking and van der Waals forces.[26] Metallogels can be classified into two gelator categories; organogels that immobilise organic solvents, and hydrogels that immobilise water. Metallogels have attracted increasing attention through the potential availability and diversity of metal-ligand coordination that controls the gel formation as well as the properties of the gel product.[27]

Elemental analysis on an air dried sample of **7** yielded a carbon and hydrogen content of 30.91% and 1.89% respectively, which is consistent with an empirical formula of [Pb(abdc)(H_2O)]. No nitrogen content was indicated in the dried metallogel, which suggests a displacement of the immobilised DMF molecules in favour of water molecules from the surrounding atmosphere during the drying process.

To gain insights into the initial solution-state behaviour of H_2abdc and lead(II) acetate trihydrate during gel formation, the aggregation process was monitored using ^{1}H-NMR spectroscopy in DMF-d_7. A neat spectrum of H_2abdc [0.0292 M] was first collected, which showed the positions of the expected allene doublet and triplet at δ 5.43 and 6.63 ppm respectively, as well as aromatic signals at δ 8.21 and 8.49 ppm from the phenyl ring. Seven aliquots of 0.125 M of $Pb(OAc)_2{\cdot}3H_2O$ were successively added at room temperature and the spectra compared after each addition. The results show a net upfield shift for all the non-acidic hydrogen atoms of H_2abdc, with the most pronounced effect seen for the aromatic hydrogens H***A*** and H***B*** (Figure 51).

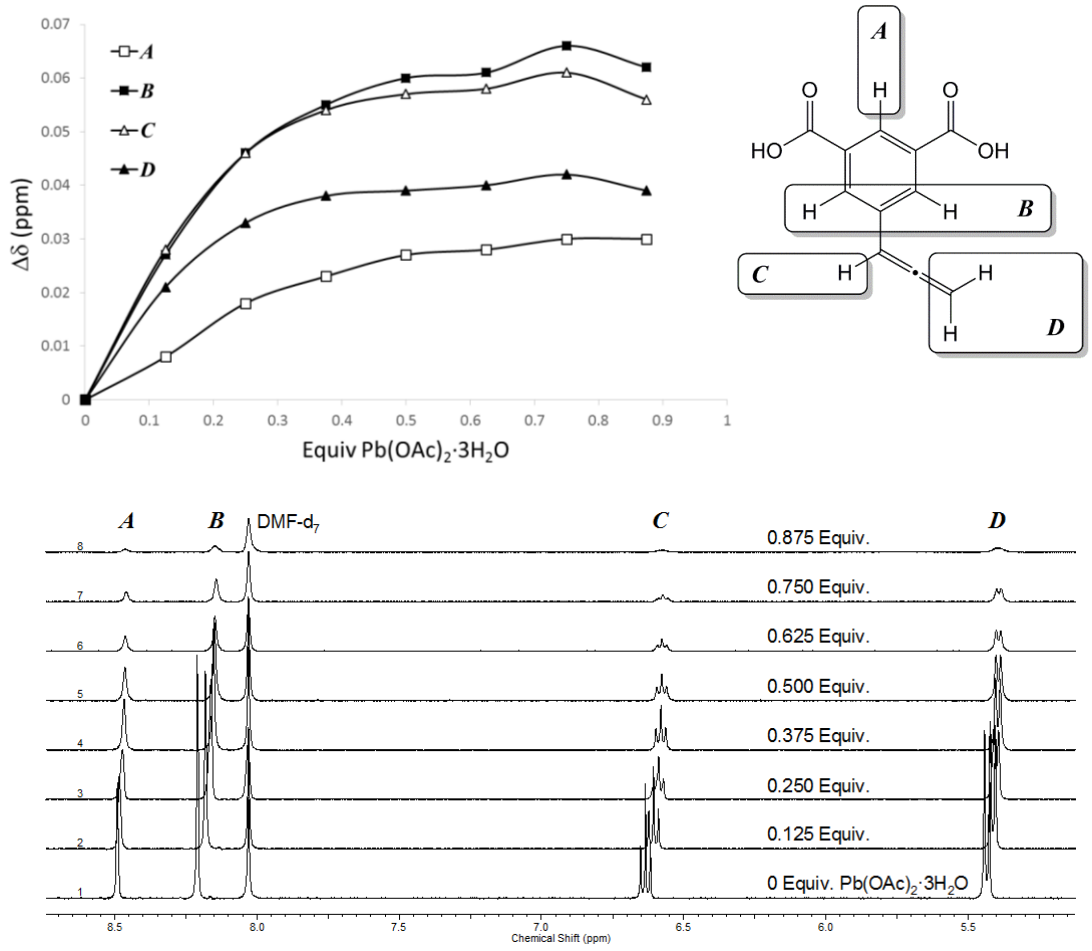

Figure 51: *Titration isotherm and NMR spectroscopic titration of the interaction between H_2abdc and $Pb(OAc)_2{\cdot}3H_2O$ in DMF-d_7.*

A small upfield shift in the NMR signals can be observed for each incremental aliquot of the lead(II) acetate added. This can be rationalised by change in the local ligand environment once deprotonation of the carboxylic acid groups occurs. Due to the gradual migration of the peaks rather than an appearance of new peaks, the deprotonation and subsequent ligand to metal coordination seems to be labile in nature. The lack of new peaks associated with coordinated DMF also suggests that any solvent interactions are also labile. As the metal to ligand molar ratios approach equivalent values, there is an increasing loss of multiplicity and significant broadening of the peaks associated with the now ligated and rapidly gelating abdc species, which affects the accuracy with which the peak positions can be determined. This effect can be attributed to the self-assembly and precipitation of large metallogel structures within the sample, slowing the rotation of the molecules.[28] The final titre yielded an equimolar mixture in which the signal broadening was too great for meaningful ^{1}H-NMR spectroscopic interpretation.

While these spectroscopic observations are consistent with the anticipated early events of self-assembly during the gelation process, only by heating at 100 °C could the mixture be 'set' into the gel form, from which reliable spectroscopic data could not be obtained.

Previously reported crystalline comparisons to gel samples represent a method by which plausible models for the amorphous analogue can be postulated.[29,30] In this method, by matching PXRD spectra from dry samples of gel and crystalline components the authors were able to readily assess the structural properties of the gel form. Due to the amorphous character of **7**, however in this case, only circumstantial evidence for the structural properties of the metallogel can be obtained.

2.2.6. 3D CP crystalline framework

In an attempt to gain insights into the structural behaviour of the molecular components in the gel, milder synthetic conditions were employed to form the product. Heating a mixture of H_2abdc and lead(II) acetate trihydrate in DMF at 60 °C for three days yielded colourless needle crystals suitable for X-ray structure determination. The crystals obtained were found to have a molecular composition of [Pb(abdc)(DMF)] (**8**). The asymmetric unit contains a single Pb(II) atom coordinated by a carboxylate group of a bridging abdc ligand and a single molecule of DMF. The metal centre is eight coordinate with a hemidirected coordination sphere, supporting four inner-sphere Pb–O coordination bonds and four outer-sphere Pb–O coordination bonds, all within the range 2.396(5) – 3.165(6) Å. The coordination sphere is comprised of four carboxylates, each of which bridges four metal centres in a $\mu_4(\mu_2+\mu_2)$ fashion, and two DMF molecules that bridge between two metal centres (Figure 52). A full list of the Pb–O bond lengths and symmetry operators can be found in Table 34 in Appendix II. The overall structure consists of inorganic 1D backbones made up of Pb–O atoms propagating along the crystallographic *c* axis (Figure 53), linked together into a 3D network by abdc ligands.

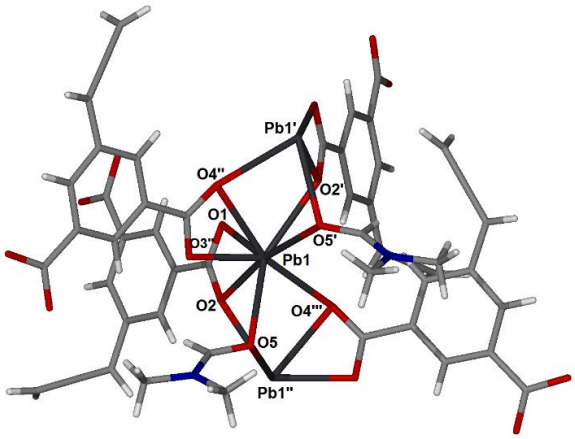

Figure 52: *Coordination environment around the Pb1 atom in* **8**. *Symmetry operators: O2' and O5' = (½ + x, – ½ + y, – ½ + z), O3'' and O4'' = (½ + x, ½ – y, ½ – z), O4''' = (1 – x, + y, – z).*

When viewed down the crystallographic *c* axis, a clear motif of squares and diamonds is visible (Figure 53). The square channels are occupied by the allene groups of the abdc ligands while the diamond channels are filled by alternating coordinated DMF molecules.

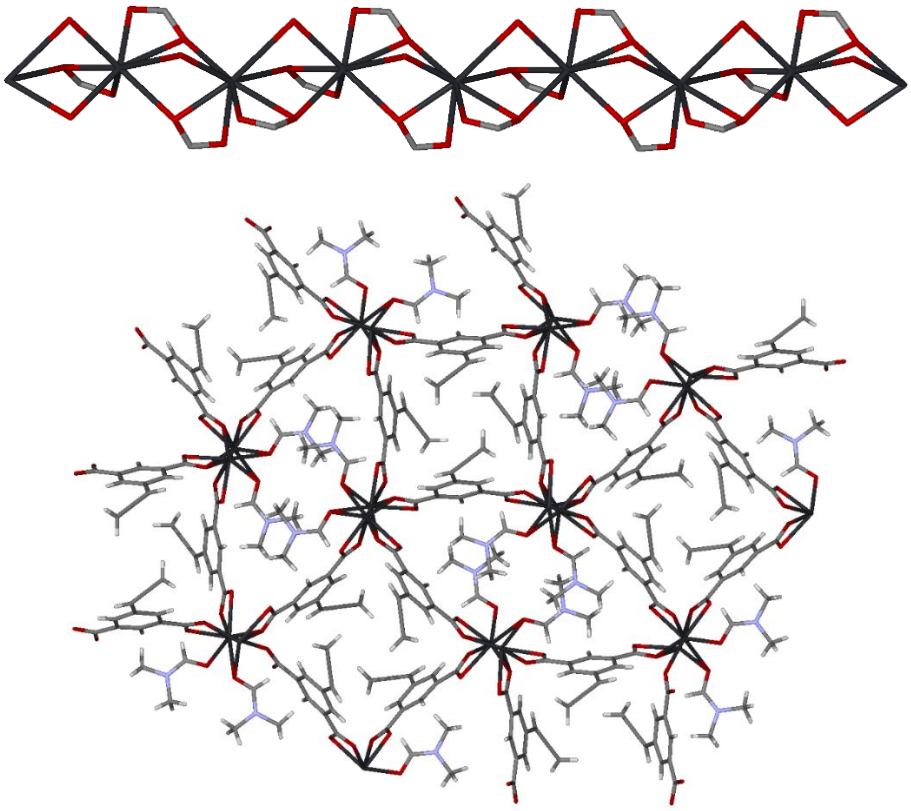

Figure 53: *Top: Inorganic backbone of* **8**, *consisting of Pb–O atoms. Bottom: The inorganic backbones bridge together into 3D motif of squares and diamonds as viewed down the crystallographic* c *axis.*

In **8**, DMF molecules coordinate to the framework rather than being immobilised by it. Ethynyl-derived weak hydrogen bonding is observed in the structure where the carbon atoms of the abdc linker donate hydrogen atoms to the surrounding oxygen atoms within the Pb–O backbones. The C9 carbon atom interacts with two adjacent carboxylate oxygen atoms O1''' and O4 as can be seen in Figure 54, *via* a bifurcated hydrogen bond. Carbon atom C8 also participates in weak hydrogen bonding to O4', although the separation between C6 and O2 is greater than the sum of van der Waals radii of the two atoms defining is as a very weak, or not significant, interaction. By contrast, the terminal allene CH_2 group protrudes into a hydrophobic channel (Figure 53) where there are no significant interactions to be made with the adjacent ligands. All existing hydrogen bond geometries are listed in Table 6.

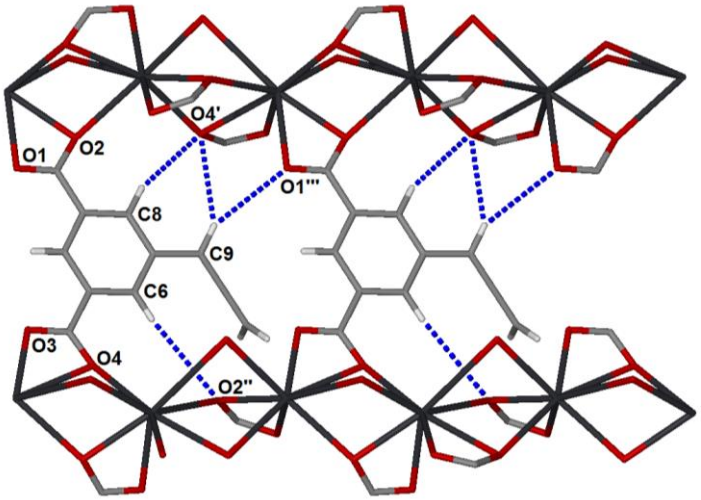

Figure 54: *Hydrogen interactions between ebdc ligand and adjacent carboxylates in* **8**, *viewed from the crystallographic* a *axis. Symmetry operators: O4' = (1 – x, y, 1 – z), O2'' = (x, 1 – y, 1 – z), O1''' = (x, y, 1 + z).*

Interaction	*D* (Å)	*d* (Å)	*θ* (°)
C8–H8···O4'	3.493(8)	2.58	161.1(4)
C6–H6···O2''	4.252(8)	3.33	162.7(4)
C9–H9···O4'	3.672(10)	2.84	145.7(5)
C9–H9···O1'''	3.784(10)	3.02	137.7(6)

Table 6: *Hydrogen interactions in* **8**, *showing bond lengths and approach angles.*

A comparison between the infrared spectra for an air-dried sample of **7** and **8** identifies similarities between these materials. The asymmetric stretching vibration for the allene group was clearly identified in both materials; at 1941 cm^{-1} in **7** and 1942 cm^{-1} in **8**. The

terminal C=CH_2 allene wagging mode was observed at 802 cm^{-1} in **8**, but appeared much weaker in the dried gel form **7** and was inferred as a shoulder present at 799 cm^{-1}. Identical carboxylate COO^- vibrational modes were present in both spectra; 1602 cm^{-1} in **7** and 1596 cm^{-1} in **8** for the asymmetric vibrational mode and 1345 cm^{-1} in **7** and 1356 cm^{-1} in **8** for the symmetric vibrational mode.[31] These similar carboxylate vibrational modes add additional evidence for ligand to lead(II) coordination in both the crystal and metallogel forms. Observations of very weak or absent vibrations have been noted in the dried spectrum of **7** for the amide functionality expected from DMF; no band was observed at 1635 cm^{-1} which is the expected location for the C=O vibration for coordinated DMF,[32] which is consistent with the observed lack of nitrogen by elemental analysis. In comparison the IR spectrum for **8** showed a strong C=O DMF peak at 1635 cm^{-1}. This evidence supports the idea that as the metallogel **7** dries in ambient atmosphere, water easily penetrates and displaces the DMF molecules from within the gel structure.

As a result of the complexity of intermolecular interactions, it is still a challenge to understand how organic ligands and metal ions aggregate into multidimensional gels. These results however indicate that the metal-ligand coordination characteristics observed in **8** persist within gel **7**, albeit in an amorphous form.

2.3. Conclusions

The organic ligand 5-ethynyl-1,3-benzenedicarboxylic acid (H_2ebdc) and metal salt $Pb(OAc)_2 \cdot 3H_2O$ were reacted together under various conditions to explore the competing self-assembly interactions between the two components. Six coordination polymers (CPs) were obtained; structures **1** and **2** as one-dimensional chain polymers and structures **3** to **6** as two-dimensional polymer nets. The propensity for weak hydrogen bonding within the reported lead(II) coordination polymers shows that directed crystallisation synthesis of the metal and ligand yields materials beyond the scope of typical 1,3-benzenedicarboxylate (bdc) coordination polymers,[33-35] and may even dictate the outcome of the structural topology.

Weak ethynyl-derived hydrogen bonding throughout structures **1** - **6** was observed by single-crystal X-ray crystallography and IR spectroscopy. The strength of each C-H···O interaction, as determined by the length and approach angle, correlated well with the expected observed bathochromic shift in the corresponding IR spectra. This relationship between hydrogen bonding and IR stretching frequency is well documented.[36]

Tuning the reaction conditions of Pb(II) and ebdc *via* solvent and temperature had clear effects on the outcome of the CP architecture. A ladder-like chain CP **1** was formed when the reaction was carried out in DMSO, compared to a much larger 1D chain motif **2**, consisting of bridged hexagonal Pb–O rings, when reacted in DMF. A higher periodicity CP was obtained as a result of increasing the temperature from 100 °C in DMF in the synthesis of **2** to 140 °C for the synthesis of **3**.

A single-crystal to single-crystal (SCSC) transition for the exchange of methanol to ethanol from structure **4** to **6** was found as well as a subsequent SCSC desolvation transition of both **4** and **6** to a desolvated form **5**. This results in significant changes to crystalline topology and packing across the three structures. The desolvation transition from **4** to **5** occurs without any need of an external trigger and was found to be complete within one hour of exposing crystals of **4** to air at room temperature, as determined by PXRD, FTIR and TGA experiments. The change from **4** to **5** resulted in more than a 20% shrinkage of the structure along the crystallographic *c* cell axis, enabling the formation of new outer sphere Pb–O coordination bonds. Solvent exchange of methanol in **4** for ethanol to give **6** caused a lateral compression of the structure along the [101] plane and delayed conversion to the desolvated form at room temperature. The

improved stability of the ethanol adduct is likely due to greater hydrophobic character coupled with decreased volatility of the solvent.

To investigate the effects of divalent lead self-assembly with an equivalent asymmetrical linker component and to observe the effects of loss of directional weak hydrogen bonding behaviour, 5-allenyl-1,3-benzenedicarboxylic acid (H_2abdc) was synthesised. Reaction of the allene-functionalised ligand with lead acetate lead to a low molecular weight metallogel (**7**). Through NMR, FTIR and a comparison to a crystalline form of the two components (**8**), a model could be postulated for the coordination structure of the metallogel.

2.4. Experimental

Starting materials and solvents were purchased from commercial sources and were used without further purification with the exception of H_2ebdc and H_2abdc. Single crystal X-ray diffraction data sets for **1** - **4** and **6** were collected on an Agilent Gemini A-Ultra diffractometer at the University of Bath using Mo Kα radiation, the crystal being cooled by an Agilent Cryojet. Data collections for network **5** were carried out on Beamline Station 11.3.1 of the Advanced Light Source (ALS), Lawrence Berkeley National Laboratory.[37] Data for **8** were collected on an Agilent Xcalibur diffractometer using Mo Kα radiation, cooled to 150 K by an Oxford Instruments nitrogen gas cryostream. More details can be found in Appendix II.

Powder X-ray diffraction patterns (PXRDs) were recorded on a Bruker AXS D8 Advance diffractometer with Cu Kα radiation of wavelength 1.5406 Å at 298 K. Calculated and experimental PXRD patterns can be found in Appendix I. Samples were placed on a flat plate, and measured with a 2θ range of 3-60°. Nuclear magnetic resonance spectra were obtained on a Bruker Avance 300 MHz Ultrashield NMR spectrometer. Infrared spectra were recorded on a PerkinElmer Spectrum 100 spectrometer equipped with an ATR sampling accessory. Elemental analyses were performed on a CE-440 elemental analyser at London Metropolitan University, analysis for **4** and **6** were not obtained due to the fast rate of solvent loss. Melting points were determined on a Stuart SMP10 Digital melting point apparatus. SEM (scanning electron microscope) images were captured on a JEOL-JSM-6480 LV scanning electron microscope at the University of Bath. Heating of single crystal samples was performed on a Mettler Toledo FP82HT Hot Stage and recorded on Studio Capture. Differential scanning calorimetry data was collected on a DSC Q20. Sonication experiments were carried out in a Fisher Scientific FB15051 sonicator. Mass spectrometry data were recorded on a Bruker MicroTOF.

CCDC Conquest 1.18 was used to build a query where the average distance between meta-substituted pairs of 1,3-benzenedicarboxylate phenyl groups were explored, where a X substituent was used, X being defined as 'any atom'. The search criteria for the centroid to centroid distance between the two phenyl groups was defined as 3.0 to 4.2 Å, and the angle of the phenyl planes 0 to 2°. The search results were exported into an excel spreadsheet and the minimum, maximum and mean values were calculated. In total 1800 search results were collated.

Dimethyl-5-(trifluoromethanesulphonyl) isophthalate (a) To a 0 °C solution of dimethyl 5-hydroxyisophthalate (3.74 g, 17.8 mmol), pyridine (3 mL, 20 mmol) and CH_2Cl_2 (50 mL) under N_2, trifluoromethanesulfonic anhydride (2.98 mL, 178 mmol) was added by syringe. The mixture was stirred for 30 min and then quenched with ≤32% HCl solution (20 mL). The layers were separated and the organic layer was washed with 1 M HCl solution (100 mL), saturated $NaHCO_3$ solution (100 mL) and saturated NaCl solution (100 mL), and dried with $MgSO_4$. The solvents were then removed under reduced pressure. The residue was taken up in CH_2Cl_2 and passed through a *ca.* 20 cm plug of silica. Removal of the solvent under reduced pressure afforded the product as a white solid (6.04 g, 99%), analytical data match those previously reported.[38]

Dimethyl-5-(trimethylsilylethynyl) isophthalate (b) Under N_2, a solution of trimethylsilylacetylene (2.37 mL, 16.8 mmol, 1.02 equiv.) was added dropwise *via* a syringe to a solution of **I** (4.79 g, 14.0 mmol, 1.0 equiv.), CuI (0.27 g, 1.40 mmol, 0.1 equiv.) and $Pd(PPh_3)_2Cl_2$ (0.49 g, 0.70 mmol, 0.05 equiv.) in THF (50 mL) and NEt_3 (10 mL). The reaction was stirred at room temperature overnight, the solvents were removed under reduced pressure and the residue was dissolved in CH_2Cl_2 (50 mL). Saturated NH_4Cl (4 × 20 mL) was added and the mixture was extracted with CH_2Cl_2 (4 × 20 mL). The combined organic phases were dried over $MgSO_4$ and the solvent was removed under reduced pressure. Purification by flash column chromatography (SiO_2, hexane/EtOAc 9:1) gave the desired product as a cream powder (3.73 g, 92%). Analytical data match those previously reported.[39]

5-Ethynyl-1,3-benzenedicarboxylic acid (c) Dimethyl-5-(trimethylsilylethynyl) isophthalate (1.61 g, 5.54 mmol) was reacted with NaOH (2.44 g, 61.0 mmol) in THF (100 ml) at room temperature for ~4 h. The precipitate formed was separated by filtration, dissolved in aq. NaOH (0.1 M, 100 mL) and stirred for 2 h at room temperature. The reaction mixture was cooled to 0 °C on an ice bath and acidified with ≤32% HCl to pH~1-2. The precipitate formed was isolated by filtration, washed with water (2 × 50 mL) and dried overnight, giving the target compound as a powder (1.04 g, 99%). The analytical data match those reported previously,[40,41] however the peak at 13.6 (br, 2H) on the ^{1}H NMR spectrum was not observed due to proton exchange.

[Pb(ebdc)(DMSO)$_2$] (1) Colourless prismatic crystals were obtained by solvothermal synthesis using $Pb(OAc)_2{\cdot}3H_2O$ (80 mg, 0.21 mmol) and H_2ebdc (40 mg, 0.21 mmol) dissolved in DMSO (5 mL) in a sealed vial and placed in a 100 °C oven for 4 days. Bulk

purity was determined by PXRD. Anal. Calcd (%) for $C_{14}H_{16}O_6PbS_2$: C, 30.48; H, 2.92. Found: C, 30.36; H, 2.83. FTIR $\bar{\upsilon}$ = 3221 (m), 3001 (w), 2913 (w), 1723 (w), 1661 (w), 1608 (m), 1592 (w), 1548 (s), 1414 (w), 1356 (s), 1122 (w), 1099 (m), 1016 (s), 993 (s), 953 (s), 790 (m), 777 (s), 743 (w), 722 (s) cm^{-1}.

[Pb(ebdc)(DMF)] (2) Colourless prismatic crystals of lead chain **2** were obtained by solvothermal synthesis of $Pb(OAc)_2{\cdot}3H_2O$ (80 mg, 0.21 mmol) and H_2ebdc (40 mg, 0.21 mmol) dissolved in DMF (5 mL) in a sealed vial and placed in a 100 °C oven for 2 days. Bulk purity was determined by PXRD. Anal. Calcd (%) for $C_{78}H_{54}N_6O_{30}Pb_6$: C, 33.48; H, 1.95; N, 3.00. Found: C, 33.42; H, 2.04; N, 3.11. FTIR $\bar{\upsilon}$ = 3247 (m), 2931 (w), 1644 (s), 1593 (m), 1517 (s), 1424 (s), 1412 (s), 1352 (s), 1233 (m), 1101 (m), 918 (m), 789 (m), 773 (s), 717 (s), 663 (s) cm^{-1}.

$[Pb_4(ebdc)_4(DMF)_8]{\cdot}H_2O$ (3) Colourless prismatic crystals were obtained by solvothermal synthesis using $Pb(OAc)_2{\cdot}3H_2O$ (80 mg, 0.21 mmol) and H_2ebdc (40 mg, 0.21 mmol) dissolved in DMF (5 mL) in a sealed vial and placed in a 140 °C oven for 4 days. Bulk purity was determined by PXRD. Anal. Calcd (%) for $C_{55}H_{53}N_5O_{24}Pb_4$ (substitution of one DMF molecule for two molecules of H_2O): C, 32.23; H, 2.81; N, 3.55. Found: C, 32.15; H, 2.61; N, 3.40. FTIR $\bar{\upsilon}$ = 3246 (m), 2931 (w), 1645(s), 1593 (m), 1518 (s), 1425 (s), 1382 (w), 1352 (s), 1233 (m), 1102 (s), 984 (w), 918 (m), 789 (w), 773 (m), 718 (s) cm^{-1}.

$[Pb(ebdc)(MeOH)]{\cdot}0.5H_2O$ (4) Compound **4** was synthesised by the slow diffusion of an aqueous solution of $Pb(OAc)_2{\cdot}3H_2O$ (40 mg, 0.11 mmol) into a methanol layer of H_2ebdc (5-ethynyl-1,3-dicarboxylic acid) (20 mg, 0.11 mmol) over seven days in a sealed vial. The layers were allowed to diffuse slowly through a 1:1 H_2O/MeOH buffer layer. Colourless needle-shaped crystals were obtained. These needles were retained in solution prior to analysis and then isolated by filtration (22 mg, 24% yield). Bulk purity was determined by PXRD. FTIR $\bar{\upsilon}$ = 3338 (m), 3249 (m), 1846 (w), 1663 (m), 1603 (m), 1593 (m), 1496 (s), 1426 (s), 1362 (s), 1234 (w), 1114 (m), 1013 (s), 934 (m), 915 (s), 809 (w), 791 (m), 773 (s), 717 (m) cm^{-1}.

[Pb(ebdc)] (5) Colourless needles of **5** were obtained by placing crystals of **4** or **6** in an enclosed environment with limited air diffusion for several days. Bulk purity was determined by PXRD. Anal. Calcd (%) for $C_{20}H_8O_8Pb_2$: C, 30.38; H, 1.02. Found: C,

30.26; H, 1.09. FTIR $\bar{\upsilon}$ = 3242 (m), 1594 (w), 1516 (s), 1428 (s), 1342 (s), 1228 (w), 1109 (w), 913 (m), 773 (s), 719 (s) cm^{-1}.

$[Pb_2(ebdc)_2(EtOH)]\cdot 0.5H_2O$ (6) Colourless needle crystals of **6** were obtained by suspending crystals of **4** in a sealed vial of reagent grade ethanol for seven days. Bulk purity was determined by PXRD. FTIR $\bar{\upsilon}$ = 3237 (m), 2976 (w), 1593 (w), 1503 (s), 1425 (s), 1354 (s), 1232 (w), 1039 (m), 932 (w), 913 (m), 791 (w), 772 (s), 720 (s) cm^{-1}.

Dimethyl-5-ethynylisophthalate (d) A mixture of dimethyl-5-(trimethylsilylethynyl) isophthalate (2.12 g, 7.30 mmol), K_2CO_3 (1.31 g, 9.49 mmol), and methanol (100 mL) was stirred under a nitrogen atmosphere for 1.5 h and then poured into water (250 mL). The resulting mixture was filtered and the solids were washed with water (2 × 50 mL) and dried under reduced pressure to afford the pure product (1.46 g, 92%). Analytical data match those previously reported.[42]

Dimethyl-5-allenylisophthalic acid (e) The alkyne from synthesis (d) (0.60 g, 2.76 mmol) was dissolved in dioxane (10 mL). Diisopropylamine (0.78 mL, 5.51 mmol) was added, followed by paraformaldehyde (0.17 g, 5.51 mmol) and CuI (0.175 g, 0.92 mmol). The mixture was refluxed for 12 hours. The resulting brown solution was cooled to 25 °C, diluted with diethyl ether (30 mL), and acidified with 0.1 M $NaHSO_4$ (aq., 30 mL). The phases were separated and the aqueous phase was washed with diethyl ether (3 × 50 mL). The combined organic washes were washed with 0.1M $NaHSO_4$ (10 mL), dried with $MgSO_4$, filtered, and evaporated under reduced pressure. The crude product was purified by flash chromatography (gradient: hexane / diethyl ether 85:15) to provide the allenyl ester as a yellow powder (0.37 g, 57%), mp 95-96 °C. δ_H (300 MHz, $CDCl_3$) 8.51 (t, 1H, J = 1.51 Hz), 8.14 (d, 2H, J = 1.51 Hz), 6.25 (t, 1H, J = 6.78 Hz), 5.27 (d, 2H, J = 6.78 Hz), 3.96 (s, 6H). δ_C (75 MHz, $CDCl_3$) 210.2, 166.2, 135.3, 131.7, 128.9, 92.9, 80.0, 52.4. *m/z* (ESI) 153, 233 (M^+), 241. FTIR v = 3009 (w), 2954 (w), 1935 (m), 1722 (s), 1599 (w), 1432 (s), 1347 (w), 1322 (m), 1301 (m), 1252 (m), 1237 (s), 1203 (s), 1126 (m), 1082 (m), 996 (s), 853 (m), 863 (m), 751 (s), 724 (m), 689 (m), 664 (m) cm^{-1}.

5-Allenyl-1,3-benzenedicarboxylic acid (f) A mixture of dimethyl-5-allenylisophthalic acid (0.5 g, 2.15 mmol), THF (40 mL) and NaOH (0.95 g, 23.7 mmol) dissolved in water (25 mL) was stirred at room temperature overnight. The organic layer was removed under reduced pressure and the remaining aqueous layer was stirred at room

temperature for a further 4 h. The reaction mixture was cooled to 0 °C, acidified with ≤32% HCl to pH~1-2. The precipitate formed was isolated by filtration, washed with water (2 × 20 mL) and dried to yield a cream powder (0.45 g, 95%). δ_H (300 MHz, DMSO-d_6) 13.30 (s, 2H), 8.29 (t, 1H, J = 1.51 Hz), 8.07 (d, 2H, J = 1.51 Hz), 6.59 (t, 1H, J = 6.78 Hz), 5.41 (d, 2H, J = 6.78 Hz). δ_C (75 MHz, CD_3OD) 211.5, 168.8, 136.9, 133.1, 132.7, 130.3, 93.5, 79.8. *m/z* (ESI) 635 (30%), 431 (100%), 227 (M^+, 79%). FTIR $\bar{\upsilon}$ = 2829 (br m), 2553 (br m), 1936 (m), 1684 (s), 1598 (s), 1420 (s), 1272 (s), 1250 (s), 1210 (m), 1113 (m), 912 (s), 856 (s), 757 (s), 685 (m), 661 (m) cm^{-1}.

Metallogel [Pb(abdc)(H_2O)]$_n$ (7) A solution of H_2abdc (63 mg, 0.31 mmol) in DMF (0.5 mL) was added to a solution of $Pb(OAc)_2 \cdot 3H_2O$ (126 mg, 0.33 mmol) in DMF (1.5 mL) and the mixture sealed in a capped vial. The solution was placed in an oven and heated at 100 °C for 72 hours. After this time gelation was observed to have occurred. Critical gelation percentage: 1%. Anal. Calcd (%) for [Pb(abdc)(H_2O)]: C 30.91, H 1.89; found C 30.71, H 1.93. FTIR (air dried sample) $\bar{\upsilon}$ = 3337 (brw), 1941 (w), 1602 (m), 1515 (s), 1405 (m), 1345 (s), 1108 (w), 914 (w), 856 (w), 772 (m), 718 (s), 663 (m) cm^{-1}.

[Pb(abdc)(DMF)] (8) A solution of H_2abdc (32 mg, 0.16 mmol) in DMF (0.5 mL) was added to a solution of $Pb(OAc)_2 \cdot 3H_2O$ (63 mg, 0.17 mmol) in DMF (1.5 mL) and the mixture sealed in a capped vial. The solution was placed in an oven and heated at 60 °C. After three days colourless needle crystals suitable for X-ray diffraction studies had appeared. Yield: 95.9%. Bulk purity was determined by PXRD. Anal. Calcd (%) for [Pb(abdc)(DMF)]: C 34.85, H 2.72, N 2.90; found C 34.67, H 2.72, N 3.00. FTIR $\bar{\upsilon}$ = 2931 (w), 1942 (m), 1635 (s), 1596 (m), 1524 (s), 1423 (m), 1356 (s), 1301 (s), 1235 (s), 1135 (w), 1097 (s), 982 (m), 919 (m), 861 (m), 802 (m), 777 (s), 725 (s), 694 (w), 59 (s) cm^{-1}.

2.5. References

[1] Catalano, J.; Murphy, A.; Yao, Y.; Yap, G. P.; Zumbulyadis, N.; Centeno, S. A.; Dybowski, C., *Dalton Trans.,* **2015**, *44*, 2340-2347.

[2] Chen, D.; Shen, W.; Wu, S.; Chen, C.; Luo, X.; Guo, L., *Nanoscale,* **2016**, *8*, 7172-7179.

[3] Esteban-Gomez, D.; Platas-Iglesias, C.; Enriquez-Perez, T.; Avecilla, F.; de Blas, A.; Rodriguez-Blas, T., *Inorg. Chem.,* **2006,** *45*, 5407-5416.

[4] Sengupta, S.; Mondal, R., *J. Mater. Chem. A,* **2014**, *2*, 16373-16377.

[5] Davidovich, R. L.; Stavila, V.; Marinin, D. V.; Voit, E. I.; Whitmire, K. H., *Coordin. Chem. Rev.,* **2009**, *253*, 1316-1352.

[6] Aboutorabi, L.; Morsali, A., *Coordin. Chem. Rev.,* **2016**, *310*, 116-130.

[7] Safarifard, V.; Morsali, A., *CrystEngComm,* **2011**, *13*, 4817.

[8] Hashemi, L.; Morsali, A.; Büyükgüngor, O., *New J. Chem.,* **2014**, *38*, 3187.

[9] Kole, G. K.; Peedikakkal, A. M.; Toh, B. M.; Vittal, J. J., *Chemistry,* **2013**, *19*, 3962-3968.

[10] Shimoni-Livny, L.; Glusker, J. P.; Bock, C. W., *Inorg. Chem.,* **1998**, *37*, 1853-1867.

[11] Yuan, Y.-Z.; Zhou, J.; Liu, X.; Liu, L.-H.; Yu, K.-B., *Inorg. Chem. Comm.,* **2007**, *10*, 475-478.

[12] Zou, X.; Huo, L.-H.; Deng, Z.-P.; Zhao, H.; Gao, S., *Inorg. Chem. Comm.,* **2014**, *46*, 305-309.

[13] Bondi, A., *J. Phys. Chem.,* **1964**, *68*, 441-451.

[14] Davidovich, R. L.; Stavila, V.; Marinin, D. V.; Voit, E. I.; Whitmire, K. H., *Coordin. Chem. Rev.,* **2009**, *253*, 1316-1352.

[15] Desiraju, G. R., *Cryst. Growth Des.,* **2011**, *11*, 896-898.

[16] Steiner, T.; Desiraju, G. R., *Chem. Comm.,* **1998**, 891-892.

[17] Bustamante, E. L.; Fernandez, J. L.; Zamaro, J. M., *J. Colloid Interface Sci.,* **2014**, *424*, 37-43.

[18] Sun, T.; Hu, J.; Ren, X.; Wang, S., *Sep. Sci. Technol.,* **2014**, *50*, 874-885.

[19] Valenzano, L.; Civalleri, B.; Chavan, S.; Bordiga, S.; Nilsen, M. H.; Jakobsen, S.; Lillerud, K. P.; Lamberti, C., *Chem. Mater.,* **2011**, *23*, 1700-1718.

[20] Bernstein, J.; Davis, R. E.; Shimoni, L.; Chang, N.-L., *Angew. Chem. Int. Ed.,* **1995**, *34*, 1555-1573.

[21] C. R. Groom, I. J. Bruno, M. P. Lightfoot and S. C. Ward, *Acta Cryst.,* **2016**, *72*, 171-179.

[22] Saha, S.; Rajput, L.; Joseph, S.; Mishra, M. K.; Ganguly, S.; Desiraju, G. R., *CrystEngComm,* **2015**, *17*, 1273-1290.

[23] Llusar, M.; Sanchez, C., *Chem. Mater.,* **2008**, *20*, 782-820.

[24] Park, J. D.; Ahn, K. H.; Lee, S. J., *Soft Matter,* **2015**, *11*, 9262-9272.

[25] Weiss, R. G.; Terech, P., *Molecular Gels: Materials with Self-Assembled Fibrillar Networks,* Springer Netherlands: Netherlands, **2006**.

[26] Nandi, G.; Titi, H. M.; Thakuria, R.; Goldberg, I., *Cryst. Growth Des.,* **2014**, *14*, 2714-2719.

[27] Tam, A. Y.; Yam, V. W., *Chem. Soc. Rev.,* **2013**, *42*, 1540-1567.

[28] Williams, D. H.; Fleming, I., *Spectroscopic Methods in Organic Chemistry*, McGraw-Hill Education, **2007**.

[29] Byrne, P.; Lloyd, G. O.; Applegarth, L.; Anderson, K. M.; Clarke, N.; Steed, J. W., *New J. Chem.,* **2010**, *34*, 2261-2274.

[30] Mallick, A.; Schön, E.-M.; Panda, T.; Sreenivas, K.; Díaz, D. D.; Banerjee, R., *J. Mater. Chem.,* **2012**, *22*, 14951-14963.

[31] Lambert, J. B., *Introduction to Organic Spectroscopy*, Macmillan, **1987**.

[32] Shapley, J. R., *Inorganic Syntheses*, Wiley-Interscience, **2004**.

[33] Yang, E.-C.; Li, J.; Ding, B.; Liang, Q.-Q.; Wang, X.-G.; Zhao, X.-J., *CrystEngComm.,* **2008**, *10*, 158-161.

[34] Zhang, L.; Qin, Y. Y.; Li, Z. J.; Lin, Q. P.; Cheng, J. K.; Zhang, J.; Yao, Y. G., *Inorg. Chem.,* **2008**, *47*, 8286-8293.

[35] Zhang, Z.; Zhou, Y.-L.; He, H.-Y., *Acta Crystallogr. E,* **2006**, *62*, 2591-2593.

[36] Desiraju, G. R.; Steiner, T., *The Weak Hydrogen Bond in Structural Chemistry and Biology*, Oxford University Press: Oxford, **1999**.

[37] Station 11.3.1, The Advanced Light Source, Berkeley Laboratory, website: [www.als.lbl.gov/als/techspecs/bl11.3.1.html].

[38] Bodwell, G. J.; Fleming, J. J.; Mannion, M. R.; Miller, D. O., *J. Org. Chem.,* **2000**, *65*, 5360-5370.

[39] Barrell, M. J.; Campana, A. G.; von Delius, M.; Geertsema, E. M.; Leigh, D. A., *Angew. Chem. Int. Ed.,* **2011**, *50*, 285-290.

[40] Esipova, T. V.; Ye, X.; Collins, J. E.; Sakadzic, S.; Mandeville, E. T.; Murray, C. B.; Vinogradov, S. A., *P. Natl. Acad. Sci. USA,* **2012**, *109*, 20826-20831.

[41] Muthiah, C.; Taniguchi, M.; Kim, H. J.; Schmidt, I.; Kee, H. L.; Holten, D.; Bocian, D. F.; Lindsey, J. S., *Photochem. Photobiol.,* **2007**, *83*, 1513-1528.

[42] Vermeij, R. J.; Miller, D. O.; Dawe, L. N.; Aprahamian, I.; Sheradsky, T.; Rabinovitz, M.; Bodwell, G. J., *Aust. J. Chem.,* **2010**, *63*, 1703.

Chapter 3

Ethynyl and allenyl functionalised 1,3-benzenedicarboxylate as linkers in a series of first-row transition metal coordination polymers

3.1. Introduction

The ethynyl- functionalised ligand 5-ethynyl-1,3-benzenedicarboxylic acid (H_2ebdc) has been observed to have great efficacy as a linker to divalent lead (as seen in Chapter 2) to generate coordination polymers (CPs) with potential switchability. The flexibility of the lead centre allows for the synthesis of unconventional frameworks, at the expense of predictability of the resulting structure. First-row transition metals, on the other hand, generally have a more rigid coordination environment, allowing for a degree of design in the CP synthesis. First-row transition metals also have the advantage over Pb in abundance, cost and ease of chemistry.[1] The chemistry of transition metals is well documented, and their large range of accessible properties lie in magnetism,[2,3] electronic functionality[4,5] and catalysis.[6,7] Many examples of structural single-crystal to single-crystal (SCSC) transitions involving transition metal CPs have also been reported.[8-10]

Typically occurring coordination geometries seen within first-row transition metals include linear, trigonal, square planar, tetrahedral and octahedral due to d- orbital crystal-field splitting (Figure 55). For each metal ion and its oxidation state, the possible coordination geometries are well-established allowing a certain geometry to be pursued, and thus can be chosen to act as nodes with 2 – 6 linker connectivity. However, with any strategic plan toward directing the self-assembly of CPs, it must be accepted that the formation of these compounds is an uncertain process and distortions or variations in particular cases cannot be engineered or avoided.

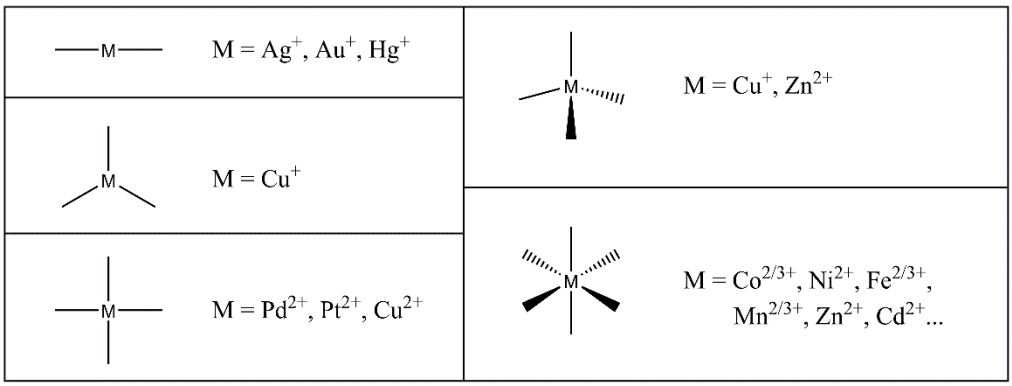

Figure 55: *Illustration of some transition metal coordination environment geometries (linear, trigonal, square planar, tetrahedral and octahedral), and common metals that form them.*[1]

Further exploration of the directing influence by weak hydrogen bonding over the assembly of CPs *via* the ethynyl group of the ebdc linker in the presence of rigidly coordinating first-row transition metals provides an interesting comparison to the work presented in Chapter 2. From this previous work, weak C–H···O hydrogen bond interactions donated from the ethynyl functional group were observed to have a directing effect on the packing of one- and two-dimensional CPs. The ebdc ethynyl group can also participate in aromatic C–H···π hydrogen bonds, and although deemed weaker[11] these also have the potential to exert some influence over solid-state packing. Generally the ebdc linker can partake in two types of intermolecular aromatic hydrogen bonds; firstly between the ethynyl donor and the phenyl group of an adjacent ebdc linker, or as a T-shaped interaction between two ethynyl groups, where one acts as a donor and the other an acceptor, similar to T-shaped phenyl···phenyl interactions illustrated in Figure 15 in Chapter 1. Illustrations of these two interactions are displayed in Figure 56. Because of the multi-atomic nature of the π acceptor within the hydrogen bond, it is often not obvious as to how to define the hydrogen bond distance and approach angle. Some authors use the distance of H to a calculated centroid within the accepting group, while some use the perpendicular distance from H to the molecular plane and others give individual distances to all C atoms. Analyses of the hydrogen bond angles *vs* the hydrogen bond distances in a report by Desiraju et al. indicate that a calculated centroid may be reasonably approximated as the acceptor site in these interactions.[12]

For the purposes of this chapter, hydrogen-bond donor to multi-atomic hydrogen-bond acceptor distances and angles will thus be measured in relation to calculated centroids; one C_6 centroid in the centre of the acceptor phenyl ring, and to a C_2 centroid of the

accepting ethynyl bond. For these interactions *D* is the donor-acceptor distance, *d* the hydrogen-acceptor distance and *θ* the approach angle.

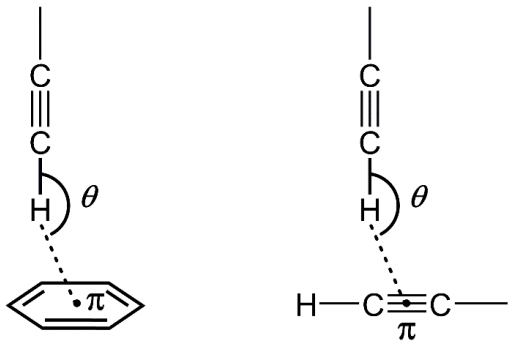

Figure 56: *Definition of geometrical ethynyl derived C–H···π hydrogen bond parameters. Left: π is the calculated C_6 centroid. Right: π is the calculated C_2 centroid.*

These C–H···π interactions can also be confirmed spectroscopically, similar to those of C–H···O interactions.[13,14] The IR vibration frequency of a non- interacting ethynyl C–H stretching band has been assigned at 3301 cm^{-1}, as determined through the solid-state H_2ebdc structure in Chapter 2. This 'non-interaction' ethynyl band provides a useful reference point for any bathochromic shifts that might occur with hydrogen bond formation in the CPs containing ebdc described below.

To assign the correct coordination number of the transition metal and subsequent topology of the material in question, a definition of coordination bond lengths is important. The divalent first-row transition metals Mn^{2+}, Co^{2+}, Ni^{2+}, Cu^{2+} and Zn^{2+} utilised in this chapter all have ionic radii ranging from 0.72 to 0.80 Å,[15] and thus can be treated similarly when determining the M–O coordination bond length. A CSD[16] database study on coordination bond lengths of these metals to carboxylate groups in the crystalline state was conducted through ConQuest, the results of which show that M–O distances range from 1.79 Å to 2.98 Å with a mean average of 2.05 Å. Details of the study can be found in Section 3.4.† The relatively low mean value for these M–O distances would suggest that longer bond lengths are less common, and indeed only 1.5% of the reported M–O distances within the study are reported as being above 2.50 Å. Thus for the purposes of this chapter, the upper limit of the M–O transition metal coordination bond will be taken as 2.50 Å.

This chapter describes the synthesis and structural characterisation of a series of new coordination polymers and coordination complexes containing select first-row transition

metals and the ethynyl (ebdc) and allenyl (abdc) functionalised 1,3-benzenedicarboxylate ligands. All M–O coordination bond lengths can be found in Appendix II.

3.2. Results

A series of coordination polymers (CPs) were synthesised from 5-ethynyl-1,3-benzenedicarboxylic acid (H_2ebdc) with a selection of divalent first row transition metal ions. In total six new compounds were prepared and characterised, one of which is isostructural to another compound including the ligand 5-allenyl-1,3-benzenedicarboxylate (abdc).

3.2.1. 5-ethynyl-1,3-benzenedicarboxylic acid

5-ethynyl-1,3-benzenedicarboxylic acid (H_2ebdc), introduced in Chapter 2, was utilised in the synthesis of first-row transition metal containing CPs. The ebdc ligand possesses two carboxylate functional groups to allow coordination of metal nodes and an ethynyl group to promote weak hydrogen-bonding interactions. Interactions that are supported by this ligand include π···π stacking derived from the central aromatic ring, weak C-H···O and C–H···π hydrogen bonding from the terminal ethynyl carbon atom as well as stronger hydrogen bonding to the carboxylate functionality. This ethynyl- derived weak C–H···π hydrogen bonding was shown to have the potential to be an influencing factor in the topology and behaviour of a CP.

3.2.2. Discrete coordination complexes

A discrete molecular structural assembly was obtained from the slow cooling of H_2ebdc and $Ni(OAc)_2{\cdot}4H_2O$ in a 4:1 methanol-to-water mixture. The resulting green block crystals contain an overall molecular formula of $[\{Ni(ebdc)(MeOH)_4\}_2]$ (**9**). The asymmetric unit consists of one half-occupancy Ni(II) metal centre coordinated to two methanol groups as well as a half of an ebdc linker. These components form discrete dimers generated from four asymmetric groups (two nickel centres, two ebdc ligands and eight methanol groups) which pack through *Cmce* symmetry (Figure 57).

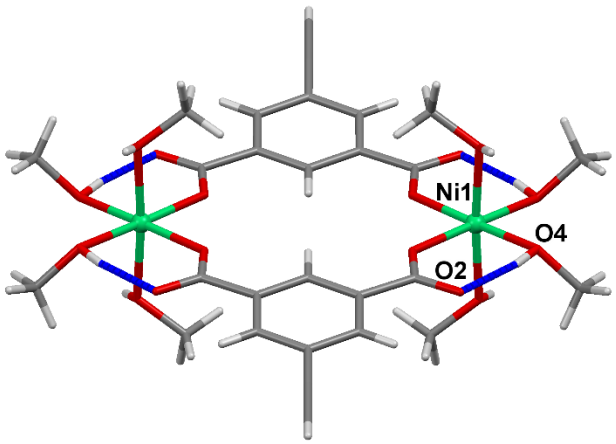

Figure 57: *Intramolecular hydrogen bonding within a discrete dimer of* ***9****, hydrogen bonds shown in blue.*

The two nickel centres within each dimer show octahedral geometries and are bridged by two ebdc ligands. The metal centre coordination spheres are each completed by four methanol groups resulting in a coordination number of six, in which the Ni-O(carboxylate) bond length is 2.0351(10) Å and the average Ni-O(MeOH) bond length is 2.0684(14) Å. The Ni–O atom distances correspond well with a bond length of 2.06 Å cited by Dubois et al.[17] and fits well with the mean first-row transition M–O distance of 2.05 Å derived from the CSD study discussed in Section 3.1. in this chapter. A strong intramolecular hydrogen bond emanates from the equatorial methanol OH group O4 to the uncoordinated oxygen O2 of the ligand carboxylate group (Figure 58), of which the metric parameters are presented in Table 7 below.

This uncoordinated carboxylate oxygen O2 also acts as a hydrogen acceptor for intramolecular hydrogen-bond interactions from the axial methanol hydroxyl oxygens (O3) in adjacent dimers (Figure 58). In addition, the ebdc ligand is observed to participate in a weak C–H···π hydrogen bond from the ethynyl group of the ebdc linker to a phenyl group of another. Cumulatively, these intermolecular interactions act to stabilise the individual complexes in the solid state.

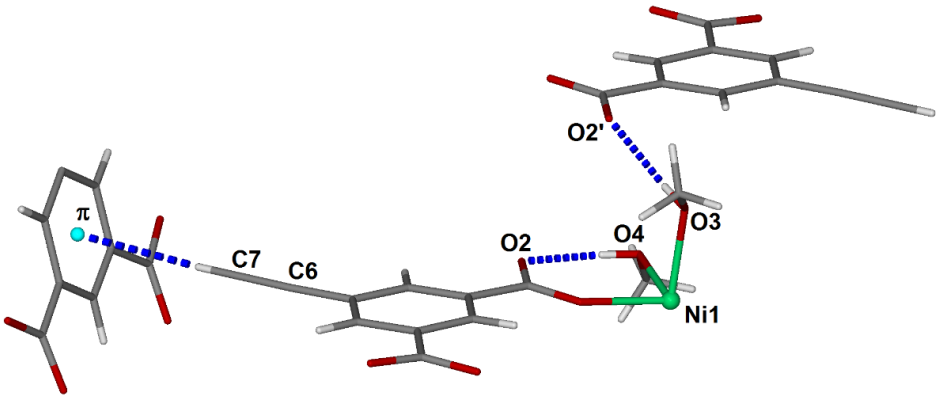

Figure 58: *Intra- and inter- molecular interactions of* ***9****, in which hydrogen bonds are highlighted in blue.*

Interaction	*D* (Å)	*d* (Å)	*θ* (°)
O4–H4···O2	2.5883(16)	1.81(3)	169(2)
O3–H3···O2’	2.6672(17)	1.96(2)	168(2)
C7–H7···π	3.777(3)	2.82	177.6(2)

Table 7: *Hydrogen bond interactions within the packed dimers of* ***9****. Symmetry operators: (’) = (½ – x, ½ – y, 1 – z), (π) = (1 – x, ½ + y, $^3/_2$ – z).*

The combination of these intermolecular interactions results in the dimers packing into an interlocked herringbone formation within the solid state (Figure 59) held together by the aforementioned hydrogen bond interactions.

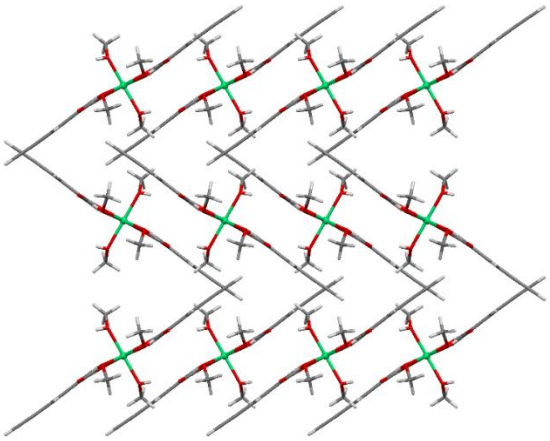

Figure 59: *Herringbone packing arrangement of Ni dimers in* ***9*** *as viewed down the crystallographic* a *axis.*

Spectroscopic IR analysis of **9** reveals a bathochromic shift in the alkyne C–H band from 3301 cm^{-1} in a non-bonded ethynyl group to 3285 cm^{-1} in **9**. This small shift of 16 cm^{-1} reflects the relative weakness of the C–H···π hydrogen bond.

3.2.3. 1D CP chains

The same cooling reaction technique was also employed on the cobalt equivalent salt $Co(OAc)_2{\cdot}4H_2O$. Equimolar amounts of cobalt acetate and H_2ebdc were dissolved in a 4:1 methanol-water mixture, heated for 1 hour and left to slowly cool over two days. The resulting pink crystals contain the molecular formula $[Co(ebdc)(MeOH)_4]$ (**10**) and pack in the *Cmce* space group, similar to structure **9**.

The asymmetric unit of **10** consists of one half-occupancy Co(II) centre coordinated to two methanol molecules where the CH_3 group of each is disordered over two positions as well as half of an ebdc linker, of which the atoms of the whole ethynyl group including one phenyl carbon atom are disordered equally over two positions. The cobalt centre within the asymmetric unit is six coordinate and bears an octahedral coordination geometry, in which the Co–O(carboxylate) bond length is 2.104(2) Å and the average Co-O(MeOH) bond length is 2.071(4) Å, which correspond well with the average first-row transition metal M–O bond length of 2.05 Å determined previously. In contrast to **9**, the cobalt centres and ligands propagate by symmetry to give a 1D zig-zag chain made up of alternating ligand and 2-connected cobalt(II) atoms, each Co(II) capped by four methanol groups (Figure 60).

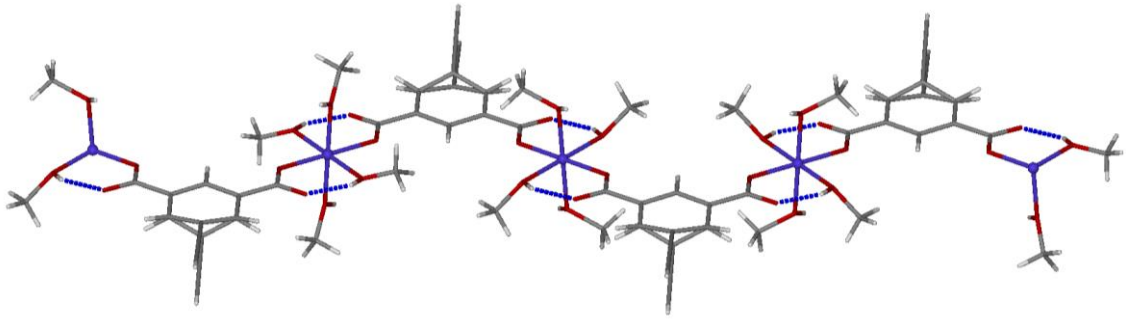

Figure 60: *Continuous one-dimensional chain of* ***10****, in which the disordered ethynyl groups are shown. Intramolecular hydrogen bonds are shown by blue fragmented lines.*

Supramolecular interactions within **10** consist of O–H···O hydrogen bonding and C-H···π interactions involving the phenyl ring (Figure 61). Similarly to compound **9**,

there are two types of O–H···O hydrogen bonds within the structure; an intramolecular hydrogen bond from the methanol hydroxy oxygen O3 to an uncoordinated carboxylate oxygen O1, and an intermolecular hydrogen bond from a methanol oxygen donor O4 to an uncoordinated carboxylate oxygen O1 in a symmetry generated adjacent chain. The hydrogen bond geometries are displayed in Table 8 below.

The disordered ebdc ethynyl functional group deviates from the molecular plane of the organic linker by 9.36° and 10.13° respectively for the two disordered orientations directed mainly at two positions within the π acceptor phenyl group; to the central position and seemingly to an apical hydrogen atom. Computational modelling has shown that the potential energy surface of X–H···π (X = C, N) interactions is very shallow and the energies associated with different contact geometries are very similar, allowing this disorder.[18] The values for the C–H···plane bond geometry (where plane is the calculated ebdc phenyl plane) in Table 8 are shown as a range of distances from the terminal C1(A) atom to the adjacent phenyl plane.

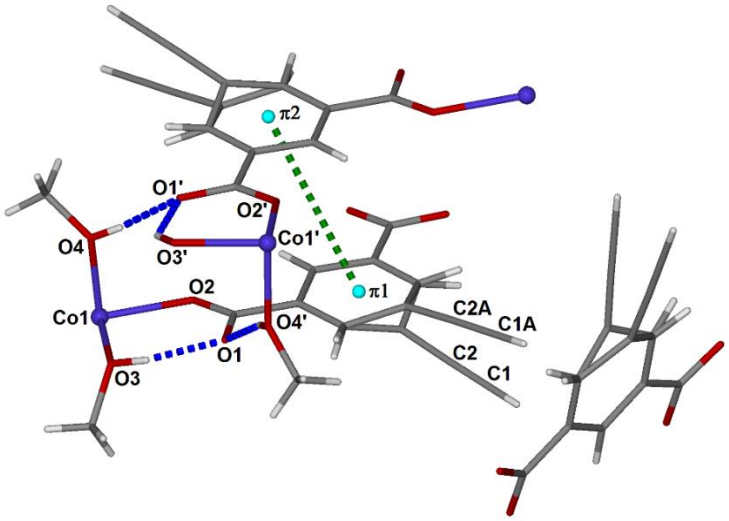

Figure 61: *Intra- and Inter- molecular interactions of* ***10****, in which hydrogen bonds are highlighted in blue, and a π1···π2 interaction is shown in green. The equally disordered ethynyl atoms C1(A) and C2(A) project toward an adjacent ebdc ligand. Symmetry operator: (') = (– x, – y, 1 – z).*

Interaction	*D* (Å)	*d* (Å)	*θ* (°)
O3–H3···O1	2.570(4)	1.85(3)	137(2)
O4–H4···O1'	2.658(4)	1.93(5)	164(5)
C1(A)–H1(A)···plane''	3.24(2) – 3.53(2)	2.44 – 2.59	160.9(15) – 175.8(18)

Table 8: *Hydrogen bond interactions within the packed chains of* ***10****. Symmetry operator: ('') = (x, – ½ + y, ³/₂ + z).*

The coordination modes of the linkers and metal as well as the solid-state packing of **10** are reminiscent to that of structure **9** (Figure 62). In the Ni(II) based structure **9** the ebdc linkers coordinate to the nickel centre in a *cis* formation and bridge across two metal centres to form dimers, and in the Co(II) based coordination polymer **10** these ebdc linkers, despite having the same coordination modes, coordinate to the cobalt centre *via* a *trans* formation, and thus each bridge to different symmetry-generated metal centres thus propagating a one-dimensional chain. The identical orientation and packing of these two structures brings up the possibility of the existence of a 1D chain form of **9** and a dimeric complex form of structure **10**, though no evidence for these alternative compounds has been observed experimentally.

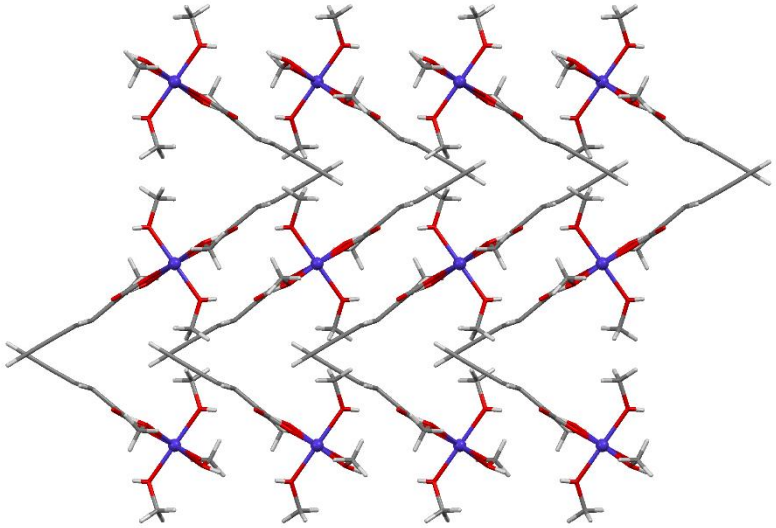

Figure 62: *Herringbone packing arrangement of Co chains in* ***10*** *as viewed down the crystallographic* a *axis. Only one position of the ethynyl group is shown for clarity.*

The intramolecular interactions of compound **10** are reflected in the spectroscopic analysis. The band intensity for the ethynyl C–H stretching vibration is both decreased and broadened with respect to H_2ebdc, and although heavily obscured by the broad OH band, it is observable at 3282 cm^{-1}. This band is red-shifted from the non-interacting ethynyl reference of 3301 cm^{-1} by 19 cm^{-1}, similar to the bathochromic shift of 16 cm^{-1} for **9**, further supporting the notion that the weak C–H···π hydrogen bonds are of similar strengths, despite the dramatic distortion of the ethynyl group in **10**.

3.2.4. 2D CP nets

The slow cooling reaction of H_2ebdc with a metal acetate salt in 4:1 methanol to water was further utilised this time with $Mn(OAc)_2{\cdot}4H_2O$. The reaction yielded colourless crystals with the molecular formula $[Mn_3(ebdc)_3(MeOH)(H_2O)_3]{\cdot}3MeOH{\cdot}H_2O$ (**11**). The crystal structure packs in the $P\,\bar{1}$ space group. The asymmetric group of **11** consists of four manganese(II) centres, with two possessing half-crystal occupancy, bridged by three ebdc linkers. One methanol and three water groups coordinate to the fully occupied Mn centres and three methanol groups as well as one two half occupancy water molecules reside in the interstitial space around the structure (Figure 63).

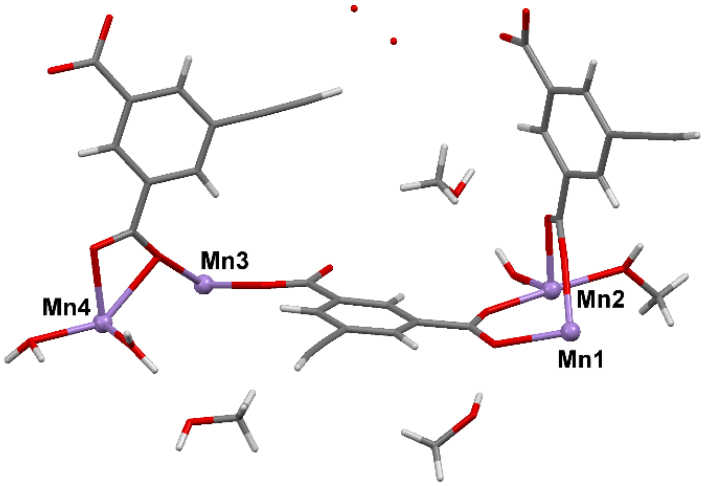

Figure 63: *Asymmetric unit of* ***11****, displaying the disordered water molecules as red dots.*

Three of the four manganese centres, Mn1, Mn2 and Mn3, within **11** support six coordination bonds whereas the remaining manganese centre, Mn4, supports a coordination number of seven with a Mn–O bond range of 2.093(3) to 2.420(3) Å. A full list of Mn–O bond lengths of **11** can be found in Appendix II. These manganese centres are paired together *via* coordination bonding in a quasi- paddlewheel formation bridged by three ebdc carboxylate groups. The $Mn_2(O_2C)_3$ units then dimerise through an inversion centre, fused by one central manganese atom. This makes up the central $[Mn_3(CO_2)_6]$ nodes, displayed in Figure 64. Mn1 and Mn2 make up one node, and Mn3 and Mn4 the other. The Mn3 and Mn4 node contains two more Mn–O bonds than the node containing Mn1 and Mn2, where O13''' coordinates to Mn4 (Mn4–O13''' bond length of 2.308(3) Å) but the equivalent carboxylate O2 does not coordinate to Mn2, the equivalent distance being 2.887(3) Å, lying outside of the determined coordination sphere limit of 2.50 Å. A result of this difference in bonding is the distance between

Mn1···Mn2 and Mn3···Mn4, which varies by 0.07 Å. Each node is also capped by different solvents; four water groups for Mn3 and Mn4, and two water groups and two methanol groups for Mn1 and Mn2 (Figure 64). Cumulatively these variations break the symmetry between the two nodes, rendering them crystallographically inequivalent. The higher coordination numbers in the Mn3···Mn4 node can be attributed to an orientational twist of the bridging ebdc linkers.

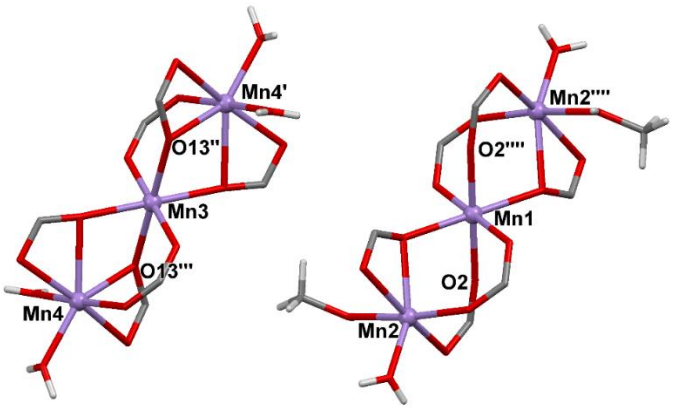

Figure 64: *A comparison of coordination environments of the Mn centres of* ***11*** *within Mn1:Mn2 and Mn3:Mn4 nodes. Mn1 and Mn3 are positioned on inversion centres. Symmetry operators: (') = (1 – x, 1 – y, 1 – z), ('') = (– x, 1 – y, 1 – z), (''') = (1 + x, y, z), ('''') = (2 – x, – y, – z).*

Overall the bridging ebdc linkers and 4-connected $[Mn_3(O_2C)_6]$ nodes form two-dimensional square-based nets (Figure 65) interdigitated by ethynyl groups and held together by extensive hydrogen bonding through the interstitial and coordinated methanol and water molecules. There are three symmetrically unique ebdc linkers within structure **11**. Two of these ebdc linkers participate in parallel-displaced π···π interactions within the vertical pillars of the 2D net (Figure 65) to their symmetry equivalents, stabilising the framework at inter-centroid distances of 3.521(3) Å and 3.443(3) Å and at phenyl planar shifts of 0.990(6)° and 0.646(7)° respectively.

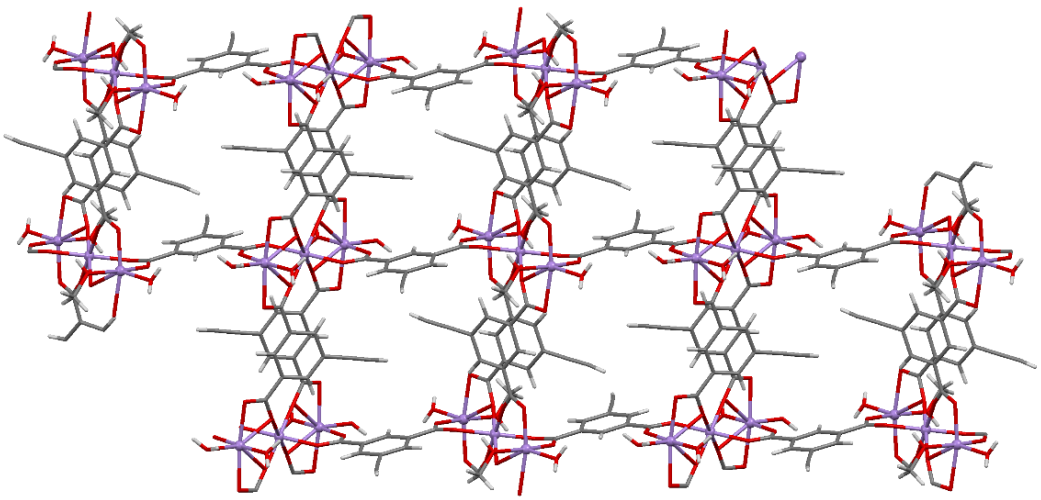

Figure 65: *Mn cluster nodes bridged by interdigitating lateral and vertical ebdc linkers in the 2D framework of* ***11****, as viewed along the crystallographic [011] plane.*

The remaining ebdc linker within **11** is oriented such that the ethynyl group extends out of the plane of the two dimensional net in Figure 65 and thus interdigitates with an adjacent symmetry equivalent ethynyl group *via* parallel π···π interactions. The inter-centroid π···π distance is 3.44724(10) Å. The interaction between adjacent layers is strengthened by additional hydrogen bonding *via* the out-of-plane coordinated aqua and methanol groups (Figure 66, Table 9).

Three unique interstitial methanol groups and one disordered water molecule reside in the interstitial space between the nets of **11.** These act as hydrogen donors and acceptors in O–H···O hydrogen interactions to adjacent carboxylate groups and coordinated methanol and aqua groups. Only the hydrogen bonds from the three methanol moieties have been assigned, as the water molecules are insufficiently ordered for reliable crystallographic refinement.

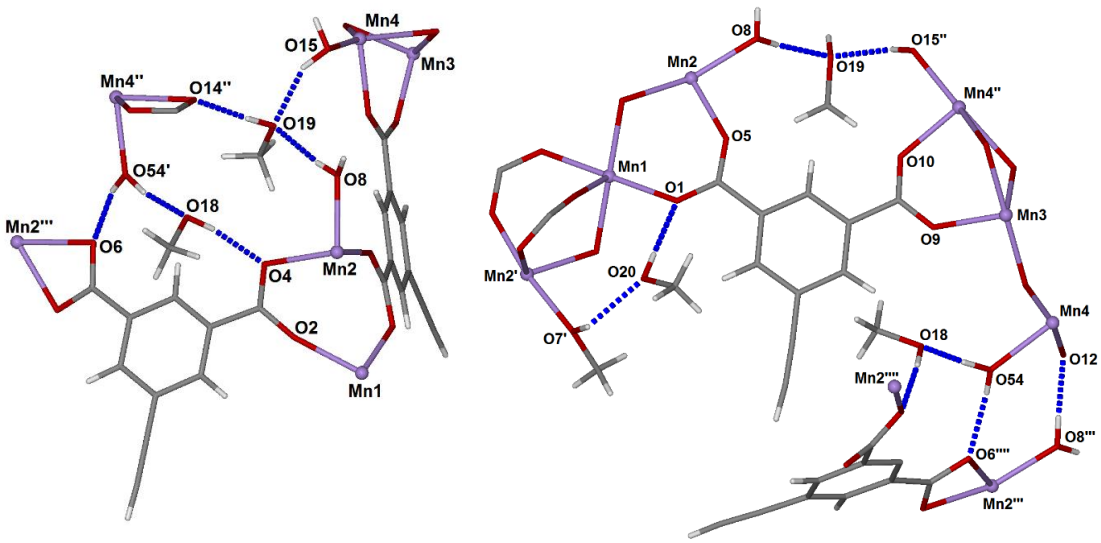

Figure 66: *Intermolecular hydrogen bonding interactions involving the interstitial methanol molecules. Symmetry operators: Left: (') = (x, – 1 + y, z), ('') = (1 + x, – 1 + y, z), (''') = (– 1 + x, y, z). Right: (') = (2 – x, – y, – z), ('') = (1 – x, 1 – y, 1 – z), (''') = (– 1 + x, 1 + y, z), (''') = (x, 1 + y, z).*

Interaction	*D* (Å)	*d* (Å)	*θ* (°)
O15–H15···O19	2.765(4)	1.94	155.1(3)
O19–H19···O14''	2.707(4)	1.84(6)	177(5)
O8–H8B···O19	2.744(4)	1.96(5)	173(4)
O54'–H54'B···O6	2.753(4)	2.02(5)	166(6)
O54'–H54'A···O18	2.694(5)	1.74(7)	169(6)
O18–H18···O4	2.732(4)	1.90	170.9(2)
O7'–H7'···O20	2.722(5)	2.09(7)	129(7)
O20–H20···O1	2.860(5)	2.02	175.3(3)
O8'''–H8'''···O12	2.679(4)	1.86(5)	175(6)

Table 9: *Intermolecular O–H···O hydrogen bond geometries within the solid-state packing of* ***11****.*

Spectroscopic analysis of **11** supported the crystallographic evidence of the absence of C–H···X (X = O, π) hydrogen bonding. A weak, broad ethynyl C–H band was observed at 3296 cm^{-1}, mostly obscured by a strong broad OH band at approximately 3350 cm^{-1} which, at a bathochromic shift of only 5 cm^{-1}, suggests that the ethynyl group is not involved in any significant hydrogen bonding within **11**.

Copper perchlorate was next utilised as a dimeric transition metal salt to be reacted with H_2ebdc. A different crystallisation method had to be employed for these two

components, due to the efficacy of the two components reacting and producing unwanted amorphous product. Thus slow layer diffusion crystallisation was used, with a drop of NEt_3 added into the H_2ebdc layer to promote carboxylic acid deprotonation.

The turquoise hexagonal crystals obtained from slow layer diffusion of $Cu(ClO_4)_2 \cdot 6H_2O$ in water and H_2ebdc and NEt_3 in methanol have the molecular formula $[Cu_3(ebdc)_3(H_2O)_{2.5}(MeOH)_{0.5}] \cdot 6H_2O$ (**12**). The asymmetric unit of CP **12** consists of two Cu(II) atoms bridging three ebdc ligands, one linker of which bridges to a third copper atom. The two central copper atoms Cu1 and Cu2 form a characteristic paddlewheel secondary building unit (SBU), with the apical coordination positions occupied by a water molecule and a 50:50 site disordered methanol/water unit on the obverse of the paddlewheel motif. The third metal centre Cu3 also forms a paddlewheel unit with a symmetry-generated equivalent. The asymmetric unit also contains six heavily disordered water molecules, only one of which does not have partial occupancy (Figure 67). The asymmetric unit packs in the monoclinic *I*2/*a* space group. All three of the copper(II) centres adopt a square-based pyramidal coordination environment geometry characteristic of paddlewheel coordination nets, where the average Cu–O coordination bond is 2.01 Å. Cu···Cu distances within the SBUs are 2.6208(7) Å in Cu1···Cu2 and 2.6247(9) Å in Cu3···Cu3'.

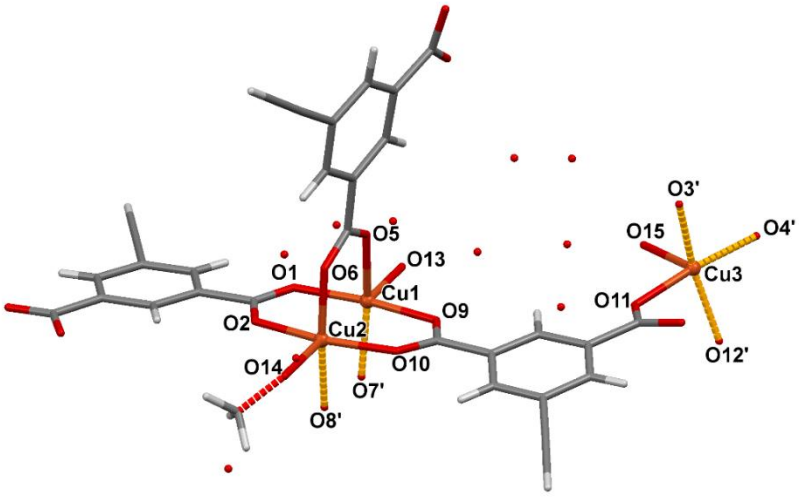

Figure 67: *The asymmetric unit of* **12** *with coordination environments of the central copper atoms displayed. Symmetry-generated coordination bonds are shown in yellow and disordered water molecules are shown as red dots. Symmetry operators: O7' and O8' = (1 – x, ½ + y, ½ – z), O3' = (1 – x, – ½ + y, ½ – z), O4' = (½ + x, – ½ + y, – ½ + z), Cu3 and O12' = (3/2 – x, y, – z).*

The extended molecular structure forms a 4-connected 2D net, whereby the paddlewheel nodes and ebdc linkers assemble into a Kagomé lattice (Figure 68). Each

2D sheet is offset relative to the sheets above and below, thus stacking in an ABA fashion. This manner of packing is similar to that formed by copper(II) with other substituted 1,3-benzenedicarboxylate (bdc) ligands, such as 5-nitro-1,3-bdc and 5-(methylsulfanylmethyl)-1,3-bdc.[19] Disordered water molecules occupy the interstitial spaces.

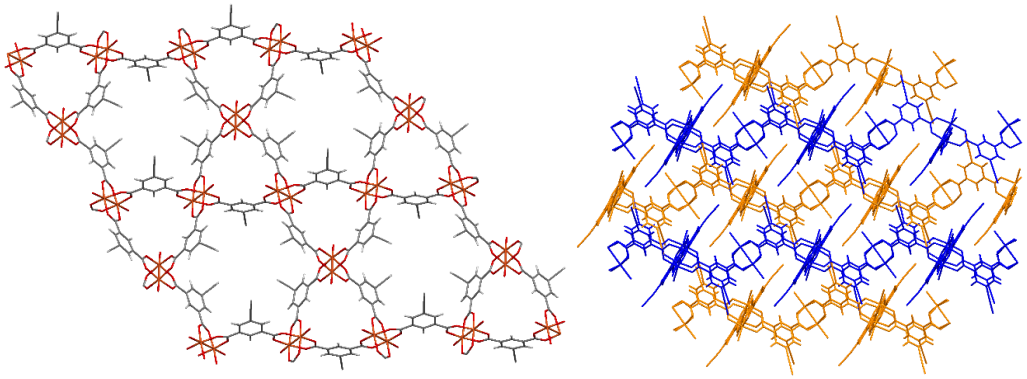

Figure 68: *Left: The 2D Kagomé pattern exhibited in a layer of network* **12** *as viewed along the crystallographic [101] plane. Right:* ABA *stacking of the 2D layers in* **12**. *Lattice waters have been omitted for clarity.*

Interactions between the stacked layers of **12** involve a mixture of π···π interactions and hydrogen bonding propagating *via* the ethynyl groups of the ebdc linkers. Of the three unique ebdc linkers within **12**, two are oriented *via* the ethynyl group toward the carboxylate groups of an adjacent layer (Figure 69, Table 10), and one is oriented toward an interstitial lattice water molecule (D = 3.249(5) Å, d = 2.45 Å and θ = 142.56°).

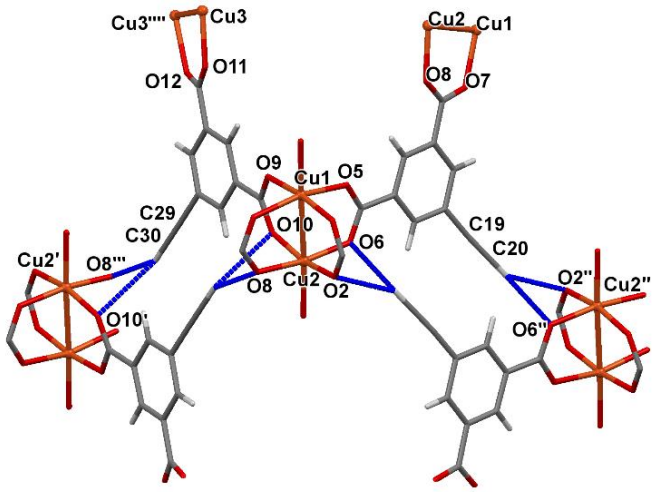

Figure 69: *Weak C–H···O hydrogen bonding between the layers of* **12**, *shown in blue. Symmetry operators: (') = (1 – x, 2 – y, – z), (") = (½ – x, 3/2 – y, ½ – z), ("') = (x, 3/2 – y, – ½ + z), (9"") = (3/2 – x, y, – z).*

Both bifurcated hydrogen bond interactions originating from C20 and C30 favour one hydrogen bond over the other; C20 favouring the O2'' carboxylate group atom and C30 favouring the O8''' carboxylate group atom through shorter interaction lengths and more linear approach angles. Table 10 below presents the geometries of both C–H···O interactions.

Interaction	*D* (Å)	*d* (Å)	*θ* (°)
C30–H30···O8'''	3.195(4)	2.32	152.28(19)
C30–H30···O10'	3.491(4)	2.83	127.18(17)
C20–H20···O2''	3.221(4)	2.35	150.74(18)
C20–H20···O6''	3.321(5)	2.70	122.87(18)

Table 10: *Intermolecular C–H···O hydrogen bond geometries within* ***12****.*

The third ebdc linker participates in a parallel-offset π···π interaction with a phenyl···phenyl inter-centroid distance of 3.67 Å (phenyl inter-planar distance of 3.60 Å), linking this ligand with its symmetry equivalent in an adjacent net (Figure 70).

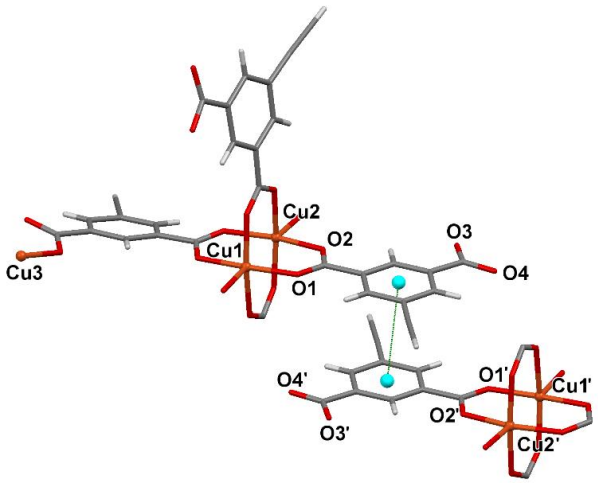

Figure 70: *Intermolecular π···π stacking in* ***12****. The phenyl π···π interaction is represented in green, between two equivalent calculated phenyl centroids shown in blue. Symmetry operations: (') = (1 – x, 2 – y, 1 – z).*

While the quality of the crystallographic data was insufficient to locate the individual hydrogen atoms of the interstitial water molecules using the electron density map, inter-oxygen distances give strong evidence for the presence of a hydrogen bonding network, exemplified by distances of 2.69 – 2.76 Å. It is likely that this hydrogen bonded network helps stabilise the 2D nets within the solid state.

The IR spectrum of **12** shows that the band intensity for the ethynyl C–H stretching vibrations centred at 3274 cm^{-1} has decreased and broadened considerably, with each effect being characteristic of multiple weak hydrogen interactions.[20] The ethynyl band displays a bathochromic shift of 27 cm^{-1}, and whilst more significant than that within compounds **9** and **10**, still shows a relatively weak interaction between the ethynyl and carboxylate moieties.

An analogous Kagomé structure to **12** was found by replacing ebdc for the allene derivative, 5-allenyl-1,3-benzenedicarboxylate (abdc). The abdc ligand was shown to be an interesting alternative asymmetrical linker adduct without the ability to participate in C–H···X (X = π, O) hydrogen bonding. The hexagonal blue crystals obtained from slow layer diffusion of $Cu(ClO_4)_2 \cdot 6H_2O$ in water and H_2abdc and NEt_3 in methanol were determined by spectroscopic and thermal analysis to have the molecular formula $[Cu(abdc)(H_2O)] \cdot 0.5H_2O$ (**13**), propagating in the trigonal $P\,\bar{3}m1$ space group.

The asymmetric unit of **13** consists of a copper centre at half crystal occupancy coordinated to half an abdc ligand, as well as a rotationally disordered aqua group at half occupancy. Heavily disordered solvent molecules occupy the interstitial void space. One carboxylate oxygen and the allenyl group of the abdc linker are equally disordered over two positions. The copper centre adopts a square-based pyramidal coordination environment geometry and dimerises into a paddlewheel motif with a symmetry equivalent copper centre, bridged by four carboxylate groups (Figure 72). The Cu–O bond length range is 1.9582(17) – 2.1398(19) Å and the Cu···Cu distance within the paddlewheel unit is 2.6031(8) Å. These copper and abdc components propagate into Kagomé type 2D nets, consisting of larger hexagonal and smaller triangular channels (Figure 71, left). These layers stack in an AAA fashion with a repeating equivalent distance of 6.76 Å (Figure 71, right).

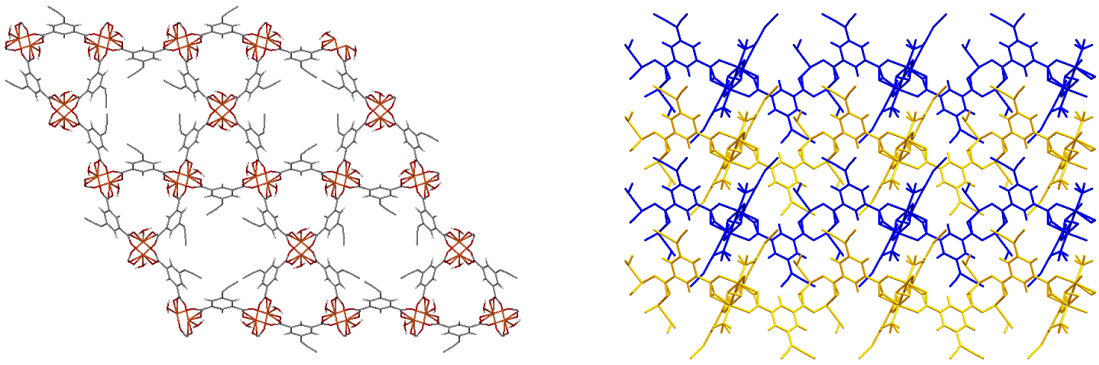

Figure 71: *Left: The Kagomé type structure of* **13** *as viewed down the crystallographic* c *axis. Only one distorted allenyl group has been shown for clarity. Right:* AAA *stacking of the 2D layers in* **13** *as viewed down the crystallographic* a *axis.*

The most prominent interaction between the two dimensional nets are O–H···O hydrogen bonds between the capped water groups of the copper paddlewheel units O3 and carboxylate oxygen atoms O1' and O1'', *via* the positionally disordered H3B hydrogen (Figure 72). These hydrogen bonds lie in a semi-occupied state, due to the rotational disorder of the water group. The distance between O3 and O1'/'' is 3.099(3) Å, where *d* (H3B···O1'/'' distance) is 2.07 Å and the approach angle C3–H3B···O1'/'' is 163.05(10)°. This hydrogen bonding may help stabilise what otherwise would be disordered carboxylate groups, as observed from the non- hydrogen-bonded carboxylate atom O2(A). The allenyl groups sit in the hydrophobic hexagonal channels and do not participate in any significant intramolecular interactions.

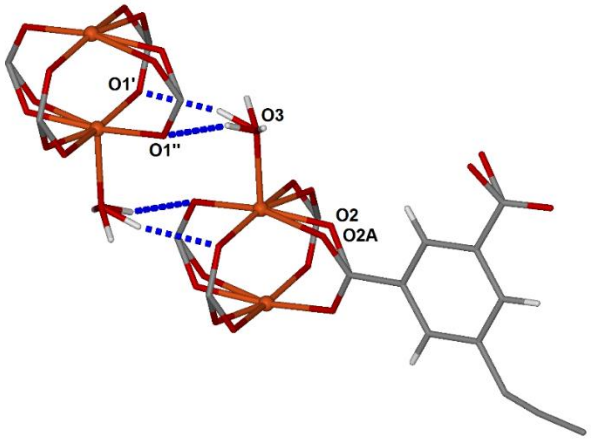

Figure 72: *Strong hydrogen bonding between the axial water groups and carboxylate oxygen atoms of the copper paddlewheel units in* **13**. *Symmetry operators: (O1') = (1 – x, 1 – y, 1 + z), (O1'') = (x, y, 1 + z).*

Spectroscopic analysis of **13** confirms the presence of the allenyl linker by the observation of a distinct C=C peak at 1944 cm^{-1}. A splitting of the carboxylate C–O band into two frequencies, 1456 and 1430 cm^{-1}, from the single frequency at 1437 cm^{-1} observed in compound **12** supports crystallographic evidence of a lengthening of select C–O bonds in **13** as a result of the disorder of the carboxylate oxygens O2 and O2A.

Residual electron density within the pores of **13** indicates there may be trace amounts of solvent trapped in the channels. To accurately evaluate the solvent type and amount within the pores, a series of crystallographic, spectroscopic and gravimetric tools were employed. First, the volume of and electron count within the calculated void spaces of **13** were determined by the crystallographic SQUEEZE tool, with the results as follows:

Void	Vol/Ang^3	#Electrons
1	242.4	32.4
2	121.6	35.1
3	121.6	30.5

The results show a total of 98 calculated electrons in the three void spaces occupying every unit cell. Taking into account that the electron count of H_2O is 10 and of MeOH is 18, it is possible from these results for either solvent to occupy this interstitial space. Details of the SQUEEZE procedure can be found in Appendix II. A sample of **13** was subsequently analysed by differential scanning calorimetry (DSC) (Figure 73) and infra-red (IR) spectroscopy to determine the type of solvent present.

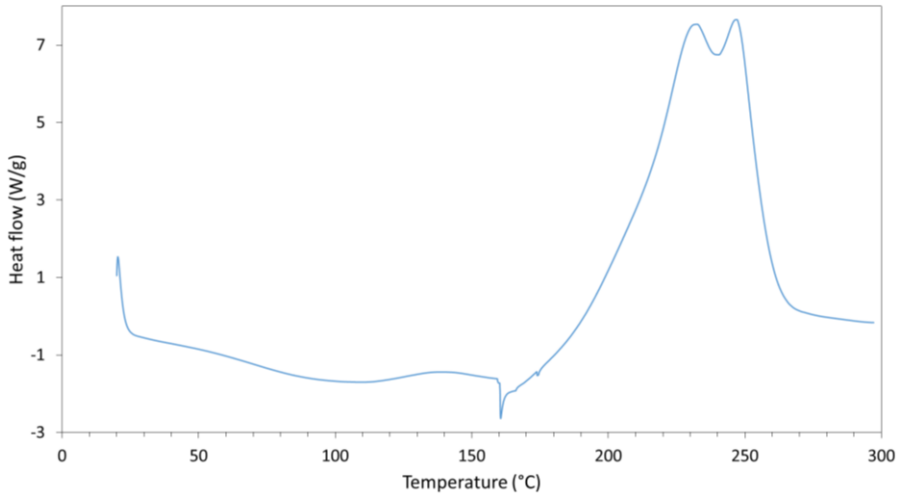

Figure 73: *DSC of a sample of* ***13****.*

DSC of **13** showed one broad endothermic event starting at 50 °C, followed by a sudden endothermic event at 160 °C, and finally a double peaked exothermic event, signifying the decomposition of the sample. The first endothermic event concentrates around 100 °C, the boiling point of water. A lack of noteworthy endothermic event around 65 °C, the boiling point of methanol, suggests the lack of methanol in the pores of the framework and presence of water only. This result was confirmed by IR analysis, in which one broad OH band was observed at 3400 cm^{-1} but no additional strong peaks corresponding to C–O–H methanol bonds were observed in the 1020 - 1200 cm^{-1} region, reaffirming the lack of methanol within the sample. The OH band at 3400 cm^{-1} thus corresponds only to hydrogen-bonded water groups. Finally, thermogravimetric (TG) analysis results show a loss of 10.14% molecular mass upon mild heating under reduced pressure (Figure 74), the loss of which equates to 0.5 H_2O per asymmetric unit.

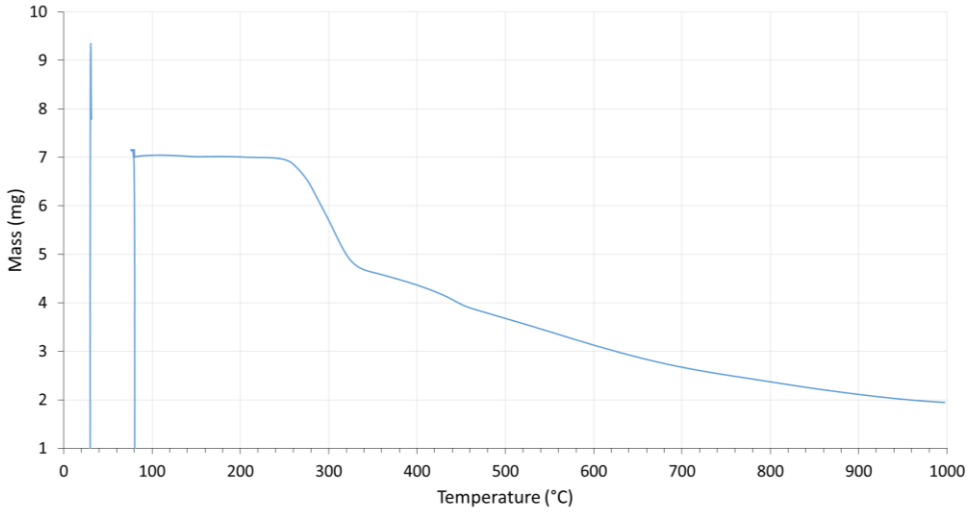

Figure 74: *TGA trace of* ***13*** *after undergoing an isothermal study at 80 °C under decreased pressure. The starting sample mass is 7.79 mg.*

Compound **13** was found to be isostructural to that of a copper Kagomé net containing another bdc derivative, 5-azido-1,3-benzenedicarboxylate, which forms a porous coordination polymer (PCP) that selectively adsorbs carbon monoxide over other small molecule gases such as N_2, in the process undergoing a CO gas-induced single-crystal to single-crystal transition.[21] Attempts to replicate this study were unsuccessful.

3.2.5. 3D CP frameworks

The same layered synthesis technique as employed in the reaction of **13** was utilised in reacting H_2ebdc with $Zn(ClO_4)_2$.

Yellow sheet crystals were obtained by a slow layer diffusion of $Zn(ClO_4)_2$ in water and H_2ebdc in methanol with NEt_3, through a buffer layer of a equimolar solution of water and methanol in a sealed vial for three days at room temperature. The asymmetric unit of the resulting coordination polymer consists of three zinc(II) atoms arrayed in a triangular cluster about a central μ^3-OH group, which are coordinated to three ebdc ligands and two aqua ligands, of which one is substitutionally disordered with a molecule of methanol. The anionic structure is charge-balanced in the lattice by a triethylammonium cation that contains one ethyl arm disordered over two positions. A methanol molecule and three molecules of water, each with partial occupancy, complete the asymmetric unit. The formula was thus determined as $[HNEt_3][Zn_3(OH)(ebdc)_3(H_2O)_{1.7}(MeOH)_{0.7}]\cdot MeOH\cdot 1.3H_2O$ (**14**).

Two of the zinc centres in **14**, Zn1 and Zn3, possess four-coordinate tetrahedral geometry, while the other, Zn2, is in a six-coordinate octahedral environment. These three zinc centres are coordinated together in a trigonal pyramidal formation bridged by one (μ^3-OH) group. The $Zn_3(OH)$ unit then dimerises through an inversion centre, fused by a bridging water molecule and a symmetry equivalent node. This makes up the central hexanuclear $[Zn_6(OH)_2(H_2O)_2]^{10+}$ aggregate, displayed in Figure 75, which acts as a 6-connected SBU when observed within the overall framework topology (Figure 76). Accounting for the twelve coordinated carboxylate groups, the overall 2- charge is balanced out by two lattice triethylammonium cations, each with disorder over one ethyl arm.

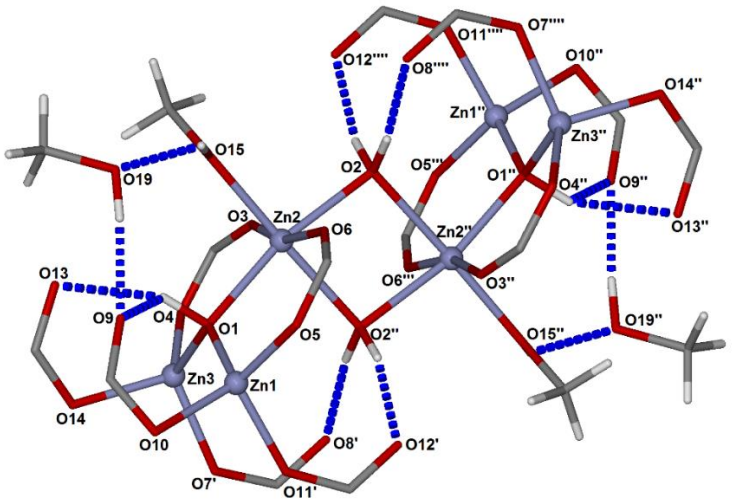

Figure 75: *Coordination environments and hydrogen bonding of central zinc clusters of framework* ***14****. Only the carboxylate nodes of the ebdc linkers have been shown as well as two interstitial methanol molecules. All other solvent molecules have been omitted for clarity. Hydrogen bonds are depicted in blue. Symmetry operators: (') = (2 – x, ½ + y, ½ – z), ('') = (2 – x, 1 – y, 1 – z), (''') = (1 – x, 1 – y, 1 – z), (''''') = (x, ½ – y, ½ + z).*

All ebdc ligands that extend from the central hexanuclear zinc cluster in **14** bridge directly to an adjacent zinc cluster. These components propagate into an extended 3D 6-connected network, two ebdc linkers extending vertically and four extending laterally from the SBUs, forming 1D channels containing solvent and counterions along the crystallographic *b* axis (Figure 76).

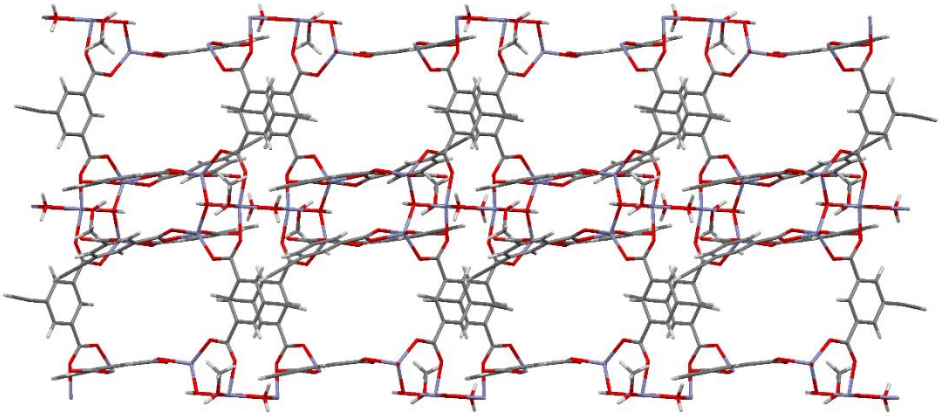

Figure 76: *A cross-section of network* ***14****, showing the lattice channels. Lattice guest molecules have been omitted for clarity.*

Strong hydrogen bonding is also observed around the central zinc cluster (Figure 75). Of the six crystallographically unique carboxylate groups coordinating to the central zinc cluster in **14**, four coordinate *via* only one oxygen to the central zinc cluster atoms, with

the other oxygen participating in hydrogen bonding from surrounding solvent molecules. Non-coordinated carboxylate oxygens O8'/O8'''' and O12'/O12'''' are hydrogen bonded to central coordinated (μ^2-H_2O) aqua ligands of which the oxygen acts as a bifurcated hydrogen donor, and the non-coordinated carboxylate oxygens O9/O9'' and O13/O13'' hydrogen bond to the coordinated (μ^3-OH) group. The remaining two carboxylate groups bridge between two zinc centres in which each oxygen coordinates to one zinc atom. Interstitial methanol groups also hydrogen bond to the central zinc cluster, acting as hydrogen bond donors to adjacent carboxylate group oxygens O9/O9'' and as hydrogen bond acceptors from coordinated methanol groups O15/O15''. Hydrogen bond geometries for these interactions are found in Table 11. Each solvent molecule present in the lattice is also involved in hydrogen bonding but due to difficulties in assigning the hydrogen positions unambiguously, only the one interstitial methanol has been included in the inter-lattice hydrogen bonding.

Interaction	*D* (Å)	*d* (Å)	*θ* (°)
O2–H2···O12''''	2.624(7)	1.75(9)	153(7)
O2–H2···O8''''	2.726(7)	1.81(6)	164(5)
O1–H1···O9	3.777(3)	2.82	177.6(2)
O1–H1···O13	2.980(8)	2.26	127.5(3)
O19–H19···O9	2.684(9)	1.86(9)	144(9)
O15–H15···O19	2.704(7)	1.77(7)	170(7)

Table 11: *Hydrogen bond interactions within the packing arrangement of* ***14****.*

The pairs of ebdc linkers that propagate structure **14** vertically (as depicted in Figure 76) are further stabilised by participating in π···π stacking. These ligands are symmetry-equivalent and partake in a parallel-offset phenyl to phenyl interaction with a centroid to centroid distance of 3.594(6) Å at a molecular plane offset of 1.226(13) Å.

There are three ebdc linkers within the 3D network of **14**. The ethynyl groups from two of these groups align in a manner suggestive of C–H···π hydrogen-bond interaction, with one acting solely as a donor from the terminal C–H ethynyl atoms and the other solely as an alkyne group π acceptor (Figure 77, left). The C20''···π distance is 3.629(6) Å, the H20''···π is 2.67 Å and the approach angle C20''–H20''···π is almost linear at 179.4(3)°, where π is a calculated centroid between the alkyl hydrogen bond acceptors C9 and C10. The remaining third ebdc linker exhibits C–H···O hydrogen bonding, in which the terminal ethynyl atom C30 acts as a hydrogen bond donor to O8 of a carboxylate group

of an adjacent ebdc group (Figure 77, right). In this case the C30···O8' distance is 3.452(7) Å, the H30···O8' distance is 2.57 Å and the approach angle 153.2(3)°.

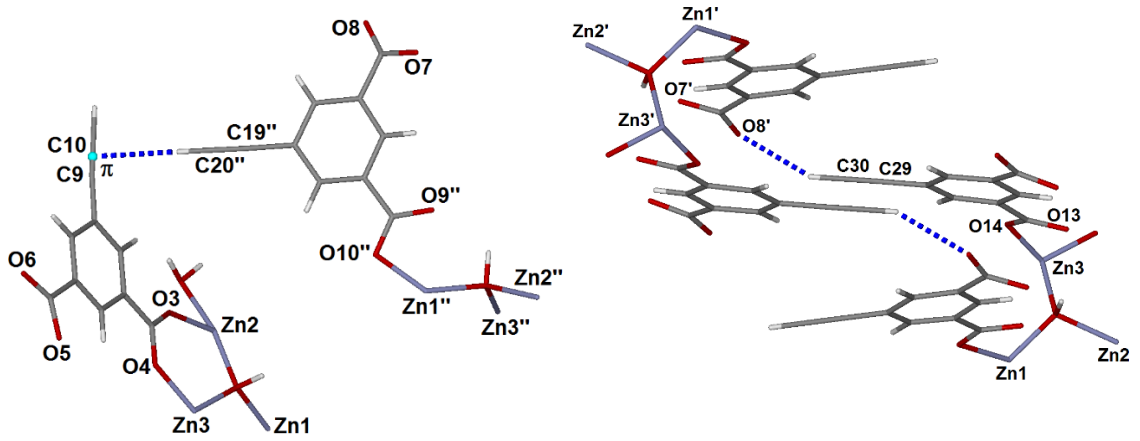

Figure 77: *Left: A weak C–H···π interaction between two ethynyl groups, oriented in a T-shaped manner within* ***14****. Right: The offset weak C–H···O hydrogen-bonding interaction between an ethynyl group and an adjacent carboxylate group within* ***14****. Symmetry operators: (') = (2 – x, 1 – y, – z), (") = (2 – x, ½ + y, ½ – z).*

Compound **14** was also analysed spectroscopically. As in the case of copper network **12**, the band intensity for the ethynyl C–H stretching vibration is both decreased and broadened; however, three unique bands were observable at 3301, 3271, and 3252 cm^{-1} that can be assigned to the three ethynyl groups. The non- hydrogen-bonding ethynyl ligand in **14** matches the frequency of the non-hydrogen-bonding reference of H_2ebdc, at 3301 cm^{-1}. The band at 3271 cm^{-1} is red-shifted by 30 cm^{-1}, which is characteristic of C–H···π bonding,[13] and also possesses the strongest intensity, which likely reflects the optimal T-shaped geometry of the interaction shown in Figure 77 (left). The final band at 3252 cm^{-1} displays a red-shift of 49 cm^{-1} and likely corresponds to the ethynyl C-H···O bond in Figure 77 (right), with its diminished intensity likely a result of poor alignment with the carboxylate.

3.3. Conclusions

5-Ethynyl-1,3-benzenedicarboxylic acid (H_2ebdc) was reacted with a series of first-row transition metal salts; Ni^{2+}, Co^{2+}, Mn^{2+}, Cu^{2+} and Zn^{2+}. Five crystalline compounds were obtained and characterised, of which **9** is a nickel-based 0D coordination complex, **10** is a cobalt-based 1D coordination polymer (CP) chain, manganese and copper- based **11** and **12** propagate *via* 2D nets and **14** is a zinc-based 3D framework. An analogue of the 2D Kagomé type topology of **12** was obtained through reaction of the allenyl equivalent of H_2ebdc, 5-allenyl-1,3-benzendicarboxylic acid (H_2abdc) and $Cu(ClO_4)_2 \cdot 6H_2O$ under the same conditions (**13**).

All five of the compounds containing ebdc display weak intermolecular hydrogen bonding derived from the ethynyl group of the ebdc linker. The weak C–H···X (X = π, O) hydrogen bond features prominently in the stabilisation of lower dimensional chains and nets, however, none of the CPs have been identified to be directly dominated by this weak hydrogen bonding through the self-assembly process. This may account for the lack of SCSC transition phenomena within these compounds, as the M–O coordination is likely too energetically favourable to overcome. First-row transition metals rely heavily on topology through coordination bond formation, as their crystal field splitting dictates the rigidity of their coordination environments. There are fewer examples of weaker long-range M–O bonds with first-row d-block metals than with p-block metals such as lead, which could impede competition from intramolecular weaker interactions.

Nickel and cobalt structures **9** and **10** both contain octahedral metal centres bridged by ebdc ligands *via* two carboxylate groups, which exhibit coordination isomerism. In **9**, the ebdc carboxylates coordinate to the metal centre in a *cis* formation, whereas in **10** the ebdc carboxylates coordinate in a *trans* geometry, leading to dimer formation in **9** and a zig-zag chain formation in **10**. Despite this, the orientation and packing of the two structures remains similar. This leads to the possibility of there being dimer and zig-zag analogues of the two structures.

Although the weak hydrogen bond cannot directly compete with first-row transition metal coordination bonding, it can influence the coordination polymer packing. This is most prominently observed in the packing differences of compounds **12** and **13**. Dimeric copper was observed to produce two-dimensional CPs from both H_2ebdc and H_2abdc. Both the ethynyl and allenyl functionalised bdc ligands formed a paddlewheel motif with

two Cu(II) centres in a Kagomé type net. The ethynyl groups within **12** take part in C-H···O hydrogen bonding bringing the ethynyl groups and copper paddlewheels together, causing the 2D nets to pack in an offset fashion. Meanwhile, the lack of ethynyl hydrogen bonding causes the nets within **13** to be stabilised by other interactions, namely O–H···O hydrogen bonding between the paddlewheel coordinated axial water groups and carboxylate oxygen atoms, causing the paddlewheel units to stack horizontally. These conditions lead to the porous allene analogue **13** and the non-porous alkyne framework **12**.

There are not many examples of systems within the literature where the same ligand serves to generate zero, one-, two- and three- dimensional architectures.[22] This series of transition metal containing H_2ebdc CPs thus is an important addition to this field.

3.4. Experimental

Caution: Metal perchlorates are potentially explosive! Only a small amount of material should be prepared and handled with great care.

Starting materials and solvents were purchased from commercial sources and were used without further purification. X-ray diffraction data for compounds **10** and **11** were collected on an Agilent Xcalibur diffractometer using Mo Kα radiation, cooled to 150 K by an Oxford Instruments nitrogen gas cryostream. Single crystal data of compounds **9**, **12**, **13** and **14** were collected on an Agilent Gemini A-Ultra diffractometer at the University of Bath using Mo Kα radiation, with the crystal being cooled to 150 K by an Agilent Cryojet. More details can be found in the Crystallography section, Appendix II. Powder X-ray diffraction patterns (PXRDs) were recorded on a Bruker AXS D8 Advance diffractometer with Cu Kα radiation of wavelength 1.5406 Å at 298 K. Samples were placed on a flat plate, and measured with a 2θ range of 3-60°.

Nuclear magnetic resonance spectra were obtained on a Bruker Avance 300 MHz Ultrashield NMR spectrometer. Infrared spectra were recorded on a PerkinElmer Spectrum 100 spectrometer equipped with an ATR sampling accessory. Elemental analyses were performed on a CE-440 elemental analyser (Exeter Analytical).

† CCDC Conquest 1.18 was used to build a query in which the distance between M, defined as Mn, Co, Ni, Cu, Zn and a carboxylate O atom was searched for. The carboxylate C atom was defined as having a sp^2 geometry. The 32,306 search results were exported into an excel spreadsheet and the minimum, maximum and mean values were calculated. A histogram of the plotted search results are displayed in Chart 1, Appendix I.

Synthesis of ligands H_2ebdc and H_2abdc can be found in the experimental section of Chapter 2. Incomplete characterisation data is present for compounds **9**, **10** and **11** due to the difficult nature of the crystallisations as well as each yielding very low quantities of crystalline material.

[{Ni(ebdc)(MeOH)$_4$}$_2$] (9) The nickel compound **9** was crystallised by slow cooling of a mixture of $Ni(OAc)_2{\cdot}4H_2O$ (26 mg, 0.11 mmol) and H_2ebdc (20 mg, 0.11 mmol) dissolved in a 4:1 MeOH/H_2O mixture (5 mL) in a sealed vial. The mixture was heated to 50 °C for 1 hour and then cooled to -5 °C over a period of 48 hours. Green block

crystals were obtained. Due to insufficient yields (only a limited number of crystals could be isolated), bulk purity of the sample through PXRD and elemental analysis could not be determined. FTIR: $\bar{\upsilon}$ = 3529 (m), 3285 (w), 2942 (m), 2831 (m), 1611 (w), 1593 (w), 1552 (s), 1421 (m), 1363 (s), 1306 (w), 1237 (w), 1138 (m), 1100 (w), 1019 (s), 943 (w), 913 (m), 769 (m), 722 (s) cm^{-1}.

[Co(ebdc)(MeOH)$_4$] (10) Pink rhombohedral crystals were obtained by the slow cooling of a mixture of $Co(OAc)_2{\cdot}4H_2O$ (26 mg, 0.11 mmol) and H_2ebdc (20 mg, 0.11 mmol) dissolved in a 4:1 MeOH/H_2O mixture (5 mL) in a sealed vial. The mixture was heated to 50 °C for 1 hour and then slowly cooled to -5 °C over a period of 48 hours. Analysis was carried out on dry samples. Due to insufficient yields (only a discreet number of crystals could be isolated), bulk purity of the sample through PXRD and elemental analysis could not be determined. FTIR: $\bar{\upsilon}$ = 3282 (brw), 1614 (m), 1542 (s), 1429 (m), 1360 (s), 1304 (w), 1237 (w), 1107 (w), 1018 (m), 913 (m), 768 (s), 718 (s) cm^{-1}.

[Mn$_3$(ebdc)$_3$(MeOH)(H$_2$O)$_3$]·3MeOH·H$_2$O (11) Colourless prismatic crystals of compound **11** crystallised by slow cooling of a mixture of $Mn(OAc)_2{\cdot}4H_2O$ (25 mg, 0.11 mmol) and 5-ethynyl-1,3-benzenedicarboxylic acid (H_2ebdc) (20 mg, 0.11 mmol) dissolved in a 4:1 MeOH/H_2O mixture (5 mL) in a sealed vial. The mixture was heated to 50 °C for 1 hour and then slowly cooled to -5 °C over 48 hours. Due to insufficient yields (only a discreet number of crystals could be isolated), bulk purity of the sample through PXRD and elemental analysis could not be determined. FTIR: $\bar{\upsilon}$ = 3296 (brs), 2948 (w), 2838 (w), 1608 (m), 1542 (s), 1430 (s), 1371 (s), 1238 (w), 1109 (m), 1014 (m), 920 (m), 801 (w), 772 (s), 727 (s), 715 (s) cm^{-1}.

[Cu$_3$(ebdc)$_3$(H$_2$O)$_{2.5}$(MeOH)$_{0.5}$]·6H$_2$O (12) Copper network **12** was prepared by layered diffusion of $Cu(ClO_4)_2{\cdot}6H_2O$ (40 mg, 0.11 mmol) in H_2O (1 mL) and H_2ebdc (20 mg, 0.11 mmol) in MeOH (1 mL) containing a drop of NEt_3 after several days. The layers were allowed to slowly diffuse over several days through a 1:1 (H_2O/MeOH) buffer layer (2 mL). Turquoise block crystals were obtained. Bulk purity was determined by PXRD. Anal. Calcd (%) for $C_{61}H_{27}Cu_6O_{41}$: C, 40.77; H, 1.51. Found: C, 40.89; H, 1.55. FTIR: $\bar{\upsilon}$ = 3274 (w), 1703 (w), 1627 (m), 1582 (m), 1437 (m), 1415 (m), 1371 (s), 1309 (w), 1239 (w), 1113 (w), 918 (w), 788 (w), 771 (s), 731 (s) cm^{-1}.

[Cu(abca)(H$_2$O)]·0.5H$_2$O (13) A precipitation reaction was carried out by the slow layer diffusion of $Cu(ClO_4)_2{\cdot}6H_2O$ (39 mg, 0.11 mmol) dissolved in H_2O (1 mL) and H_2abdc

(23 mg, 0.11 mmol) dissolved in MeOH (0.5 mL) a one drop of NEt_3 solution for several days at room temperature in a sealed vial. The layers were allowed to slowly diffuse through a 1:1 H_2O/MeOH buffer layer. Turquoise block crystals were obtained. Bulk purity was determined by PXRD. Elemental analysis could not be obtained. FTIR: $\bar{\upsilon}$ = 3400 (brm), 1944 (w), 1430 (m), 1583 (m), 1456 (m), 1430 (w), 1306 (w), 1373 (s), 1306 (m), 1257 (w), 1117 (w), 1000 (w), 921 (w), 860 (m), 848 (m), 799 (w), 778 (s), 730 (s), 689 (w), 669 (m) cm^{-1}.

$[HNEt_3][Zn_3(OH)(ebdc)_3(H_2O)_{1.7}(MeOH)_{0.7}]\cdot MeOH\cdot 1.3H_2O$ (14) Zinc compound **14** was obtained by slow layering of $Zn(ClO_4)_2\cdot 6H_2O$ (40 mg, 0.11 mmol) in H_2O and H_2ebdc (20 g, 0.11 mmol) in MeOH with trace amounts of NEt_3 for several days at room temperature in a sealed vial. The layers were allowed to slowly diffuse through a 1:1 (H_2O/MeOH) buffer layer. Yellow plate crystals were obtained. Despite repeated attempts on multiple batches of crystalline material, satisfactory PXRD and elemental analysis data could not be obtained. FTIR: $\bar{\upsilon}$ = 3270 (w), 1612 (m), 1575 (m), 1432 (m), 1403 (w), 1359 (s), 1236 (w), 1108 (w), 1008 (w), 912 (m), 771 (s), 723 (s) cm^{-1}.

3.5. References

[1] Batten, S. R.; Neville, S. M.; Turner, D. R., *Coordination Polymers: Design, Analysis and Application*, The Royal Society of Chemistry: Cambridge, **2009**.

[2] Bovill, S. M.; Dixey, R. J. C.; Saines, P. J., *CrystEngComm,* **2017**, *19*, 1831-1838.

[3] Liu, H.; Chang, L.; Bai, C.; Chen, L.; Luque, R.; Li, Y., *Angew. Chem. Int. Ed.,* **2016**, *55*, 5019-5023.

[4] Dong, X. Y.; Li, B.; Ma, B. B.; Li, S. J.; Dong, M. M.; Zhu, Y. Y.; Zang, S. Q.; Song, Y.; Hou, H. W.; Mak, T. C., *J. Am. Chem. Soc.,* **2013**, *135*, 10214-10217.

[5] Hui, J. K.; Kishida, H.; Ishiba, K.; Takemasu, K.; Morikawa, M. A.; Kimizuka, N., *Chemistry,* **2016**, *22*, 14213-14218.

[6] Zhou, Z.; He, C.; Yang, L.; Wang, Y.; Liu, T.; Duan, C., *ACS Cat.,* **2017**, *7*, 2248-2256.

[7] Wani, M. A.; Kumar, A.; Pandey, M. D.; Pandey, R., *Polyhedron,* **2017**, *126*, 142-149.

[8] Forster, P. M.; Burbank, A. R.; Livage, C.; Ferey, G.; Cheetham, A. K., *Chem. Commun.,* **2004**, 368-369.

[9] Tzeng, B.-C.; Selvam, T.; Tsai, M.-H., *J. Solid State Chem.,* **2016**, *243*, 70-76.

[10] Albalad, J.; Arinez-Soriano, J.; Vidal-Gancedo, J.; Lloveras, V.; Juanhuix, J.; Imaz, I.; Aliaga-Alcalde, N.; Maspoch, D., *Chem. Commun.,* **2016**, *52*, 13397-13400.

[11] Desiraju, G. R., *Acc. Chem. Res.,* **2002**, *35*, 565-573.

[12] Ciunik, Z.; Desiraju, G. R., *Chem. Commun.,* **2001**, 703-704.

[13] Desiraju, G. R.; Steiner, T., *The Weak Hydrogen Bond in Structural Chemistry and Biology*. Oxford University Press: Oxford, **1999**.

[14] Saha, S.; Rajput, L.; Joseph, S.; Mishra, M. K.; Ganguly, S.; Desiraju, G. R., *CrystEngComm,* **2015**, *17*, 1273-1290.

[15] Nicholls, D., *Complexes and First-Row Transition Elements*, The Macmillan Press Ltd: London and Basingstoke, **1981**.

[16] Groom, C. R.; Bruno, I. J.; Lightfoot, M. P.; Ward, S. C., *Acta Crystallogr. B. Struct. Sci. Cryst. Eng. Mater.,* **2016**, *72*, 171-179.

[17] Cramer, R. E.; Van Doorne, W.; Dubois, R., *Inorg. Chem.,* **1975**, *14*, 2462-2466.

[18] Desiraju, G. R., *Cryst. Growth Des.,* **2011**, *11*, 896-898.

[19] Burrows, A. D.; Frost, C. G.; Mahon, M. F.; Winsper, M.; Richardson, C.; Attfield, J. P.; Rodgers, J. A., *Dalton Trans.,* **2008**, 6788-6795.

[20] Lutz, B. T. G.; Jacob, J.; van der Maas, J. H., *Vib. Spec.,* **1996**, *12*, 197-206.

[21] Sato, H.; Kosaka, W.; Matsuda, R.; Hori, A.; Hijikata, Y.; Belosludov, R. V.; Sakaki, S.; Takata, M.; Kitagawa, S., *Science,* **2014**, *343*, 167-170.

[22] Thirumurugan, A.; Rao, C. N. R., *J. Mater. Chem.,* **2005**, *15*, 3852-3858.

Chapter 4

Exploring structure-property relationships within a series of silver 4-(phenylethynyl)pyridine complexes

4.1. Introduction

An improved understanding of structure-property relationships is fundamental to getting closer to the concept of 'crystal design'. Crystal engineering is a useful strategy to this end, whereby the prediction of molecular self-assembly at the individual interaction level is used to guide synthetic efforts towards a target architecture and properties.[1] Through the understanding of simple systems and a consequential methodical up-scaling thereof, a bottom up approach can be utilised to build more complicated, multi-component systems. The main obstacle to this strategy is predicting which of the competing molecular interactions will dominate within the assembly of the crystal structure, in particular one containing complex mixtures of Lewis acids and bases. Only by learning from relevant model systems can our current levels of understanding be improved.

A series of silver(I) complexes has been chosen to focus on using this approach, and will be described within this chapter. Silver coordination polymers are receiving considerable attention because of their anti-antimicrobial,[2,3] anti-tumour[4] and luminescent[5] properties. Due to its flexible d^{10} coordination sphere,[6] the Ag(I) ion exhibits abundant coordination geometries, varying from linear to trigonal, tetragonal, square pyramidal and octahedral. These geometries reflect a variable coordination number of 2 to 7.[7] The flexibility of the Ag(I) coordination sphere affords a good opportunity to study the mechanism of the self-assembly process, since Ag–ligand interactions are labile and even a slight change of reaction conditions may drastically alter the resulting structure topology.[8] These conditions include variation of functional groups,[9] counterions[10-12] and solvent.[13]

With the understanding that coordination bonds to silver(I) centres compete with weaker intramolecular interactions, the potential for metastability within these compounds can be explored. By manipulating which interactions dominate the self-assembly of the crystal structure through the interplay of steric and electrostatic factors, a higher energy structural arrangement can potentially be stabilised thus offering the potential for switchability.

To date, a large number of silver(I) coordination polymers with diverse dimensionalities (1D, 2D and 3D) have been constructed,[8] featuring mostly multi-dentate ligands. Monodentate ligand models have been far less studied as a building block for the synthesis of silver coordination polymers. The structural flexibility that a monodentate ligand offers enables weak intermolecular interactions to play a stronger role in the coordination polymer self-assembly process. 4-(Phenylethynyl)pyridine (pep) (Figure 78) was chosen as a linear, non-sterically hindering monodentate ligand with an ethynyl spacer and a terminal phenyl ring, each of which can readily promote π- oriented interactions.

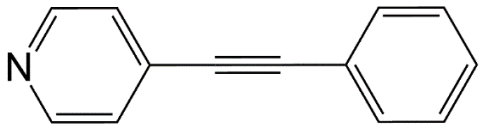

Figure 78: *4-(phenylethynyl)pyridine (pep) ligand.*

Through the inclusion of aromatic rings at the terminal positions of the alkyne group, intramolecular π···π stacking interactions can be targeted, namely T-shaped and parallel displaced interactions, as described in Chapter 1. For the purposes of this chapter, the single atomic hydrogen donor to the multi-atomic hydrogen acceptor bond distances and angles will be measured in relation to a calculated centroid within the phenyl ring, π (Figure 79). Analyses of the hydrogen bond angle *vs* the hydrogen bond distance[14] indicates that the centroid may be reasonably approximated as the acceptor site in these interactions.

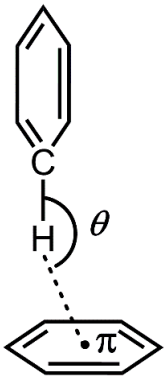

Figure 79: *Definition of geometrical T-shaped C–H···π hydrogen bond parameters, where π is the calculated C_6 centroid.*

A CSD database study on the nature of T-shaped phenyl-phenyl interactions was conducted through ConQuest,[15] the results from which average C–H···π interaction geometries in the crystalline state were calculated (Table 12), where *D* is the donor-acceptor distance, *d* is the hydrogen-acceptor distance and *θ* is the approach angle. Details of the study can be found in Section 4.4. of this chapter.†

Interaction	C–H···π
No. of entries	1379
D (Å)	3.75
d (Å)	2.94
θ (°)	145.9

Table 12: *Mean geometries of C–H···π hydrogen bonds in crystal structures from a CSD study.*

To determine the correct topology of the CP in question, a definition of coordination bond lengths is important. The length of an Ag···Ag interaction varies from 2.76 to 3.17 Å based on a study by Pyykko et al.[16] The limit of a covalent Ag–X interaction, where (X = N, O), is defined here as 2.54 Å based on a study by Nilsson's group.[17] The Ag–S bond contains considerably more ionic than covalent character[18] and hence exhibits much longer bond lengths, ranging from 3.01 Å to 3.40 Å according to computational studies,[18,19] in which the lower distance is identified as the limit of covalent bonding. Interactions beyond covalent-bonding distances but within the sum of the van der Waals radii of the metal and coordinating atom are termed outer-sphere or long-range coordination bonds. Recommended crystallographic van der Waals radii in this case are Ag···Ag: 4.2 Å, Ag···O: 3.65 Å, Ag···N: 3.7 Å and Ag···F: 3.6 Å.[20]

The lability of Ag-ligand interactions (the Ag–N bond is approximately equivalent in strength to a strong hydrogen bond; 47.0(5) kJ mol^{-1}),[21] ensures that weak interactions such as the aforementioned π···π interactions, Ag···Ag interactions and C–H···X (X = O, N, π) interactions play a prominent role in solid-state self-assembly. Given the neutral nature of the pep ligand, the silver(I) cation component necessitates the inclusion of a counterion as a charge-balance, which can exert a significant influence on the assembly and topology of the resulting crystal structure.[22,23] With continuity provided by the silver and pep components, variation of the silver counterion provides a way of affecting these weak non-coordination interactions to control the solid-state packing. In doing so, the variation of the anion allows the solid-state interaction hierarchy to be explored.

Various Ag(I) salts and pep were crystallised together in a 1:2 molar ratio from either acetonitrile or methanol solution. Nine different counterions were investigated: PF_6^-, BF_4^-, NO_2^-, NO_3^-, $MeCO_2^-$, $CF_3CO_2^-$, $MeSO_3^-$, Tos^- and SCN^- to provide trends to probe correlations between structure/property relationships. X-ray data for all crystalline samples are given in Appendix II.

4.2. Results

Twelve crystal structures containing 4-(phenylethynyl)pyridine (pep) and a series of silver(I) salts were obtained exhibiting different topologies and packing in the solid state as a result of the crystallisation conditions. Two of the twelve structures are derived from single-crystal to single-crystal (SCSC) transitions from other structures reported herein. The compounds synthesised are labelled **15** – **26**.

4.2.1. 4-(phenylethynyl)pyridine

4-(Phenylethynyl)pyridine (pep) was obtained by a one-step Sonogashira coupling reaction (Scheme 6) under reflux, then purified by column chromatography.

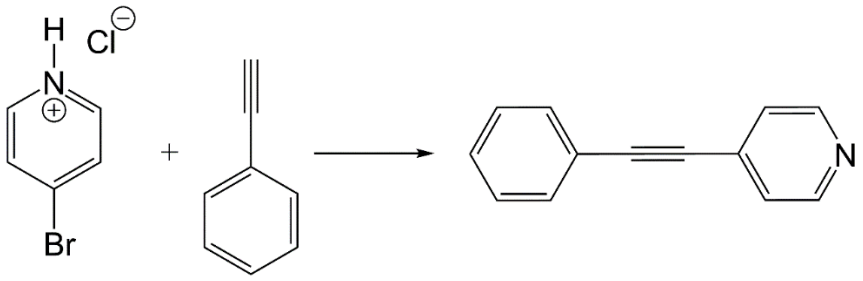

Scheme 6: *One-step reaction for the synthesis of pep; $Pd(PPh_3)_2Cl_2$, CuI, NEt_3 under reflux at 80 °C for 4 days.*

The resulting molecule is a linear monodentate ligand consisting of pyridine and phenyl rings bridged by an ethynyl group. An IR spectroscopic analysis shows a prominent peak at 2222 cm^{-1} which corresponds to the C≡C ethynyl group, as well as a peak at 1606 cm^{-1} corresponding to the pyridyl group. An X-ray crystal structure of pep was also obtained from which the solid-state packing of the uncoordinated ligand was observed.

Single crystals of pep suitable for X-ray data collection were obtained by slow evaporation from methanol, and crystallise in the $P\,2_12_12_1$ space group in the form of a herringbone motif when viewed down the crystallographic *b* axis. Weak C-H···N hydrogen bonds connect the herringbone motifs as seen in Figure 80 (left); ortho- pyridyl carbon atoms and para- phenyl C–H bonds donate hydrogen bonds to one nitrogen pyridine acceptor. Atom distances *D* and *d* as well as approach angles are listed in Table 13 below. Aromatic C–H···π hydrogen bonding was also observed in the solid-state pep structure, consistent with a herringbone arrangement of pep molecules (Figure 80, right), no π···π interactions were observed. Four unique C–H···π interactions were observed per pep

molecule with an average distance D of 3.55 Å and average approach angle of 132.03°; these values correspond well to the known mean geometries (D = 3.69 Å, θ = 142°, Table 13) of aromatic hydrogen bonds within the crystalline state. The molecular plane to plane angle θ, as highlighted in yellow in Figure 80 (right), is 59.5°. This type of herringbone feature is well known in the packing of aromatic molecules[24,25] and is a consequence of the optimisation of C–H···π interactions. The presence of this herringbone arrangement of pep molecules in any subsequent crystal structures containing this ligand can give insight into the preferred interaction of the crystallisation components.

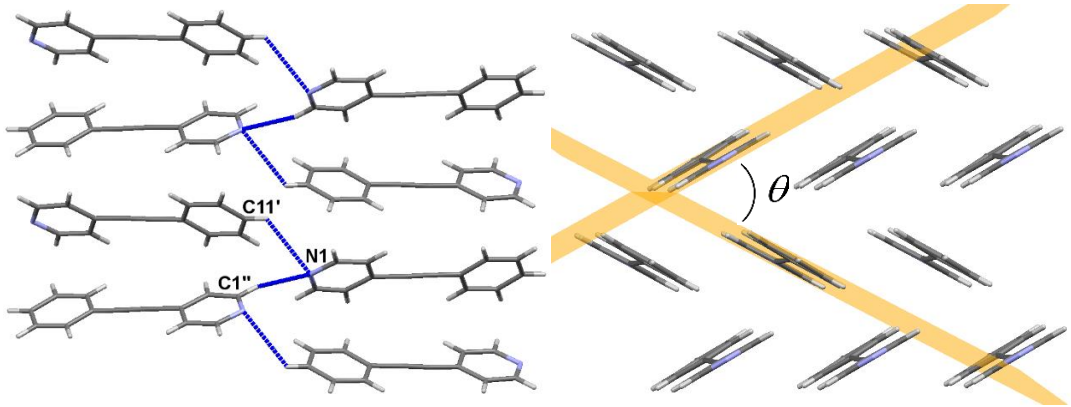

Figure 80: *Left: Hydrogen bonding between sheets of pep molecules, as viewed down the crystallographic* a *axis. Symmetry operators: (') = (½ + x, 3/2 – y, – z), ('') = (3/2 – x, 1 – y, – ½ + z). Right: Herringbone arrangement of the pep molecules, in which two intersecting molecular planes are highlighted in orange; θ = 59.5°.*

Interaction	D (Å)	d (Å)	θ (°)
C1''–H1···N1	3.548(4)	2.61	167.36(18)
C11'–H11···N1	3.520(4)	2.94	120.01(19)
C5–H5···π'''	3.601(3)	2.89	132.55(17)
C13–H13···π'''	3.513(3)	2.81	131.90(16)
C10–H10···π''''	3.555(3)	2.87	130.26(17)
C2–H2···π''''	3.522(3)	2.81	132.88(17)

Table 13: *Hydrogen interactions between pep ligands in the solid state. Symmetry operators: (''') = (2 – x, – ½ + y, ½ – z), ('''') = (1 – x, ½ + y, ½ – z).*

The C–H···π hydrogen bond distances in crystalline pep are up to 0.2 Å lower on average to the values found in the CSD study. This difference is likely due to the included pyridine functionality, which would influence the hydrogen bonding.

4.2.2. Compounds containing non-coordinating AgX salts

To investigate the solid-state assembly of the Ag(I) and pep components in the presence of non-coordinative anions, the salts silver hexafluorophosphate and silver tetrafluoroborate were used. These two anions are generally assumed to be non-coordinating, thus enable the study of primary interactions between the Ag(I) metal and pep ligands.

Slow evaporation of a mixture of two equivalents of pep and one equivalent $AgPF_6$ from acetonitrile yields $[Ag(pep)_2][PF_6]\cdot MeCN$ (**15**), crystallising in the $P\bar{1}$ space group. The asymmetric unit contains two linear $[Ag(pep)_2]^+$ complexes which are orthogonally spaced with respect to each other. Each complex interacts with an acetonitrile group through outer-sphere coordination bonding as well as a loosely associated $[PF_6]^-$ counter-ion. Both Ag(I) centres support two coordination bonds to the pyridine groups of the pep ligands within the range 2.132(7) - 2.165(7) Å, in almost linear coordination environments (N–Ag–N angles of 177.4(3)° for Ag1 and 178.4(3)° for Ag2), as well as one long-range coordination bond to an acetonitrile molecule at an Ag–N distance of 2.80(1) Å for Ag1 and 2.821(10) Å for Ag2 (Figure 81). The Ag–N–C angle adopted by acetonitrile coordinating to silver varies between the two complexes by 5°. Similarly, the closest Ag···F contact distances between the metal centre and PF_6^- counterion are unique for each complex, varying by ~ 0.1 Å. Cumulatively these variations break the symmetry between the two complexes, rendering them crystallographically inequivalent. Overall, each silver centre in **15** supports two inner- and one outer- sphere coordination bonds, with two additional van der Waals Ag···F interactions that are beyond the covalent coordination radii of both atoms but within the sum of the van der Waals radii. A full list of coordination bond distances and significant interactions of **15** can be found in Table 41 in Appendix II.

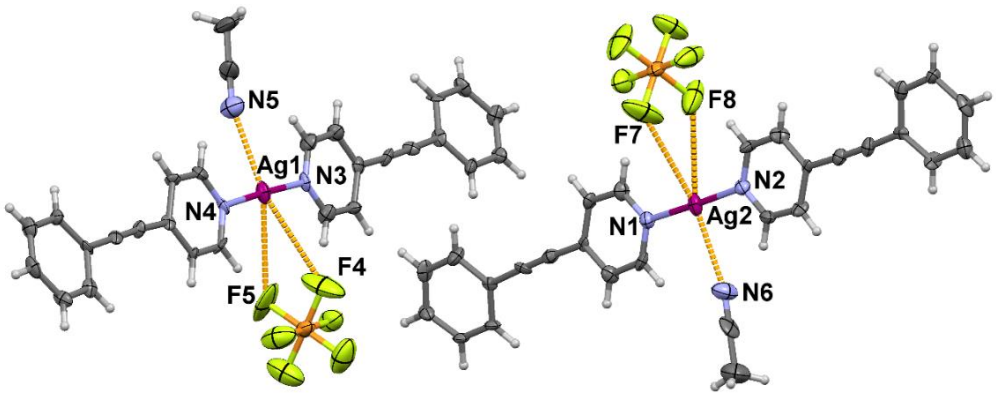

Figure 81: *The asymmetric unit of* **15** *with long-range coordination contacts shown in gold. Ellipsoids are at 50% probability.*

Individual $[Ag(pep)_2]^+$ units of structure **15** pack together in layers that resemble a herringbone arrangement, held together by π···π and Ag···π interactions, which propagate infinitely along the crystallographic *a* axis (Figure 82). The average separation distance between stacked $[Ag(pep)_2]^+$ units is 3.27 Å. Acetonitrile and hexafluorophosphate groups reside between the herringbone sheets, in open channels running also along the crystallographic *a* axis. Although C–H···F hydrogen bonding between pep aromatic hydrogen atoms and PF_6^- anions (average C···F distance of 3.55 Å) was observed to stabilise the herringbone sheets, no other strong intermolecular interactions were observed in **15**, suggesting the π···π stacking of the $[Ag(pep)_2]^+$ unit represents the dominant packing interaction.

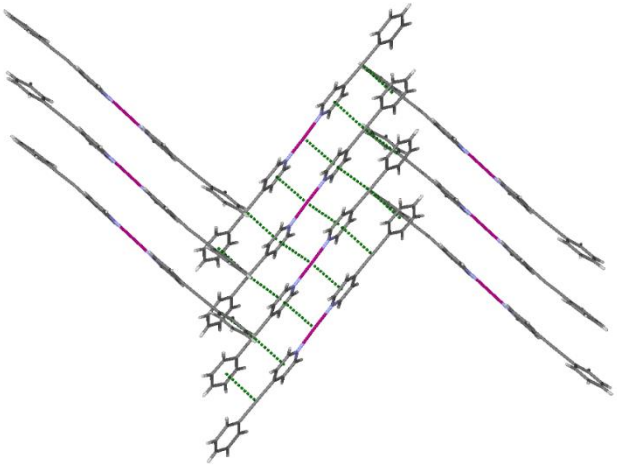

Figure 82: *Herringbone packing arrangement of* **15** *viewed down the crystallographic* b *axis with* π···π *and Ag*···π *interactions shown.*

An isostructural packing arrangement was found when the $AgPF_6$ and pep components were reacted in methanol solvent giving $[Ag(pep)_2][PF_6]$·MeOH, with methanol

molecules coordinating to the Ag(I) centre *via* the oxygen atom. However, single crystal X-ray data collected from this structure could not be fully refined due to substantial twinning of the crystals.

The open channels of **15** in which the volatile solvent molecules sit, is likely the cause of spontaneous solvent loss and the consequent single-crystal to single-crystal (SCSC) rearrangement observed when crystals of **15** were removed from the acetonitrile medium. A rapid loss of the acetonitrile solvent facilitates the transition of **15** into a fully desolvated structure $[Ag(pep)_2][PF_6]$ (**16**). Monitoring of the SCSC transformation from **15** to **16** was not possible quantitatively, as the transformation was too rapid. Crystals of a quality good enough for single crystal X-ray diffraction were eventually obtained by suspending single crystals of **15** in water for 14 days. The diffusion of the acetonitrile from the pores of the crystals was slow enough for crystallinity to be retained.

Crystallographic study of this SCSC transformation reveals the $[Ag(pep)_2]^+$ units of **15** bending and twisting to accommodate the formation of voids within the structure as a result of removal of the acetonitrile (Figure 83). The coordination number of Ag(I) decreases by one whilst the whole $[Ag(pep)_2]^+$ unit bends up to 24°, as measured from calculated centroids in the terminal phenyl groups *via* the silver centre. One of the two pep ligands within the unit also undergoes a rotation along the alkyne group, in which the resulting torsion twist is 54.8°. Additionally, during the transformation the PF_6^- counterion rotates to accommodate the wider steric space created by the bending of the $[Ag(pep)_2]^+$ unit to take part in three long range Ag···F interactions as opposed to two interactions in structure **15**. The resulting N–Ag–N angle in **16** equals 165.77(10)°, compared to the almost linear $[Ag(pep)_2]^+$ units in **15**. Two of the six fluorine atoms within the PF_6^- counterion in **16** are disordered over two positions, likely due to the loss of C–H···F hydrogen bonds between the pep aromatic hydrogens and PF_6^- anion.

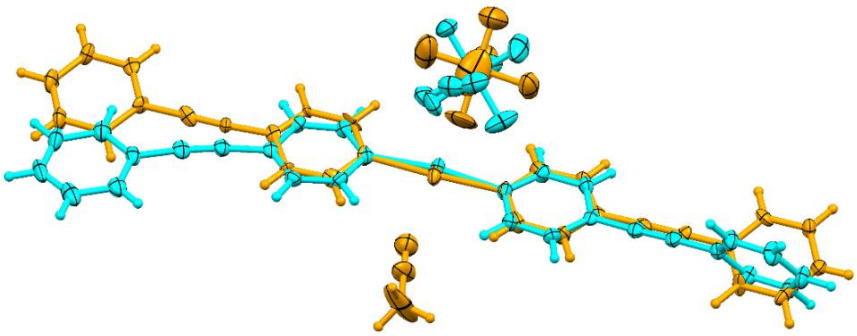

Figure 83: *An overlay showing the change in $[Ag(pep)_2]^+$ unit of* ***15*** *(orange) to* ***16*** *(blue), noting the lack of acetonitrile and significant distortion of the pep ligands in* ***16****. Ellipsoids are at 50% probability.*

The transformation from **15** to **16** also causes the $[Ag(pep)_2]^+$ units to shift laterally, disrupting Ag···π and phenyl–alkyne interactions and forming dimers held together by two phenyl stacking interactions and one Ag···Ag interaction (Figure 84).

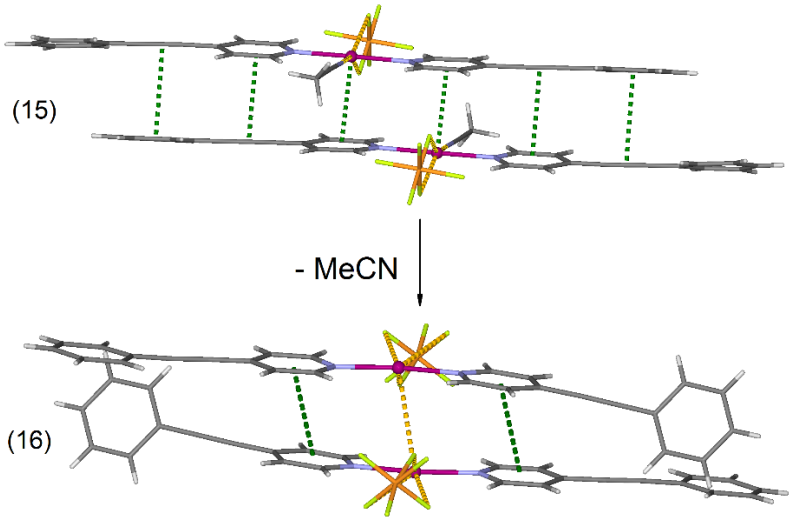

Figure 84: *Comparison of the $[Ag(pep)_2]^+$ alignment in structures* ***15*** *and* ***16****. The slip resulting from the SCSC reduces the Ag···Ag distance from 4.7852(15) Å in* ***15*** *to 3.6108(6) Å in* ***16****.*

Substitution of the hexafluorophosphate for tetrafluoroborate salt yields a similarly packed compound to **16** with an overall molecular formula of $[Ag(pep)_2][BF_4]$ (**17**) (Figure 85). Colourless crystals of **17** were obtained from the slow evaporative crystallisation of one molar equivalent of $AgBF_4$ and two molar equivalents of pep from either methanol or acetonitrile. The asymmetric unit contains a single $[Ag(pep)_2]^+$ unit loosely coordinated to a $[BF_4]^-$ counterion. Similarly to **16**, structure **17** packs in the $P\,\bar{1}$ space group. The isostructural nature of **16** and **17** is not unexpected; PF_6^- and BF_4^- counterions have very similar properties in terms of sterics and interaction behaviour,

and have been reported to direct the self-assembly of compounds in an identical manner.[26,27]

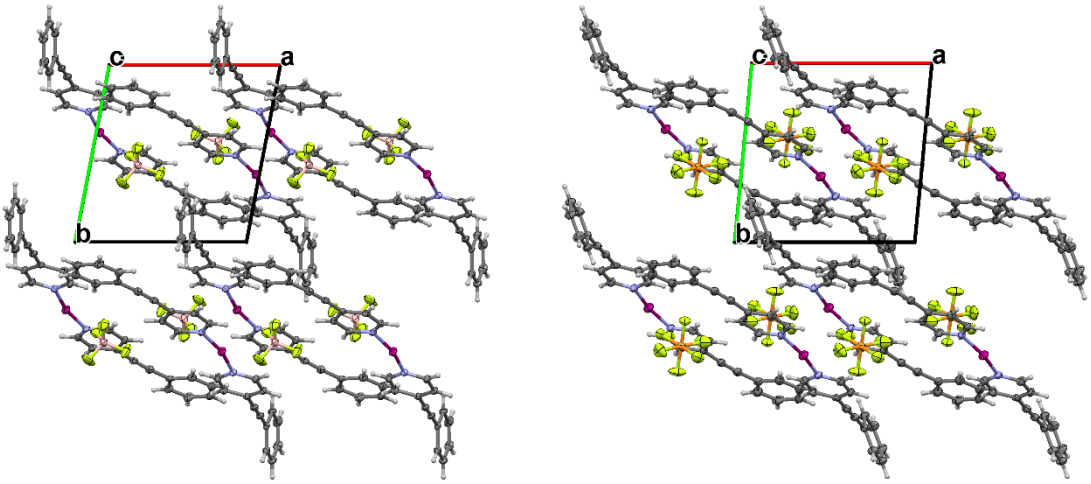

Figure 85: *Comparison between isostructural compounds* **17** *(left) and* **16** *(right) as viewed down the crystallographic* c *axis. Ellipsoids are at 50% probability.*

This similarity between **16** and **17** indicates that tetrafluoroborate could also have a solvated structure analogous to **15**, however attempts at growing these crystals were unsuccessful.

4.2.3. Compounds containing AgNOx salts

Two NOx anions, nitrite and nitrate, were used as counterions within the AgX salt to explore how promoting relatively unrestricted anion-derived bridging modes influences the solid-state packing.

Colourless crystals $[Ag(pep)_2][Ag(NO_2)_2]$ (**18**) were obtained from slow evaporation of a mixture of pep and $AgNO_2$ in methanol. The asymmetric unit contains one $[Ag(pep)_2]^+$ complex and two additional crystallographically unique silver metal atoms, one equally disordered over two positions, each ligated by two full occupancy nitrite anions, where each nitrite anion chelates *via* both oxygen atoms to their respective silver atoms. The Ag1 silver centre within the $[Ag(pep)_2]^+$ unit supports six coordination bonds in total, hence displaying a distorted octahedral coordination geometry. The coordination environment of Ag1 contains two inner coordination bonds at 2.217(4) Å and 2.214(4) Å that are the Ag-N bonds and the rest outer-sphere coordination bonds with Ag–O distances ranging from 2.740(5) to 2.904(4) Å. The silver atoms Ag2 and Ag3 only

coordinate to oxygen atoms of surrounding nitrite anions, resulting in a distorted octahedral geometry for Ag2 and a distorted square-based pyramidal geometry for Ag3 (Figure 86). A full list of coordination bond lengths are located in Table 44, Appendix II.

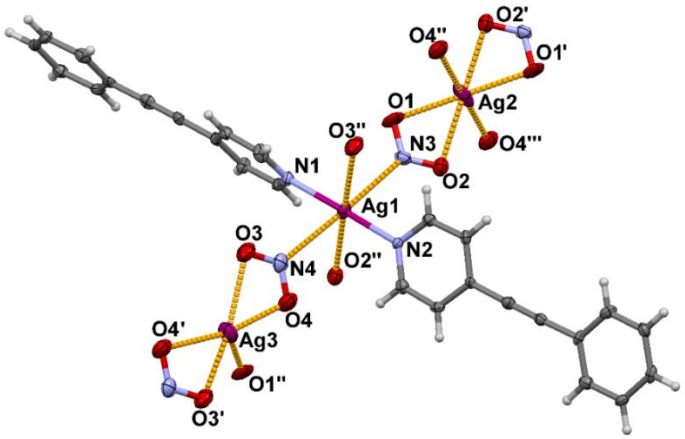

Figure 86: *The asymmetric unit of* ***18****, including coordination geometries of the three silver centers Ag1, Ag2 and Ag3. Symmetry operators: O1', O2' = (– x, – y, 1 – z), O3', O4' = (2 – x, 1 – y, 1 – z), O1'' = (1 + x, y, z), O2'', O4''' = (1 – x, – y, 1 – z), O3'' = (1 – x, 1 – y, 1 – z), O4'' = (– 1 + x, y, z). Ellipsoids are at 50% probability.*

The $[Ag(pep)_2]^+$ unit is interesting in that the two pep ligands within the complex do not have planar alignment, exhibiting a ligand to ligand torsion angle of 55.61(3)°. Each nitrite anion coordinates to four silver(I) centres along the crystallographic *b* axis of the crystal structure. This creates a 2D sheet based on weak silver-nitrite interactions (Figure 87, left). Orthogonal to this sheet motif are the pep ligands, which are arrayed in continuous rows aligned with the silver-nitrile sheet and ligate every alternating silver atom (Figure 87, right). This spacing of the ligands allows the CP layers to interdigitate, aligning the hydrophobic aromatic regions.

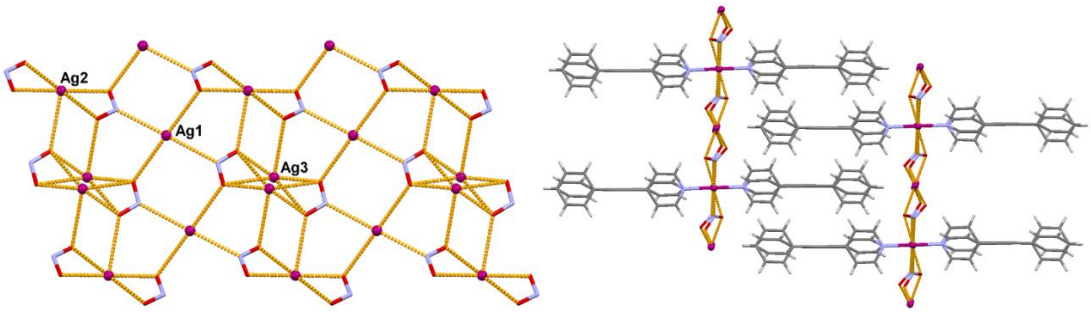

Figure 87: *Left: The 2D network of Ag-NO_2 interactions, where Ag1 is ligated to pep ligands out of plane and Ag2 and Ag3 only coordinate with O atoms of the surrounding nitrite anions. Right: Interdigitated nets of* **18** *as viewed down the crystallographic* b *axis.*

Between the inorganic silver-nitrite layers the pep ligands pack together in a herringbone fashion similar to that of the pure pep structure, suggesting that cumulative aromatic hydrogen interactions in the hydrophobic region drive the crystal packing. Each pep ligand interacts through four unique (eight in total) C–H···π bonds to adjacent pep ligands, interacting intra- as well as inter-molecularly. Due to the diagonal configuration of the pep ligands, only the T-shaped aromatic interaction type is present. The molecular plane to plane angle is 55.6°, which is the same as the torsion angle of the two pep ligands within the cationic unit. The herringbone motif is further discussed in Section 4.3. The hydrogen bond geometries within structure **18** are presented in Table 14 below.

Hydrogen bond	*D* (Å)	*d* (Å)	*θ* (°)
C2–H2···π'	3.494(5)	2.84	128.3(3)
C10–H10···π'	3.482(5)	2.83	127.5(3)
C15''–H15···π	3.555(6)	2.83	134.8(3)
C23''–H23···π	3.536(6)	2.87	128.7(3)

Table 14: *Aromatic C–H···π hydrogen bond geometries between pep ligands of* **18**. *Symmetry operators: (') = (1 – x, 1 – y, 1 – z), ('') = (x, y, 1 + z).*

The aromatic hydrogen bond angles C–H···π in **18** range from 127° to 135°, and all hydrogen bond distances lie within the range of C–H···π hydrogen bond geometries collected in the CSD study noted earlier. Additionally, the pep interaction geometries are similar to those in pure pep. (Average geometries of pep: D = 3.55 Å, d = 2.85 Å, θ = 131.9°, average geometries of **18**: D = 3.52 Å, d = 2.84 Å, θ =129.8°).

This herringbone pattern formed within the hydrophobic pep layers was not found in structures **15** to **17**, suggesting that interactions between the anions and metal centres is a directing influence in the self-assembly mechanism.

A similar inorganic 2D network topology was observed when silver(I) nitrate and pep were crystallised under the same conditions. Colourless crystals of $[Ag(pep)_2][Ag(NO_3)_2]$ (**19**) were obtained from slow evaporative crystallisation of $AgNO_3$ and pep in methanol. The asymmetric unit of **19** contains two Ag(I) centres, one within a $[Ag(pep)_2]^+$ complex and the other coordinated to two nitrate counterions. The two Ag atoms interact *via* an Ag···Ag interaction with a distance of 2.9704(6) Å which is within the range of known silver-silver interaction lengths (2.76 to 3.17 Å).[17] The $[Ag(pep)_2]^+$ unit is distorted, particularly the angle made by the coordination of one pep group which deviates from the ideal coordination angle of 180° by more than 17° measured from the pyridyl centroid to the silver *via* the coordinating nitrogen atom. This distortion may be due to steric congestion, owing to the adjacent pep ligands and coordination environment of the silver centre (Figure 88).

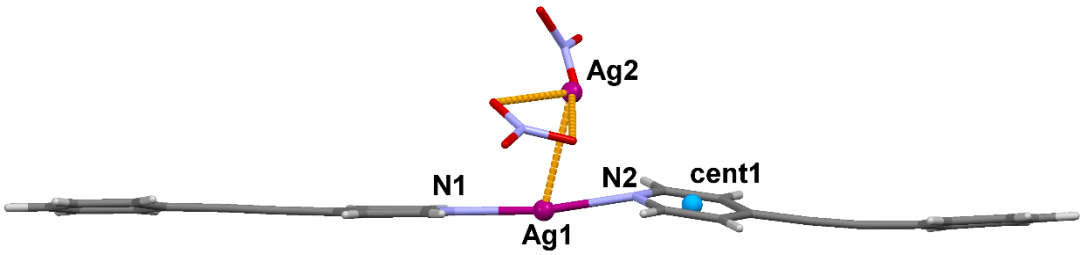

Figure 88: *The kinked ligand coordination within the asymmetric unit of* ***19****, where the bend angle is measured from cent1 to Ag1 through N2.*

In addition to the two pep ligands and the adjacent silver centre, Ag1 also interacts with two nitrate anions, with the Ag···O distances ranging from 2.603(4) Å to 3.132(5) Å. The second silver centre Ag2 is coordinated to three bidentate nitrate anions as well as supporting an Ag···Ag interaction to Ag1. The range of these Ag-O distances is 2.310(5) – 3.005(5) Å. In total, each of Ag1 and Ag2 supports six coordination bonds each, in which five are inner- coordination sphere bonds, as well as one metal-metal bond. The silver-nitrate interactions of **19** form the basis of an inorganic 2D network analogous to that in **18** (Figure 89), in which the 2D net propagates along the crystallographic [001] plane. The pep ligands coordinate orthogonally to the net and interdigitate with adjacent ligands, as shown in Figure 89. In this nitrate structure however, one of the two NO_3^-

counterions sits in a perpendicular plane to the inorganic 2D net, bridging two non pep-coordinating Ag2 centres.

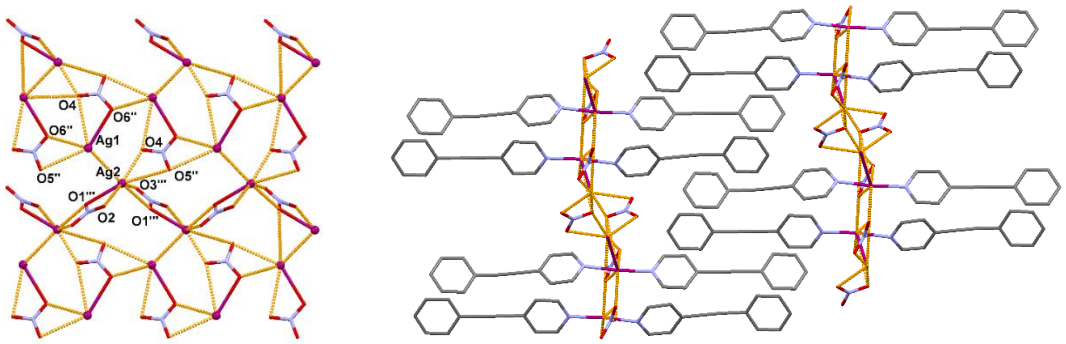

Figure 89: *Left: The 2D network formed by coordination bonding in* **19**, *comprised of* Ag^+ *and* NO_3^-. *Pep ligands has been omitted for clarity. Right: Arrayed pillars of pep ligands, as viewed down the approximate crystallographic* b *axis. Hydrogen atoms have been excluded for clarity.*

There is no significant difference in the topologies of **18** and **19**, indicating that the change in anion from NO_2^- to NO_3^- does not affect the assembly of the structure, instead suggesting that aromatic hydrogen bonding from the interdigitation of the pep ligands is a prominent interaction between the components present. Interdigitation of the 2D layered structure of **19** dominates the crystal packing between layers.

Similar to **18**, compound **19** adopts a herringbone motif between the interdigitated pep ligands within the hydrophobic region. Weak T-shaped C–H···π hydrogen bonding is present surrounding the pep ligands, so that three unique interactions around each are observed, in which the molecular plane angles between the pep ligands intersect at angles of 66.5°, 72° and 61°. The C–H···π hydrogen bond geometries are presented in Table 15. Figure 89 (right) shows the pep ligands interacting in clusters of four vertically positioned layers when viewed down the crystallographic b axis; at every fourth pep ligand the vertical C–H···π bonding is disrupted. This is due to the aforementioned out of plane NO_3^- anion which sterically inhibits the pep ligands from fully interdigitating.

Hydrogen bond	*D* (Å)	*d* (Å)	*θ* (°)
C1–H1···π'	3.885(5)	3.18	134.1(3)
C9–H9···π'	3.506(9)	2.87	126.1(3)
C4–H4···π''	3.438(5)	2.74	131.6(3)
C12–H12···π''	3.618(6)	3.01	123.9(4)
C15'''–H15···π	3.568(6)	2.78	142.4(3)
C23'''–H23···π	3.611(6)	2.95	129.1(4)

Table 15: *Aromatic hydrogen bond geometries between pep ligands of* **19**. *Symmetry operators: (') = (1 – x, – ½ + y, – z), ('') = (1 – x, ½ + y, 1 – z), (''') = (1 – x, ½ + y, – z).*

A difference in topology was observed upon the crystallisation of the $AgNO_3$ and pep components from acetonitrile. Whereas the methanol solvated structures **18** and **19** formed interdigitated 2D nets, acetonitrile solvated structure **20** is formed of one-dimensional chains with a significant inclusion of water molecules within the framework. Compound **20** was isolated from the mother liquor as colourless crystals and contains an overall molecular formula of $[Ag(pep)_2][NO_3]\cdot 2H_2O$ (**20**). Bulk purity of **19** and **20** were measured using powder X-ray diffraction (PXRD) (Figure 90), which confirmed that both compounds crystallised in a single phase. This suggests that compounds **19** and **20** could be preferentially synthesised by a change in solvent.

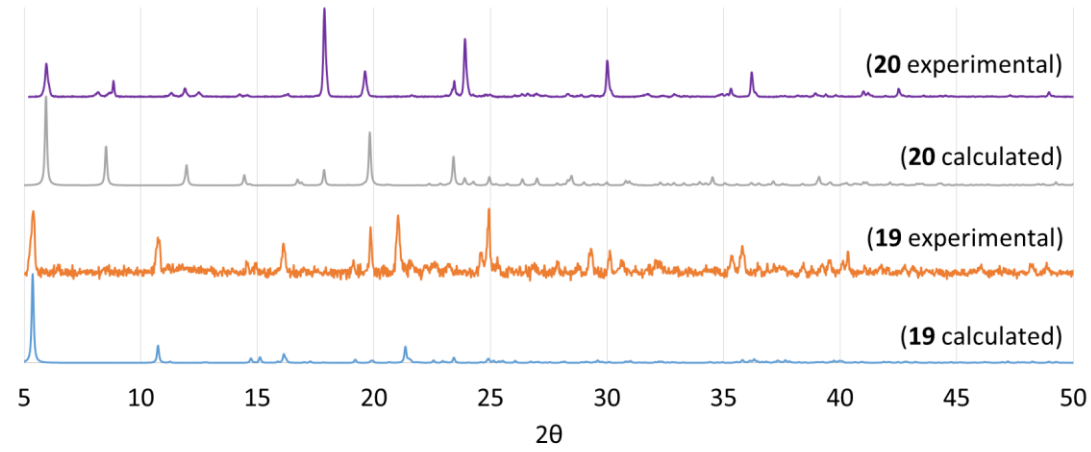

Figure 90: *PXRD patterns of* **19** *and* **20** *each showing monophasic crystals for evaporation from methanol and acetonitrile respectively. Contamination of $AgNO_3$ salt is suspected in the experimental pattern of* **20** *due to additional peaks at 24, 30 and 36 2θ.*

The asymmetric unit of the hydrated structure **20** contains a single $[Ag(pep)_2]^+$ complex with a nitrate counterion and two water molecules. The Ag(I) centre formally has a linear coordination environment supporting two covalent bonds with pep, but four

outer-sphere coordination bonds derived from three nitrate anions give a total coordination number of six (Figure 91). The two inner-sphere coordination bonds Ag1–N1 and Ag1–N2 have bond lengths of 2.181(3) Å and 2.193(4) Å respectively, and the weaker interactions range from 2.638(4) to 3.421(4) Å. The Ag(I) coordination bond distances for **20** can be found in Table 46 in Appendix II.

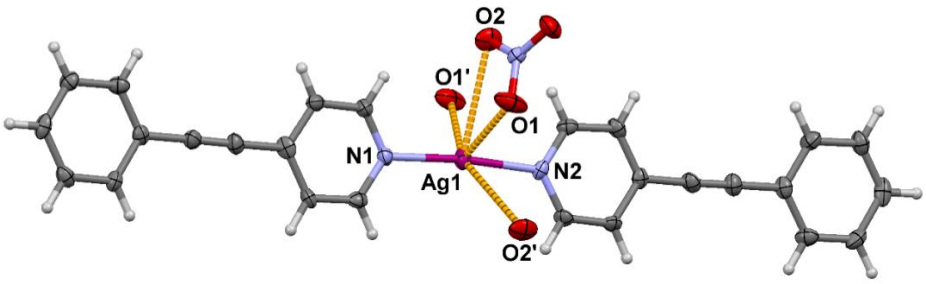

Figure 91: *Asymmetric unit of* **20** *showing the coordination environment of the silver centre. Ellipsoids are shown at 50%. Symmetry operators for O1' = (– x, 1 – y, – ½ + z), O2' = (– x, 1 – y, ½ + z).*

The Ag–O interactions in **20** create a 1D ladder of alternating Ag–NO_3 units, in which each linker and node are 3-connected, and are sandwiched along the crystallographic [010] plane by hydrogen-bonded water molecules (Figure 92). This repeat hydrogen bonded motif can be described using the Etter and Bernstein[28] graph set notation as $R_5^5(12)$. The combination of the inorganic Ag–NO_3 and hydrogen-bonded water molecules forms a 2D sheet, to which pep ligands coordinate *via* the Ag(I) centres orthogonally. As in structures **18** and **19**, the alignment of pep ligands creates an interdigitated hydrophobic layer that serves to partition the polar cation···anion and hydrogen-bonded water regions (Figure 92, right). Also consistent with **19** is an abundance of strong inter-ligand C–H···π interactions, in which each ligand participates in eight such interactions, however in **20** the hydrogen bond motif is uninterrupted, due to lack of steric bulk of the counterions that would disrupt the C–H···π hydrogen bonded interdigitation of the pep ligands.

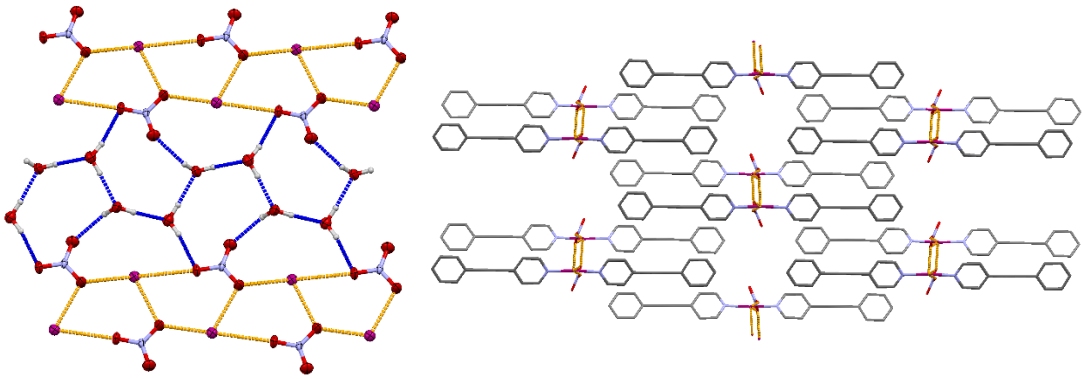

Figure 92: *Left: Network formed by the coordination and hydrogen bonds observed within* **20**, *linking together solvent and inorganic bands. Pep ligands have been omitted for clarity. Right: Interdigitation of pep ligands as viewed down the approximate crystallographic* c *axis. Hydrogen atoms and water molecules have been excluded for clarity.*

The $[Ag(pep)_2]^+$ unit within **20** is almost linear at an angle of 179.57°, measured from calculated terminal phenyl centroids *via* the silver atom. This linearity is likely due to the lack of steric effects observed in **19**. Interdigitation and aromatic hydrogen bonding between the pep ligands of **20** dominates the crystal packing between layers as displayed in Figures 89 and 92. When viewed down the crystallographic *b* axis, the pep ligands are observed to form the favourable herringbone arrangement as observed in **18**, **19** and solid-state pep. This suggests that T-shaped aromatic interactions are prominent in the self-assembly of pep in the presence of NOx silver salts. In **20** the pep ligands sit in molecular planes that intersect at an angle of 60.1°.

Hydrogen bond	*D* (Å)	*d* (Å)	*θ* (°)
C15–H15···π'	3.572(6)	2.87	131.0(4)
C23–H23···π'	3.701(6)	3.08	124.1(4)
C17–H17···π''	3.675(6)	2.99	129.3(3)
C25–H25···π''	3.595(6)	2.96	124.9(4)
C5'''–H5···π	3.667(6)	3.04	124.3(3)
C13'''–H13···π	3.612(6)	2.96	126.2(4)
C2''''–H2···π	3.602(6)	2.93	128.7(4)
C10''''–H10···π	3.687(6)	3.01	129.0(4)

Table 16: *Aromatic C–H···π hydrogen bond geometries between pep ligands of* **20**. *Symmetry operators: (') = (½ – x, ½ + y, ½ + z), ('') = (– x, 1 – y, – ½ + z), (''') = (– x, 1 – y, ½ + z), ('''') = (½ – x, ½ + y, – ½ + z)*

4.2.4. Compounds containing carboxylate and sulfonate AgX salts

Changing the NOx anions for acetate leads to a directional narrowing of the available anion-chelation region through the introduction of a non-bonding methyl group. The resulting crystals have the molecular structure of $[Ag(pep)_2(MeCO_2)]\cdot 1.5H_2O$ (**21**) and pack in the *Pna*2_1 space group. The asymmetric unit of **21** contains one $[Ag(pep)_2]^+$ complex with a coordinated acetate counterion and one and a half water molecules (Figure 93). The coordination environment of the silver centre within the $[Ag(pep)_2]^+$ unit is formally linear, in which the metal center coordinates *via* inner coordination sphere bonds to N atoms from two pep ligands with bond lengths of 2.267(8) Å and 2.285(8) Å and a slightly distorted N–Ag–N angle of 159.0(3)°. Despite this central coordination geometry distortion, the overall $[Ag(pep)_2]^+$ unit remains approximately linear at an angle of 174.71°, stemming from a calculated phenyl centroid of one pep ligand to a calculated phenyl centroid of the second ligand *via* the central Ag atom. The rest of the silver(I) coordination sphere comprises one inner- and two outer- sphere coordination bonds to O atoms from surrounding counterions with Ag–O coordination distances ranging from 2.484(6) to 2.708(10) Å.

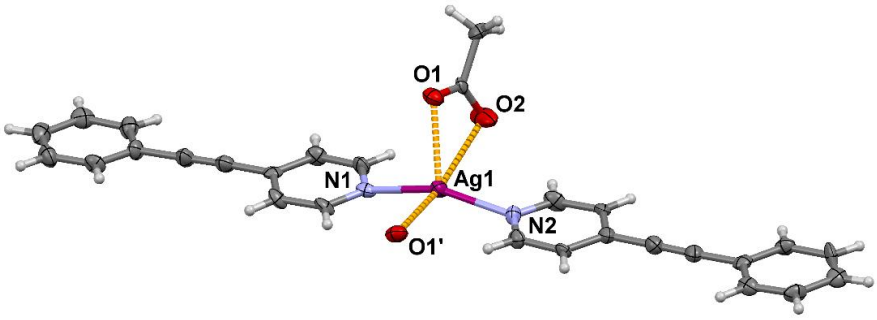

Figure 93: *Asymmetric unit of* **21** *showing the coordination environment of the silver centre. Ellipsoids are shown at 50%. Symmetry operators for O1' = (1 – x, 1 – y, ½ + z).*

The Ag–acetate interactions form a coordination bonded zig-zag 1D chain sandwiched together by water molecules, comparable to structure **20** (Figure 92). Unlike **20**, however, the bulky methyl group of the acetate in **21** prevents rigid hydrogen-bonding interactions between the hydrophilic $-CO_2^-$ group of the counterions and the sandwiched lattice water molecules, causing a decrease in their solid-state ordering. Consequently, the positions of the solvent water molecules in **21** are highly disordered, and thus are omitted from the crystallographic model. The presence of three water molecules was determined by the crystallographic SQUEEZE tool (details in Appendix II) and through thermogravimetric analysis (Appendix I). The interdigitated packing

motif of **21** was found to be isostructural with the motif exhibited by **20** (Figure 94), where aromatic hydrogen bonding between the pep ligands dominates the packing.

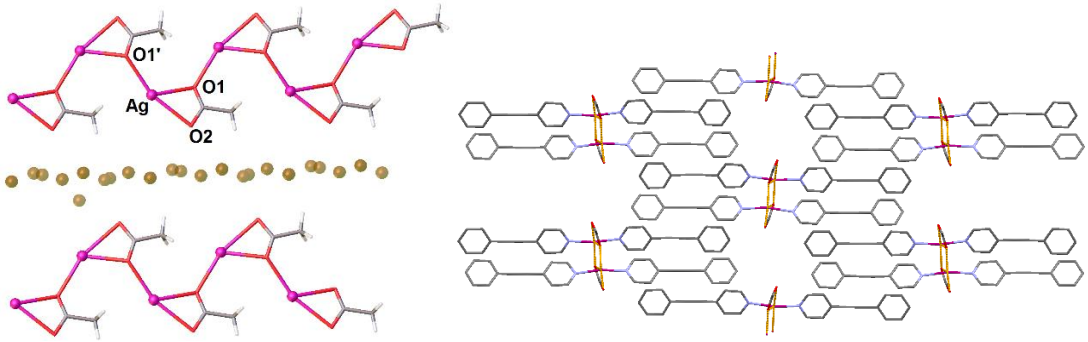

Figure 94: *Left: Diffuse hydrogen-bonded network within* **21**, *linking together inorganic bands. Q-peaks are represented in gold, and pep ligands have been omitted for clarity. Right: Interdigitation of pep ligands as viewed down the crystallographic* c *axis. Hydrogen atoms have been excluded for clarity.*

Similar to structure **20**, the pep ligands in **21** also exhibit C–H···π bonding, and thus pack into an ordered herringbone formation in the hydrophobic regions (Figure 94). This ligand-oriented packing suggests that although bulkier, the acetate counterions influence self-assembly in a similar manner to the NOx anions, by which the one-dimensional silver and acetate chains largely coordinate around the silver centres, creating hydrophilic and hydrophobic regions within the crystal structures. The hydrogen bond distances (*D*, *d*) and angles (*θ*) are shown in Table 17 below. The molecular plane to plane angle is 60.5°.

Hydrogen bond	*D* (Å)	*d* (Å)	*θ* (°)
C2–H2···π'	3.65(1)	2.99	128.6(7)
C10–H10···π'	3.641(12)	3.02	124.8(8)
C4–H4···π''	3.55(1)	2.83	135.0(6)
C12–H12···π''	3.707(16)	3.05	129.2(9)
C17'''–H17···π	3.566(9)	2.87	131.7(5)
C25'''–H25···π	3.710(15)	3.05	128.6(10)
C22''''–H22···π	3.626(10)	2.99	126.4(7)
C14''''–H14···π	3.751(10)	3.15	123.3(6)

Table 17: *Aromatic hydrogen bond geometries of pep ligands within* **21**. *Symmetry operators: (') = (1 – x, 1 – y, ½ + z), ('') = (3/2 – x, – ½ + y, – ½ + z), (''') = (3/2 – x, – ½ + y, ½ + z), ('''') = (1 – x, 1 – y, – ½ + z).*

Colourless crystals obtained from evaporation of the fluorinated analogue $AgCF_3CO_2$ and pep in acetonitrile were determined to be $[Ag(pep)_2][CF_3CO_2]$ (**22**). In comparison to **21**, the change from methyl to trifluoromethyl causes a rotation in the carboxylate coordination to disfavour the 1D chain formation observed in **21**. The resulting structure is based on a $[Ag(pep)_2]^+$ based dimer consisting of four pep ligands and two trifluoroacetate groups around two silver centres (Figure 95), linked by a Ag···Ag interaction of length 3.1209(5) Å and π···π interactions between the parallel phenyl rings of the pep ligands, with centroid-to-centroid interaction distances of 3.6514(10) Å. The silver center supports two inner- and two outer-coordination sphere bonds thus adopting a distorted square-planar coordination environment. Two trifluoroacetate anions bridge the two Ag(I) centres and form a pseudo-paddlewheel building unit with Ag–X (X = N, O) interaction distances within the range 2.175(2) to 2.7805(19) Å. A full list of coordination bonds around the silver centre Ag1 can be found in Table 48 in Appendix II.

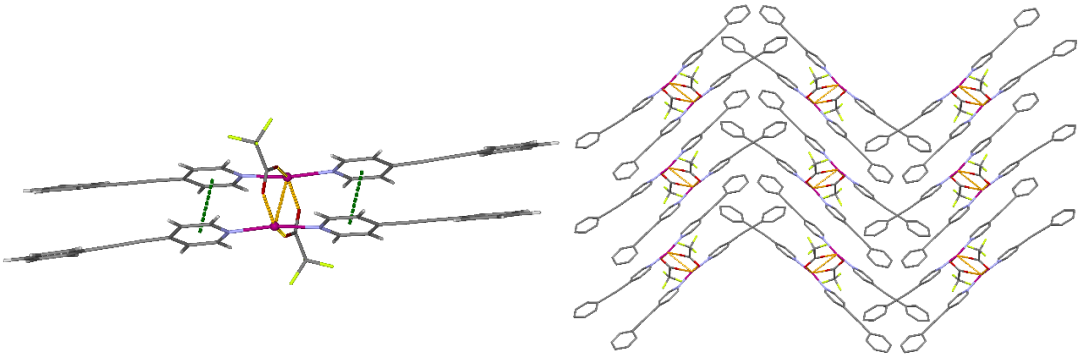

Figure 95: *Left: The pseudo-paddlewheel configuration within structure* **22**, *π···π interactions are shown in green, and the Ag···Ag interaction in gold. Right: The herringbone packing arrangement of* **22** *as viewed down the crystallographic* c *axis.*

The dimers of **22** are reminiscent to an alkene containing coordination compound synthesised by MacGillivray et al., comprising Ag and trans-1-(4-pyridyl)-2-(phenyl)ethylene units.[29] The research group found that these units dimerised upon exposure to UV light through [2+2] photodimerisation of the alkene units. Exposing compound **22** to UV radiation did not reveal any such photoreactivity; the samples were observed to decompose.

The packing of **22** forms a herringbone motif, wherein the pseudo-paddlewheels align in an offset manner (Figure 95). Interestingly, the only weak interactions discerned between the paddlewheel motifs are C–H···F hydrogen bonds from the aromatic pyridine

hydrogen atoms to adjacent trifluoroacetate fluorine atoms (D = 3.221(3) Å, d = 2.46 Å, θ = 137.15(18)°). These hydrogen bonds are known to be weak, however,[30] and thus likely do not play a large part in the packing of the dimers. One intramolecular parallel-displaced π···π interaction per pair of dimers is present, from a pyridine ring of one dimer to a pyridine ring of the adjacent dimers at a centroid to centroid distance of 3.93 Å and a pyridine plane to plane shift of 2.20 Å. No potential Ag···π interactions are observed; the silver atoms and π groups are misaligned and are separated by distances greater than 4.1 Å. These observations suggest that the dimeric 2{[Ag(pep)$_2$]$_2$[CF$_3$CO$_2$]} may initially self-assemble in solution, followed by relatively inefficient packing upon crystallisation, inhibiting ligand to ligand C–H···π interactions and leading to the lack of formation of the pep herringbone pattern.

The stability of **22** was tested by differential scanning calorimetry (DSC) by heating a sample of **22** from room temperature to 250 °C. The DSC scan (Figure 96) revealed two endothermic events, a phase transition occurring over the range of 165 – 169 °C, followed by a clear melting event in the range of 199 – 201 °C. Heating a crystalline sample above the phase-transition temperature results in a colour change of the sample from colourless to orange and conversion of **22** to a polymorphic form of [Ag(pep)$_2$][CF$_3$CO$_2$] (**23**) (Figure 97).

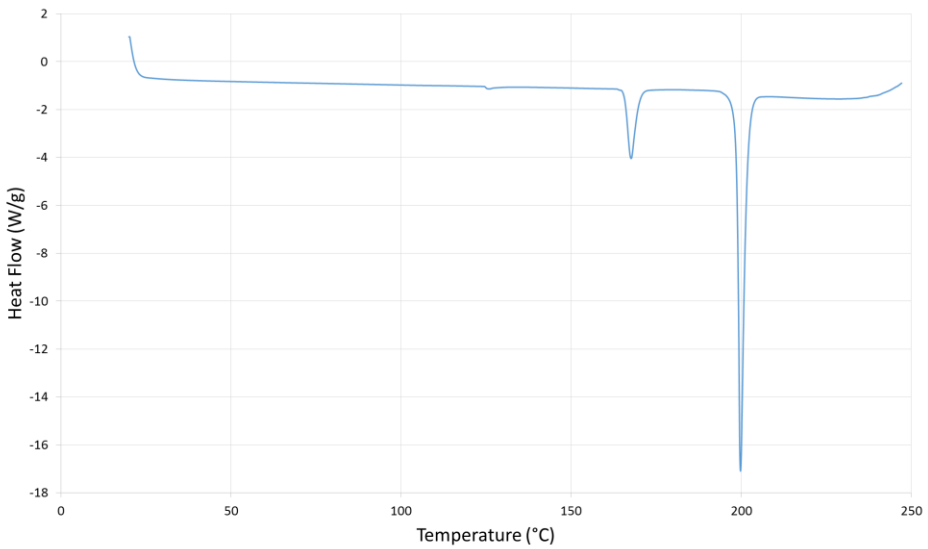

Figure 96: *DSC of* **22** *showing the endothermic polymorphic change from* **22** *to* **23** *at 165.7 °C and a subsequent endothermic melt event (of* **23***) at 198.8 °C.*

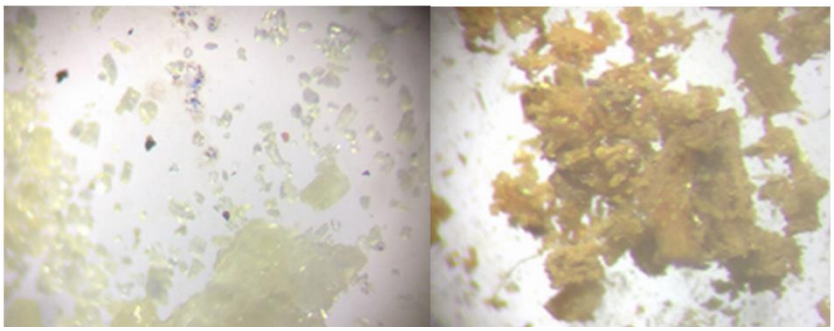

Figure 97: *Crystalline sample of* **22** *(left) before and after heating above 170 °C for 1 hour, yielding the orange product* **23** *(right).*

A clean PXRD pattern of crystals of colourless **22** could not be obtained due to the crystallisation product yielding a minor component of **23**. Similarly, a PXRD pattern of **23** could not be obtained due to the small amount of single crystals converted from colourless to orange.

Analysis of the crystalline product **23** by single crystal X-ray diffraction studies identified a new, albeit closely related, structure to the pseudo-paddlewheel structure of **22**. An overlay of the dimeric motifs (Figure 98) shows increased interaction between the silver and the trifluoroacetate anion in **23** (Ag···O = 2.6039(16) Å for **22**; 2.550(3) Å for **23**), concomitant with an increase in the distance between the metal centres (Ag···Ag = 3.1171(3) Å for **22**; 3.1830(6) Å for **23**).

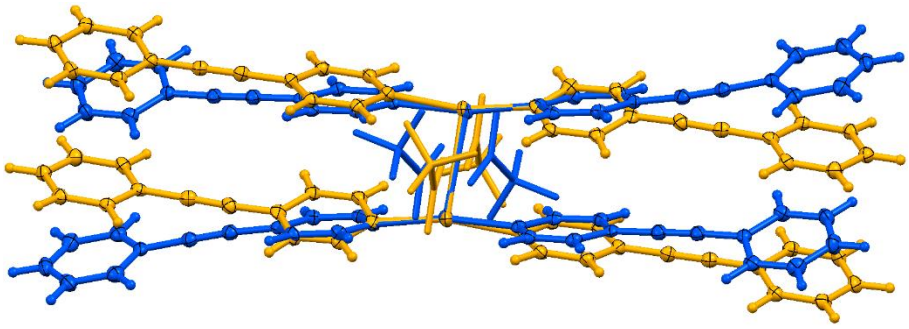

Figure 98: *An overlay of dimers* **22** *(blue) and* **23** *(yellow), showing the changes in configuration.*

Changes to the overall solid-state packing between the two structures are far more pronounced (Figure 99). While the herringbone motif of the $[Ag(pep)_2]^+$ dimers is retained in **23**, shifting of the pep ligands and the relative positions of the pseudo-paddlewheels allows each $[Ag(pep)_2]^+$ unit to participate in a total of ten π···π interactions with an average centroid-to-centroid distance of 3.65 Å. This amounts to more than two times the number of aromatic interactions relative to **22**.

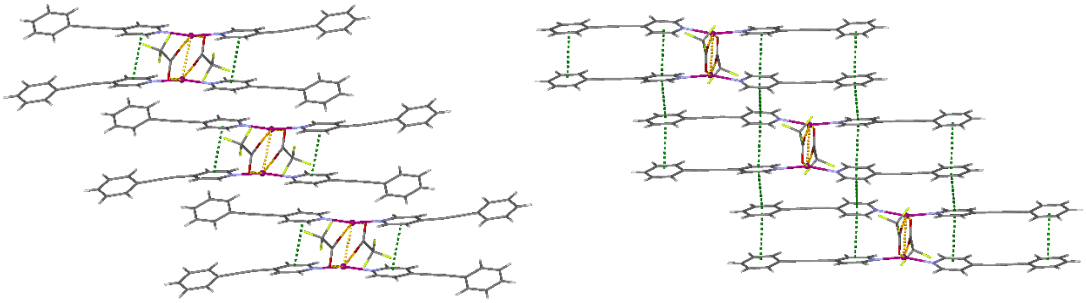

Figure 99: *Changes in the packing through the phase transition of* **22** *to* **23** *resulting in more widespread π···π interactions that stabilise the latter. Hydrogen atoms have been omitted for clarity.*

The planes of the phenyl groups in **23** participating in π···π interactions are offset by an average 1.49 Å (phenyl plane to plane offset), so that the resulting interactions are parallel-displaced π···π bonds.

To establish the microscopic origin of the colour change on conversion from **22** to **23**, first-principles computational modelling on the two systems was carried out using periodic density functional theory (DFT). The modelling and calculations were performed by Dr. Johnathan Skelton.

Computationally modelled density plots of the frontier orbitals of the two systems (Figure 100c, d) established that the highest-occupied crystal orbitals (HOCOs) of both **22** and **23** are composed mainly of Ag d_{z^2} orbitals, whereas the lowest-unoccupied crystal orbitals (LUCOs) are formed of the ligand π systems. DFT calculations found that the structural changes occurring through the SCSC transition lead to a general upward shift in the energies of the HOCOs, together with a lowering in the energy of the LUCOs. This collectively leads to a decrease in the energy gap between crystal orbitals from 3.838 eV in the colourless **22** to 3.768 eV in the orange **23**.

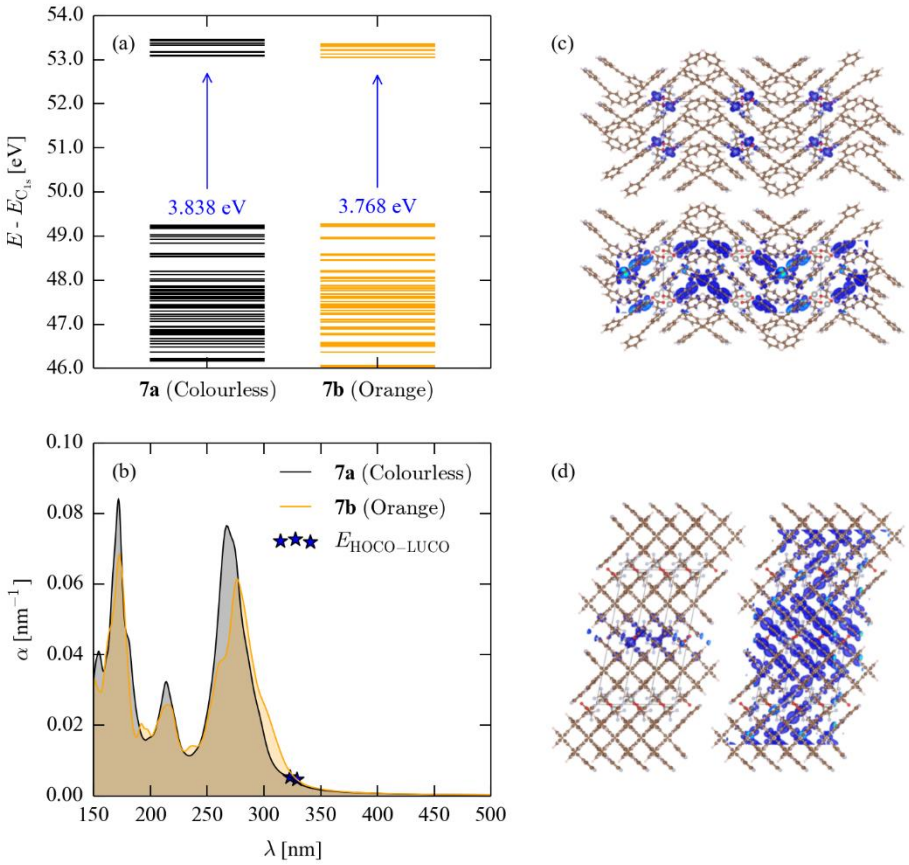

Figure 100: *Computational modelling of the electronic structure and optical properties of the colourless* **22** *and the orange* **23**. *(a) Energy-level spectrum of the two materials, with the energy gaps between the highest-occupied and lowest-unoccupied crystal orbitals (HOCO/LUCO) marked in blue. (b) Simulated wavelength-dependent absorption coefficients. The positions of the HOCO-LUCO gaps are marked on the two spectra by blue stars. (c, d) Density plots of the HOCO (top/left) and LUCO (bottom/right) of* **22** *(c) and* **23** *(d). The images in (c) and (d) were prepared using VESTA software.*[31]

This change in energy of the crystal orbitals and corresponding colour change can be interpreted in terms of the main structural changes across the two crystal structures. An increase in the Ag···Ag interaction distance, which, if the metal d_{z^2} orbitals on adjacent Ag atoms interact in phase, would destabilise the HOCO, and an increase in π···π interactions between ligands would stabilise the LUCO. The simulated absorption spectrum (Figure 100b) additionally predicts a red shift in the absorption profile of **23** compared to **22**, which is consistent with the observed colour change.

Changing the chelating group from carboxylate to sulfonate in **22** while retaining the trifluoromethane group yields colourless crystals containing the molecular formula $[Ag(pep)_2][CF_3SO_3]$ (**24**). The asymmetric group of **24** contains one $[Ag(pep)_2]^+$ unit coordinated to a trifluoromethanesulfonate counterion through the sulfonate group, of

which the Ag1–O1 distance is 2.906(4) Å. Each sulfonate anion coordinates to three $[Ag(pep)_2]^+$ units through each of its oxygen atoms (Figure 101). The central silver atom Ag1 possesses a linear coordination environment by the coordination to N atoms of two pep ligands, which becomes a distorted trigonal bipyramid once outer-sphere Ag–O coordination bonds are included. The sum of the silver-anion coordination interactions forms alternating 1D Ag–SO_3 ladders along the crystallographic *b* axis. The five coordination bond distances for this structure can be found in Table 24 of Appendix II.

The hydrophobic trifluoromethyl group sterically shields the sulfonate group, removing the possibility of forming the type of extended 2D inorganic net seen in structures **18** and **19**. This, coupled with the larger size of the sulfonate anions, allows a similar packing motif to that in nitrate species **20** and acetate species **21** to occur without the need for additional silver anion equivalents or solvent molecules to fill void space. The protruding $-CF_3$ groups take part in weak C–H···F hydrogen bonding from surrounding phenyl and pyridyl hydrogen atoms of pep ligands, at an average *d* distance of 2.76 Å.

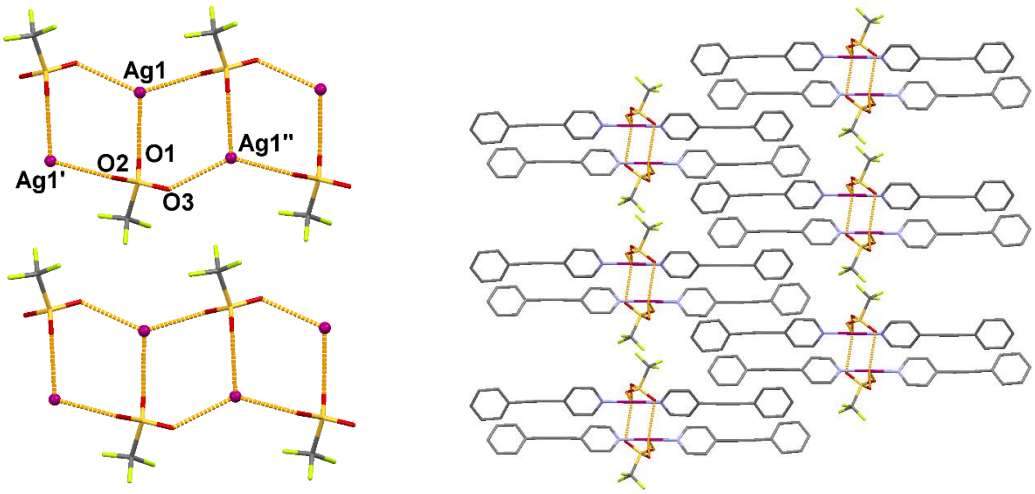

Figure 101: *Left: Weak anion-derived interactions yielding a 1D chain motif in* **24**. *Coordination bonds are shown in blue and pep ligands have been omitted for clarity. Symmetry operations: (') = (1 – x, – ½ + y, 1 – z), (") = (1 – x, ½ + y, 1 – z). Right: Sterically bulky triflate anion fills the void between chains of* $[Ag(pep)_2]^+$ *units as viewed down the crystallographic* b *axis. Hydrogen bonds have been removed for clarity.*

Much like structures **18** to **21**, structure **24** also exhibits pep interdigitation between the silver-anion chains and therefore T-shaped C–H···π hydrogen bonding, forming hydrophobic layers along the crystallographic *b* axis. Although weak C–H···F hydrogen bonding is present between the one-dimensional chains, C–H···π hydrogen bonds between pep ligands in **24** are the most prominent and abundant interactions and thus can be attributed to influencing the solid-state packing. The C–H···π hydrogen bonding

of the interdigitating pep ligands is disrupted in a similar manner to that in structure **19**, due to the steric bulk of the $–CF_3$ groups, resulting in the vertical pep interactions being disrupted every fourth layer (Figure 101). This results in the first and fourth pep ligand in every cluster being involved in four C-H···π hydrogen bonds each as opposed to eight hydrogen bonds each for the second and third layered ligands. The pep molecular plane to plane intersection angles are 61.6, 71.9 and 66.8°.

Hydrogen bond	*D* (Å)	*d* (Å)	*θ* (°)
C15–H15···π'	3.422(5)	2.70	132.5(3)
C23–H23···π'	3.644(6)	3.06	120.9(4)
C18–H18···π''	3.728(5)	2.97	136.9(3)
C26–H26···π''	3.599(5)	2.97	124.5(3)
C4'''–H4···π	3.563(6)	2.75	1443.6(4)
C12'''–H12···π	3.606(6)	2.89	132.9(4)
C23''''–H23···π	3.644(6)	3.06	120.9(4)
C15''''–H15···π	3.422(5)	2.70	132.5(3)

Table 18: *Aromatic hydrogen bond geometries of pep ligands within* **24**. *Symmetry operators: (') = (– x, – ½ + y, – z), ('') = (1 – x, ½ + y, 1 – z), (''') = (1 – x, – ½ + y, 1 – z), ('''') = (– x, ½ + y, – z).*

Further increasing the steric bulk of the sulfonate anion by substituting the triflate anion for tosylate yields a similar gross structure to that observed in **24**. Slow evaporation of a 2:1 ratio of pep and silver *p*-toluene sulfonate from either acetonitrile or methanol yields a structure with a molecular composition of $[Ag(pep)_2]Tos{\cdot}0.25pep$ (**25**). The asymmetric unit of **25** contains one $[Ag(pep)_2]^+$ unit coordinated to a *p*-toluene sulfonate anion *via* an oxygen atom, and a quarter-occupancy non-coordinated pep ligand. The coordination environment of the central silver atom is similar to that in **24**, where Ag1 possesses a distorted trigonal bipyramidal coordination geometry *via* two N atoms from the pep ligands and three O atoms of surrounding sulfonate counterions (Figure 102) that fall into a range of 2.170(3) – 2.864(3) Å, consisting of two inner- and three outer- sphere coordination bonds. A full list of coordination interactions of **25** can be found in Table 51 of Appendix II. The 1D silver-sulfonate ladders are also similar to that in **24**, however the larger *p*-tosyl group forces the ladders apart, creating a channel containing a continuous chain of non-coordinating pep molecules (Figure 102, right). These interstitial pep molecules stabilise the 1D motifs through intercalation by hydrogen bonding and van der Waals interactions derived from the tosyl counterion group and surrounding coordinated pep ligands.

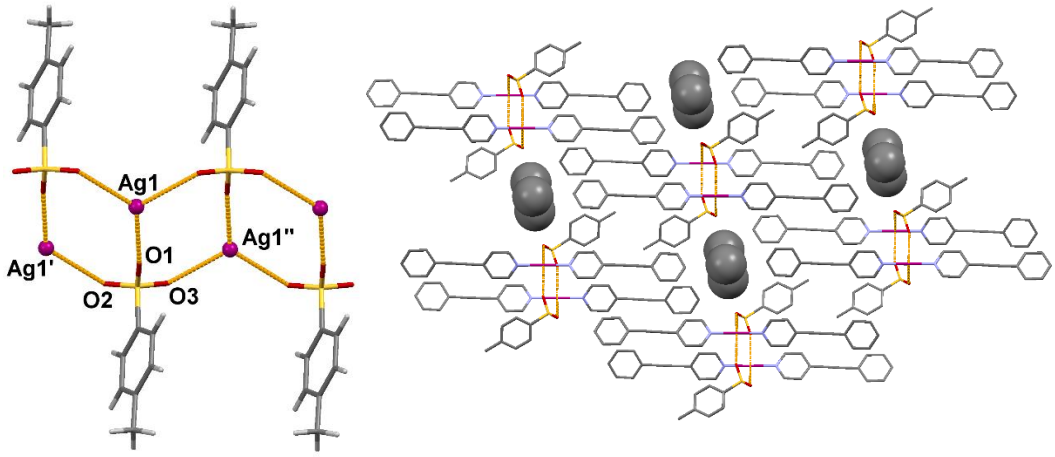

Figure 102: *Left: 1D chain motif observed in* **25**, *which is isostructural to* **24**. *Coordination bonds are shown in blue. Pep ligands have been omitted for clarity. Symmetry operations: (') = (1 – x, 2 – y, 1 – z), ('') = (1 – x, 1 – y, 1 – z). Right: Inclusion of non-coordinated pep ligands (shown with space-filling atoms) into the voids formed due to the inclusion of the tosylate anion, viewed here down the crystallographic* b *axis. Hydrogen atoms have been excluded for clarity.*

The herringbone pattern observed between coordinated pep ligands in pure pep is also present in **25**. Six unique C–H···π interactions connect every four rows of pep ligands, separated by the bulky tosylate counterions, which help propagate the continuous weak C–H···π hydrogen bonding stabilising the hydrophobic regions. The interdigitating pep ligands sit on molecular planes that are at angles of 51.1, 53.8 and 48.4° from each other.

Hydrogen bond	*D* (Å)	*d* (Å)	*θ* (°)
C12–H12···π'	3.479(4)	2.82	127.0(2)
C4–H4···π'	3.406(4)	2.71	130.6(2)
C1–H1···π''	3.532(4)	2.83	131.0(2)
C9–H9···π''	3.499(4)	2.80	130.9(2)
C23'''–H23···π	3.453(4)	2.79	127.0(2)
C15'''–H15···π	3.461(4)	2.77	130.2(2)

Table 19: *Aromatic hydrogen bond geometries of pep ligands within* **25**. *Symmetry operators: (') = (½ – x, – ½ + y, ½ – z), ('') = (1 – x, 2 – y, 1 – z), (''') = (1 – x, 1 – y, 1 – z).*

Two phenyl groups of the tosylate anion reside in one pep position, in which each phenyl group participates in T-shaped C–H···π hydrogen bonding to surrounding pep ligands. Table 20 below displays the C–H···π interaction geometries.

Hydrogen bond	*D* (Å)	*d* (Å)	*θ* (°)
C32–H32···π'	3.386(4)	2.68	130.6(2)
C29–H29···π''	3.469(4)	2.77	130.6(2)
C25'''–H25···π	3.628(4)	3.06	119.5(2)
C18''''–H18···π	3.643(4)	3.13	115.6(2)

Table 20: *Aromatic hydrogen bond geometries of pep ligands within* **25**. *Symmetry operators: (') = (1 – x, 1 – y, 1 – z), ('') = (– ½ + x, ½ + y, z), (''') = (– ½ + x, – ½ + y, z), ('''') = (1 – x, 2 – y, 1 – z).*

The less favourable orientation of the tosylate phenyl group, as seen from the longer hydrogen bond distances and more acute approach angles, can be attributed to the restricted orientation of the phenyl group due to coordination to the silver centres.

4.2.5. Compound containing AgSCN

The final structure in the study proved exceptional in that the $[Ag(pep)_2]^+$ unit did not form when pep was combined with silver thiocyanate. Instead a 2D sheet network propagated by silver-thiocyanate interactions was observed, with a composition of [Ag(pep)(SCN)], forming structure **26**. The asymmetric unit of **26** contains one central silver atom coordinated to one pep ligand and one SCN counterion, *via* the N atom. The 2D sheet in **26** is comprised entirely of Ag–N and Ag–S coordination bonds resulting in the central silver atom supporting four coordination bonds and thus adopting a distorted tetrahedral coordination geometry.

The Ag–N bonds involving the pep ligands are longer than in **15** - **25**, with a coordination bond distance of 2.305(2) Å. The pep ligands form the familiar herringbone pattern (Figure 103, right) that propagates along the crystallographic *c* axis, promoting stability within the ligand layers, meanwhile the thiocyanate anions form 3-connected 2D sheets between the hydrophobic layers. Consequently, interdigitation of the pep ligands manifests in alternating pillared arrays and dominates the crystal packing between layers.

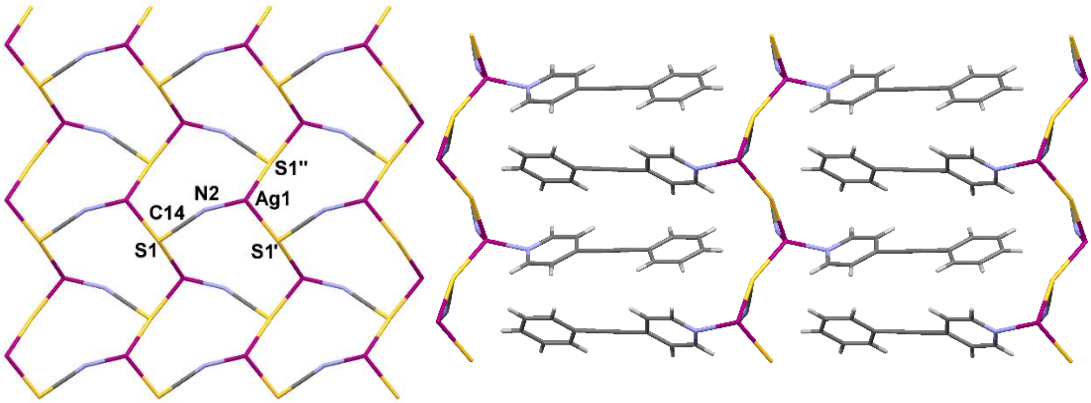

Figure 103: *Left: The 2D sheet motif of* **26** *comprised of covalent Ag–N and Ag–S bonds from thiocyanate as viewed down the crystallographic* c *axis. Pep ligands have been omitted for clarity. Right: Interdigitated pep ligands as observed along the crystallographic* a *axis.*

Each pep ligand participates in eight total and four unique C–H···π hydrogen bonds described in Table 21 below. The interdigitating pep ligands sit on molecular planes that intersect at an angle of 61.2°.

Hydrogen bond	*D* (Å)	*d* (Å)	*θ* (°)
C4–H4···π'	3.596(3)	2.83	137.8(2)
C12–H12···π'	3.750(4)	3.07	128.9(2)
C1–H1···π''	3.720(4)	2.97	135.9(3)
C9–H9···π''	3.633(4)	2.92	132.5(3)

Table 21: *Aromatic hydrogen bond geometries of pep ligands within* **26**. *Symmetry operators: (') = (2 – x, – ½ + y, 1 – z), ('') = (1 – x, ½ + y, 1 – z).*

4.3. Discussion and conclusions

The ligand 4-(phenylethynyl)pyridine (pep) and various silver(I) salts were crystallised by evaporation from methanol and acetonitrile to explore the competing self-assembly interactions within the reaction mixture. Twelve coordination polymers were obtained, two of which were the result of single-crystal to single-crystal transitions. All compounds crystallised from both solvents except those containing NO_3^- and SCN^-, which only yielded crystals under methanol and acetonitrile respectively. Only the NO_2^- counterion showed differing crystal structures depending on whether methanol or acetonitrile was used.

Of the twelve structures analysed, three overall gross topologies were found: compounds **15**, **16**, **17**, **22** and **23** assembled as discrete complexes, structures **20**, **21**, **24**, **25** as one-dimensional chain polymers and structures **18**, **19** and **26** as two-dimensional polymer nets. Only in the extended structures were hydrophobic regions of interdigitated pep ligands found, and only discrete compounds exhibited SCSC transitions. A range of silver coordination environments were observed within the obtained coordination polymers including linear, tetrahedral, trigonal bipyramidal, square-based pyramidal, square planar and octahedral geometries which corresponded with the wide range of silver coordination numbers also observed; 2 to 6. Interestingly, the coordination environments of the included silver(I) centres followed a dimensional trend of increasing coordination number with structure dimensionality, where non-dimensional structures contained silver centres with 2 - 4 coordination bonds and extended structures contained silver centres supporting 4 - 6 total coordination bonds.

Extensive T-shaped C–H···π bonding through the interdigitation of pep ligands was reported in all dimensional crystal structures, which were derived from a range of counterions comprising NO_2^-, NO_3^-, $CO_2CH_3^-$, $CF_3SO_3^-$, Tos^- and SCN^-, in which the herringbone motif exhibited was comparable to the crystal structure of pure pep (Figure 104).

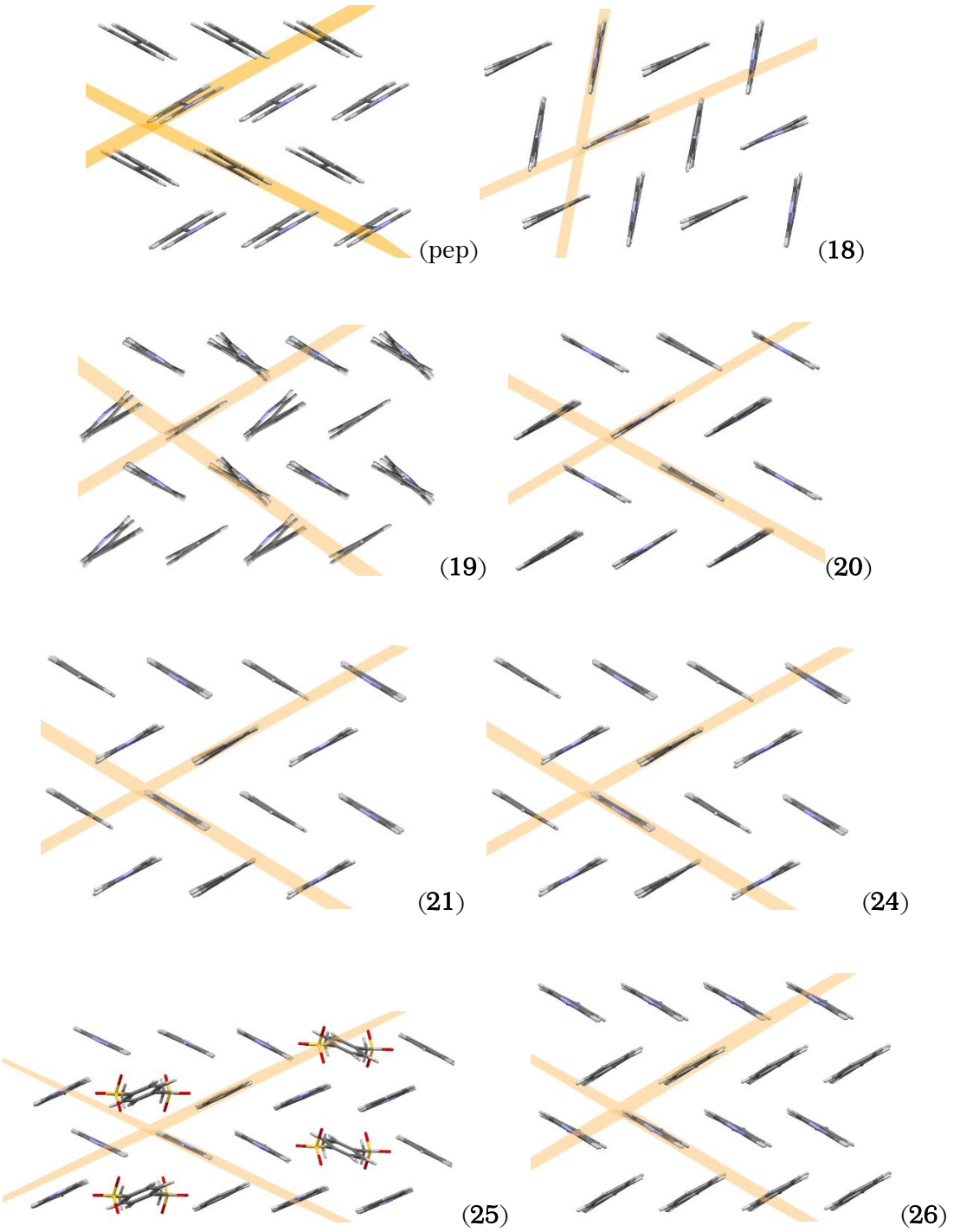

Figure 104: *The herringbone motif formed by interdigitated pep ligands, in which two intersecting molecular pep planes within each structure are highlighted in orange.*

This propensity for weak C–H···π hydrogen bonding within the coordination polymers suggests that these interactions are able to dominate the coordination bonding between the metal and counterion, and ultimately direct the outcome of the structural topology. In this case, the pep ligand evidently prefers packing in the herringbone motif to coordination with silver-counterion components. Molecular planes of the pep ligands of

each structure shown above were calculated, the intersect angle for each noted in Table 22 below.

Compound	Intersect angle (°)
pep	59.5
18	55.6
19	66.5, 72.0, 61.0
20	60.1
21	60.5
24	61.6, 71.9, 66.8
25	51.1, 53.8, 48.4
26	61.2

Table 22: *The intersecting pep molecular plane angles of structures pep,* ***18*** *-* ***21*** *and* ***24*** *-* ***26****.*

The molecular intersect angles in compounds **18** – **21** and **24** – **26** are within 13° of the molecular plane to plane angle of pure pep, although this is not usual as C-H···π hydrogen bonds can be easily distorted by other interactions, hence the slight differences in the herringbone motif across the structures.[32]

In structures where pep interdigitation did not occur, two examples of single-crystal to single-crystal (SCSC) transition behavior were found, initiating from arrayed 0D complexes in which T-shaped C–H···π hydrogen bonding was not observed, derived from counterions comprising PF_6^- and $CF_3CO_2^-$. These discrete complexes were found to undergo SCSC transitions upon desolvation (**15** to **16**) and heating (**22** to **23**). Of these, the **15** to **16** transition occurred with desolvation and bending of the $[Ag(pep)_2]^+$ unit by more than 24°, while the **22** to **23** transition was concomitant with an increase in the amount of π···π stacking and a decrease in Ag···Ag interactions, causing a change in the colour of the crystals. This crystal transition was explored using DFT calculations, which attributed the change in colour to changes in the frontier-orbital energies due to the differences in packing.

The correlation between the coordinative properties of the silver salt and the resulting structure of the crystalline compound can lead to the ability to predict the outcomes of synthesis using silver counterions that have not been explored within this series. ClO_4^- and SbF_6^- for example are common counterions in silver salts that have not been explored in this chapter. Both of these anions are known to be non-coordinating therefore would likely form a 0D discrete complex topology similar to that in **15**, **16** and

17 if crystallised with silver(I) and pep. The systematic variation of single components within these crystallisations reveals the fundamental aspects of self-assembly hierarchy in these complicated systems and can be used as the foundation for future work exploring such silver complexes and their potential to exhibit interesting structural or functional behaviour.

4.4. Experimental

Starting materials and solvents were purchased from commercial sources and were used without further purification with the exception of 4-(phenylethynyl)pyridine (pep). X-ray diffraction data collections for **15** - **17**, **19** - **22**, **24** and **25** were collected on an Agilent Supernova diffractometer at the University of Bath using Mo Kα radiation, the crystal being cooled by an Agilent Cryojet. Data for **18** was collected on an Agilent Xcalibur diffractometer using Mo Kα radiation, cooled to 150 K by an Oxford Instruments nitrogen gas cryostream. Single crystal data for **23** and **26** were collected on Station 11.3.1 of The Advanced Light Source (ALS), Lawrence Berkeley National Laboratory,[33] cooled to 100 K. More details can be found in the Appendix II.

Powder X-ray diffraction patterns (PXRDs) were recorded on a Bruker AXS D8 Advance diffractometer with Cu Kα radiation of wavelength 1.5406 Å at 298 K. Calculated and experimental PXRD patterns can be found in Appendix I. Samples were placed on a flat plate, and measured with a 2θ range of 3-60°. Nuclear magnetic resonance spectra were obtained on a Bruker Avance 300 MHz Ultrashield NMR spectrometer. Infrared spectra were recorded on a PerkinElmer Spectrum 100 spectrometer equipped with an ATR sampling accessory. Elemental analyses were performed on a CE-440 elemental analyser (Exeter Analytical). Differential scanning calorimetry data was collected on a DSC Q20. Thermogravimetric analysis (TGA) was performed using a Setsys Evolution TGA 16/18 from Setaram with Calisto software to collect and process the data. Samples were placed in 170 μL alumina crucibles and prior to experiments the analytical chamber was purged from ambient air using argon flow at 200 mL/min for 40 min. Sample pans were analysed under argon flow at 20 mL/min.

† CCDC Conquest 1.18 was used to build a query where two phenyl groups each supporting one substituent group X were drawn, X being defined as 'any atom'. A centroid (cent1) was built on one phenyl ring. Three search criteria between the two phenyl groups were defined over three positions, one C and one H atom of one phenyl group and the cent1 centroid of the second phenyl group: H···cent1 at a distance of 2.7 ±0.5 Å; C···cent1 at a distance of 3.7 ±0.5 Å and C–H···cent1 angle of 130 – 180°. The connection between the phenyl rings was defined as inter- as well as intra-molecular. The 1,379 search results were exported into an Excel spreadsheet in which the minimum, maximum and mean values were calculated.

4-(phenylethynyl)pyridine 4-Bromopyridine hydrochloride (100 mg, 50 mmol), bis(triphenyphosphine)palladium dichloride (72.3 mg, 2 mol%) and CuI (9.8 mg; 1 mol%) were placed in a flask, degassed and back-filled three times with N_2. Degassed NEt_3 (2.1 mL) was added to the reaction flask. The reaction mixture was heated to 80 °C, at which point phenylacetylene (0.55 mL, 5.0 mmol) dissolved in acetonitrile (5 mL) was added. The reaction was refluxed over four days under N_2. The solvents were evaporated, sodium bicarbonate solution was added and extracted with ether. The organic layers were washed with water followed by brine before drying and evaporating. The residue was chromatographed using an ethyl acetate / hexane mixture (1:9 → 1:4) to obtain the by-product bis(4-N,N-dimethylaminophenyl)butadiene, butadiene and cross-coupled product. Yield of isolated product: 760 mg (85%). Analytical data match those reported previously.[34,35]

General procedure for synthesising silver coordination complexes *Note: Ag(I) salts decompose in ambient light and therefore all crystallisations were covered in aluminium foil for the duration of the reaction. After that, all crystalline samples were found to be stable when exposed to light.* A solution of 4-(phenylethynyl)pyridine (5 mg, 0.027 mmol) dissolved in methanol or acetonitrile (0.6 ml) was added to the appropriate silver(I) salt (0.014 mmol) and subjected to sonication. If undissolved, the mixture was sealed and heated to 40 °C for 30 mins in the absence of light. After cooling to room temperature, the vial was opened slightly to allow slow evaporation of the solvent while protecting the solution from light to promote crystal formation. The resulting crystals were washed with a small amount of 1:4 MeOH/H_2O mixture prior to characterisation.

[Ag(pep)$_2$][PF$_6$]·MeCN (15) Colourless needles suitable for X-ray diffraction were obtained after 48 hours from acetonitrile. Yield: 79% based on the Ag salt. Bulk purity was determined by PXRD. Despite repeated attempts, single crystals of **15** sent for elemental analyses matched expected ratios for **16**, suggesting SCSC conversion *en route*. FTIR: $\bar{\upsilon}$ = 3102 (w), 2261 (w), 2219 (m), 1607 (s), 1542 (w), 1505 (m), 1427 (m), 1222 (m), 1148 (w), 1065 (w), 1028 (w), 820 (s), 755 (s), 686 (s), 554 (s) cm^{-1}.

[Ag(pep)$_2$][PF$_6$] (16) Prismatic crystals suitable for X-ray diffraction were obtained by a SCSC transition after air-drying **15**. Yield: Quantitative based on **15**. Despite repeated attempts, bulk purity could not be determined by PXRD. Anal. Calcd (%) for $C_{26}H_{18}AgF_6N_2P$: C, 51.09; H, 2.97; N, 4.58. Found: C, 50.98; H, 2.89; N, 4.66. FTIR $\bar{\upsilon}$

= 2223 (m), 1608 (m), 1504 (w), 1428 (m), 1221 (m), 1066 (w), 1027 (w), 818 (s), 761 (s), 693 (s) cm^{-1}.

$[Ag(pep)_2][BF_4]$ (17) Colourless plate crystals suitable for X-ray diffraction were obtained after 48 hours from methanol or acetonitrile. Yield: 45% based on the Ag salt. Bulk purity was determined by PXRD. Anal. Calcd (%) for $C_{26}H_{18}AgBF_4N_2$ (553.1): C, 56.46; H, 3.28; N, 5.06. Found: C, 56.31; H, 3.45; N, 5.04. FTIR $\bar{\upsilon}$ = 3527 (w), 2220 (m), 1607 (m), 1501 (m), 1426 (m), 1282 (w), 1218 (m), 1017 (s), 828 (s), 755 (s), 687 (s) cm^{-1}.

$[Ag(pep)_2][Ag(NO_2)_2]$ (18) Colourless prismatic crystals suitable for X-ray diffraction were obtained after 48 hours from methanol. Elemental and PXRD analysis determined the bulk sample to contain a small excess of silver nitrite. Yield: 78% based on the Ag salt. Anal. Calcd (%) for $[Ag(pep)_2(NO_2)\cdot 1.2AgNO_2]$: C, 44.81; H, 2.60; N, 8.44. Found: C, 44.83; H, 2.64; N, 8.50. FTIR $\bar{\upsilon}$ = 3079 (w), 2222 (m), 2165 (w), 1604 (m), 1542 (w), 1499 (m), 1442 (w), 1416 (m), 1216 (s), 1069 (w), 1015 (w), 925 (w), 829 (s), 766 (s), 692 (s) cm^{-1}.

$[Ag(pep)_2][Ag(NO_3)_2]$ (19) Colourless block crystals suitable for X-ray diffraction were obtained after 48 hours from methanol. Yield: 64% based on the Ag salt. Bulk purity was determined by PXRD. Anal. Calcd (%) for $C_{26}H_{18}Ag_2N_4O_6$: C, 44.73; H, 2.60; N, 8.02. Found: C, 45.21; H, 2.63; N, 7.87. FTIR $\bar{\upsilon}$ = 3363 (m), 2220 (m), 1501 (w), 1419 (w), 1376 (w), 1290 (s), 1215 (m), 1069 (w), 1018 (m), 924 (w), 830 (s), 810 (m), 763 (s), 689 (s) cm^{-1}.

$[Ag(pep)_2][NO_3]\cdot 2H_2O$ (20) Colourless needles suitable for X-ray diffraction were obtained after 48 hours from acetonitrile. Yield: 67% based on the Ag salt. Bulk purity was determined by PXRD. Anal. Calcd (%) for $AgC_{26}H_{20.5}N_3O_{4.25}$ elemental analysis matched a reduction in the amount of water of **20**, suggesting a loss of water occurring *en route*: C, 56.69; H, 3.75; N, 7.63. Found: C, 56.81; H, 3.81; N, 7.63. FTIR $\bar{\upsilon}$ = 3248 (m), 2222 (m), 1605 (m), 1502 (w), 1427 (w), 1339 (s), 1217 (m), 1160 (w), 1069 (m), 1018 (w), 883 (s), 766 (s), 691 (s) cm^{-1}.

$[Ag(pep)_2(MeCO_2)]\cdot 1.5H_2O$ (21) Colourless needles suitable for X-ray diffraction were obtained after 48 hours from acetonitrile or methanol. Yield: 60% based on silver salt. Bulk purity was determined by PXRD. Despite repeated attempts, satisfactory elemental analysis data could not be obtained for this material. FTIR $\bar{\upsilon}$ = 3363 (w), 3071 (w), 2223

(m), 1552 (m), 1497 (m), 1395 (m), 1214 (s), 1071 (w), 1007 (w), 922 (m), 834 (s), 760 (s), 690 (s) cm^{-1}.

$[Ag(pep)_2][CF_3CO_2]$ (22, 23) Colourless needle crystals **22** and orange needle crystals **23** were obtained in the same vial after 48 hours from acetonitrile or methanol. Elemental analysis determined the bulk sample to contain a small excess of silver triflate. Yield: 11.6 mg of crystalline material obtained. Bulk purity of **22** was determined by PXRD. Anal. Calcd (%) for $[Ag_{1.1}(pep)_2 \cdot 1.1(CF_3CO_2)]$: C, 56.32; H, 3.02; N, 4.66. Found: C, 55.94; H, 2.96; N, 4.62. FTIR $\bar{\upsilon}$ = 3443 (m), 3065 (w), 2219 (m), 1666 (s), 1606 (s), 1544 (w), 1502 (m), 1428 (m), 1180 (s), 1111 (s), 1021 (m), 924 (w), 829 (s), 795 (s), 752 (s), 717 (s), 688 (s) cm^{-1}.

$[Ag(pep)_2][CF_3SO_3]$ (24) Colourless irregular crystals suitable for X-ray diffraction were obtained after 48 hours from methanol or acetonitrile. Bulk purity was determined by PXRD. Yield: 99% based on the Ag salt. Anal. Calcd (%) for $C_{27}H_{18}AgF_3N_2O_3S$: C, 52.70; H, 2.95; N, 4.55. Found: C, 52.73; H, 2.86; N, 4.59. FTIR $\bar{\upsilon}$ = 2222 (m), 1608 (m), 1544 (w), 1503 (w), 1429 (m), 1252 (s), 1219 (s), 1172 (m), 1141 (m), 1069 (w), 1023 (s), 923 (w), 855 (w), 826 (s), 766 (s), 690 (s), 632 (s) cm^{-1}.

$2\{[Ag(pep)_2][Tos]\} \cdot pep$ (25) Colourless plate crystals suitable for X-ray diffraction were obtained after 48 hours from methanol or acetonitrile. Bulk purity was determined by PXRD. Yield: 42% based on the Ag salt. Anal. Calcd (%) for $C_{144}H_{108}Ag_4N_9O_{12}S_4$: C, 63.68; H, 4.01; N, 4.64. Found: C, 63.64; H, 3.96; N, 4.78. FTIR $\bar{\upsilon}$ = 3061 (w), 2219 (m), 2165 (w), 1601 (m), 1538 (w), 1498 (w), 1442 (w), 1413 (m), 1188 (s), 1117 (m), 1031 (m), 1009 (m), 922 (w), 821 (s), 761 (s), 677 (s) cm^{-1}.

[Ag(pep)(SCN)] (26) Colourless block crystals suitable for X-ray diffraction were obtained after 48 hours from acetonitrile. Yield: 99% based on the Ag salt. Bulk purity was determined by PXRD. Anal. Calcd (%) for $C_{14}H_9AgN_2S$: C, 48.72; H, 2.63; N, 8.12. Found: C, 47.19; H, 2.90; N, 7.86. FTIR $\bar{\upsilon}$ = 2220 (m), 2112 (s), 1601 (m), 1589 (m), 1538 (w), 1497 (w), 1441 (w), 1412 (m), 1213 (w), 1003 (w), 825 (s), 762 (s), 691 (s) cm^{-1}.

4.5. References

[1] Moulton, B.; Zaworotko, M. J., *Chem. Rev.,* **2001**, *101*, 1629-1658.

[2] Medici, S.; Peana, M.; Crisponi, G.; Nurchi, V. M.; Lachowicz, J. I.; Remelli, M.; Zoroddu, M. A., *Coordin. Chem. Rev.,* **2016**, *327-328*, 349-359.

[3] Jaros, S. W.; Guedes da Silva, M. F.; Florek, M.; Smolenski, P.; Pombeiro, A. J.; Kirillov, A. M., *Inorg. Chem.,* **2016**, *55*, 5886-5894.

[4] Deegan, C.; McCann, M.; Devereux, M.; Coyle, B.; Egan, D. A., *Cancer Lett.,* **2007**, *247*, 224-233.

[5] Yang, D.; Xu, W.; Cao, X.; Zheng, S.; He, J.; Ju, Q.; Fang, Z.; Huang, W., *Inorg. Chem.,* **2016**, *55*, 7954-7961.

[6] Pearson, R. G., *Inorg. Chem.,* **1988**, *27*, 734-740.

[7] Semitut, E.; Komarov, V.; Sukhikh, T.; Filatov, E.; Potapov, A., *Crystals,* **2016**, *6*, 138-150.

[8] Hong, M.-C.; Chen, L., *Design and Construction of Coordination Polymers*, Wiley, **2009**.

[9] Bassanetti, I.; Atzeri, C.; Tinonin, D. A.; Marchiò, L., *Cryst. Growth Des.,* **2016**, *16*, 3543-3552.

[10] Skoch, K.; Uhlik, F.; Cisarova, I.; Stepnicka, P., *Dalton Trans.,* **2016**, *45*, 10655-10671.

[11] Avdeeva, V.; Malinina, E.; Sivaev, I.; Bregadze, V.; Kuznetsov, N., *Crystals,* **2016**, *6*, 60-145.

[12] Feazell, R. P.; Carson, C. E.; Klausmeyer, K. K., *Eur. J. Inorg. Chem.,* **2005**, *2005*, 3287-3297.

[13] Sun, D.; Wei, Z.-H.; Wang, D.-F.; Zhang, N.; Huang, R.-B.; Zheng, L.-S., *Cryst. Growth Des.,* **2011**, *11*, 1427-1430.

[14] Ciunik, Z.; Desiraju, G. R., *Chem. Commun.,* **2001**, 703-704.

[15] C. R. Groom, I. J. Bruno, M. P. Lightfoot and S. C. Ward, *Acta Cryst.*, **2016**, B72, 171-179.

[16] Pyykkö, P., *Chem. Rev.,* **1997**, *97*, 597-636.

[17] Persson, I.; Nilsson, K. B., *Inorg. Chem.,* **2006**, *45*, 7428-7434.

[18] Pakiari, A. H.; Jamshidi, Z., *J. Phys. Chem. A.,* **2010**, *114*, 9212-9221.

[19] Pedicini, A. F.; Reber, A. C.; Khanna, S. N., *J. Chem. Phys.,* **2013**, *139*, 164317-164325.

[20] Batsanov, S. S., *Inorg. Mater.,* **2001**, *37*, 871-885.

[21] Khlobystov, A. N.; Blake, A. J.; Champness, N. R.; Lemenovskii, D. A.; Majouga, A. G.; Zyk, N. V.; Schröder, M., *Coord. Chem. Rev.,* **2001**, 222, 155-192.

[22] Campos-Fernandez, C. S.; Schottel, B. L.; Chifotides, H. T.; Bera, J. K.; Bacsa, J.; Koomen, J. M.; Russell, D. H.; Dunbar, K. R., *J. Am. Chem. Soc.,* **2005**, *127*, 12909-12923.

[23] Halper, S. R.; Do, L.; Stork, J. R.; Cohen, S. M., *J. Am. Chem. Soc.,* **2006**, *128*, 15255-15268.

[24] Gavezzotti, A.; Desiraju, G. R., *Acta Crystallogr. B,* **1988**, *44*, 427-434.

[25] Gavezzotti, A., *Chem. Phys. Lett.,* **1989**, *161*, 67-72.

[26] Shi, H.-Y.; Huang, Y.-L.; Sun, J.-K.; Jiang, J.-J.; Luo, Z.-X.; Ling, H.-T.; Lam, C.-K.; Chao, H.-Y., *RSC Adv.,* **2015**, *5*, 89669-89681.

[27] Bassanetti, I.; Mezzadri, F.; Comotti, A.; Sozzani, P.; Gennari, M.; Calestani, G.; Marchio, L., *J. Am. Chem. Soc.,* **2012**, *134*, 9142-9145.

[28] Bernstein, J.; Davis, R. E.; Shimoni, L.; Chang, N.-L., *Angew. Chem. Int. Ed.,* **1995**, *34*, 1555-1573.

[29] Chu, Q.; Swenson, D. C.; MacGillivray, L. R., *Angew. Chem. Int. Ed.,* **2005**, *44*, 3569-3572.

[30] Grepioni, F.; Cojazzi, G.; Draper, S. M.; Scully, N.; Braga, D., *Organometallics,* **1998**, *17*, 296-307.

[31] Knichal, J. V.; Gee, W. J.; Cameron, C. A.; Skelton, J. M.; Gagnon, K. J.; Teat, S. J.; Wilson, C. C.; Raithby, P. R.; Burrows, A. D., *Eur. J. of Inorg. Chem.,* **2017**, *2017*, 1855-1867.

[32] Desiraju, G. R.; Steiner, T., *The Weak Hydrogen Bond in Structural Chemistry and Biology*, Oxford University Press: Oxford, **1999**.

[33] Station 11.3.1, The Advanced Light Source, Berkeley Laboratory. Website: [www.als.lbl.gov/als/techspecs/bl11.3.1.html]

[34] Elangovan, A.; Wang, Y. H.; Ho, T. I., *Org. Lett.,* **2003**, *5*, 1841-1844.

[35] Zeidan, T. A.; Kovalenko, S. V.; Manoharan, M.; Clark, R. J.; Ghiviriga, I.; Alabugin, I. V., *J. Am. Chem. Soc.,* **2005**, *127*, 4270-4285.

Chapter 5

An iodine-induced cyclisation in a crystalline molecular flask

5.1. Introduction

One of the many uses of porous coordination polymers (PCPs) is their ability to act as crystalline molecular flasks (CMFs), otherwise known as crystalline molecular sponges.[1] As discussed in Chapter 1, highly crystalline structures can be used to organise guest molecules periodically within their pores. The open framework of a PCP can act as a matrix for isolating and ordering the structures of these moieties, and as a crystalline molecular containment unit. This concept has had broad scope for development as an analytical tool in the crystallographic visualisation of chemical processes where obtaining single crystal data of a target molecule presents a significant challenge.[2,3] It additionally offers potential for obtaining insights into chemically reactive species that can be stabilised within the pore network.

The stabilisation and crystallographic analysis of guest molecules within CMFs has enabled observation of a range of chemical transformations, including the conversion of amines into imines,[4,5] Diels–Alder reactions,[6] and brominations.[7] All these processes occurred upon immersing a CMF that contained a modified intercalated triphenylene moiety into solutions with appropriate chemical reactants. As illustrated in Figure 105, attaching an aromatic anchor such as a triphenylene on the reactive group is one of three common strategies employed for the successful infusion of a target species into CMFs. Phenyl groups for example promote π···π interactions and can act as anchors that stabilise the guest within the usually aromatic hydrophobic pores.[8] Another guest stabilisation strategy employed within CMF chemistry is the matching of spatial dimensions of guest molecules with pore cavities. The limited space within a filled cavity stabilises the guest enough for crystallographic observation. This approach has been used to probe photo-switching reactions,[9] catalyse isomerisation reactions,[10,11] separate organic dyes,[12] and identify organic species,[13,14] all with the notable advantage of requiring only nanogram to microgram quantities of the analyte. Intercalation of the

guest by direct self-assembly is also a viable strategy for guest-driven templating and avoiding interpenetration of the framework.[15]

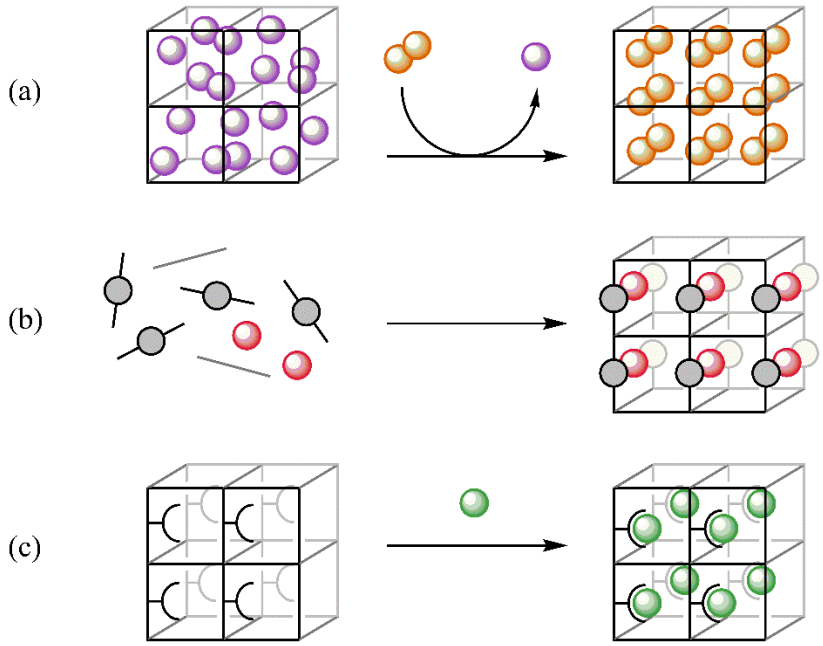

Figure 105: *A schematic representation of three approaches to include guest molecules within the pores of a PCP. Metal nodes in the framework are not represented and coloured spheres represent guest molecules. (a) Guest exchange resulting in ordering within the host framework; (b) self-assembly of the framework in the presence of a templating cartridge molecule (c) affixing a guest molecule at an anchoring point post-synthetically.*[16]

1,8-Bis(phenylethynyl)naphthalene (bpen) was chosen as a target guest molecule for inclusion within a CMF. Bpen undergoes a cyclisation by molecular iodine to give cyclised 7-iodo-12-phenylindeno[2,1-α]phenalene (ipp) as presented in Scheme 7. This thermal cyclisation is a useful step in the production of polycyclic aromatic hydrocarbons used for organic light-emitting diodes (OLEDs), solar cells, and near-infrared dyes.[17-19] The reaction of bpen to ipp has previously only been studied in solvent, requiring conditions of up to 50 °C and yielding an optimised yield of 92%.[20]

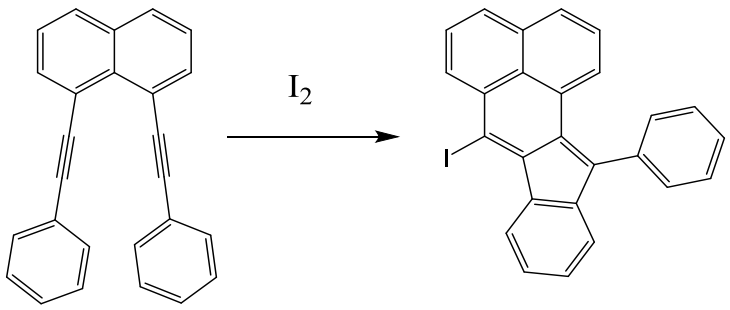

Scheme 7: *Cyclisation of bpen with iodine vapour to produce ipp.*

When two ethynyl units are *peri*- fixed in a macrocyclic structure, for example in bpen, the compound has high reactivity and tends to undergo intramolecular thermal cyclisation to relieve the steric congestion between the *peri*- triple bonds. The naphthalene and phenyl rings containing the ethynyl groups within bpen also act as a natural aromatic handle for π···π stabilisation within the pores of the prospective host, making bpen a good guest molecule candidate.

The porous CMF $[(ZnI_2)_3(tpt)_2]$ (tpt = 2,4,6-tris(4-pyridyl)-1,3,5-triazine), first reported by Fujita et al.,[21] was chosen as the flexible porous coordination polymer to accommodate the bpen to ipp cyclisation reported in this chapter (Figure 106, top). $[(ZnI_2)_3(tpt)_2]$ CMF is derived from tpt linkers and zinc halide nodes, which through coordination bonding form interpenetrated 3-connected 2D nets consisting of large channels that propagate down the crystallographic *b* axis and the [101] direction, and are able to swell and contract upon solvent addition and loss,[22] thus undergoing guest exchange in a single-crystal to single-crystal manner (Figure 106, bottom).[23]

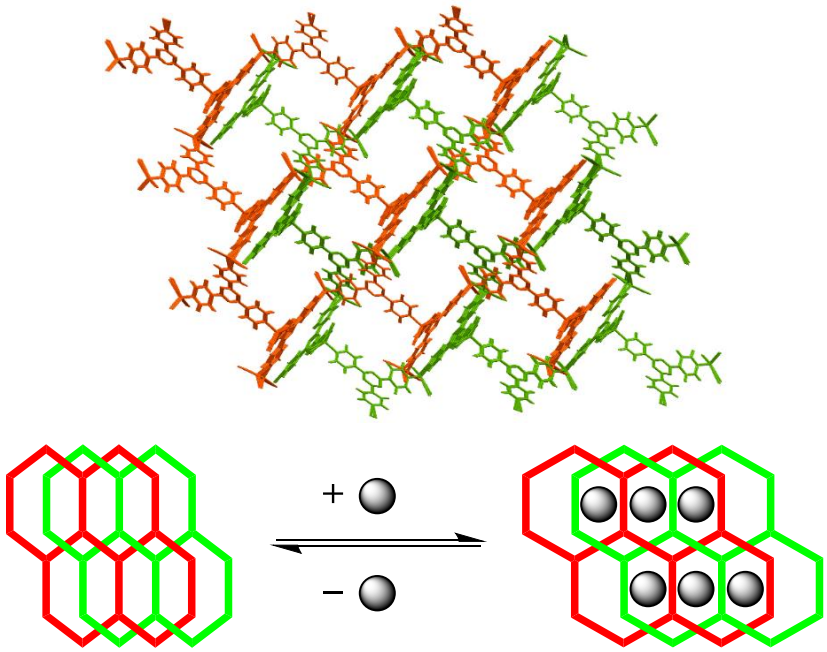

Figure 106: *Top: Channels of the interpenetrated [(ZnI$_2$)$_3$(tpt)$_2$] framework as viewed down the crystallographic* b *axis. Interstitial solvent molecules have been omitted for clarity.*[24] *Bottom: Representation of [(ZnI$_2$)$_3$(tpt)$_2$] framework expanding on the absorption of guest molecules and compressing on the desorption of guest molecules.*

The channels within [(ZnI$_2$)$_3$(tpt)$_2$] are of a sufficient size to allow bpen to infuse into the crystals and are flexible enough to allow for subsequent transformation reactions. [(ZnI$_2$)$_3$(tpt)$_2$] has been employed in many guest encapsulation studies utilising its flexibility.[25-27] These reactions have involved suspending the CMF in a solution containing the desired reactant. No example of a chemical reaction combining gas-phase reagents and a CMF has been reported, despite the common use of solid-gas reactivity in the field of organometallics[28] and porous coordination polymer gas adsorption.[29-31] Avoiding the use of solvents in such solid–gas processes has potential economic and environmental benefits.

A successful conversion of bpen to ipp within a CMF was initiated in this work at room temperature and pressure by the passive infusion of molecular iodine vapour.

5.2. Results and discussion

An iodine-vapour mediated cyclisation of 1,8-bis(2-phenylethynyl)naphthalene (bpen) to 7-iodo-12-phenylindeno[2,1-α]phenalene (ipp) is reported within this chapter. The reaction takes place within the previously reported $[(ZnI_2)_3(tpt)_2]\cdot x(G)$ (tpt = 2,4,6-tri(4-pyridyl)-1,3,5-triazine) crystalline molecular flask (CMF), where G=guest. The cyclisation reaction was found to occur quantitatively, under mild conditions and in the absence of solvent.

5.2.1. Solid-gas reaction between bpen and iodine

To test whether employing a CMF is necessary for cyclisation of bpen in the solid state, single crystals of pure bpen were placed in a small open vial, which was placed into a larger vial containing iodine crystals. The larger vial was closed so that an iodine atmosphere was allowed to develop, surrounding the single crystals of bpen. The reaction was monitored over the course of seven days, during which the crystals progressively became darker over time. At the end of the seven days the sample had lost all crystallinity and had changed in colour from yellow to black, marking a reaction with the iodine vapour. The product was digested and then subjected to ^{1}H NMR analysis to measure the yield of conversion, however, the sample was only partially soluble and no identifiable compounds were found in the proton spectrum. This is likely due to the formation of side products from intermolecular polymerisation of closely-packed bpen molecules within the solid state, in which the closest intermolecular ethynyl-ethynyl contact distance is 4.7 Å (Figure 107), mediated by the highly reactive iodine vapour. Intramolecular iodine-mediated ethynyl group polymerisation reactions have been reported previously in solution.[32]

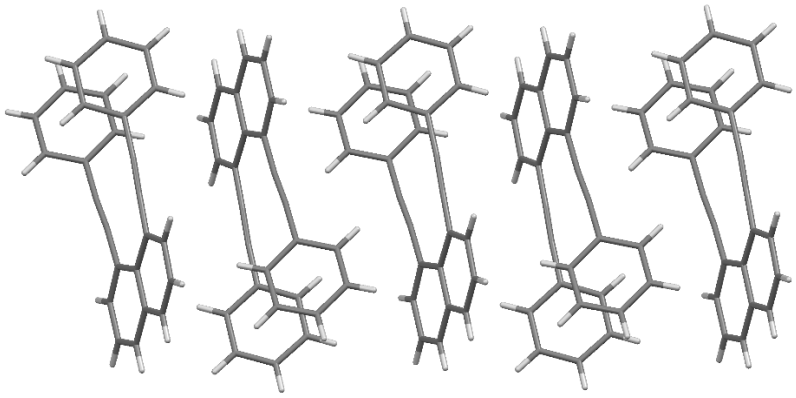

Figure 107: *Stacked 1,8-bis(2-phenylethynyl)naphthalene (bpen) molecules within a crystalline sample of bpen.*

Therefore, the need for bpen to be incorporated into the CMF also allows for its selective cyclisation with iodine vapour in the solid state was confirmed, this isolation preventing major side reactions from taking place, and for visualisation of the reaction via crystallographic analysis.

5.2.1. CMF activation and bpen loading

The $[(ZnI_2)_3(tpt)_2]$ CMF framework was synthesised by the diffusion of a methanol solution of ZnI_2 layered onto a nitrobenzene/methanol solution of tpt. The yellow crystals obtained were then activated by immersion in cyclohexane for one week at 50 °C to replace the nitrobenzene and methanol with an inert non-polar solvent, as reported by Fujita et al.[13] Bulk purity analysis of the activated CMF framework was carried out by PXRD (Figure 108), although due to the inherent flexibility of the framework coupled with the volatility of cyclohexane, matching the powder patterns is a considerable challenge. However, the overall profiles of the calculated and experimental patterns are similar and no major additional peaks beyond 40° were observed, indicating that the crystalline bulk sample does not contain impurities which would affect the guest uptake and subsequent iodination.

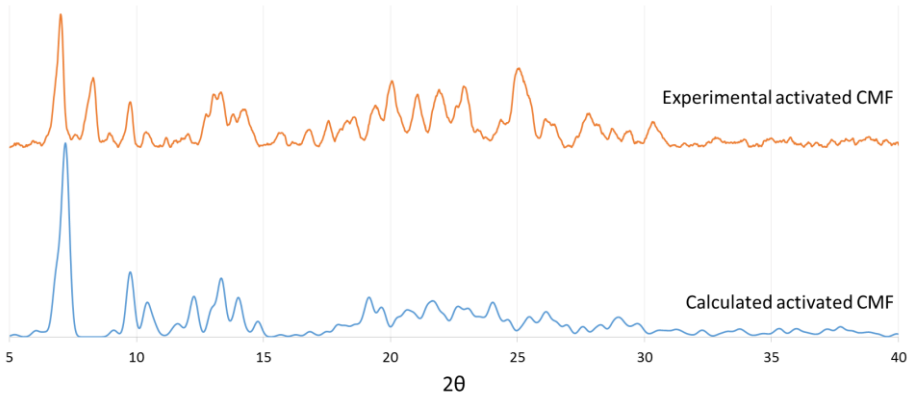

Figure 108: *Calculated and experimentally derived powder patterns of the activated* $[(ZnI_2)_3(tpt)_2]$ *CMF framework.*

Subsequently immersing the crystals loaded with cyclohexane into a concentrated solution of bpen in chloroform for two days resulted in the crystals changing colour from pale to dark yellow, marking the enclathration of the framework and bpen guest. Analysis of the yellow crystals by single-crystal X-ray diffraction determined a high bpen loading in the CMF, and along with elemental analysis revealed an occupancy of 0.75 with the remainder of the pores being occupied by chloroform and water, giving an overall composition of $[(ZnI_2)_3(tpt)_2]\cdot 0.75\,\text{bpen}\cdot 2.25\,CHCl_3\cdot H_2O$ (**27**). The asymmetric unit of **27** contains three ZnI_2 units bridged by two tpt ligands as well as one interstitial bpen molecule, two chloroform molecules and one disordered water molecule (Figure 110). As expected, the original $[(ZnI_2)_3(tpt)_2]$ framework remains intact and no cyclohexane, nitrobenzene or methanol molecules are observed in the pores. The location of bpen guests within the CMF framework **27** is shown in Figure 109.

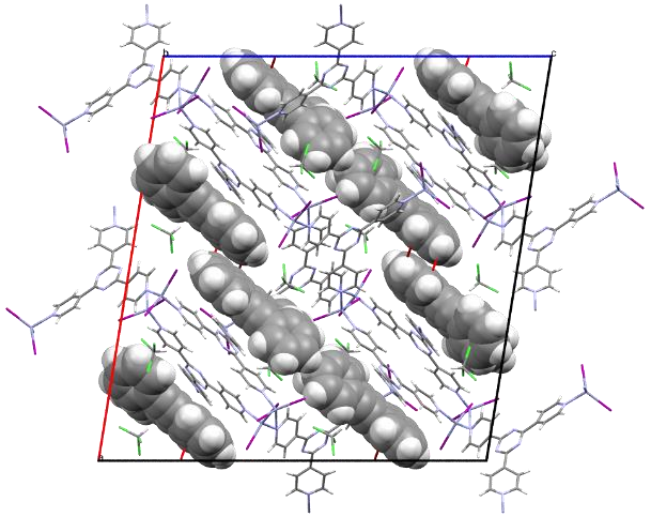

Figure 109: *The location of the bpen guests (space-filled molecules) within the* $[(ZnI_2)_3(tpt)_2]$ *CMF framework* **27** *(wire-frame representation).*

Although the bpen carbon atoms within **27** are poorly defined due to the molecule adopting multiple orientations, causing the atom ellipsoids to become elongated, the bpen guest takes part in intramolecular hydrogen bonding from adjacent chloroform molecules and intramolecular π···π interactions from parallel tpt linkers (Figure 110). The chloroform hydrogen atom attached to C65 is well aligned to participate in a weak C-H···π hydrogen bond to an alkyne group of bpen equidistant between C56 and C57, with a C65···π7 observed distance of approximately 3.46 Å, where π7 is a calculated centroid between atoms C56 and C57. This hydrogen bond distance corresponds with literature reports of weak C–H···π hydrogen bond lengths, where the average C···π distance is 3.69 Å.[33] The intercalated bpen is also involved in a pair of π···π parallel-displaced stacking interactions between the adjacent tpt ligand and the naphthalene ring (with a π3···π5 3.8 Å ring inter-centroid distance) and one alkyne group (with a π6···π8 3.8 Å ring–alkyne inter-centroid distance) of bpen. These interactions, coupled with parallel displaced π1···π3 and π2···π4 interactions between naphthalene groups of interstitial adjacent bpen molecules (naphthalene plane to plane distance of 3.73 Å, plane offset 2.34 Å) serve to order the guests within the pores of **27**.

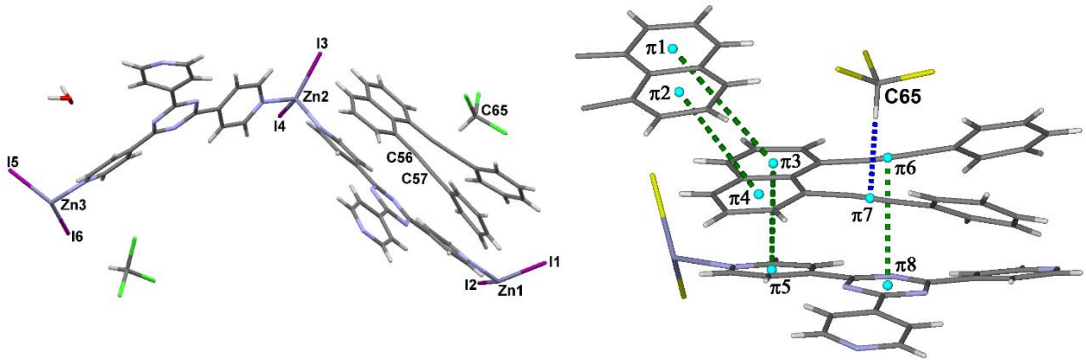

Figure 110: *Left: Orientation of the bpen molecule within the asymmetric unit of* **27**. *Cl atoms are in green, I atoms are coloured purple. Right: π···π interactions and hydrogen bond stabilising the intercalated bpen guest. Cl and I atoms are in yellow.*

5.2.2. Exposure of the bpen loaded CMF to iodine vapour

In order to expose the guest bpen molecules to iodine vapour, crystals of **27** were removed from their mother liquor, briefly dried in air, and placed in a small open glass vial. This small vial was transferred into a larger vial containing solid iodine crystals and sealed, creating an atmosphere of iodine vapour in air capable of infusing into the crystals. Over several days the crystals changed colour from yellow to black, coinciding with the uptake of molecular iodine.

Single-crystal X-ray diffraction was performed on the black crystals after seven days, resulting in the identification of the original CMF framework containing molecular iodine and instead of bpen a region of highly disordered electron density, which was identified as the likely location of the guest cyclisation product ipp (7-iodo-12-phenylindeno[2,1-α]phenalene), as presented in Scheme 7. As expected, the structure of the resultant CMF framework is comparable with that of **27**, and the proposed ipp guests remain in similar interstitial orientations (Figure 112).

Although the overall quality of the X-ray data was relatively low, the presence of ipp was unambiguously confirmed by a combination of analytical techniques from which the molecular formula was determined to be $[(ZnI_2)_3(tpt)_2]\cdot 0.75ipp\cdot 0.25CHCl_3\cdot 2I_2$ (**28**). This result was based on NMR spectroscopy and mass spectroscopy to determine the nature of the guest species, as well as crystallographic and thermogravimetric evidence to ascertain the ratios of iodine and solvent molecules, the results of which will be discussed throughout this chapter.

The asymmetric unit of **28**, which includes one heavily restrained ipp molecule modelled within the region of highly disordered electron density, is shown in Figure 111. The asymmetric unit contains three ZnI_2 units bridged by two tpt ligands as well as one interstitial ipp molecule, disordered molecular iodine and one disordered water molecule. It must be stressed that the ipp moiety shown in Figures 111 and 112 serves only as a guide of its likely location, and does not constitute definitive crystallographic evidence. The crystallographic modelling for the disordered ipp containing structure **28** was performed by Dr. Helena Shepherd.

Although the gross structure of the CMF does not change during the transition of bpen to ipp, the unit cell does increase slightly from 33.69 Å in **27** to 34.59 Å in **28** along the crystallographic *a* axis. This coincides with the slight increase in the unit cell volume, 15570.2(3) $Å^3$ in **27** to 15823.2(11) $Å^3$ in **28**. Both structures retain the same orthorhombic space group *C* 2/c.

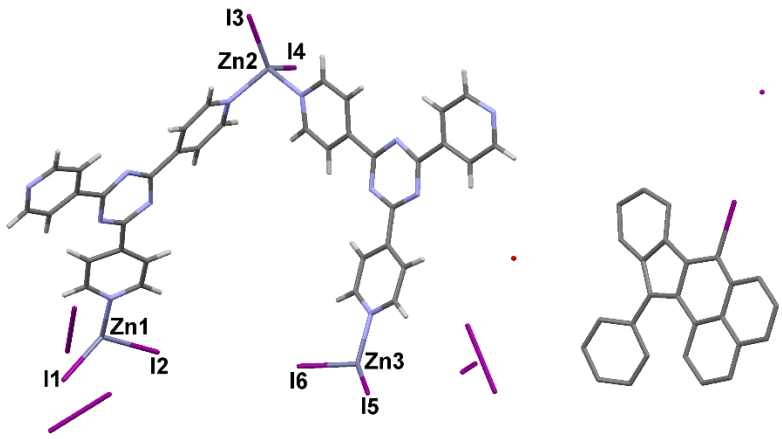

Figure 111: *The estimated position and orientation of ipp within the asymmetric unit of* **28**. *A disordered water molecule and iodine atom are shown as red and purple dots, respectively.*

The increase in disorder of the cyclised ipp guest within the crystalline structure **28** relative to that of bpen in **27** may be partially due to the displacement of ordering solvent molecules by the molecular iodine. While the substantial disorder prevented the unambiguous identification of a single location for the ipp molecule, a structural model is presented in Figure 112 in which the partially occupied, heavily restrained ipp molecule is included to illustrate its likely location within the pore of the ordered framework.

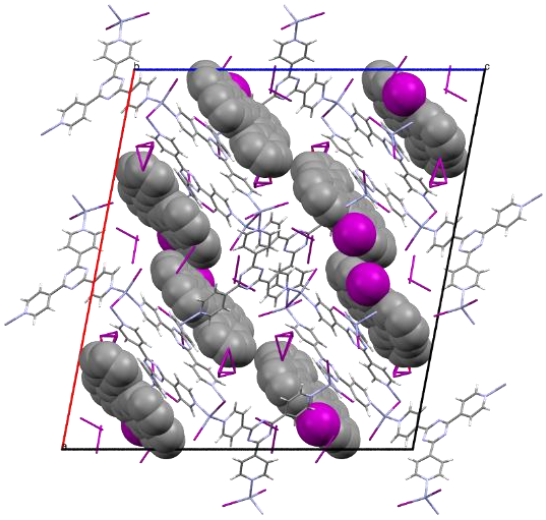

Figure 112: *The likely locations of the cyclised product ipp (space-filled molecules) within the pores of* $[(ZnI_2)_3(tpt)_2]$ *CMF framework* **28** *(wire-frame representation).*

The same model of structure **28** with the ipp fragments excluded was also examined for comparison. In both structures molecular iodine is observed within the pores, disordered over several identifiable and discrete positions. In each case, the total

occupancy of I_2 is between 1.75 and 2.1 molecules per $[(ZnI_2)_3(tpt)_2]$ unit, although the highly disordered nature of this material means that these values should be interpreted with caution. The amount of molecular iodine adsorbed into the pores of **27** per sample would also be expected to vary experimentally depending on the single crystal size distribution, amount of iodine provided to the sample and the amount of time exposed to the iodine vapour.

To further develop evidence for the existence of the cyclised ipp product within **28**, single crystals of **28** were digested in $[D_7]$DMF, and the resulting mixture was analysed by ^{1}H NMR spectroscopy. The spectrum of **28** contained no evidence of bpen; however, two new cyclised species were identified in a ratio of 1.6:1. The digested sample was then subjected to column chromatography using hexane as the eluent to separate the two components. The major component eluted first and was determined by H^1 NMR to be the expected cyclisation product 7-iodo-12-phenylindeno[2,1-a]phenalene (ipp). The minor component from the chromatography column was only isolable in trace amounts, but high-resolution mass spectrometry (Figure 135, Appendix I) determined the unknown molecular ion to have an *m*/*z* ratio of 509.0005 ([*M*+Na] = 509.0014). This species was matched to an oxidised product of ipp, yielding 12-hydroxy-7-iodo-2-phenylindeno[2,1-α]phenalen-1(12*H*)-one (hipp) (Scheme 8) that is formed by reaction with molecular oxygen. The conversion of ipp into hipp in the presence of molecular oxygen has been observed previously,[32] albeit in solution and only after several weeks.

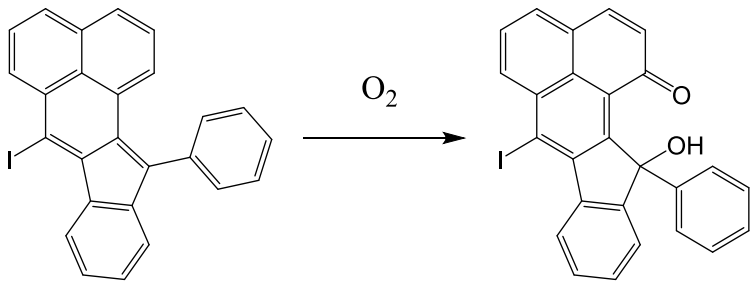

ipp hipp

Scheme 8: *Oxidation of ipp to hipp by molecular oxygen.*

The FTIR spectra of the isolated products ipp and hipp were recorded, in which an additional broad band at 3291 cm^{-1} corresponds to the –OH group and a band at 1734 cm^{-1} can be attributed to the ketone group within the oxidised hipp molecule. Proton ^{1}H NMR spectra of the two isolated products were also taken, and the proton peaks of each were matched with peaks of the original digested CMF **28** spectrum

(Figure 113). While the peak positions within the ipp spectrum match those within CMF **28**, peak positions of pure hipp have shifted both upfield and downfield compared to those corresponding to this moiety hosted within CMF **28** as indicated by the arrows above the highlighted parts of the hipp spectrum. These shifts are likely due to coordination of digested zinc(II) centres to the carbonyl groups within solution, affecting the relative shielding environment of the molecule. The peak positons of hipp from 7.8 ppm to 7.4 ppm are obscured by signals corresponding to ipp. Prominent signals at *ca* 8.2, 8.9 and 9.2 ppm correspond to DMF-d7 and the aromatic signals from tpt, respectively.

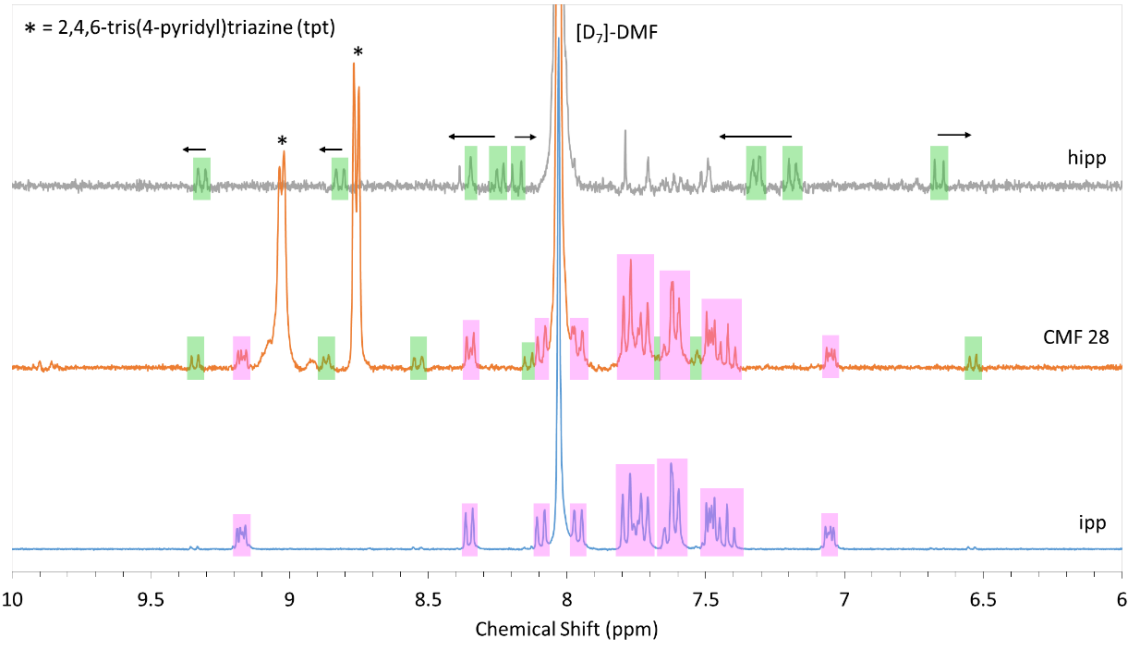

Figure 113: *^{1}H NMR spectrum of* **28** *digested in [D$_7$]DMF. Spectra of pure ipp and hipp are included as a reference. Proton peak positions for ipp are matched in pink and peak positions for hipp are matched in green.*

These results demonstrate the ability of the CMF to host not only the iodine-induced solvent-free quantitative cyclisation of bpen, but also consecutive gas-mediated reactions (ipp to hipp) in an un-optimised yield of more than 35%, which greatly exceeds the trace amounts achieved from a solvated state in past reports.[32]

To better quantify the initial cyclisation of bpen to ipp, the iodine infusion experiment was repeated in the inert argon atmosphere of a glove box, to avoid unwanted subsequent oxidation of the guest molecules to hipp. Single crystals held in an inert environment of iodine vapour were analysed by ^{1}H NMR spectroscopy at intervals of

12 hours, 3 days, and 7 days (Figure 114). Digestion in [D_7]DMF was undertaken in the glove box, and ^{1}H NMR samples were protected from atmospheric O_2 using Youngs NMR tubes. Pure crystalline ipp obtained from solution-based reactions, detailed in Appendix I, was also dissolved in [D_7]DMF in the absence of O_2 and included as a reference.

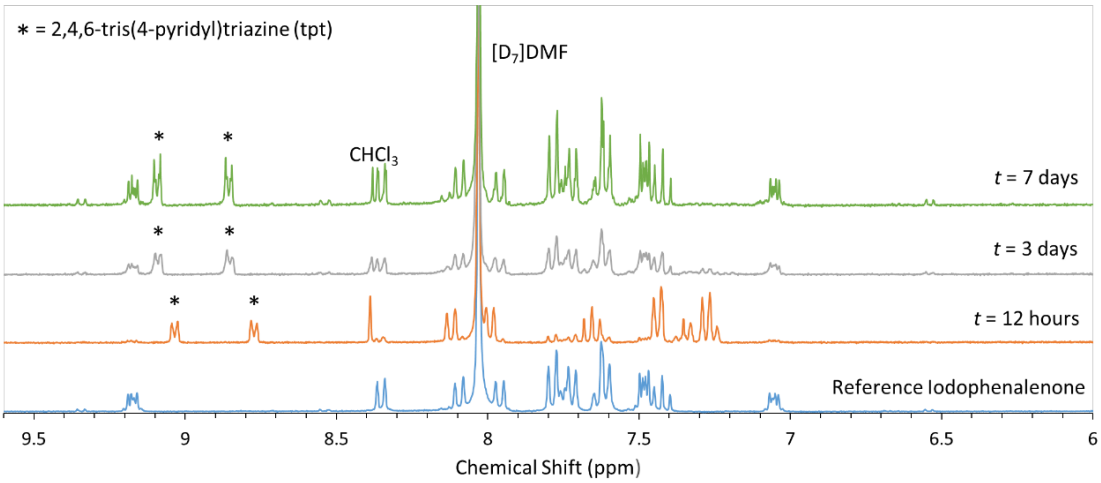

Figure 114: *^{1}H NMR spectra for CMF* **27** *digested in [D_7]DMF. The degree of cyclisation was evaluated at t = 12 h, 3 days, and 7 days. The spectrum of 7-iodo-12-phenylindeno[2,1-a]phenalene (ipp) is included as a reference.*

The results show that very little conversion to the ipp product (<5 %) had occurred after 12 hours despite the dramatic change in crystal colour from yellow to black, suggesting that either iodine infuses into the crystal prior to mediating the cyclisation, or that only the surface of the crystals has undergone reaction at this time. After three days, however, 85% of the loaded bpen had cyclised to ipp, as determined by comparing the ratio of the residual *meta*-phenyl resonances of bpen at δ 7.26 ppm to the new aromatic resonances of ipp at δ 7.05 ppm and δ 9.17 ppm. After seven days, bpen was no longer observable spectroscopically, and apart from residual tpt derived from digestion of the CMF and a signal at δ 8.39 ppm which was assigned to chloroform, ipp was the dominant species observed. Interestingly, despite rigorous exclusion of oxygen from the point of iodine introduction, trace amounts of hipp were still observed in the spectra recorded after three and seven days. These findings can be attributed to the uptake of small amounts of molecular oxygen by **27** during the air-drying step prior to transfer into the glove box.

When the bpen-infused CMF **27** was kept in atmospheric air for twelve hours without first being exposed to iodine gas, no evidence of hipp was observed, demonstrating the necessity of the iodine-mediated cyclisation step to occur prior to hipp formation. This

supports the conclusion that ipp is initially formed in the iodine-gas-mediation cyclisation with subsequent transformation to hipp within the molecular flask in the presence of O_2.

A mechanism has been previously proposed for this two-step process by Wu et al.[32] shown below in Scheme 9. The cyclisation of bpen to ipp is triggered by an addition of one iodine atom to an ethynyl group. The resulting carbocation causes a cascading cyclisation throughout the molecule, which ends in the liberation of a proton. The remaining iodide likely forms gaseous hydrogen iodide, which is liberated from the CMF under inert conditions. Under aerobic conditions, the cyclised product undergoes a Diels–Alder cycloaddition, and subsequent rearrangement, with molecular atmospheric oxygen to give the oxidised hipp product. This mechanism is consistent with the present observation of the bpen-ipp-hipp sequential reaction within the CMF mediated by iodine vapour.

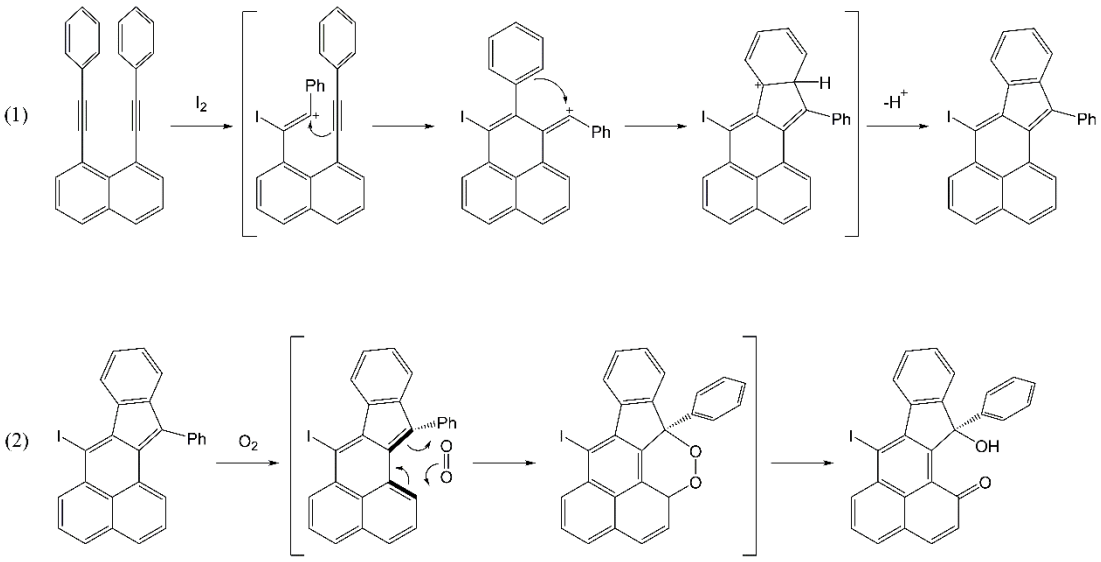

Scheme 9: *Previously reported mechanism of the cyclisation of bpen to ipp by molecular iodine (1) and the subsequent oxidation of ipp to hipp by atmospheric oxygen (2).*[32]

Crystals of the bpen-loaded CMF **27** were also exposed to bromine vapour. Using the same setup as in the iodine vapour method, several drops of bromine were allowed to vapourise into a crystalline sample of **27**. After 24 hours the sample turned from yellow to brown and lost all crystallinity. This is likely due to the higher reactivity of molecular bromine over iodine. The resulting sample was not amenable to characterisation.

5.2.3. Investigation into the degree of solvation within loaded CMFs

To accurately evaluate the degree of solvation within CMFs **27** and **28**, thermogravimetric analysis (TGA) was employed (Figure 115).

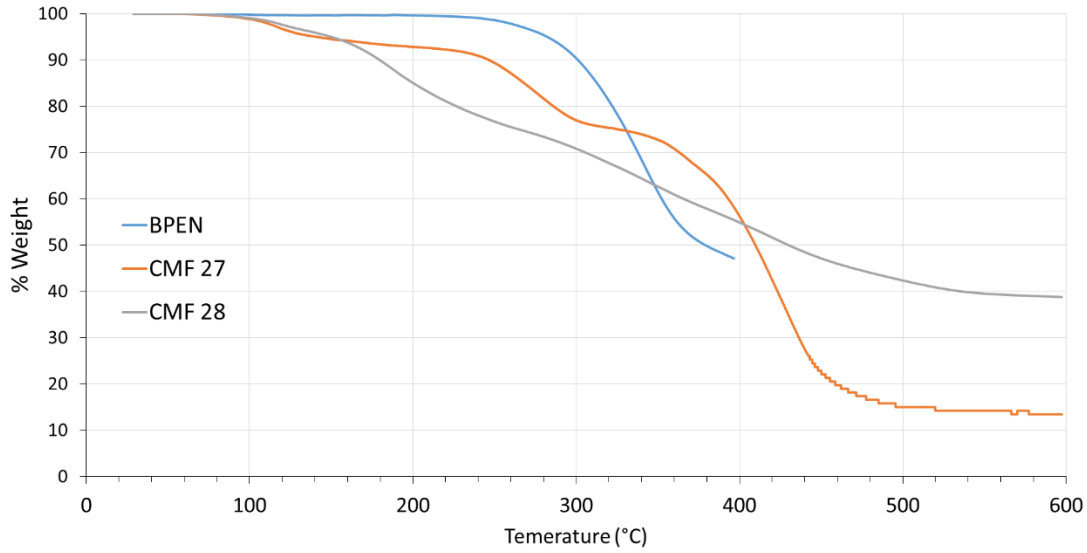

Figure 115: *Overlayed thermogravimetric traces of bpen,* **27** *and* **28**.

TGA of bpen prior to loading into the CMF showed that the guest is thermally stable up to 230 °C, after which time it loses approximately 50% of its mass up to 400 °C. CMF **27** loses 8.1% by mass in two steps up to a temperature of 200 °C, which is consistent with the crystallographic assignment of two and a quarter chloroform molecules and one water molecule (predicted: 11.8%). The iodine-infused CMF **28** was found to have lost 19.9% of its mass by 230 °C, which is consistent with the presence of two equivalents of molecular iodine within the CMF (predicted: 20.0%).

The elemental analysis results for framework **27** were indicative of incomplete bpen loading, likely involving substitutional disorder of chloroform, with a ratio of 75% bpen to 25% $CHCl_3$, providing matching C, H, and N percentages (Calcd [%]: C 32.79, H 1.92, N 7.95; found [%]: C 32.76, H 1.68, N 7.95). This composition was used to fix the occupancy of the bpen molecule in **27** in the crystal structure, but it should be noted that it is possible to obtain variation between individual crystals with regard to guest loading, which is a known phenomenon in CMF systems.[13] Elemental analysis performed on **28** was also consistent with a bpen loading ratio of 0.75, and 0.25 residual chloroform based on ^{1}H NMR spectroscopic and thermogravimetric evidence (Calcd [%]: C 27.22, H 1.45, N 6.83; found [%]: C 27.01, H 1.29, N 7.34).

5.3 Conclusions

1,8-Bis(2-phenylethynyl)naphthalene (bpen) guest molecules were loaded into a $[(ZnI_2)_3(tpt)_2]$ (tpt = 2,4,6-tri(4-pyridyl)-1,3,5-triazine) crystalline molecular flask (CMF) and shown to undergo two sequential gas-mediated reactions that occurred under mild conditions, when exposed to iodine vapour and atmospheric oxygen. The reaction of the bpen guest molecules occurred in the absence of solvent and without the need of a catalyst. In the absence of the molecular flask, no significant reaction was observed upon exposing bpen crystals to iodine vapour. Powder diffraction patterns for the frameworks in this chapter were not collected as the flexible nature of the $[(ZnI_2)_3(tpt)_2]$ frameworks lead to poor quality PXRD patterns.

In the absence of atmospheric oxygen, bpen guest molecules within the CMF **27** were converted into the cyclised product 7-iodo-12-phenylindeno[2,1-α]phenalene (ipp), resulting in CMF **28**, by molecular iodine after seven days as monitored by ^{1}H NMR spectroscopy. A 100% conversion of bpen to ipp was found in the CMF, compared to a previously reported optimised yield of 92% conversion in solution.[20] Single-crystal X-ray and NMR data confirmed full penetration of the molecular iodine throughout the CMF. Molecular formulae for both **27** and **28** were confirmed through thermogravimetric and elemental analysis.

Exposing **27** to iodine vapour in the presence of atmospheric oxygen resulted in a process of sequential gas-mediated reactions, first iodine-mediated conversion of bpen into ipp, followed by an oxidation of ipp to 12-hydroxy-7-iodo-2-phenylindeno[2,1-α]phenalen-1(12*H*)-one (hipp). The latter oxidation step proceeded with a conversion of more than 35% after seven days, greatly improving on previously reported solution-based reactions, in which only trace amounts were obtained after a number of weeks.[32]

This work represents the first report of sequential gas-mediated reactions in a CMF system, and is a good demonstration of the potential for undertaking cascade reactions in a crystalline “one-pot” flask.

5.4. Experimental

Starting materials and solvents were purchased from commercial sources and were used without further purification. The synthesis and characterisation of bpen, the $[(ZnI_2(tpt)_2)_3]$ CMF were based on reports from literature,[13] as was the activation of the CMF. X-ray diffraction data collections for **27** and **28** were collected on an Agilent Supernova diffractometer at the University of Bath using Mo Kα radiation, the crystal being cooled by an Agilent Cryojet. Full crystallographic details can be found in Appendix II.

Nuclear magnetic resonance spectra were obtained on a Bruker Avance 300 MHz Ultrashield NMR spectrometer. Infrared spectra were recorded on a PerkinElmer Spectrum 100 spectrometer equipped with an ATR sampling accessory. Elemental analyses were performed on a CE-440 elemental analyser (Exeter Analytical). Melting points were determined on a Stuart SMP10 Digital melting point apparatus. Thermogravimetric analysis (TGA) was performed using a Setsys Evolution TGA 16/18 from Setaram with Calisto software to collect and process the data. Samples were placed in 170 μL alumina crucibles and prior to experiments the analytical chamber was purged from ambient air using argon flow at 200 mL/min for 40 min. Sample pans were analysed under argon flow at 20 mL/min. Mass spectrometry data were recorded on a Bruker MicroTOF spectrometer. Melting points were determined on a Stuart SMP10 Digital melting point apparatus.

1,8-bis(phenylethynyl)naphthalene (bpen) To a solution of 1,8-diiodonaphthalene (380 mg, 1 mmol) and ethynylbenzene (408 mg, 1 mmol) in dry NEt_3 (40 mL), $Pd(PPh_3)_2Cl_2$ (35.1 mg, 0.05 mmol), CuI (19.1 mg, 0.10 mmol) and PPh_3 (26.2 mg, 0.10 mmol) were added at ambient temperature. The reaction mixture was purged with nitrogen for 10 minutes. The flask was then sealed and the stirring solution heated at 40 °C overnight or until completion determined by TLC. The NEt_3 was removed and the residue was dissolved in ether (40 mL), washed with water (2 × 20 mL), and dried with $MgSO_4$. After filtration, the ether was removed under reduced pressure and the residue was purified via flash chromatography on silica gel (hexane : DCM 98:2). Yield: 72%, m.p. 99 – 100 °C. Anal. Calcd (%) for $C_{26}H_{16}$ C 95.09, H 4.91; found C 94.90, H 5.03. ^{1}H NMR (300 MHz, $CDCl_3$) δ 7.91 (dd, 2H, J = 7.2, 1.1 Hz), 7.85 (dd, 2H, J = 8.3, 1.1 Hz), 7.48 (dd, 2H, J = 8.3, 7.2 Hz), 7.36 (m, 4H), 7.24 – 7.18 (m, 2H), 7.13 (m, 4H). ^{13}C NMR (75 MHz, $CDCl_3$) δ_C 134.9, 131.5, 129.6, 127.9, 127.8, 125.6, 123.7,

120.8, 96.6. FTIR $\bar{\upsilon}$ =3051 (w), 2924 (w), 2208 (w), 1951 (w), 1881 (w), 1596 (w), 1568 (m), 1487 (m), 1441 (m), 1376 (m), 1208 (w), 1176 (w), 1068 (m), 1028 (m), 916 (m), 825 (s), 792 (w), 751 (s), 714 (w), 688 (s), 610 (m) cm^{-1}. Analytical data match those reported previously.[34]

7-iodo-12-phenylindeno[2,1-*α*]phenalene (ipp) To a solution of 1,8-bis(phenylethynyl)naphthalene (50 mg, 0.15 mmol) in chloform (3 mL), a molar excess of iodine was added (77 mg, 0.30 mmol). The solution was heated to 50 °C and stirred for 48 hours. Afterwards, the reaction mixture was cooled and a saturated aqueous solution of sodium thiosulfate was added. The organic layer was washed with brine, dried over anhydrous $MgSO_4$, and then evaporated to dryness in vacuum. The residue was purified by flash column chromatography through silica gel with hexane as the eluent to give the product as a red solid. Analytical data match those reported previously.[32] Due to the small yields and limited amounts of material to work with, elemental analysis, melting point and ^{13}C NMR could not be obtained. ^{1}H NMR (300 MHz, DMF-d_7) δ 9.17 (dd, 2H, *J* = 5.7, 3 Hz), 8.35 (d, 1H, *J* = 7.5 Hz), 8.10 – 7.95 (m, 1H), 7.75 (m, 4H), 7.62 (m, 2H), 7.46 (m, 3H), 7.05 (dd, 2H, *J* = 5.5, 3.2 Hz). FTIR $\bar{\upsilon}$ = 3040 (w), 2924 (w), 1561 (m), 1487 (w), 1439 (m), 1306 (w), 1231 (s), 1183 (s), 1118 (s), 981 (s), 859 (w), 828 (m), 763 (s), 700 (s) cm^{-1}.

12-hydroxy-7-iodo-2-phenylindeno[2,1-α]phenalen-1(12*H*)-one (hipp) Crystals of **28** were exposed to atmospheric conditions for seven days. The sample was then digested in DMF and subjected to column chromatography through silica gel with hexane as the eluent. An un-optimised yield of 35% was obtained. Due to the small yields and limited amounts of material to work with, elemental analysis, melting point and ^{13}C NMR could not be obtained. ^{1}H NMR (300 MHz, DMF-d_7) δ 9.31 (d, *J* = 7.9 Hz, 1H), 8.82 (m, 2H), 8.28 (m, 4H), 7.79 – 7.71 (m, 3H), 7.52 – 7.48 (m, 1H), 7.34 – 7.17 (m, 2H), 6.66 (d, *J* = 9.4 Hz, 1H). *m/z* (ESI) 144 (15%), 360 (13%), 509 (M^+, 100%), 510 (27%). FTIR $\bar{\upsilon}$ = 3291 (b), 2920 (m), 2850 (m), 1734 (m), 1628 (s), 1547 (s), 1461 (s), 1376 (m), 1260 (s), 1179 (w), 1051 (s), 1027 (s), 973 (m), 924 (w), 905 (w), 842 (s), 797 (s), 768 (m), 751 (w), 699 (s) cm^{-1}.

[(ZnI_2(tpt)$_2$)$_3$] Single crystals of the CMF were prepared by layering a MeOH solution of ZnI_2 (9.6 mg in 1 mL) onto a nitrobenzene solution of 2,4,6-tri(4-pyridyl)-1,3,5-triazine (6.3 mg in 4 mL). After the solution was allowed to stand for seven days, the crystals formed were isolated in 63% yield, by filtration. The resulting CMF was activated by

immersion in cyclohexane for one week at 50 °C. Synthesis and subsequent activation of the CMF was based on previous methodology, and analytical data matched those reported.[13]

$[(ZnI_2)_3(tpt)_2]\cdot 0.75bpen\cdot 2.25CHCl_3\cdot H_2O$ (27) Single crystals of $[(ZnI_2(tpt)_2)_3]$ were activated by performing a solvent exchange by immersing the crystals in cyclohexane for one week at 50 °C. The activated crystals were then subsequently immersed in a concentrated solution of 1,8-bis(phenylethynyl)naphthalene (bpen) in chloroform for two days. A colour change was observed from colourless to yellow indicating the successful loading of bpen. Anal. Calcd (%) for $[(ZnI_2)_3(tpt)_2]\cdot 0.75bpen\cdot 2CHCl_3\cdot H_2O$ C 27.22, H 1.45, N 6.83; found C 27.01, H 1.29, N 7.34. ^{1}H NMR (300 MHz, DMF-d_7) δ 9.18 (m, 2H), 9.09 (d, J = 5.3 Hz, 6H), 8.85 (d, J = 4.9 Hz, 6H), 8.36 (m, 1H), 8.13 – 7.95 (m, 1H), 7.70 (m, 4H), 7.62 (m, 2H), 7.47 (m, 3H), 7.06 (m, 2H). FTIR $\bar{\upsilon}$ = 3051 (w), 2918 (m), 2849 (m), 1619 (w), 1568 (w), 1516 (s), 1487 (m), 1441 (m), 1422 (m), 1375 (s), 1345 (m), 1212 (m), 1059 (m), 1026 (m), 915 (w), 826 (m), 804 (s), 751 (s), 705 (m), 690 (m), 668 (m), 655 (s) cm^{-1}.

$[(ZnI_2(tpt)_2)_3]\cdot 0.75ipp\cdot 0.25CHCl_3\cdot 2I_2$ (28) Single crystals of **27** were placed in a small open vial immersed in minimal chloroform and transferred into a glovebox. This vial was placed in a larger vial containing iodine crystals and sealed. The iodine crystals were allowed to create an iodine vapour atmosphere around the crystals for seven days. A colour change from yellow to black was observed, and a 100% conversion was determined by ^{1}H NMR. Anal. Calcd (%) for $[(ZnI_2)_3(tpt)_2]\cdot 0.75ipp\cdot 0.25CHCl_3)\cdot 2I_2$: C, 32.79; H, 1.92; N, 7.95; found: C, 32.76; H, 1.68; N, 8.47. FTIR $\bar{\upsilon}$ = 3051 (w), 2921 (m), 2851 (m), 1619 (w), 1573 (w), 1514 (s), 1439 (w), 1421 (m), 1371 (s), 1313 (m), 1233 (m), 1212 (m), 1157 (w), 1120 (w), 1057 (s), 1027 (s), 982 (w), 864 (w), 833 (w), 801 (s), 775 (s) 655 (s) cm^{-1}.

5.5. References:

[1] Inokuma, Y.; Kawano, M.; Fujita, M., *Nat. Chem.,* **2011**, *3*, 349-358.

[2] Inokuma, Y.; Yoshioka, S.; Ariyoshi, J.; Arai, T.; Hitora, Y.; Takada, K.; Matsunaga, S.; Rissanen, K.; Fujita, M., *Nature,* **2013**, *495*, 461-466.

[3] Bloch, W. M.; Champness, N. R.; Doonan, C. J., *Angew. Chem. Int. Ed.,* **2015**, *54*, 12860-12867.

[4] Haneda, T.; Kawano, M.; Kawamichi, T.; Fujita, M., *J. Am. Chem. Soc.,* **2008**, *130*, 1578-1579.

[5] Kawamichi, T.; Kodama, T.; Kawano, M.; Fujita, M., *Angew. Chem. Int. Ed.,* **2008**, *47*, 8030-8032.

[6] Murase, T.; Horiuchi, S.; Fujita, M., *J. Am. Chem. Soc.,* **2010**, *132*, 2866-2867.

[7] Ikemoto, K.; Inokuma, Y.; Rissanen, K.; Fujita, M., *J. Am. Chem. Soc.,* **2014**, *136*, 6892-6895.

[8] Ohmori, O.; Kawano, M.; Fujita, M., *CrystEngComm,* **2005**, *7*, 255-259.

[9] Ramamurthy, V.; Sivaguru, J., *Chem. Rev.,* **2016**, *116*, 9914-9993.

[10] Ohara, K.; Kawano, M.; Inokuma, Y.; Fujita, M., *J. Am. Chem. Soc.,* **2010**, *132*, 30-31.

[11] Ohara, K.; Inokuma, Y.; Fujita, M., *Angew. Chem. Int. Ed.,* **2010**, *49*, 5507-5509.

[12] Wang, K.; Li, C.; Liang, Y.; Han, T.; Huang, H.; Yang, Q.; Liu, D.; Zhong, C., *Chem. Eng. J.,* **2016**, *289*, 486-493.

[13] Inokuma, Y.; Yoshioka, S.; Ariyoshi, J.; Arai, T.; Fujita, M., *Nat. Protoc.,* **2014**, *9*, 246-252.

[14] Vinogradova, E. V.; Muller, P.; Buchwald, S. L., *Angew. Chem. Int. Ed.,* **2014**, *53*, 3125-3128.

[15] Tanaka, D.; Kitagawa, S., *Chem. Mater.,* **2008**, *20*, 922-931.

[16] Bloch, W. M.; Champness, N. R.; Doonan, C. J., *Angew. Chem. Int. Ed.,* **2015**, *54*, 12860-12867.

[17] Beni, A. S.; Zarandi, M.; Madram, A. R.; Bayat, Y.; Chermahini, A. N.; Ghahary, R., *Mol. Cryst. Liq. Cryst.,* **2016**, *629*, 29-43.

[18] Wu, J.; Pisula, W.; Mullen, K., *Chem. Rev.,* **2007**, *107*, 718-747.

[19] Bhowmick, D. K.; Stegemann, L.; Bartsch, M.; Strassert, C. A.; Zacharias, H., *J. Phys. Chem. C,* **2016**, *120*, 3275-3288.

[20] Chen, X.; Lu, P.; Wang, Y., *Chemistry,* **2011**, *17*, 8105-8114.

[21] Kawano, M.; Kawamichi, T.; Haneda, T.; Kojima, T.; Fujita, M., *J. Am. Chem. Soc.,* **2007**, *129*, 15418-15419.

[22] Biradha, K.; Fujita, M., *Angew. Chem. Int. Ed.,* **2002**, *41*, 3392-3395.

[23] Ohmori, O.; Kawano, M.; Fujita, M., *J. Am. Chem. Soc.,* **2004**, *126*, 16292-16293.

[24] Ohara, K.; Marti-Rujas, J.; Haneda, T.; Kawano, M.; Hashizume, D.; Izumi, F.; Fujita, M., *J. Am. Chem. Soc.,* **2009**, *131*, 3860-3861.

[25] Mart-Rujas, J.; Islam, N.; Hashizume, D.; Izumi, F.; Fujita, M.; Kawano, M., *J. Am. Chem. Soc.,* **2011**, *133*, 5853-5860.

[26] Ohmori, O.; Kawano, M.; Fujita, M., *J. Am. Chem. Soc.,* **2004**, *126*, 16292-16293.

[27] Kawamichi, T.; Kodama, T.; Kawano, M.; Fujita, M., *Angew. Chem. Int. Ed.,* **2008**, *47*, 8030-8032.

[28] Pike, S. D.; Weller, A. S., *Philos. Trans. A Math. Phys. Eng. Sci.,* **2015**, *373*, 1-24.

[29] Britt, D.; Tranchemontagne, D.; Yaghi, O. M., *P. Nat. Acad. Sci. USA,* **2008**, *105*, 11623-11627.

[30] Li, Y.; Yang, R. T., *Langmuir,* **2007**, *23*, 12937-12944.

[31] Khan, N. A.; Hasan, Z.; Jhung, S. H., *J. Hazard Mater.,* **2013**, *244-245*, 444-456.

[32] Huang, X.; Zeng, L.; Zeng, Z.; Wu, J., *Chemistry,* **2011**, *17*, 14907-14915.

[33] Braga, D.; Grepioni, F.; Tedesco, E., *Organometallics,* **1998**, *17*, 2669-2672.

[34] Wu, Y. T.; Hayama, T.; Baldridge, K. K.; Linden, A.; Siegel, J. S., *J. Am. Chem. Soc.,* **2006**, *128*, 6870-6884.

Overview of thesis and conclusion

This thesis focuses on solid-state single-crystal to single-crystal (SCSC) transitions within coordination compounds and coordination polymers (CPs) through the lens of structure-property determination. Weak intermolecular interactions were analysed crystallographically and spectroscopically through the systematic variation of components and synthetic conditions within separate series of coordination complexes and polymers.

Ebdc (5-ethynyl-1,3-benzenedicarboxylate) was chosen as a linker with weak hydrogen bond donor and acceptor functionality and was combined with various divalent metal salts including those of Pb^{2+}, Mn^{2+}, Co^{2+}, Ni^{2+}, Cu^{2+} and Zn^{2+}. In total nine coordination compounds from these components were synthesised, including an additional two which were the result of SCSC transitions.

Tuning the reaction conditions of Pb(II) and ebdc by changing solvent and temperature had clear effects on the outcome of the CP architecture. A ladder-like chain CP was formed when the reaction was carried out in DMSO, compared to a 1D motif containing bridged hexagonal Pb–O rings, when the reaction was in DMF. A higher periodicity CP was obtained as a result of increasing the temperature from 100 °C in DMF to 140 °C. A layer diffusion synthesis using ebdc in methanol and the metal salt in water at room temperature was carried out using three metal salts. Lead(II) acetate gave rise to labile interdigitated 2D nets comprising of continuous Pb–O backbones, zinc perchlorate gave a 3D structure consisting of 6-connected secondary building units and copper perchlorate gave an interdigitated 2D Kagomé net.

Weak ethynyl-derived hydrogen bonding was observed in the lead(II) structures through both crystallographic and spectroscopic techniques. The strength of the ethynyl-derived C–H···O interactions correlated well with the observed ν(C–H) bands in the corresponding IR spectra. Although some C–H···O hydrogen bonding was observed in the transition metal (TM) series, the packing of most of the structures seemed to be driven mainly by stronger O–H···O hydrogen bonds through carboxylate groups, coordinated methanol molecules and water molecules. Some weak ethynyl-derived C-H···π bonding was observed within the TM series, but arose more as a consequence of the spatial orientation of the coordinated molecules.

5-Allenyl-1,3-benzenedicarboxylic acid (H_2abdc) was synthesised to investigate the effects of an asymmetric functional group and consequently the loss of directional weak hydrogen bonding behaviour. Reacting H_2abdc with lead(II) acetate at 100 °C resulted in formation of a metallogel, compared to the 1D CP chain motif synthesised from H_2ebdc. The influence of the functional group of abdc and ebdc was most clearly observed in the packing of isostructural Cu based 2D Kagomé layers; in which the structure containing abdc formed channels whereas the ebdc structure was non-porous.

Overall, four bridging binding modes of functionalised 1,3-benzenedicarboxylate to metal centres were observed: $\mu_2(\mu_1+\mu_1)$ (μ_1 from one carboxylate group and μ_1 from the other),[1] $\mu_3(\mu_1+\mu_2)$, $\mu_4(\mu_2+\mu_2)$, $\mu_4(\mu_1+\mu_3)$. Within these bonding modes, up to five configurations of coordination bonding were observed (figure 116). The number and variety of these bonding modes highlights the flexible coordination nature of these linkers.

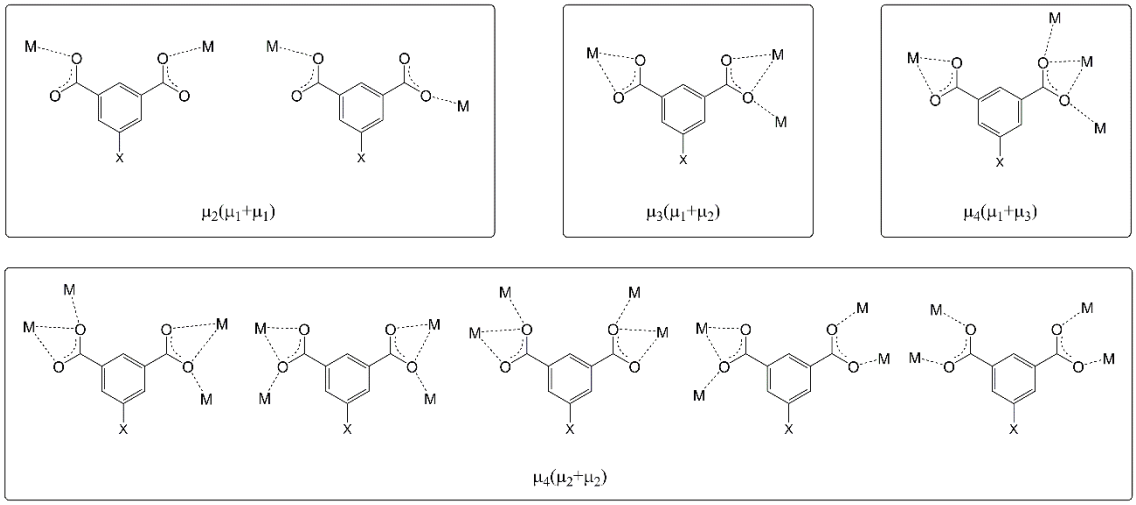

Figure 116: *Observed binding modes of ebdc and abdc within CPs.*

In order to explore competing self-assembly interactions within more labile CP systems, 4-(phenylethynyl)pyridine (pep) and various silver(I) salts were reacted together and the products crystallised by slow evaporation. In total twelve coordination polymers and compounds were obtained, two of which were the result of SCSC transitions.

Broad conclusions can be made relating the influence of the Ag counterion to the resulting coordination compound within Chapter 4. Traditionally non-bonding counterions such as PF_6^- and BF_4^- were observed to produce discrete complexes comprising two pep ligands coordinated to one Ag centre ($[Ag(pep)_2]^+$ units), between

which minimal interactions were observed. The inclusion of highly coordinating anions, whether directional (RCO_2^-, RSO_3^-) or non-directional (NOx^-), resulted in interdigitated higher dimensional structures: 1D chains as well as 2D nets with the exception of $CF_3CO_2^-$, which produced dimers. The highly coordinating thiocyanate anion, SCN^-, also formed an interdigitated two-dimensional net.

In the seven CPs within the series, extensive T-shaped weak C–H···π hydrogen bonding derived through the interdigitation of pep ligands was observed, in which the individual hydrogen-bonded herringbone motifs exhibited are comparable to those in the crystal structure of pep. This propensity for weak C–H···π hydrogen bonding within the CPs suggests that these interactions are able to dominate the coordination bonding between the metal and counterion, and ultimately dictate the outcome of the structural topology. Only in the extended structures were these pep-derived herringbone motifs found, and only in discrete compounds SCSC transitions were observed. The correlations between the coordinative properties of the silver salt and the resulting properties can be extrapolated to predict the outcomes of properties of coordination compounds and coordination polymers that have not yet been explored within this series. For example ClO_4^- and SbF_6^- are common counterions in silver salts known to be strongly non-coordinating therefore would likely form 0D discrete complexes, with SCSC transition potential.

Three SCSC solvent-induced transitions were observed within one lead-based ebdc CP system described in Chapter 2; one solvent exchange transition and two solvent loss transitions. This structural dynamism was likely a result of the labile nature of the lead coordination sphere coupled with stabilising forces of the weak C–H···O hydrogen bonding provided by the ethynyl group of the ebdc linker. In contrast, no SCSC transitions were observed in Chapter 3, in which ebdc was reacted with first-row transition metals. In the silver-based pep coordination compound series within Chapter 4, two examples of SCSC transition behaviour were observed, initiating from arrayed 0D complexes in which pep derived T-shaped C–H···π hydrogen bonding was not observed. These discrete complexes were found to undergo rapid transitions upon desolvation and heating.

From this data it can be surmised that systems containing flexible metal centres such as lead(II) and silver(I) which do not have a tendency to create SBUs have a larger potential to undergo SCSC rearrangements. Therefore for weaker interactions to be able

to direct or dominate a coordination polymer in order to facilitate a SCSC rearrangement comparable to the ones observed in this thesis, flexible systems should be focused upon.

In Chapter 5, 1,8-bis(2-phenylethynyl)naphthalene (bpen) guest molecules were loaded into a crystalline molecular flask (CMF) and shown to undergo two sequential gas-mediated reactions that occurred under mild conditions, when exposed to iodine vapour and subsequently atmospheric oxygen. A combination of crystallographic, gravimetric and spectroscopic analyses confirmed the conversion of bpen guest molecules into the cyclised product 7-iodo-12-phenylindeno[2,1-α]phenalene (ipp), and the oxidation of ipp to an oxidised product 12-hydroxy-7-iodo-2-phenylindeno[2,1-α]phenalen-1(12*H*)-one (hipp). Both reaction yields were found to greatly improve on previously reported solution-based reactions. The work in this chapter is the first report of sequential gas-mediated reactions in a CMF system.

CMFs are a useful tool for hosting SCSC transitions in the form of reactions within the pores, or guest/solvent exchange. Their flexibility enables SCSC transitions to occur within the framework voids without risk of extensive crystal degradation.

References

[1] Zhang, Z.; Zhou, Y.-L.; He, H.-Y., *Acta Crystallogr. E,* **2006**, *62*, 2591-2593.

Future work

The work carried out in this thesis has potential to be expanded upon and continued in the future. Potential applications of metallogel **7** synthesised in Chapter 2 were not explored. Metallogel usage in separations of dyes or heavy metal contaminants has been reported,[1] thus further investigation into the properties of **7** would be valuable.

In Chapter 3, nickel and cobalt based structures **9** and **10** exhibit coordination isomerism, resulting in a nickel based 0D dimer complex and a cobalt based 1D chain CP. Additional synthesis studies could yield structural analogues of the two compounds, yielding a 0D dimer structure and a 1D chain structure from both metal salts. Further investigation into the adsorption properties of copper-based CP **13** could yield a material with selective gas separation properties. Analogues of **13** have shown the unusual property of switchable adsorption mechanisms, thus allowing for controlled adsorption and separation of molecules.[2,3]

A large limitation of the single-crystal to single-crystal (SCSC) transitions observed in this thesis is that all the transitions are non-reversible, and therefore have restricted use in switchable material applications. Further investigation into the thermally-induced SCSC transition of compound **22** to **23** in Chapter 4, perhaps with an altered linear ligand, could yield a reversible thermal sensor. In the long term, the data collected from these future studies could yield a series of reversible dynamic CPs.

The two-step reaction of 1,8-bis(2-phenylethynyl)naphthalene within the pores of the CMF in Chapter 5 proceeds through several intermediate steps as shown in the proposed mechanism. In theory, this reaction can be significantly slowed at low temperatures, and with high intensity synchrotron X-ray diffraction, in-situ snapshots could be recorded, providing visual evidence of the reaction mechanism. A proof-of-concept study of the isolation of a transient intermediate within a reaction has been performed by Fujita et al.[4]

References

[1] Sengupta, S.; Mondal, R., *J. Mater. Chem. A*, **2014**, 2, 16373-16377.

[2] Mohideen, M. I.; Xiao, B.; Wheatley, P. S.; McKinlay, A. C.; Li, Y.; Slawin, A. M.; Aldous, D. W.; Cessford, N. F.; Duren, T.; Zhao, X.; Gill, R.; Thomas, K. M.; Griffin, J. M.; Ashbrook, S. E.; Morris, R. E., *Nat. Chem.,* **2011**, *3*, 304-310.

[3] Sato, H.; Kosaka, W.; Matsuda, R.; Hori, A.; Hijikata, Y.; Belosludov, R. V.; Sakaki, S.; Takata, M.; Kitagawa, S., *Science,* **2014**, *343*, 167-170.

[4] Kawamichi, T.; Haneda, T.; Kawano, M.; Fujita, M., *Nature,* **2009**, *461*, 633-635.

Appendix I

Supplementary information

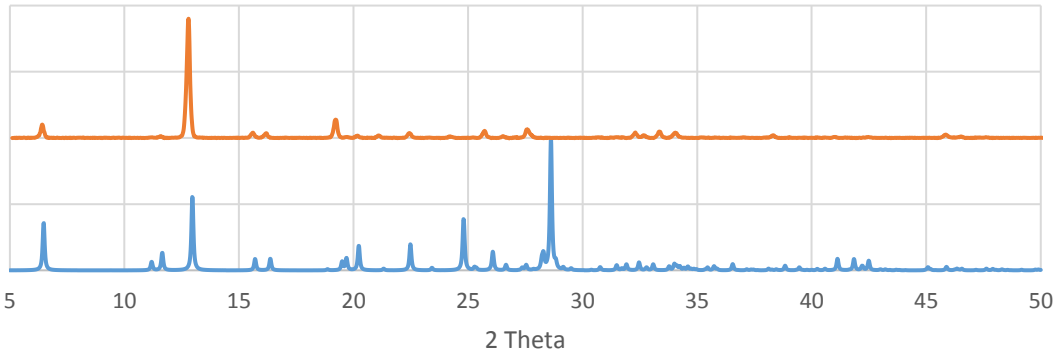

Figure 117: *Powder XRD pattern of H_2ebdc, calculated pattern in blue and experimental in orange.*

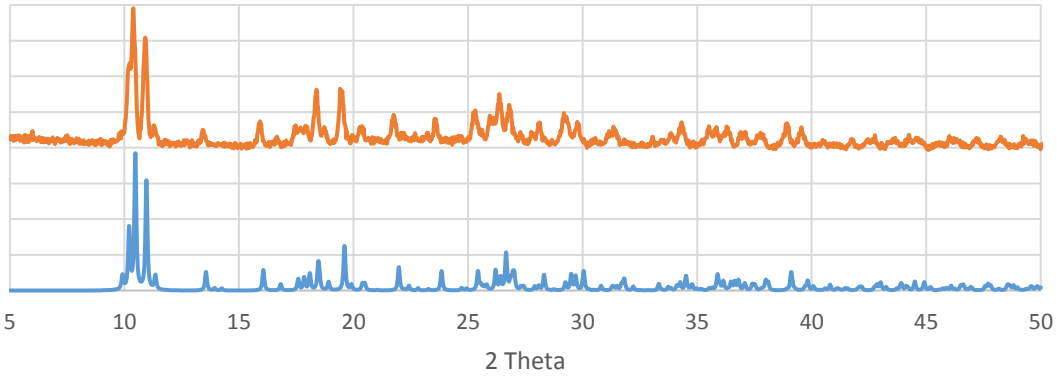

Figure 118: *Powder XRD pattern of* ***1****, calculated pattern in blue and experimental in orange.*

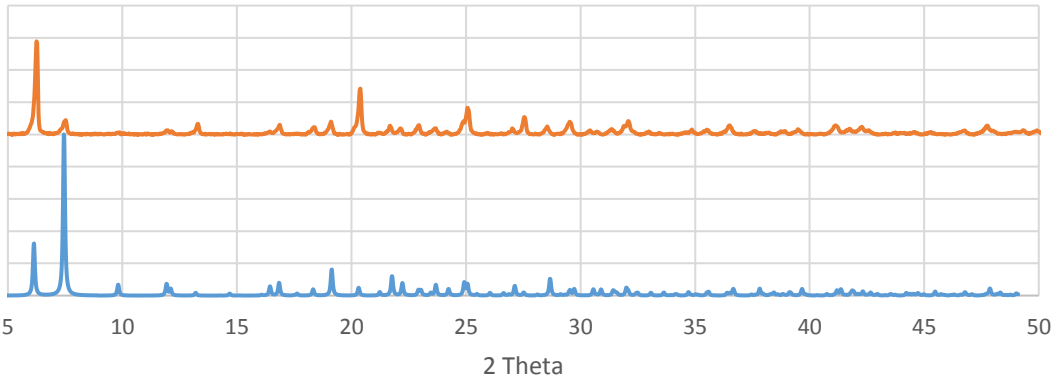

Figure 119: *Powder XRD pattern of* **2**, *calculated pattern in blue and experimental in orange.*

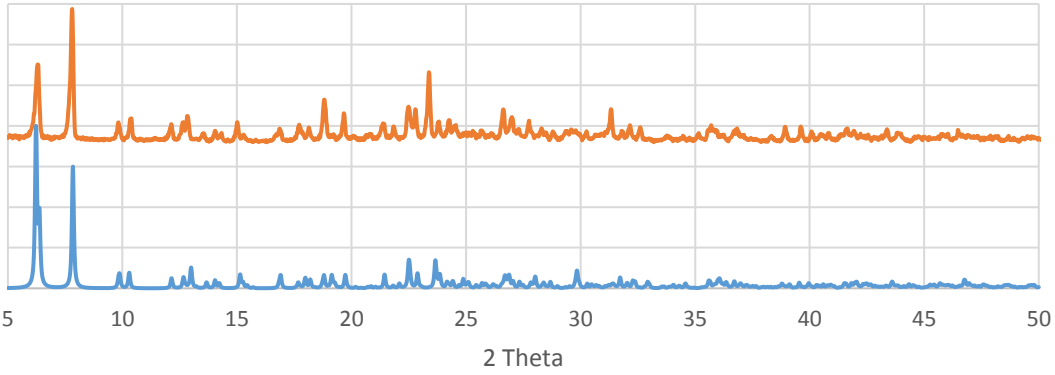

Figure 120: *Powder XRD pattern of* **3**, *calculated pattern in blue and experimental in orange.*

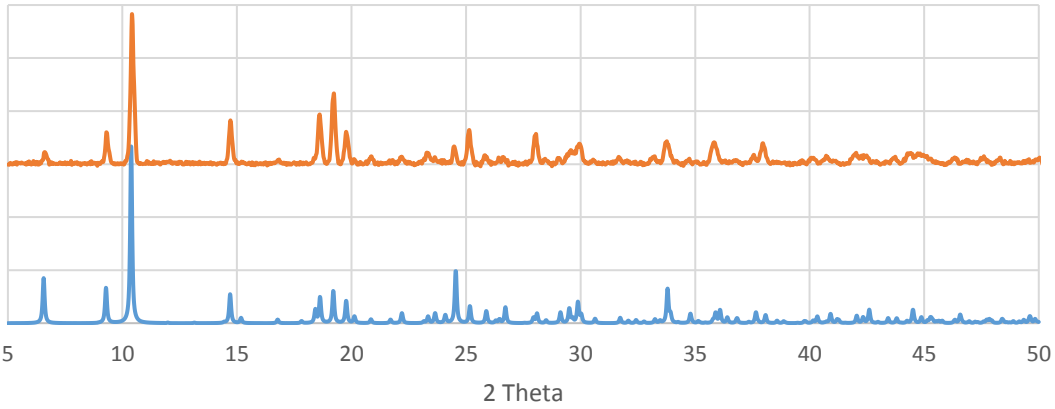

Figure 121: *Powder XRD pattern of* **8**, *calculated pattern in blue and experimental in orange.*

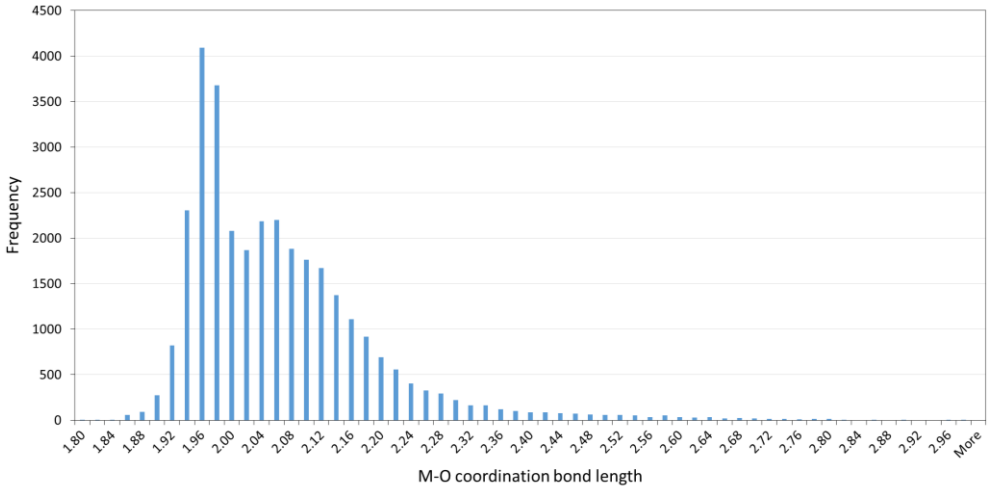

Chart 1: *Histogram showing distribution of reported M–O (M = Mn, Co, Ni, Cu, Zn) coordination bond lengths, collected from the CSD database.*

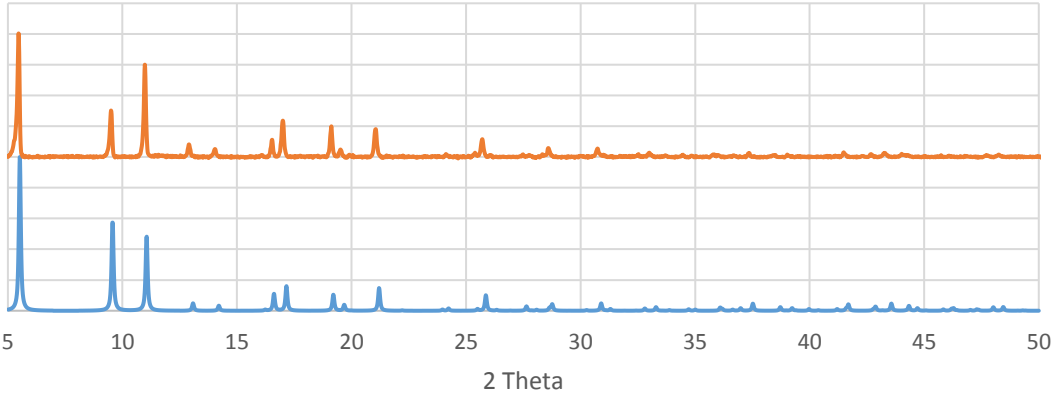

Figure 122: *Powder XRD pattern of* ***13****, calculated pattern in blue and experimental in orange.*

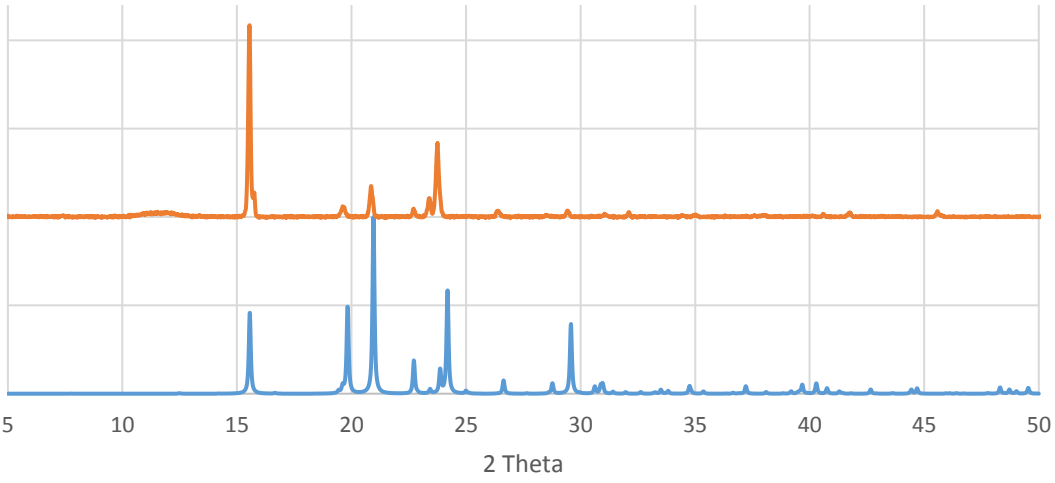

Figure 123: *Powder XRD pattern of pep, calculated pattern in blue and experimental in orange.*

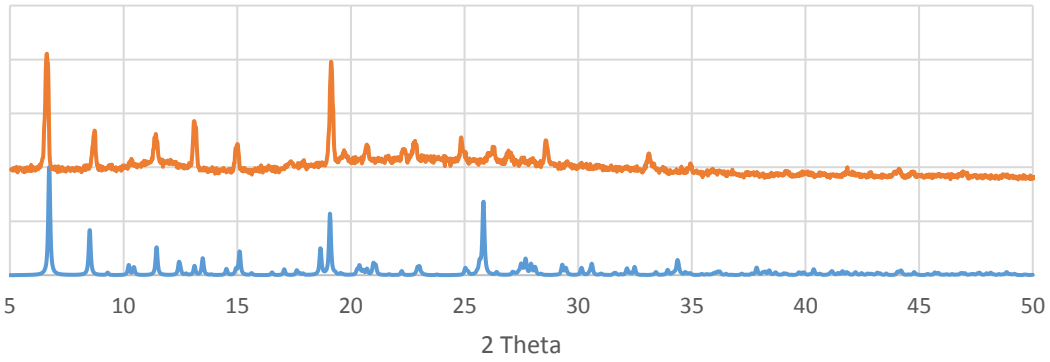

Figure 124: *Powder XRD pattern of* ***15****, calculated pattern in blue and experimental in orange.*

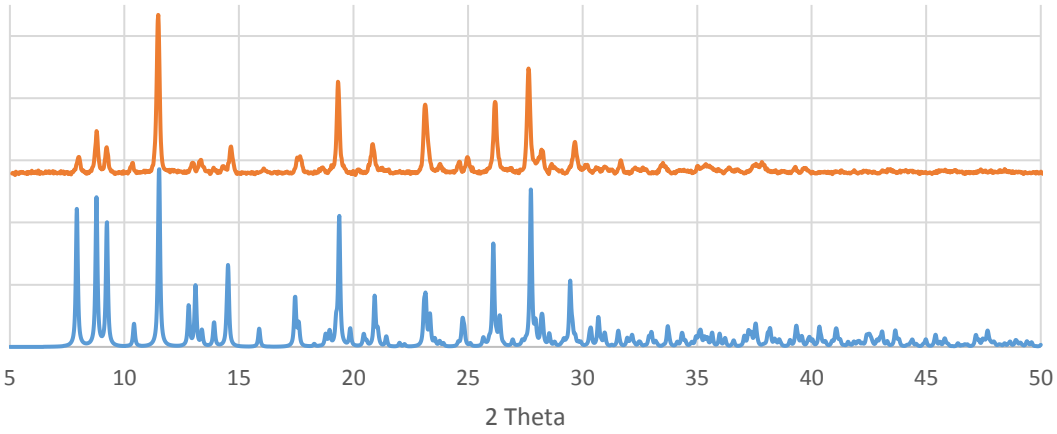

Figure 125: *Powder XRD pattern of* ***17****, calculated pattern in blue and experimental in orange.*

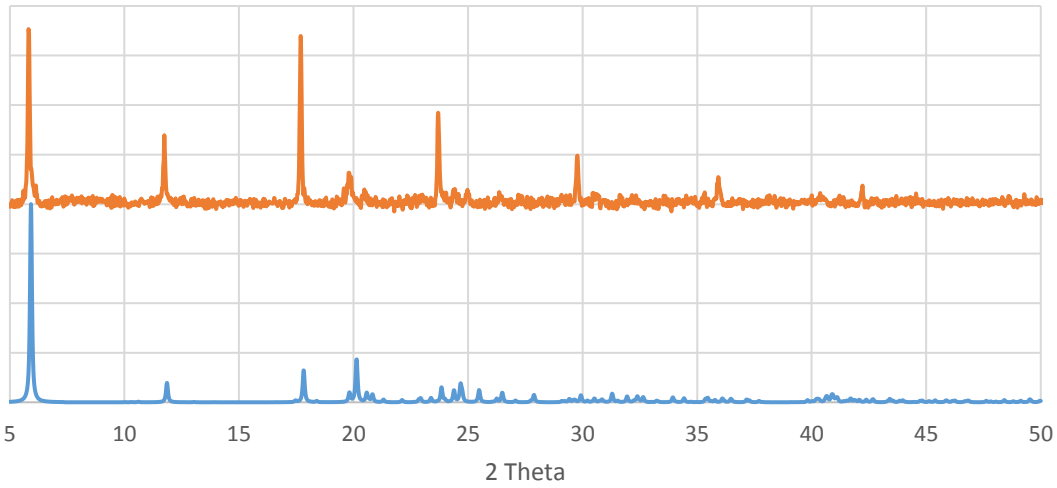

Figure 126: *Powder XRD pattern of* ***18****, calculated pattern in blue and experimental in orange.*

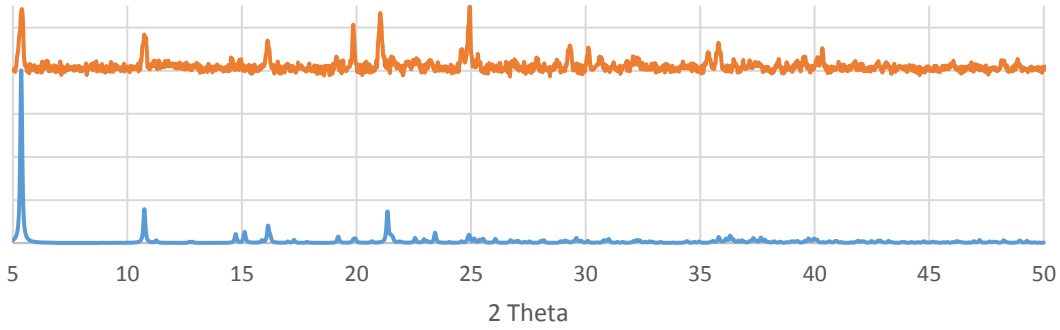

Figure 127: *Powder XRD pattern of* ***19****, calculated pattern in blue and experimental in orange.*

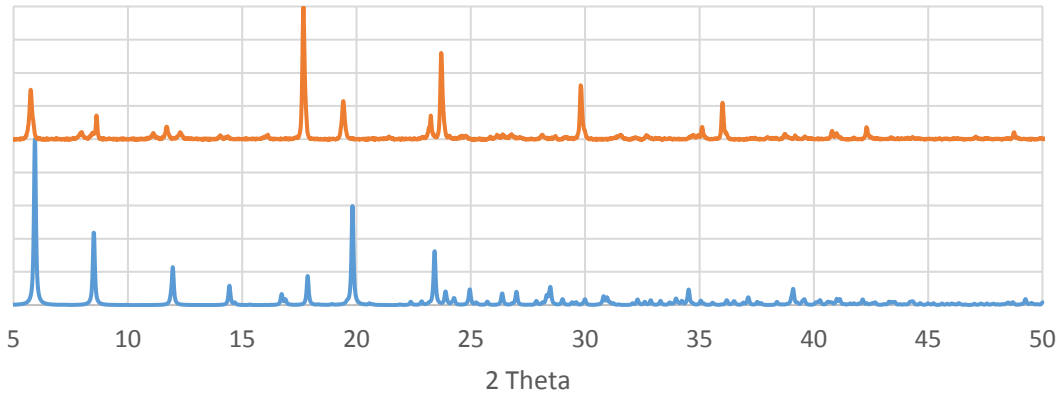

Figure 128: *Powder XRD pattern of* ***20****, calculated pattern in blue and experimental in orange. Contaminated with silver salt despite best efforts to wash sample.*

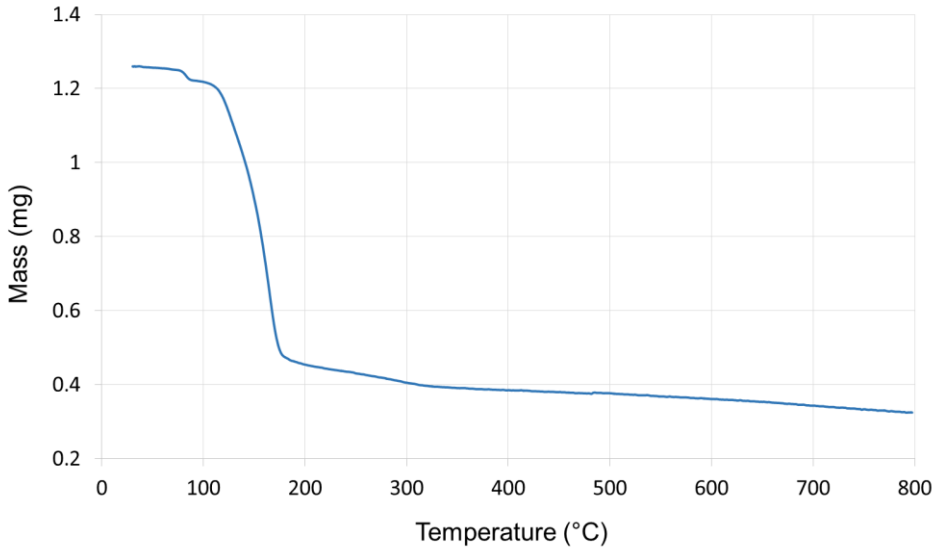

Figure 129: *TGA of* ***21****, showing a desolvation event at 80 °C. Decomposition of the sample starts at 120 °C.*

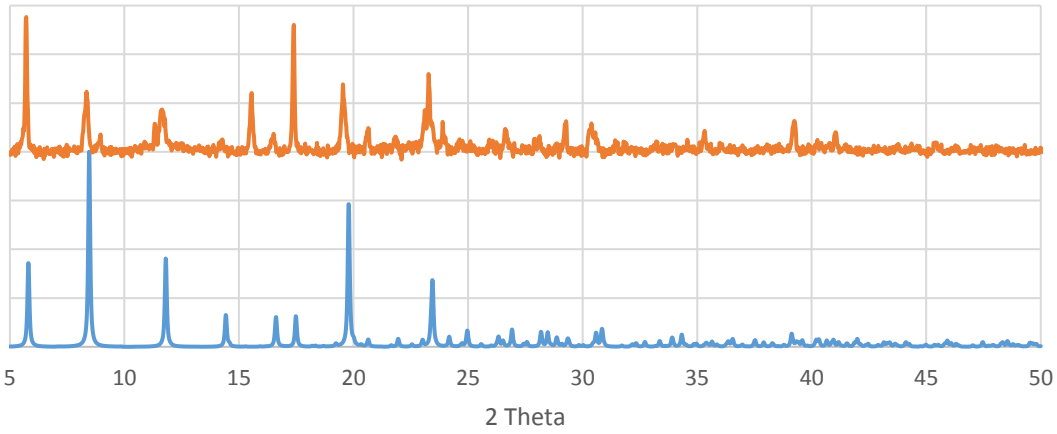

Figure 130: *Powder XRD pattern of* **21**, *calculated pattern in blue and experimental in orange.*

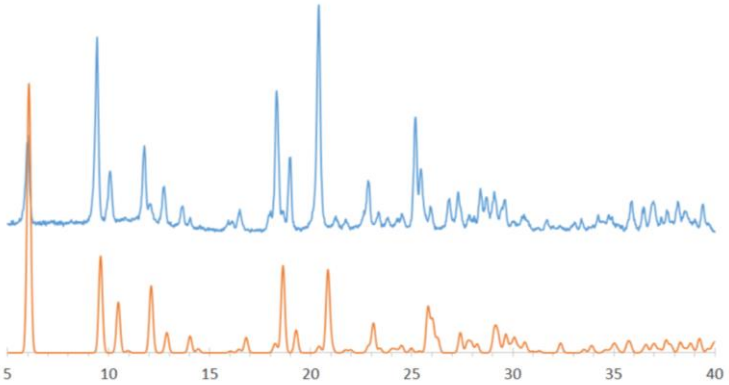

Figure 131: *Powder XRD pattern of* **22**, *calculated pattern in orange and experimental in blue.*

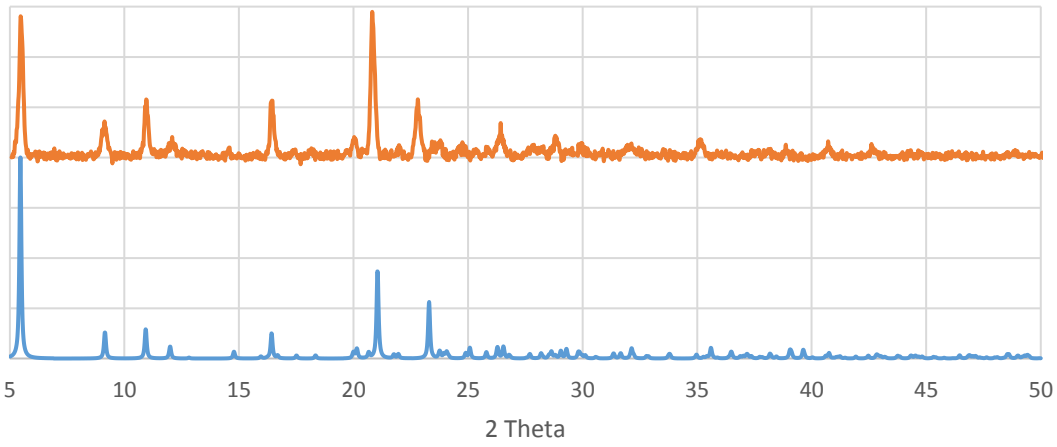

Figure 132: *Powder XRD pattern of* **24**, *calculated pattern in blue and experimental in orange.*

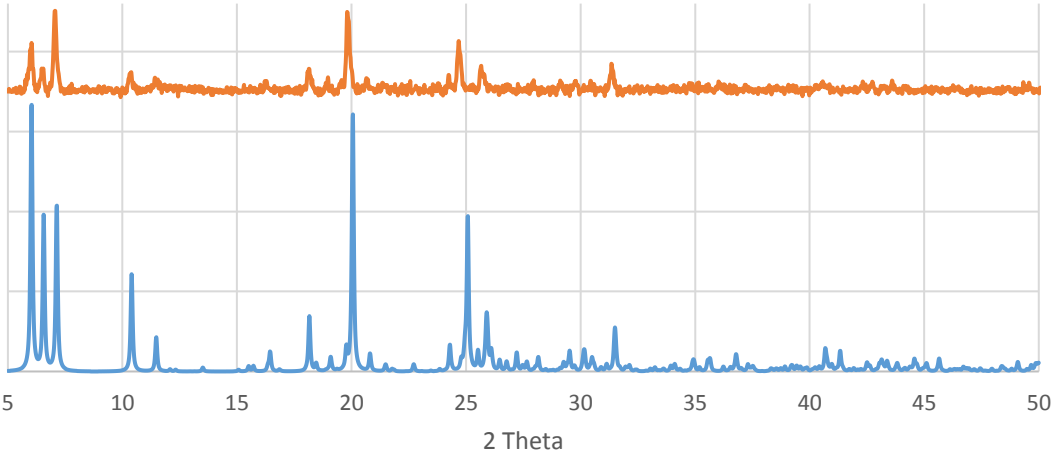

Figure 133: *Powder XRD pattern of* **25**, *calculated pattern in blue and experimental in orange.*

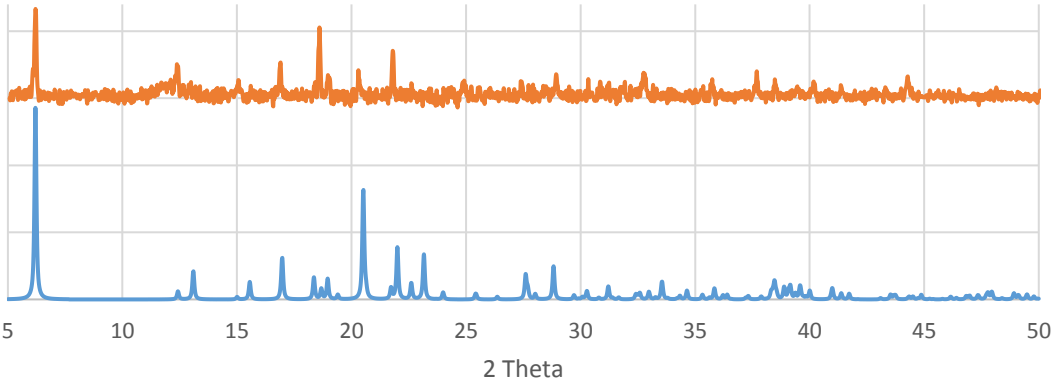

Figure 134: *Powder XRD pattern of* **26**, *calculated pattern in blue and experimental in orange.*

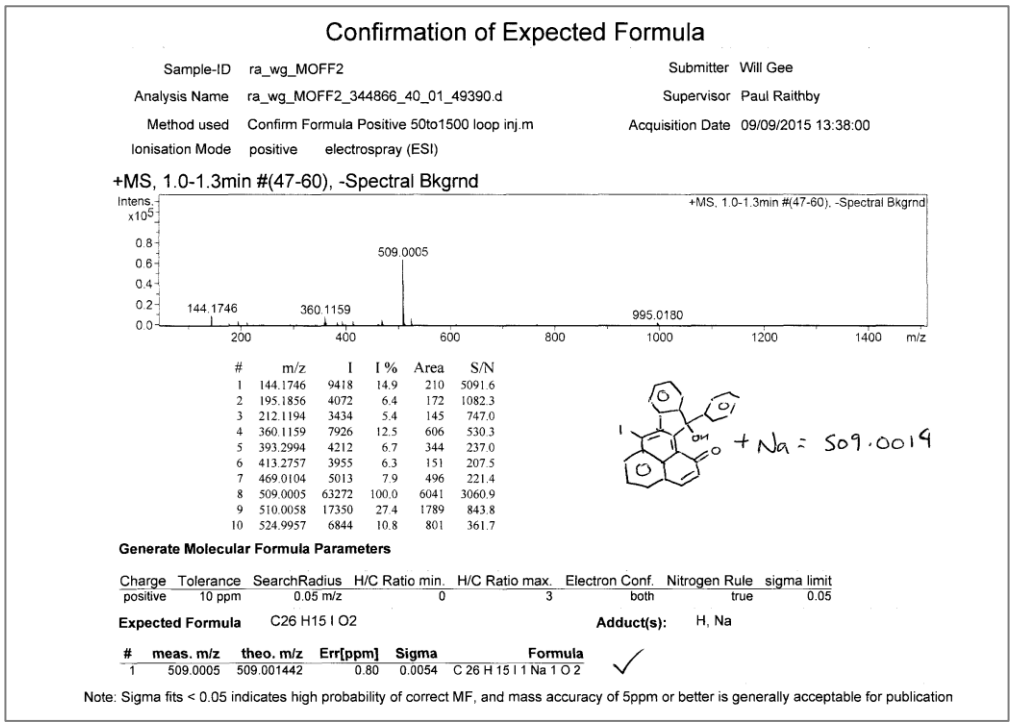

Figure 135: *Mass spectrometry data determining the product 7-iodo-12-phenylindeno[2,1-α]phenalene (ipp).*

7-iodo-12-phenylindeno[2,1-α]phenalene (ipp)

A sample of bpen was dissolved with a molar excess of iodine in cyclohexane, which was heated to 50 °C and stirred for 48 hours under atmospheric conditions. The resulting red solution was worked up and the cyclised ipp product was isolated as red crystals.

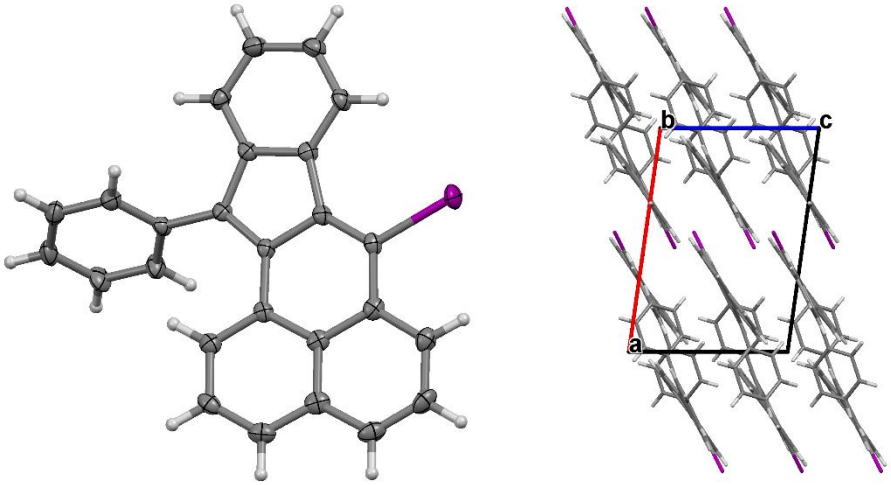

Figure 136: *Left: Molecular structure of ipp, ellipsoids are shown at 50% probability. Right: Packing arrangement of ipp viewed along the crystallographic* b *axis.*

Appendix II

Crystallographic refinement details

Data collection and processing

The crystal data and details of the data collections are collected in Tables 23-27. Single crystals were isolated and selected in fomblin oil and mounted on plastic mounts.

Data collections for H_2ebdc, **1**, **2**, **3**, **4** and **6** were performed on an Agilent Gemini A-Ultra diffractometer at the University of Bath using Mo Kα radiation, the crystal being cooled by an Agilent Cryojet.

Data collections for pep, **15**, **16**, **17**, **19**, **20**, **21**, **22**, **24**, **25**, bpen, **27**, **28** were performed on an Agilent Supernova diffractometer using either Mo Kα or Cu Kα radiation, the crystal being cooled by an Agilent Cryojet.

Data collections for **8** and **18** were performed on an Agilent Xcalibur diffractometer at the University of Bath using Mo Kα radiation, cooled to 150 K by an Oxford Instruments nitrogen gas cryostream.

All data from Gemini, Supernova and Excalibur were processed through CrysAlis^{Pro}.

Data collections for **5**, **23** and **26** were performed at Beamline Station 11.3.1 of the Advanced Light Source (ALS), Lawrence Berkeley National Laboratory, cooled to 100 K.[1] Data processing and absorption corrections at the ALS was performed using APEX3 and SADABS 2.03.[2,3]

All crystal data were collected at 150 K, with the exception of **27**, which were collected at 100 K. Crystal symmetry was analysed through XPREP[4] and then processed using Olex[2],[5] solved with the ShelXS[6] or ShelXT[7] structure solution program via Direct Methods and refined with the ShelXL refinement package using Least Squares minimisation. Figures were prepared using Mercury,[8] Olex[2] and Xseed[9] with PovRay.[10]

Special details relating to the refinements

Some hydrogen atoms have been isotropically refined and some hydrogen positions have been calculated through the HTAB function.

One of the two DMSO molecules in **1** was found to be disordered over two positions, and was refined to half occupancy. Two of the three DMF molecules in **2** were disordered, where all disordered atoms were given an occupancy of 0.5. In structure **3** the carbon atoms of one DMF molecules were disordered, and refined to half occupancy. A water molecule in **6** resides in an occupancy of 0.5.

The ethynyl group of the ebdc linker in **10** was disordered over two positions, and thus each part was refined to half occupancy. The two coordinated methanol groups were also positionally disordered, and these were freely refined to 0.7 and 0.3 occupancy in each case. Hydrogen atoms of the interstitial water molecules in **11**, **12** and **14** were too disordered to be identified, and thus these molecules were refined as single oxygen atoms. One coordinated methanol molecule in **12** was substitutionally disordered with a water molecule, and was refined at half occupancy. One carboxylate oxygen atom within **13** was disordered over two positions, with each part refined to half occupancy. The residual solvent electron density within the framework of **13** was analysed by the Olex[2] SQUEEZE tool. Details of the SQUEEZE calculation can be found in file '13-mask.log' in the electronic supplementary files. One of the ethyl arms of the interstitial NEt_3 in **14** was disordered over two positions, and each arm was refined at half occupancy.

Two of the six fluorine atoms with the counterion of **16** were disordered over two positions, and were thus refined to half occupancy. Crystals of **20** were twinned and the structure was refined under the twin law (-1.0, 0.0, 0.0, 0.0, 1.0, 0.0, 0.0, 0.0, -1.0). The PLATON SQUEEZE tool was used for determining the seriously disordered solvent molecules within structure **21**. SQUEEZEing of the residual electron density was performed through the help of Dr. C. Cameron following a methodology by A. L. Spek (2015).[11] The results of the SQUEEZE calculations were as follows:

Void	X(av)	Y(av)	Z(av)	Volume Ang^3	El-Count (e-)	Vol/Electron	Vol/Atom
1	0.500	-0.000	-0.047	104	33	3.2	25
2	-0.000	0.500	-0.044	104	33	3.2	25

Details of the SQUEEZE calculations can be found in file '21-mask.lis' in the electronic supplementary files. Structure **21** was also twinned and thus refined under the twin law (-1.0, 0.0, 0.0, 0.0, 1.0, 0.0, 0.0, 0.0, -1.0). Symmetry of the pep ligand caused the interstitial pep within structure **25** to appear as an overlapping infinite chain, and thus restraints EADP and EXYZ were used to differentiate between carbon and nitrogen atoms. Crystals of **26** were twinned, and the structures was refined under the twin law (-1.0, 0.0, 0.0, 0.0, -1.0, 0.0, 0.0, 0.0, -1.0).

Some large residual electron density peaks were observed in the density map of CMF **27**. They are all located close to the iodine atoms of the framework and are attributed to absorption effects caused by the copper X-rays used during the experiment. The light-atom guest located in the framework pore was resolved using Cu radiation. The usual procedure of fixing the atomic displacement parameters (ADPs) and refining the occupancy for the guest molecule directly was not considered reliable due to the ADPs of the guest molecules being much larger than that of the framework, therefore occupation of the bpen guest was inferred at 75% from TGA and elemental analyses, and one water molecule was modelled as disordered over 3 positions. However the ADPs of the guest bpen molecule were sensible when modelled with this occupancy. This value of 75% obtained from XRD should be treated as a reasonable estimation rather than an absolute reflection of the loading percentage in that particular crystal.

The large pores of CMF **28** contained a significant amount of disordered molecular iodine, ipp molecules and possibly solvent molecules. Some locations for partially occupied iodine molecules could be inferred from pairs of similarly sized electron density peaks separated by the expected I-I interatomic distance and were modelled with equal ADPs of both atoms with the occupancy allowed to refine freely. A large single peak that did not appear to be attributable to molecular iodine was ascribed to one possible location of the iodine atom on the ipp molecule. However, no discrete carbon positions that can be unambiguously attributed to the ipp were found in the residual electron density map. Consequently the rest of the atoms in that molecule were placed at calculated positions and refined with partial occupancy and heavily restrained and constrained. The aim of providing this model is merely to demonstrate one possible location of the ipp product molecule and show that it fits within the available pore space.

Crystallographic tables

Network	**H_2ebdc**	**1**	**2**	**3**	**4**	**5**
Empirical formula	$C_{10}H_8O_4$	$C_{14}H_{16}O_6PbS_2$	$C_{78}H_{65}N_6O_{30}Pb_6$	$C_{58}H_{58}N_6O_{23}Pb_4$	$C_{22}H_{17}O_{11}Pb_2$	$C_{20}H_8O_8Pb_2$
Formula weight	208.17	549.72	2809.50	2035.86	871.73	790.64
Temperature/K	150(1)	150(1)	150(1)	150(1)	150(1)	150(1)
Crystal system	triclinic	monoclinic	triclinic	tetragonal	monoclinic	triclinic
Space group	P $\bar{1}$	P $2_1/n$	P $\bar{1}$	P $\bar{4}2_1c$	C 2/c	P $\bar{1}$
a/Å	3.6577(3)	9.9878(5)	10.1240(4)	11.66870(10)	15.2233(11)	9.379
b/Å	9.5850(7)	17.8249(6)	15.0418(5)	11.66870(10)	17.6983(7)	10.013
c/Å	13.6770(14)	10.5770(4)	15.0480(6)	25.1110(4)	10.0370(8)	10.318
α/°	86.970(7)	90	73.172(3)	90.00	90	100.15
β/°	86.852(8)	115.088(6)	75.343(3)	90.00	124.145(11)	91.41
γ/°	79.019(6)	90	71.172(3)	90.00	90	107.94
Volume/Å^3	469.57(7)	1705.39(14)	2043.60(14)	3419.08(7)	2238.1(4)	904.2
Z	2	4	1	2	4	2
ρ_{calc} g/cm^3	1.4722	2.141	2.283	1.978	2.587	2.904
μ/mm^{-1}	0.120	10.163	12.401	9.896	15.088	18.645
Radiation	Mo Kα	Mo Kα	Mo Kα	Mo Kα	Mo Kα	Mo Kα
2Θ range for data collection/°	7.22 to 52.74	6.244 to 60.91	5.592 to 57.874	5.9 to 58.44	6.468 to 58.786	5.838 to 63.162
Reflections collected	5034	14229	20687	20310	6767	13225
Unique reflections	1909	4512	8937	4246	2606	5621
Data/restraints/parameters	1909/0/167	4512/0/224	8937/12/499	4246/3/191	2606/3/166	5621/0/271
GOOF	1.030	1.008	1.083	1.098	1.021	1.017
R_1 [I>=2σ (I)]	0.0470	0.0589	0.0590	0.0313	0.0405	0.0505
wR_2 [I>=2σ (I)]	0.1015	0.1049	0.1097	0.0671	0.0865	0.1064
Largest diff. peak/hole / e Å^{-3}	0.40/-0.46	2.95/-1.54	2.57/-2.58	1.50/-1.06	2.84/-2.27	2.82/-2.45

Table 23: *Crystallographic details of H_2ebdc and **1** – **5**.*

Network	**6**	**8**	**9**	**10**	**11**	**12**
Empirical formula	$C_{44}H_{29}O_{19}Pb_4$	$C_{14}H_{13}NO_5Pb$	$C_{28}H_{40}Ni_2O_{16}$	$C_{14}H_{20}CoO_8$	$C_{34}H_{34}Mn_3O_{20}$	$C_{61}H_{27}Cu_6O_{41}$
Formula weight	1690.43	482.44	750.02	375.25	927.43	1797.07
Temperature/K	150(1)	150(1)	150(1)	150(1)	150(1)	150(1)
Crystal system	monoclinic	tetragonal	orthorhombic	orthorhombic	triclinic	monoclinic
Space group	I 2	P $\bar{4}2_1c$	Cmce	Cmce	P $\bar{1}$	I 2/a
a/Å	9.988(2)	19.0391(2)	16.7782(4)	16.7289(8)	9.7944(3)	22.3063(4)
b/Å	17.698(4)	19.0391(2)	12.8980(3)	13.1414(5)	13.6714(5)	18.2460(3)
c/Å	12.489(3)	8.00733(16)	17.2649(6)	16.7493(15)	16.6547(6)	21.5618(4)
α/°	90	90	90	90	83.340(3)	90.00
β/°	95.59(3)	90	90	90	84.456(3)	95.649(2)
γ/°	90	90	90	90	71.084(3)	90.00
Volume/Å^3	2197.1(8)	2902.57(9)	3736.19(18)	3682.2(4)	2091.29(13)	8733.0(3)
Z	2	8	4	8	2	4
ρ_{calc} g/cm^3	2.555	2.208	1.333	1.354	1.473	1.367
μ/mm^{-1}	15.360	11.645	1.071	0.965	0.968	1.517
Radiation	Mo Kα	Mo Kα	Mo Kα	Mo Kα	Mo Kα	Mo Kα
2Θ range for data collection/°	5.492 to 59.182	6.65 to 58.968	7.888 to 59.106	6.662 to 58.76	6.662 to 58.486	5.86 to 59.24
Reflections collected	24817	16891	8724	11461	18275	50261
Unique reflections	5531	3585	2364	2367	9558	10996
Data/restraints/parameters	5531/9/222	3585/2/198	2364/0/121	2367/21/149	9558/3/606	10996/48/489
GOOF	1.026	1.052	1.065	1.034	1.082	1.054
R_1 [I>=2σ (I)]	0.0479	0.0283	0.0293	0.0600	0.0607	0.0570
wR_2 [I>=2σ (I)]	0.0855	0.0409	0.0708	0.0978	0.1183	0.1726
Largest diff. peak/hole / e Å^{-3}	2.31/-1.81	0.87/-0.89	0.36/-0.24	0.32/-0.29	1.12/-0.63	2.42/-0.81

Table 24: *Crystallographic details of compounds* ***6*** *–* ***12****.*

Network	**13**	**14**	**pep**	**15**	**16**	**17**
Empirical formula	$C_{33}H_{18}Cu_3O_{15}$	$C_{75.34}H_{71.02}N_2O_{34.66}Zn_6$	$C_{13}H_9N$	$C_{56}H_{42}Ag_2F_{12}N_6P_2$	$C_{26}H_{18}AgF_6N_2P$	$C_{26}H_{18}AgBF_4N_2$
Formula weight	845.08	1951.22	179.21	1304.63	611.26	553.10
Temperature/K	150(1)	150(1)	150(1)	150(1)	150(1)	150(1)
Crystal system	trigonal	monoclinic	orthorhombic	triclinic	triclinic	triclinic
Space group	P $\bar{3}$m1	P 2_1/c	P $2_12_12_1$	P $\bar{1}$	P $\bar{1}$	P $\bar{1}$
a/Å	18.4689(5)	11.1171(3)	5.7718(5)	9.6598(5)	10.3864(7)	9.7678(4)
b/Å	18.4689(5)	14.9906(6)	7.4499(5)	10.4506(5)	10.5527(8)	10.4847(5)
c/Å	6.76204(18)	24.3281(8)	22.7629(19)	26.8570(15)	11.7212(9)	11.4723(6)
α/°	90	90.00	90	83.490(4)	104.522(6)	102.164(4)
β/°	90	93.217(3)	90	79.690(5)	99.244(6)	93.819(4)
γ/°	120	90.00	90	89.998(4)	92.935(6)	99.813(4)
Volume/Å^3	1997.51(13)	4047.9(2)	978.80(14)	2649.7(2)	1221.85(16)	1125.30(9)
Z	2	2	4	2	2	2
ρ_{calc} g/cm^3	1.405	1.601	1.216	1.635	1.661	1.632
μ/mm^{-1}	1.644	1.840	0.071	0.887	0.954	0.946
Radiation	Mo Kα	Mo Kα	Mo Kα	Mo Kα	Mo Kα	Mo Kα
2Θ range for data collection/°	6.024 to 58.614	5.54 to 61.08	7.16 to 58.618	6.692 to 59.018	5.378 to 58.848	6.688 to 58.55
Reflections collected	14786	33693	6503	25029	10447	8877
Unique reflections	1882	11001	2281	12242	5626	5136
Data/restraints/parameters	1882/9/105	11001/13/508	2281/0/127	12242/96/687	5626/0/345	5136/0/307
GOOF	1.059	1.154	1.105	1.015	1.052	1.044
R_1 [I>=2σ (I)]	0.0372	0.0964	0.0614	0.0946	0.0489	0.0329
wR_2 [I>=2σ (I)]	0.0850	0.2168	0.1219	0.1620	0.0737	0.0631
Largest diff. peak/hole / e Å^{-3}	0.38/-0.45	1.67/-1.21	0.25/-0.20	1.27/-1.03	0.61/-0.63	0.49/-0.53

Table 25: *Crystallographic details of compounds* ***13***, ***14***, *pep and* ***15 – 17***.

Network	**18**	**19**	**20**	**21**	**22**	**23**
Empirical formula	$C_{26}H_{18}Ag_2N_4O_4$	$C_{26}H_{18}Ag_2N_4O_6$	$C_{104}H_{88}Ag_4N_{12}O_{20}$	$C_{28}H_{21}AgN_2O_2$	$C_{28}H_{18}AgF_3N_2O_2$	$C_{28}H_{18}AgF_3N_2O_2$
Formula weight	666.18	698.18	2254.73	525.34	579.31	579.31
Temperature/K	150	150	150	150(1)	150(1)	150(1)
Crystal system	triclinic	monoclinic	orthorhombic	orthorhombic	monoclinic	monoclinic
Space group	P $\bar{1}$	P 2_1	P $na2_1$	P $na2_1$	P $2_1/c$	C 2/c
a/Å	9.1122(9)	10.0155(3)	11.0778(4)	11.1164(6)	8.5365(3)	19.3008(10)
b/Å	9.2733(9)	7.5869(2)	29.7697(13)	30.4072(19)	29.1680(12)	9.5411(5)
c/Å	15.8574(16)	16.7367(5)	7.5926(3)	7.5811(2)	9.7504(4)	26.0553(15)
α/°	75.376(8)	90	90	90	90	90
β/°	73.607(9)	100.355(3)	90	90	91.489(3)	110.332(3)
γ/°	75.656(8)	90	90	90	90	90
Volume/$Å^3$	1221.1(2)	1251.05(6)	2503.91(17)	2562.6(2)	2426.96(16)	4499.2(4)
Z	2	2	1	4	4	8
ρ_{calc} g/cm^3	1.812	1.853	1.495	1.362	1.585	1.710
μ/mm^{-1}	1.644	1.615	0.845	0.812	0.882	1.197
Radiation	Mo Kα	Mo Kα	Mo Kα	Mo Kα	Mo Kα	Mo Kα
2Θ range for data collection/°	6.584 to 58.71	6.778 to 59.058	5.366 to 58.668	4.54 to 58.66	6.578 to 58.684	6.042 to 73.226
Reflections collected	10070	5797	7996	8736	10981	4891
Unique reflections	5591	4492	4394	4493	5542	4891
Data/restraints/parameters	5591/0/331	4492/7/343	4394/1/323	4493/1/300	5542/6/325	4891/0/398
GOOF	0.989	1.010	1.094	1.196	1.043	1.068
R_1 [I>=2σ (I)]	0.0576	0.0316	0.0406	0.0635	0.0384	0.0355
wR_2 [I>=2σ (I)]	0.0674	0.0570	0.0696	0.1721	0.0682	0.0815
Largest diff. peak/hole / e $Å^{-3}$	0.66/-0.59	0.61/-0.51	0.69/-0.71	2.07/-0.85	0.72/-0.60	0.52/-0.76

Table 26: *Crystallographic details of compounds* ***18*** *–* ***23****.*

Network	**24**	**25**	**26**	**bpen**	**27**	**28**
Empirical formula	$C_{54}H_{36}Ag_2F_6N_4O_6S_2$	$C_{145}H_{108}Ag_4N_9O_{12}S_4$	$C_{14}H_9AgN_2S$	$C_{26}H_{16}$	$C_{64}H_{42}Cl_6I_6N_{12}OZn_3$	$C_{44.37}H_{24}I_{8.57}N_{12}OZn_3$
Formula weight	1230.73	2728.12	345.16	328.39	2165.30	2025.17
Temperature/K	150(1)	150(1)	100(1)	150(1)	100(2)	150(1)
Crystal system	monoclinic	monoclinic	monoclinic	monoclinic	monoclinic	monoclinic
Space group	P 2_1	C 2/c	P 2_1	P 2_1/n	C 2/c	C 2/c
a/Å	10.12120(10)	31.4069(10)	5.9402(2)	9.9151(7)	33.6915(3)	34.5945(15)
b/Å	7.62970(10)	7.0972(2)	7.6749(4)	11.6704(9)	14.64953(11)	14.8186(5)
c/Å	16.93930(10)	28.8675(10)	14.3366(6)	14.9305(10)	31.9520(3)	31.4219(12)
α/°	90	90	90	90	90	90
β/°	107.2340(10)	111.174(4)	96.730(2)	91.382(6)	99.1389(10)	100.794(4)
γ/°	90	90	90	90	90	90
Volume/Å^3	1249.35(2)	6000.2(4)	649.11(5)	1727.2(2)	15570.2(3)	15823.2(11)
Z	1	2	2	4	8	8
ρ_{calc} g/cm^3	1.636	1.510	1.766	1.263	1.847	1.700
μ/mm^{-1}	0.945	0.782	3.911	0.072	22.025	27.585
Radiation	Mo Kα	Mo Kα	Mo Kα	Mo Kα	Cu Kα	Cu Kα
2Θ range for data collection/°	4.214 to 52.312	6.58 to 50.088	7.682 to 93.366	6.982 to 58.656	8.378 to 144.512	9.82 to 132.048
Reflections collected	33721	23252	12054	7010	139605	24416
Unique reflections	4700	5306	4742	3898	15244	13225
Data/restraints/parameters	4700/1/334	5306/2/392	4742/1/164	3898/0/235	15244/0/828	13225/78/654
GOOF	1.067	1.125	1.001	1.085	1.054	1.353
R_1 [I>=2σ (I)]	0.0301	0.0428	0.0293	0.0628	0.0615	0.1341
wR_2 [I>=2σ (I)]	0.0805	0.1195	0.0530	0.1275	0.1517	0.3548
Largest diff. peak/hole / e Å^{-3}	0.42/-0.54	0.84/-0.81	0.48/-0.43	0.26/-0.26	3.15/-2.97	3.99/-2.22

Table 27: *Crystallographic details of compounds* **24** *–* **26**, *bpen and* **27** *–* **28**.

Significant atom interactions

Coordination Interaction	Atom distance (Å)	Interaction type
Pb1–O6	2.355(6)	Inner
Pb1–O5	2.611(6)	Inner
Pb1–O3	2.525(7)	Inner
Pb1–O2' (2 – x, –y, 2 – z)	3.079(6)	Outer
Pb1–O4	2.473(6)	Inner
Pb1–O4'' (1 – x, –y, 2 – z)	3.248(6)	Outer
Pb1–O2	2.526(6)	Inner
Pb1–O1	2.752(7)	Outer

Table 28: *Pb(II)–O coordination bond lengths of* ***1*** *with symmetry operators of O atoms.*

Coordination Interaction	Atom distance (Å)	Interaction type
Pb1–O1	2.695(8)	Inner
Pb1–O5	2.460(8)	Inner
Pb1–O7' (–1 + x, y, z)	2.840(8)	Outer
Pb1–O8' (–1 + x, y, z)	2.509(9)	Inner
Pb1–O9	2.509(11)	Inner
Pb1–O12' (– x, 2 – y, – z)	2.753(8)	Outer
Pb1–O14' (1 – x, 2 – y, – z)	3.134(8)	Outer
Pb1–O13' (–1 + x, y, z)	3.036(9)	Outer
Pb1–O6	2.606(8)	Inner
Pb2–O7	2.411(9)	Inner
Pb2–O1	2.882(8)	Outer
Pb2–O2' (1 + x, y, z)	2.436(8)	Inner
Pb2–O10	2.648(12)	Inner
Pb2–O4	2.415(8)	Inner
Pb2–O3	2.586(8)	Inner
Pb2–O11	3.106(8)	Outer
Pb3–O3	2.875(8)	Outer
Pb3–O13' (1 – x, 2 – y, – z)	2.540(8)	Inner
Pb3–O6	2.826(8)	Outer
Pb3–O13' (–1 + x, y, z)	3.092(7)	Outer
Pb3–O14' (–1 + x, y, z)	2.476(8)	Inner
Pb3–O15	2.647(9)	Inner
Pb3–O12	2.474(8)	Inner
Pb3–O11	2.512(8)	Inner

Table 29: *Pb(II)–O coordination bond lengths of* ***2*** *with symmetry operators of O atoms.*

Coordination Interaction	Atom distance (Å)	Interaction type
Pb1–O5	2.484(6)	Inner
Pb1–O4' (x, 1 + y, z)	3.021(5)	Outer
Pb1–O6	2.904(3)	Outer
Pb1–O4' (1 – x, 2 – y, z)	2.910(6)	Outer
Pb1–O1	2.429(5)	Inner
Pb1–O2	2.514(5)	Inner
Pb1–O4' (1 – x, y, 2 – z)	2.786(4)	Outer
Pb1–O3' (1 – x, y, 2 – z)	2.372(4)	Inner

Table 30: *Pb(II)–O coordination bond lengths of* ***3*** *with symmetry operators of O atoms.*

Coordination Interaction	Atom distance (Å)	Interaction type
Pb1–O4' (½ – x, ½ – y, 1 – z)	2.837(5)	Outer
Pb1–O1	2.415(6)	Inner
Pb1–O2	2.531(6)	Inner
Pb1–O5	2.646(7)	Inner
Pb1–O3' (1 – x, y, $^3/_2$ – z)	2.440(5)	Inner
Pb1–O3' (x, y, 1 + z)	2.876(6)	Outer
Pb1–O4' (x, y, 1 + z)	2.520(6)	Inner

Table 31: *Pb(II)–O coordination bond lengths of* ***4*** *with symmetry operators of O atoms.*

Coordination Interaction	Atom distance (Å)	Interaction type
Pb1–O10' (2 – x, 1 – y, 2 – z)	2.719(8)	Outer
Pb1–O10	2.448(7)	Inner
Pb1–O3	2.506(7)	Inner
Pb1–O1	2.414(8)	Inner
Pb1–O7' (1 – x, 1 – y, 2 – z)	2.817(8)	Outer
Pb1–O4' (x, –1 + y, z)	2.989(7)	Outer
Pb2–O2' (x, 1 + y, z)	2.410(7)	Inner
Pb2–O1' (x, 1 + y, z)	2.771(7)	Outer
Pb2–O4	2.407(8)	Inner
Pb2–O4 (1 – x, 2 – y, 2 – z)	2.975(7)	Outer
Pb2–O7	2.639(8)	Inner
Pb2–O9	2.330(8)	Inner

Table 32: *Pb(II)–O coordination bond lengths of* ***5*** *with symmetry operators of O atoms.*

Coordination Interaction	Atom distance (Å)	Interaction type
Pb1–O3' (1 – x, y, 1 – z)	2.414(10)	Inner
Pb1–O3' (1 + x, y, z)	2.884(12)	Outer
Pb1–O4' (1 + x, y, z)	2.604(15)	Inner
Pb1–O5	2.862(12)	Outer
Pb1–O1	2.428(14)	Inner
Pb1–O2	2.451(11)	Inner
Pb1–O9	2.640(14)	Inner
Pb2–O4	2.622(14)	Inner
Pb2–O7	2.319(15)	Inner
Pb2–O8	2.565(10)	Inner
Pb2–O6' (1 – x, y, 2 – z)	2.482(10)	Inner
Pb2–O9' (– 1 + x, y, z)	2.880(12)	Outer
Pb2–O5' (– 1 + x, y, z)	2.381(14)	Inner

Table 33: *Pb(II)–O coordination bond lengths of* ***6*** *with symmetry operators of O atoms.*

Coordination Interaction	Atom distance (Å)	Interaction type
Pb1–O5' (½ + x, –½ + y, –½ + z)	3.165(6)	Outer
Pb1–O4' (½ + x, ½ – y, ½ – z)	2.788(5)	Outer
Pb1–O5	2.693(5)	Inner
Pb1–O2	2.446(4)	Inner
Pb1–O3' (1 – x, + y, – z)	2.396(5)	Inner
Pb1–O1	2.527(4)	Inner
Pb1–O4' (1 – x, + y, – z)	2.777(5)	Outer
Pb1–O2' (½ + x, –½ + y, –½ + z)	2.705(5)	Outer

Table 34: *Pb(II)–O coordination bond lengths of* ***8*** *with symmetry operators of O atoms.*

Coordination Interaction	Atom distance (Å)
Ni1–O1	2.0351(10)
Ni1–O4	2.0696(11)
Ni1–O3	2.0672(14)
Ni1–O4 (x, – y, 1 – z)	2.0696(11)
Ni1–O1 (x, – y, 1 – z)	2.0351(10)
Ni1–O3 (x, – y, 1 – z)	2.0672(14)

Table 35: *Ni(II)–O coordination bond lengths of* ***9****.*

Coordination Interaction	Atom distance (Å)
Co1–O4	2.069(3)
Co1–O2	2.103(2)
Co1–O3	2.068(2)
Co1–O4' (½ – x, ½ – y, 1 – z)	2.069(3)
Co1–O2' (½ – x, ½ – y, 1 – z)	2.103(2)
Co1–O3' (½ – x, ½ – y, 1 – z)	2.068(2)

Table 36: *Co(II)–O coordination bond lengths of* ***10****.*

Coordination Interaction	Atom distance (Å)
Mn1–O1	2.166(3)
Mn1–O2	2.106(3)
Mn1–O3	2.201(2)
Mn1–O1 (2 – x, – y, – z)	2.166(3)
Mn1–O2 (2 – x, – y, – z)	2.106(3)
Mn1–O3 (1 – x, – y, – z)	2.201(2)
Mn2–O3 (1 + x, y, z)	2.249(3)
Mn2–O4	2.175(3)
Mn2–O7	2.207(3)
Mn2–O8	2.118(3)
Mn2–O6 (1 + x, y, z)	2.374(3)
Mn2–O5	2.093(3)
Mn3–O9	2.100(3)
Mn3–O11	2.134(3)
Mn3–O13 (– x, 1 – y, 1 – z)	2.199(3)
Mn3–O9 (1 – x, 1 – y, 1 – z)	2.100(3)
Mn3–O11 (1 – x, 1 – y, 1 – z)	2.134(3)
Mn3–O13 (1 + x, y, z)	2.199(3)
Mn4–O10 (1 – x, 1 – y, 1 – z)	2.114(3)
Mn4–O15	2.164(3)
Mn4–O14 (1 + x, y, z)	2.359(3)
Mn4–O54	2.154(3)
Mn4–O13 (1 + x, y, z)	2.308(3)
Mn4–O11	2.420(3)
Mn4–O12	2.318(3)

Table 37: *Mn(II)–O coordination bond lengths of* ***11****.*

Coordination Interaction	Atom distance (Å)
Cu1···Cu2	2.6208(7)
Cu1–O9	1.962(3)
Cu1–O5	1.982(3)
Cu1–O13	2.144(3)
Cu1–O1	1.951(3)
Cu1–O7 (1 – x, ½ + y, ½ – z)	2.016(3)
Cu2–O6	1.926(3)
Cu2–O10	1.965(3)
Cu2–O14	2.144(4)
Cu2–O8 (1 – x, ½ + y, ½ – z)	1.931(3)
Cu2–O2	1.954(3)
Cu3···Cu3 (3/2 – x, y, – z)	2.6247(9)
Cu3–O3 (1 – x, – ½ + y, ½ – z)	1.979(3)
Cu3–O4 (½ + x, – ½ + y, – ½ + z)	1.933(3)
Cu3–O15	2.137(3)
Cu3–O12 (3/2 – x, y, – z)	2.032(3)
Cu3–O11	1.939(3)

Table 38: *Cu(II)–O coordination bond lengths of* ***12****.*

Coordination Interaction	Atom distance (Å)
Cu1···Cu1 (1 – x, 1 – y, 1 – z)	2.6033(6)
Cu1–O1 (1 – x, 1 – y, 1 – z)	1.9582(17)
Cu1–O1 (x, y, 1 – z)	1.9582(17)
Cu1–O3	2.1397(18)
Cu1–O2	2.036(8)
Cu1–O2 (1 – x, 1 – y, z)	2.036(8)

Table 39: *Cu(II)–O coordination bond lengths of* ***13****.*

Coordination Interaction	Atom distance (Å)
Zn1–O9	2.494(8)
Zn1–O1	1.997(5)
Zn1–O5 (1 + x, y, z)	1.930(5)
Zn1–O10	2.021(5)
Zn1–O11 (2 – x, ½ + y, ½ – z)	1.911(6)
Zn2–O1	2.059(5)
Zn2–O6 (1 + x, y, z)	2.023(6)
Zn2–O15	2.088(6)
Zn2–O2	2.143(5)
Zn2–O3	2.035(6)
Zn3–O1	1.984(5)
Zn3–O4	1.932(6)
Zn3–O7 (2 – x, ½ + y, ½ – z)	1.919(6)
Zn3–O14	1.960(5)

Table 40: *Zn(II)–O coordination bond lengths of* ***14****.*

Coordination Interaction	Interaction length (Å)
Ag1–N3	2.145(7)
Ag1–N4	2.165(7)
Ag2–N1	2.138(8)
Ag2–N2	2.132(7)
Ag1–N5	2.80(1)
Ag2–N6	2.821(10)
Ag1···F4	3.454(10)
Ag1···F5	3.435(10)
Ag2···F7	3.324(10)
Ag2···F8	3.343(9)

Table 41: *Ag(I)–X interactions within* ***15****.*

Coordination Interaction	Interaction length (Å)
Ag1–N1	2.132(2)
Ag1–N2	2.138(2)
Ag1···F4	3.449(4)
Ag1···F6	3.32(8) – 3.80(3)
Ag1···F3	2.65(1) – 2.85(3)
Ag1···F3' (1 – x, 1 – y, 1 – z)	3.181(13) – 3.41(2)

Table 42: *Ag(I)–X interactions of* ***16****. Atoms F6 and F3 are disordered over two positions.*

Coordination Interaction	Interaction length (Å)
Ag1–N1	2.1426(19)
Ag1–N2	2.1421(18)
Ag1···F3	2.7296(17)
Ag1···F4	2.8041(15)
Ag2···F4' (2 – x, 1 – y, 1 – z)	3.1862(16)

Table 43: *Ag(I)–X interactions of* ***17****.*

Coordination Interaction	Interaction length (Å)
Ag1–N4	2.833(6)
Ag1–N2	2.218(4)
Ag1–O2' (1 – x, – y, 1 – z)	2.867(4)
Ag1–N3	2.740(5)
Ag1–N1	2.214(4)
Ag1–O3' (1 – x, 1 – y, 1 – z)	2.904(4)
Ag2–O4' (1 – x, – y, 1 – z)	3.042(5)
Ag2–O1' (– x, – y, 1 – z)	2.705(5)
Ag2–O2' (– x, – y, 1 – z)	2.416(4)
Ag2–O4' (– 1 + x, y, z)	3.042(5)
Ag2–O1	2.414(5)
Ag2–O2	2.416(4)
Ag3–O1' (1 + x, y, z)	3.050(6)
Ag3–O4	2.256(6)
Ag3–O3	2.567(6)
Ag3–O4' (2 – x, 1 – y, 1 – z)	2.474(6)
Ag3–O3' (2 – x, 1 – y, 1 – z)	2.316(6)

Table 44: *Ag(I)–N/O coordination bond lengths of* ***18*** *with symmetry operators of O atoms.*

Coordination Interaction	Interaction length (Å)
Ag1···Ag2	2.9704(6)
Ag1–N1	2.168(4)
Ag1–N2	2.184(4)
Ag1–O6' $(1-x, \frac{1}{2}+y, -z)$	2.681(4)
Ag1–O4' $(1-x, \frac{1}{2}+y, -z)$	3.132(5)
Ag1–O6' $(x, 1+y, z)$	2.603(4)
Ag1–O5' $(x, 1+y, z)$	3.078(5)
Ag2–O1	2.453(5)
Ag2–O2	2.500(5)
Ag2–O4	2.310(5)
Ag2–O5	3.005(5)
Ag2–O1' $(-x, -\frac{1}{2}+y, -z)$	2.468(5)
Ag2–O3' $(-x, -\frac{1}{2}+y, -z)$	2.720(5)

Table 45: *Ag(I)–X interactions of* ***19*** *with symmetry operators of O atoms.*

Coordination Interaction	Interaction length (Å)
Ag1–N1	2.181(3)
Ag1–N2	2.193(4)
Ag1–O2	3.112(6)
Ag1–O1	2.642(5)
Ag1–O1' $(-x, 1-y, -\frac{1}{2}+z)$	2.638(4)
Ag1–O2' $(-x, 1-y, \frac{1}{2}+z)$	3.061(5)

Table 46: *Ag(I)–X interactions of* ***20*** *with symmetry operators of O atoms.*

Coordination Interaction	Interaction length (Å)
Ag1–N1	2.285(8)
Ag1–N2	2.267(8)
Ag1–O1	2.484(8)
Ag1–O2	2.708(10)
Ag1–O1' $(1-x, 1-y, \frac{1}{2}+z)$	2.551(7)

Table 47: *Ag(I)–X interactions of* ***21*** *with symmetry operators of O atoms.*

Coordination Interaction	Interaction length (Å)
Ag1···Ag1'	3.1209(5)
Ag1–N1	2.176(2)
Ag1–N2	2.175(2)
Ag1–O1	2.613(2)
Ag1–O2' $(1-x, 1-y, 1-z)$	2.7805(19)

Table 48: *Ag(I)–X interactions of* **22** *with symmetry operators of O atoms.*

Coordination Interaction	Interaction length (Å)
Ag1···Ag1'	3.1829(6)
Ag1–N1	2.186(3)
Ag1–N2	2.182(3)
Ag1–O2	2.861(3)
Ag1–O1	2.550(3)
Ag1–O1' (½– x, $^{3}/_{2} - y$, $1 - z$)	2.827(3)

Table 49: *Ag(I)–X interactions of* **23** *with symmetry operators of O atoms.*

Coordination Interaction	Interaction length (Å)
Ag1–N1	2.139(3)
Ag1–N2	2.153(4)
Ag1–O1	2.906(4)
Ag1–O2' ($1 - x$, ½ + y, $1 - z$)	2.751(5)
Ag1–O3' ($1 - x$, – ½ + y, $1 - z$)	2.969(4)

Table 50: *Ag(I)–X interactions of* **24** *with symmetry operators of O atoms.*

Coordination Interaction	Interaction length (Å)
Ag1–N1	2.170(3)
Ag1–N2	2.175(4)
Ag1–O1	2.636(3)
Ag1–O2' ($1 - x$, $2 - y$, $1 - z$)	2.831(3)
Ag1–O3' ($1 - x$, $1 - y$, $1 - z$)	2.863(3)

Table 51: *Ag(I)–X interactions of* **25** *with symmetry operators of O atoms.*

Coordination Interaction	Interaction length (Å)
Ag1–N1	2.305(3)
Ag1–N2	2.165(3)
Ag1–S1' (– x, – ½ + y, $2 - z$)	2.6138(9)
Ag1–S1' ($1 + x$, y, z)	2.6404(9)

Table 52: *Ag(I)–X interactions of* **26** *with symmetry operators of S atoms.*

Published crystallographic data for crystal structures **1** – **8**, **12** and **14** – **28** can be obtained free of charge from the Cambridge Crystallographic Data Centre *via* [https://www.ccdc.cam.ac.uk/structures/]. Supplementary electronic .cif files can be found in the Supplementary Electronic Files CD attached to this thesis.

References:

[1] Beamline 11.3.1. at The Lawrence Berkeley laboratory ALS. Website: [http://chemcryst.lbl.gov/]

[2] Francart, T.; van Wieringen, A.; Wouters, J., *J. Neurosci. Methods,* **2008**, *172*, 283-293.

[3] Sheldrick, G. M., *SADABS: Program for Empirical Absorption Correction*, University of Gottingen: Germany, **1996**.

[4] SMART, SAINT and XPREP programs are part of Bruker crystallographic software package for single crystal data collection, reduction and preparation.

[5] Dolomanov, O. V.; Bourhis, L. J.; Gildea, R. J.; Howard, J. A. K.; Puschmann, H., *J. Appl. Cryst.* **2009**, 42, 339-341.

[6] Sheldrick, G. M., *Computational Crystallography,* Delft University Press: Delft, **1978**.

[7] Sheldrick, G. M., *Acta Crystallogr. A. Found. Adv.,* **2015**, *71*, 3-8.

[8] Macrae, C. F.; Bruno, I. J.; Chisholm, J. A.; Edgington, P. R.; McCabe, P.; Pidcock, E.; Rodriguez-Monge, L.; Taylor, R.; van de Streek, J.; Wood, P. A., *J. Appl. Crystallogr.,* **2008**, *41*, 466-470.

[9] Barbour, L. J., *J. Supramol. Chem.,* **2001**, *1*, 189-191.

[10] Persistence of Vision Pty. Ltd., Persistence of Vision Raytracer, **2004**. Computer software retrieved from: [http://www.povray.org/download/]

[11] Spek, A. L., *Acta Crystallogr. C. Struct. Chem.*, **2015**, *71*, 9-18.